PALEOENVIRONMENTAL HISTORY OF THE CHILEAN FJORD REGION AND THE ADJACENT SOUTHEAST PACIFIC OVER THE LAST 60 kyr BP: A MULTIPROXY ANALYSIS ON HIGH RESOLUTION SEDIMENT CORES

Dissertation zur Erlangung des Doktorgrades
am Fachbereich Geowissenschaften
der Universität Bremen

vorgelegt von

ANA MAGALY CANIUPAN
Alfred Wegener Institute for Polar and Marine Research

Bremen, April 2011

To my parents Ana y Domingo

Abstract

The Chilean Fjord region offers a unique opportunity to study past oceanographic and environmental changes as it is the only land mass in the Southern Hemisphere intercepting the Southern Westerly Winds (SWW) which are of global significance. Three sediment cores from the Chilean Fjord region and the adjacent southeast Pacific were used to study past sea surface temperature variations and their relationship to climate changes during most of the last glacial period and the Holocene. Core MD07-3128 was recovered at ~53°S at the Pacific entrance of the Strait of Magellans. Carbon-14 ages and paleomagnetic chronology indicate that core MD07-3128 covers the last ~60 kyr BP. Its high-sedimentation rates allow to depict millennial-scale sea surface temperature (SST) and paleoproductivity changes over the last ~60 kyr BP. Cores MD07-3124 and JPC-42, on the other hand, were recovered at ~51° S and ~50°S, from Canal Concepción and Canal Wide, respectively. These cores were used to reconstruct the first continuous SST records over the entire Holocene.

Alkenone-derived SST data from the southernmost record MD07-3128 (~53°S) show that glacial temperatures were *ca*. 7 °C colder than early Holocene SST values. Substantial millennial-scale variability of 2–3 °C characterized the last glacial period, while a very strong warming of ~7 °C was recorded over the last deglaciation. A cooling trend culminating during the Last Glacial Maximum (LGM) has been recorded. This regional cooling has been related to the proximal location of the core site to the large Patagonian Ice Sheet (PIS) and related melt-water supply, at least during the LGM. An increase in the relatively abundances of $C_{37:4}$ alkenones, a proxy for low salinity waters, support the idea of large meltwater input during this time interval. On millennial-scale time scales, changes in marine plankton productivity were also recorded. An increase in the siliceous plankton community over the calcareous characterized the colder intervals while during the warmer ones this pattern was reversed. These marine productivity changes can be associated with a northward shift of the Southern Ocean fronts and the opal belt during glacial cold periods and/or changes in the nutrient advection consistent with our lower planktonic foraminiferal $\delta^{13}C$ data. Interestingly, the siliceous community was comparatively lower around the LGM suggesting a reduced biological productivity probably due to enhanced melt-water input from the large PIS resulting in high surface water stratification.

During the Holocene, cores JPC-42 and MD07-3124 show no evidence for an early Holocene climate optimum as previously described for the Chilean continental margin further north. In contrast, SST were warmer than present during most of the Holocene except for the prominent cooling centered at ~5 kyr BP and the cooling trend recorded in the latest Holocene. The absence of an early Holocene warm phase in the inner fjord has been associated with a combination of factors including decreased inflow of open marine waters due to lower sea-level, enhanced advection of colder and fresher inner fjord water, stronger westerly wind, and reduced local summer insolation. The fact that alkenones in the inner fjord core JPC-42 (located near to the southern Patagonian icefield) were only present after ~8 kyr BP point to substantially reduced surface water salinities during the early Holocene, strongly consistent with increasing precipitation and runoff in the core of the SWW.

A comparison of SST results based on core MD07-3124 and terrestrial proxy data for glacier clay input provide additional insights for forcing mechanisms of glacier changes in the southernmost Andes during the Holocene. These records show that glaciers from the southern Patagonian icefield advanced even when regional SSTs were relatively high. The main glacier advances labeled A6-A1 occurred only partly during regional cooling intervals (e.g., A2 and A6). Other glacier advances, (e.g., A5) occurred during warmer phases like the globally known Medieval Warm Period (MWP). Taken together, these results show that glacier advances, in very humid and westerly wind influenced mountain range areas, are driven by a strong increase in accumulation mass-balance and only by minor temperature changes.

During the latest Holocene, on the other hand, a cooling of *ca*. 2 °C was recorded. The comparison with previously published high-resolution SST records from the Chilean margin and Northern Patagonia fjords shows that this cooling was not a local event but a regional feature affecting an area of ca. 10° latitude from ~41°S to ~51°S. In the offshore records (GeoB 3313-1; 41°S and GeoB 7186; 44°S) this cooling has a substantially lower amplitude compared with the highest amplitude recorded in the Jacaf fjord (PC33; ~44°S) and in the inner SST fjord records (JPC-42 and MD07-3124), suggesting an amplification of the SST signal in the interior of the Chilean fjords and corroborating the high sensitivity of the fjord system for tracking regional climate changes.

Kurzfassung

Die chilenische Fjordregion bietet eine einzigartige Gelegenheit, frühere ozeanographische und ökologische Veränderungen zu studieren, da sie die einzige Landmasse in der südlichen Hemisphäre darstellt, die von den global bedeutenden südhemisphärischen Westwinden (SHW) ganzjährig beeinflusst wird. Es wurden drei Sedimentkerne aus der chilenischen Fjordregion und des angrenzenden südöstlichen Pazifiks verwendet, um frühere Temperaturschwankungen der Meeresoberfläche und ihre Beziehung zu Klimaveränderungen während des größten Teils der letzten Eiszeit und dem Holozän zu untersuchen. Der Sedimentkern MD07-3128 wurde bei etwa 53°S vor dem pazifischen Eingang der Magellanstraße gewonnen. Das ^{14}C-Alter und die paläomagnetische Chronologie zeigen, dass der Kern MD07-3128 Sedimentabfolgen der letzten rund 60.000 Jahre umfasst. Seine hohen Sedimentationsraten erlauben die detaillierte Analyse von Veränderungen der Wasseroberflächentemperaturen (SST) und der Paläoproduktivität in dieser Zeitspanne. Die weiteren Sedimentkerne MD07-3124 und JPC-42 stammen hingegen aus den Fjorden in der Region des Canal Concepción und Canal Wide, bei ca. 51°S und ca. 50°S. Mit Hilfe dieser Kerne wurden die ersten Paläo-SST Datensätze aus den chilenischen Fjorden für das gesamte Holozäns erstellt.

Alkenon-basierende SST-Daten des am Kontinentalhang gelegenen Kerns MD07-3128 (53°S) zeigen, dass die Temperaturen während der letzten Eiszeit bis zu ca. 7°C niedrigerals während des frühen Holozäns waren. Erhebliche SST-Schwankungen von 2-3°C im Jahrtausend-Zeitbereich charakterisieren die letzte Eiszeit. Darüber hinaus lässt sich eine längerfristige Tendenz zur Abkühlung erkennen, die während des letzten glazialen Maximums (LGM) ihren Höhepunkt fand. Diese regionale Abkühlung steht in Zusammenhang mit der Nähe der Bohrlokation zum patagonischen Eisschild (PIS) und der damit verbundenen Menge an Schmelzwasser insbesondere während des LGMs. Eine Erhöhung der relativen Häufigkeiten von $C_{37:4}$ Alkenonen, charakteristisch für niedrigere Salzgehalte, bekräftigte die Idee großer Schmelzwasserzufuhr während dieser Zeitspanne. Auf identischen Zeitskalen wurden ebenfalls Veränderungen der Produktivität des marinen Planktons erfasst. Eine Erhöhung der Anteile des kieselsäurehaltigen Planktons gegenüber dem kalkhaltigen Plankton charakterisiert die kälteren Perioden, während Perioden der Erwärmung ein umgekehrtes Muster zeigen. Diese Produktivitätsänderungen deuten auf eine substanzielle Verschiebung der Südozeanfronten und des “opal belt“ während der eiszeitlichen Kälteperioden hin. Dieser Befund steht im Einklang mit Kohlenstoffisotopendaten (δ^{13}C) an planktonischen Foraminiferen , die auf Änderungen des Nährstofftransports hindeuten. Interessanterweise war der Anteil des kieselsäurehaltigen Planktons während des LGM vergleichsweise kleiner, was auf eine reduzierte biologische Produktivität vermutlich wegen des erhöhten Schmelzwasserzuflusses vom PIS und der damit verbundenen Wassermassen-Stratifizierung zurückzuführen ist.

Während des Holozäns zeigen die Sedimentkerne GPA-42 und MD07-3124 keine Anzeichen für ein klimatisches Optimum des frühen Holozäns wie zuvor für den weiter nördlich gelegenen chilenischen Kontinentalrand beschrieben. Die Oberflächentemperaturen waren während großer Teile des Holozäns sogar höher als heutzutage, außer während einer markanten Abkühlungsphase vor ca. 5.000 Jahren. Das Fehlen einer Erwärmungsphase im

inneren Fjordbereich kann mit vielen Faktoren in Verbindung gebracht werden, wie vermindertem Zufluss von relativ warmen Oberflächenwasser des offenen Ozeans aufgrund eines niedrigeren Meeresspiegels, verstärkte Advektion von kälterem und relativ salzärmeren Wasser des inneren Fjordes, stärkeren Westwinden sowie regional verminderter Sonneneinstrahlung. Die Tatsache, dass Alkenone im Sedimentkern GPA-42 des inneren Fjordbereichs (in der Nähe des südlichen patagonischen Eisfeldes) nur in Schichten älter als 8.000 Jahre nachweisbar waren, lässt auf einen wesentlich reduzierten Salzgehalt des Oberflächenwassers im frühen Holozän schließen, verbunden mit erhöhtem Niederschlag und Abfluss im Einflussbereich der südlichen Westwinde (SWW).

Ein Vergleich der Oberflächentemperaturen (SST) basierend auf dem Sedimentkern MD07-3124 und verschiedenen Proxy-Daten für Gletscherschwankungen bieten zusätzliche Einblicke in die Antriebsmechanismen für die Veränderung der Gletscher in der südlichsten Andenregionen während des Holozäns. Diese Befunde zeigen, dass sich die Gletscher aus dem südlichen patagonischen Eisfeldern auch dann vorstießen, wenn die lokalen Oberflächenwassertemperaturen relativ hoch waren. Die hauptsächliche Ausbreitung der Gletscherverstöße A6-A1 erfolgte nur teilweise während der lokalen Abkühlungsperioden (z.B., A2 und A6). Andere Gletscherverstöße (z.B. A5) erfolgten dagegen während der wärmeren Phasen, wie z.B. der weltweit bekannten mittelalterlichen Wärmeperiode (MWP). Insgesamt zeigen diese Ergebnisse, dass die Ausbreitung von Gletschern in sehr feuchten und von Westwinden beeinflussten Gebirgsregionen durch erhöhte Niederschläge und nur geringe Temperaturschwankungen verursacht werden.

Andererseits wurde während des jüngsten Holozäns eine Abkühlung von ca. 2°C gemessen. Der Vergleich mit bisher veröffentlichten hochaufgelösten Messungen der Oberflächenwassertemperaturen vom chilenischen Kontinentalhang und den nördlichen patagonischen Fjorden zeigt, dass es sich bei dieser Abkühlung nicht um ein lokales Ereignis, sondern um eine regional Abkühlung, die sich über mindestens 10 Breitengraden erstreckte (von ca. 41°S bis ca. 51°S). Im offenen Ozeanbereich, am Kontinentalhang (GeoB 3313-1; 41°S und GeoB 7186; 44°S) ergaben die Messungen der Abkühlung eine wesentlich geringere Amplitude verglichen mit der höchsten Amplitude, die im Jacaf Fjord (PC33, ca. 44°S) und in den inneren Fjorden (GPA-42 und MD07-3124) aufgezeichnet wurde, was auf eine Verstärkung des SST Signals im Inneren der chilenischen Fjorde hindeutet und die hohe Empfindlichkeit des Fjordsystems für regionaler Klimaänderungen bestätigt.

Resumen

La región de los fiordos Chilenos ofrece oportunidades únicas para estudiar cambios oceanográficos y climáticos en el pasado debido a que es la única área en el Hemisferio Sur que intercepta los vientos de deriva del oeste (westerlies) que tienen una importancia climática global. Tres testigos de sedimento marino extraídos desde la región de los fiordos Chilenos y del océano Pacífico suroriental fueron utilizados para estudiar las variaciones de la temperatura superficial del mar (sea surface temperature; SST) y su relación con cambios climáticos ocurridos durante el último periodo glacial y el Holoceno. El testigo MD07-3128 fue obtenido a los ~53°S desde la entrada pacífica del Estrecho de Magallanes. Las edades radiocarbono y la cronología paleomagnética indican que el testigo MD07-3128 cubre los últimos 60 mil años antes del presente (thousand of years before the present; kyr BP). Sus altas tasas de sedimentación permiten discutir cambios en SST y productividad marina a escala de tiempo de milenios. Los testigos MD07-3124 y JPC-42, por otra parte, fueron recuperados a los ~51°S y ~50° desde el canal Concepción y canal Wide, respectivamente. Estos testigos fueron utilizados para reconstruir el primer registro continuo de SST durante el Holoceno.

La SST derivada de las alquenonas en el testigo MD07-3128, el testigo más austral de este estudio, revela que durante el último período glacial la SST fue *ca*. 7°C más fría que durante el Holoceno temprano. El último período glacial fue caracterizado por una variabilidad en SST de 2–3°C en escala de milenios. La deglaciación, por otra parte, fue caracterizada por un fuerte calentamiento de 7°C. Un enfriamiento regional que culmina cerca del último glacial máximum (Last Glacial Maximum; LGM) también es registrado. Este enfriamiento regional estaría asociado a la cercanía del testigo al casquete de hielo de la Patagonia (Patagonian Ice Sheet; PIS) y a su deshielo, al menos durante el LGM. El incremento en las abundancias de las tetra-insaturadas alquenonas ($C_{37:4}$) soportan esta interpretación ya que ha sido previamente sugerido que un aumento en su abundancia reflejaría un incremento en el aporte de aguas bajas en salinidad. Este testigo también muestra que a escala de milenios se produjeron importantes cambios en la comunidad plantónica. Un incremento en la comunidad silícea por sobre los calcareos caracterizó los períodos más fríos, en cambio durante los períodos más cálidos, este patrón fue inverso. El incremento en la comunidad silícea (principalmente diatomeas) en los períodos más fríos podría estar relacionado a una migración de los frentes oceánicos que rodean la Antarctica, incluyendo una migración hacia el norte del "opal belt" (un área de gran exportación de ópalo), o a cambios en la advección de nutrientes, como lo sugiere los bajos valores de isótopos de carbono ($\delta^{13}C$) medidos en foraminíferos plantónicos. Resulta interesante que la comunidad silícea y la calcárea fuese comparativamente más baja alrededor del LGM lo que sugiere una reducción en la productividad primaria. Esta disminución en productividad podría estar relacionada al incremento del agua de deshielo proveniente del PIS y al efecto de la estratificación superficial.

Durante el Holoceno, los testigos JPC-42 y MD07-3124 no muestran evidencia de un clima óptimo ocurrido en el Holoceno temprano, a diferencia de lo observado en registros de paleotemperatura localizados más al norte en el margen Chileno. Por el contrario, las SST fueron más cálidas que el presente durante la mayor parte del Holoceno, excepto por el prominente enfriamiento observado a los ~5 kyr BP y la tendencia al enfriamiento observado

durante el Holoceno tardío. La ausencia de un clima óptimo durante el Holoceno temprano en los fiordos chilenos ha sido asociado a una combinación de factores incluyendo un menor aporte de las aguas oceánicas debido a un bajo nivel del mar, un incremento en el aporte de aguas frías y frescas proveniente de los fiordos, fuertes westerlies y/o una disminución en la insolación de verano. El hecho de que las alquenonas no estuviesen presentes en el testigo JPC-42 previo a los ~8 kyr BP sugiere una disminución de la salinidad durante el Holoceno temprano, esto sería congruente con recientes investigaciones que sugieren un incremento en precipitación y correntía costera, en el área del núcleo de los westerlies, durante el Holocene temprano.

Una comparación de los datos de SST del testigo MD07-3124 con indicadores terrestres de aporte de arcilla glacial en Patagonia, otorga adicionales señales de los mecanismos que fuerzan cambios en la actividad de los glaciares en el sur de Chile durante el Holoceno. Estos registros muestran que los glaciares de campo de Hielo Sur avanzaron incluso cuando las temperaturas regionales fueron más cálidas. Los principales avances de glaciares, denominados A6-A1 ocurrieron parcialmente durante intervalos de enfriamiento regional (ej. A2 and A6). Otros glaciares, en cambio, avanzaron (ej. A5) en épocas más cálidas como en el Período Cálido del Medioevo ocurrido globalmente. Estos resultados muestran que los avances de glaciares, en áreas muy húmedas e influenciadas por los westerlies, estarían conducidos por fuertes incrementos en el balance de acumulación de masa y en menor grado por cambios en SST.

Durante el Holoceno tardío, por otra parte, una tendencia al enfriamiento con una magnitud de *ca*. 2°C fue observado. Al comparar estos nuevos datos de SST con previas reconstrucciones obtenidas desde el margen Chileno y fiordos localizados en Patagonia Norte, se observa que este enfriamiento no es un evento local sino un evento regional afectando un área de 10° de latitud, desde los ~41°S hasta ~51°S. En los testigos más oceánicos (GeoB-3313; 41°S y GeoB 7186; 43°S) este enfriamiento tiene una amplitud mas baja comparada con las altas amplitudes registradas en el fiordo Jacaf (PC33; ~44°S) así como también en los testigos localizados dentro de los fiordos (JPC-42 y MD07-3124), lo que sugiere una amplificación de la señal de SST en el interior de los fiordos Chilenos corroborando la alta sensibilidad de los sistemas de fiordos para el estudio de cambios climáticos regionales.

Acknowledgments

I would like to thank so many people that directly or indirectly contributed to this work.

First of all, I would like to thank Frank Lamy, my supervisor. Frank is one of those persons you never forget; he has been a big influence in my life and work. Thanks Frank for your fruitful advices, for your enthusiasm and motivation, for your human and friendly being and for giving me the opportunity to perform my PhD. at the Alfred Wegener Institute (AWI). I also want to thank Ralf Tiedemann, the chair of the department, and also member of my thesis committee. Thanks Ralf for assessing this work together with Frank.

From the University of Concepción, I would like also to say thank you to Carina Lange, for encouraging me to initiate my PhD. at AWI, also for her valuable contribution to my work and for acting as a second reviewer of this thesis. Thank you also to Lilian Nuñez, for her guidance in the analysis of alkenones and also for her friendship. I also thank Silvio Pantoja who has introduced me to the world of alkenones during my master studies at UDEC.

From the University of Bremen, I thank Gesine Mollehauer for giving me the opportunity to work at the "alkenone" laboratory and for her great advices and discussions of data. I am also grateful to Raph Kreutz for his help and advices in the lab.

Thank you also to people from other universities with whom I discussed data and for their helpful ideas, especially, Helge Arz and Rolf Kilian. I also want to thank several collegues that have put to my disposal unpublished data for this thesis, especially Tania Leon, Julia Wellner, Silvio Pantoja and Naomi Harada.

I am also grateful to Reza Ahi and Hendrik Grotheer for helping me with the sampling of the sediment cores and the processing of samples. I especially thank Axel Dreumer, Sze Ling Ho and Gema Martínez-Méndez for the last minute corrections of this thesis.

Furthermore, I would like to thank my dear friends with whom I shared all these years in Bremen, Isabel Caamaño, Eusevia Torrico, Catalina González, Rosana Herrero, Sergio Contreras, Libertad Chavez, Jonathan Montalvo, Alejandro Espinoza, Natalia Zapata, Nicole Schmal, Loreto Vío, Citlali Guerra, María Zuluaga, Daniel Rincón, Gina Paola, Katherine Cuevas, Thomas, María Paz Esquella, Claudia and Pamela. I also want to thank my colleagues at AWI for their support and friendship and to the laboratory staff for technical help.

Finally, I would like to thank my family, specially my parents Ana and Domingo, my sister Mony and brother Kike for their unconditional support, love and friendship.

CONTENTS

ABSTRACT **iii**
KURZFASSUNG **v**
RESUMEN **vii**
LIST OF FIGURES **xiii**
LIST OF TABLES **xiv**

1 INTRODUCTION **1**
1.1 Motivation and Objectives of Research..... 1
1.2 The last glacial period –climate changes across the hemispheres-..... 7
1.2.1 Global pattern..... 7
1.2.2 The last glacial period in southern South America (Chile)..... 11
1.3 The Holocene..... 15
1.3.1 Global pattern..... 15
1.3.2 The Holocene climate in southern Chile..... 17

2 DESCRIPTION OF THE STUDY AREA **19**
2.1 Present-day oceanography..... 19
2.2 Present-day climate..... 21
2.2.1 Past behavior of the southern westerly winds..... 24
2.3 Present-day vegetation..... 25
2.3.1 Past vegetation distribution..... 26
2.4 Geological and tectonic setting..... 27
2.5 Icefields..... 29

3 MATERIAL AND METHODS **31**
3.1 Sampling..... 31
3.2 Dating Method..... 34
3.3 Reconstruction of paleotemperature..... 35
3.4 Biogenic components in the bulk sediment using a geochemical approach..... 36
3.5 Oxygen and Carbon Isotope composition..... 38
3.6 Ice Rafted Debris..... 38
3.7 Relative abundances of $C_{37:4}$ alkenones as proxy for low salinity waters..... 39

4 MANUSCRIPTS **41**
4.1 Millennial-scale surface water changes in the Southeast Pacific off 41

southernmost Chile over the past ~60 kyr…….
4.2 Holocene sea surface temperature variability in the Chilean Fjord Region. 73
4.3 Accumulation-sensitivity of Holocene glaciers in the superhumid southernmost Andes…….. 95
4.4 Holocene changes of the Southern Westerlies on centennial to multi-millennial timescales inferred from southern Chilean fjord sediments records…… 135

5 SUMMARY AND CONCLUSIONS…… **169**
6 REFERENCES…… **175**

LIST OF FIGURES

1-1 Map of the SE Pacific showing previous cruises carried out in southern Chile and the adjacent Pacific Ocean…… 5

1-2 Map of the study area…… 6

1-3 Millennial-scale climate changes during the last glacial period…… 9

1-4 Climate changes over the last 800 yr BP…….. 10

1-5 Temperature variability in the SE Pacific and Antarctica over the last 70 kyr BP…… 13

1-6 Holocene climate variability in the North Atlantic…….. 15

2-1 Map of the SE Pacific showing modern atmospheric and oceanographic pattern…… 19

2-2 Map of southern Chile showing modern salinity distribution and water surface circulation in the fjords…….. 20

2-3 Map of the Chilean continental margin showing climate and precipitation regimes…… 21

2-4 Map of the Chilean Fjord Region showing precipitation gradients and the present-day rain shadow effect of the Andes Cordillera…… 23

2-5 Map of southern Chile showing modern distribution of plant communities and precipitation gradients…… 26

2-6 Generalized map of southern Chile showing the main tectonic features and icefields…… 28

3.1 Map of the study area showing the long-cores and the surface sediment samples analyzed in this study…… 31

List of Tables

Table 1 Geographic position of long-cores collected from the Chilean Fjord Region 32

Table 2 Location of surface sediment samples collected from the Chilean Fjord Region 33

1 Introduction

1.1 Motivation and Objectives of Research

The Chilean continental margin offers unique opportunities to study Southern Hemisphere paleoenvironmental changes during the Holocene and the last glacial as it covers a large latitudinal range from ~20°S to ~55°S (Fig. 1-1). Climatically these latitudes include an extreme gradient in precipitation from the hyper-arid Atacama Desert in the north, across the winter-rain climate of central Chile, to year-round rainfall in the south reaching the worldwide highest precipitation amounts outside the tropics (of up to >10 m/year; *Schneider et al.*, 2003). Rainfall in Chile is entirely originating from Pacific moisture related to the Southern Westerly wind belt (SWW). Oceanographically, the Chilean margin is dominated by the Humboldt Current system originating from the northern branch of the Antarctic Circumpolar Current (ACC) that impinges the continent between ~40°S and 45°S (*Strub et al.*, 1998). The southern branch flows as the strong Cape Horn Current (*Chaigneau and Pizarro*, 2005) towards the Drake Passage where it mixes with the main ACC flow in vicinity of the Subantarctic Front (SAF) and the Antarctic Polar Front (PF) (*Orsi et al.*, 1995). Therefore, paleoenvironmental studies based on sediment records from the Chilean margin provide insights into paleoceanographic and paleoclimatic changes of a region that is critical for a better understanding of large scale atmospheric and oceanographic processes in the Southern Hemisphere.

During various research cruises (RV Sonne cruises SO-102 (*Hebbeln and Scientists*, 1995), SO-156 (*Hebbeln and Scientists*, 2001); and ODP Leg 201 (*Mix et al.*, 2003), numerous surface sediment samples and sediment cores were collected from the Chilean margin between approximately 23°S and 44°S. Strong continental paleoclimate variability is recorded on both millennial and orbital time-scales in the continental margin sediments. These changes are primarily related to shifting precipitation patterns induced by latitudinal movements of the SWW (*Lamy et al.*, 1998, 1999, 2000, 2001, 2004; *Kaiser et al.*, 2005, 2008). Detailed reconstructions of paleoproductivity have been obtained from the accumulation rate records of biogenic components (*Klump et al.*, 2001; *Hebbeln et al.*, 2002), while paleoceanographic changes are well reflected in the species composition of planktic foraminifera (*Marchant et al.*, 1999; *Hebbeln et al.*, 2002; *Mohtadi and Hebbeln*, 2004; *Mohtadi et al.*, 2005) and in paleo-sea surface temperature estimates based on the unsaturated index of alkenones (*Kim et al.*, 2002; *Lamy et al.*, 2002, 2004; *Kaiser et al.*, 2005, 2008).

The sediment data reveal a persistent trend of increasing productivity and overall sedimentation-rates from north to south, which is mainly linked to a parallel increase in onshore precipitation (*Hebbeln et al.*, 2000, 2002; *Hebbeln et al.*, 2007). Besides describing an average sea surface temperature (SST) difference between the

Last Glacial Maximum (LGM) and the Holocene optimum of ~6-7°C (*Kim et al.*, 2002; *Lamy et al.*, 2004; *Kaiser et al.*, 2005, 2008), the available records reveal significant millennial scale variability within the Holocene (*Marchant et al.*, 1999; *Lamy et al.*, 2001, 2002) as well as within the last glacial (*Hebbeln et al.*, 2002; *Lamy et al.*, 2004; *Kaiser et al.*, 2005). While south of 30°S the observed variability generally follows an Antarctic timing (e.g., *Lamy et al.*, 2004), there is evidence for substantial tropical influence off northern Chile (e.g., *Mohtadi and Hebbeln*, 2004). For example, investigations of sediment cores obtained from the Chilean continental slope at ~27°S reveal precession-driven paleoenvironmental variations marked by increased onshore precipitation related to relatively northward positions of the SWW during precession maxima and vice versa (*Lamy et al.*, 1998, 1999). These data suggest that the northernmost margin of the SWW reacts sensitively to insolation changes.

Up to recent years, very little information was available on paleoenvironmental changes of the southernmost part of the Chilean margin. Here, within the Chilean Fjord Region, the margin is comprised of a continuous series of deep basins formed by glacial erosion during the Quaternary and tectonic sinking of the central Chilean valley followed by a rise in sea level and flooding of the basins which created a complex system of fjords, channels, inlets, and embayments (e.g., *Silva and Prego*, 2002; *Rabassa*, 2008). Glacial erosion in the southern part of the Chilean margin is related to the Patagonian ice-sheet that covered the entire Andean part of southern South America between ~38° S and 56° S (e.g., *Glasser and Jansson*, 2008). Although little is known about the extent of this ice sheet on the Pacific continental margin, it is assumed that glaciers advanced towards the continental shelf edge and terminated in iceberg-calving fronts (*DaSilva et al.*, 1997).

Fjord sediments have been studied mainly in the vicinity of the Magellan Strait (e.g., *Kilian et al.*, 2007a, 2007b; *Lamy et al.*, 2010) and document the postglacial environmental history. Furthermore, various, up to 6 m long, sediment cores have been drilled in 1991 at the western entrance of the Strait of Magellan (*Bartole et al.*, 2000; *Brambati*, 2000; *Melis et al.*, 2000). However, these cores have not been dated in detail and the available information suggests that they are partly affected by sediment reworking and/or erosion.

Also further offshore in the Southeast Pacific, paleoceanographic changes in the Southeast Pacific sector (SEPS) of the Southern Ocean (SO) are poorly known primarily because high resolution sediment records from this region are very scarce (*Gersonde et al.*, 2005; *MARGO Project Members*, 2009). In the SEPS, only a few records have been retrieved around the SAF between ~100°W and ~120°W (*Mashiotta et al.*, 1999; *Gersonde et al.*, 2005). However, new records from these region have recently become available through the Polarstern cruise Ant26-2 (*Gersonde and participants*, 2010) and are currently beeing investigated.

During the R/V Marion Dufresne cruise Pachiderme (February 2007), long CALYPSO piston cores have been recovered from a latitudinal transect between ~42 and ~53°S. These cores include both sediment records from the inland fjords and offshore on the continental slope. Furthermore, several long sediment cores have been recovered in 2005 within the fjords during the NBP05-05 Palmer Cruise with RVIB Nathaniel B. Palmer.

The present PhD thesis is primarily based on three long sediment cores, two inshore within the fjords and one offshore on the continental margin (Fig. 1-2. Map fjords):

- Core JPC-42 (12.5 m length), was recovered between the Europa and Penguin fjords in the Wide Channel (49°54.90'S; 74°22.65'W; 904 m water depth) during the Palmer cruise. This core provides the most inland record closest to the modern southern Patagonian ice-field.
- Core MD07-3124 (22.25 m length) was retrieved from Canal Concepción (50°30.96'S; 74°58.33'W; 564 m water depth) in 2007 during the XV-MD-159-PACHIDERME cruise on board R/V Marion Dufresne. This core is located in the outer fjord region under comparatively strong open marine influence.
- Core MD07-3128 (30.33 m length) was recovered from the upper continental slope off the Strait of Magellan (52°39.57'S, 75° 33.97'W; 1032 m water depth), likewise during the XV-MD-159-PACHIDERME cruise on board R/V Marion Dufresne. The core was chosen in order to obtain an offshore open Pacific sediment record extending back into the last glacial period and beyond.

Additionally, surface sediments collected during previous expeditions in the Chilean fjord region were analyzed in order to detect the potential seasonality in the modern signal of alkenone-derived SST. These include: 13 core-top samples from box cores (collected in austral spring 2001 during the Chilean CIMAR FIORDO 7 Expedition on board R/V AGOR Vidal Gormáz), 7 core-top samples from kasten cores (collected in austral winter 2005 during the above mentioned RVIB Palmer cruise), and 2 core-top samples from multi corers (collected in austral spring 2003 during the Japanese BEAGLE cruise on board R/V Mirai).

The major objectives of my PhD project were originally related to a comparison of the inshore fjord records to the open ocean continental slope record. However, the two fjord cores JPC-42 and MD07-3124 do not extend beyond the Holocene, whereas the slope core MD07-3128 reaches back to *ca*. 60 kyr BP with high sedimentation rates during the last glacial. However, this core reveals unexpected low Holocene sedimentation-rates and thus does not allow for a detailed comparison to the high resolution Holocene fjord cores. Therefore, my project has focused on the

Holocene for the two fjord cores and the last glacial for the open ocean core MD07-3128.

The major research topics of the present thesis are:

- The evolution of the Holocene sea surface temperature of the Chilean fjords based on alkenone paleotemperatures including a validation of the alkenone signal in surface sediments from the region.
- Reconstruction of Holocene changes in the extent of the Patagonian ice-fields and their relation to rainfall variations controlled by the SWW.
- Paleoceanographic changes at the continental margin off southernmost Chile during the last glacial and deglaciation.
- Last glacial record of southern Patagonian ice-sheet variations on the Pacific side of the Andes and comparison to the terrestrial record on the eastern side of the Southern Andes.

My work primarily focuses on alkenone SST reconstruction. However, I greatly benefitted from data sets provided by colleagues from Chile (COPAS, Concepcion), Germany (University of Trier, IOW Warnemünde), Potsdam (GFZ) and Norway (University of Bergen) that were integrated in this thesis.

The data generated within the framework of this thesis will be available in the PANGAEA database (http://www.pangaea.de).

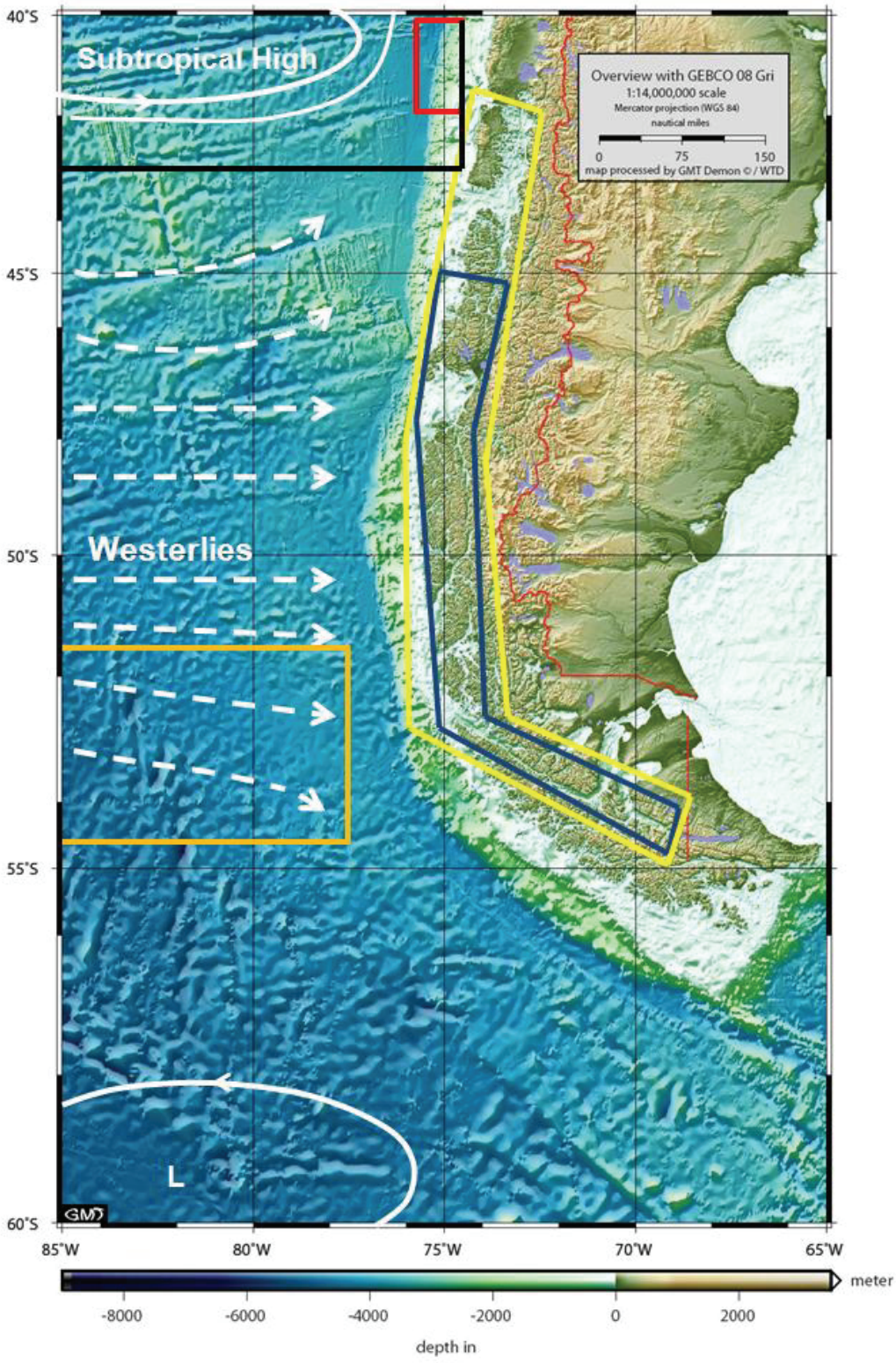

Fig. 1-1: Map of the SE Pacific showing previous cruises carried out in southern Chile and the adjacent Pacific Ocean (colour boxes) including RV SONNE cruises: SO-102 (black) and SO-156, Leg 202 (red); XV-MD-159-PACHIDERME (yellow), Palmer (blue) and Ant26-2 (orange) cruises. Map also show main atmospheric circulation pattern.

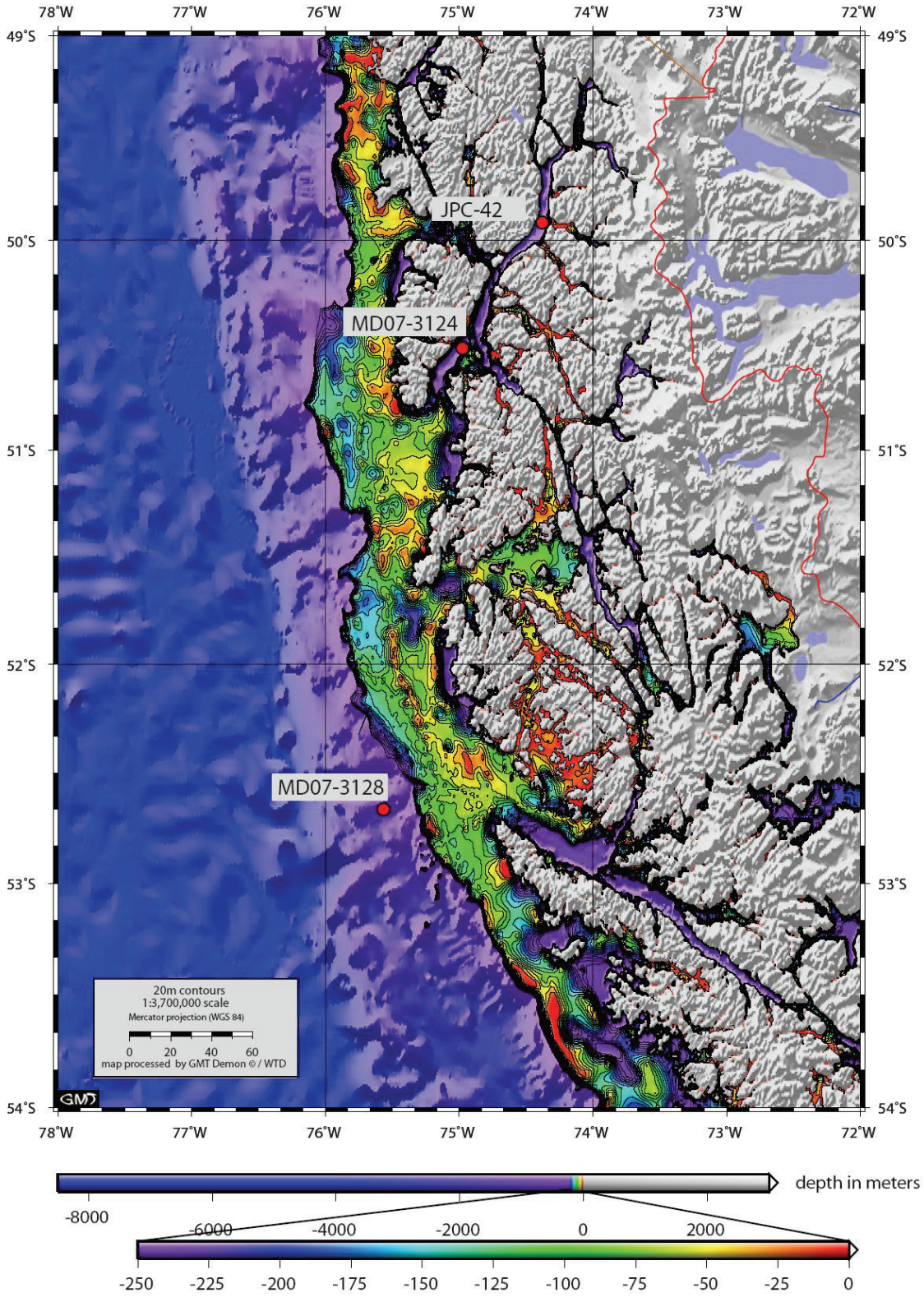

Fig. 1-2: Map of the study area showing the bathymetry (in meters) and sediment cores analyzed in this study.

1.2 The last glacial period –climate changes across the hemispheres–

1.2.1 Global pattern

Marine and ice core records from both, the northern and southern hemispheres have provided evidence that the last glacial period, between about 70 and 10 kyr before the present (BP), was characterized by abrupt climate and environmental changes on millennial time scales (e.g., *North Greenland Ice Core Project members*, 2004; *EPICA Community Members*, 2006; *Ahn and Brook*, 2008). The most prominent examples of this mode of climate variability include the large and abrupt fluctuations in the atmospheric temperatures recorded by the Greenland's ice core records, the so-called Dansgaard-Oeschger (DO) events (*Dansgaard et al.*, 1984) and the abrupt iceberg discharges documented in the polar North Atlantic region, known as Heinrich (H) events (*Heinrich*, 1988; *Broecker et al.*, 1992).

The Greenland's DO events, also recorded in deep-sea (Bond et al., 1993; Elliot et al., 2002) and continental records (e.g., *Genty et al.*, 2003) of the North Atlantic region, were cycles characterized by abrupt warming of 8–16 °C, that occurred within a few decades or less, followed by gradual cooling over several hundred to several thousand years (Fig. 1-3). Reorganizations of the Atlantic meridional overturning circulation (AMOC), which transports massive amounts of heat northwards from the tropics (it carries warm upper waters into far-northern latitudes and returns cold deep waters southward across the Equator), is believed to be the dominant player of the millennial-scale changes in temperature documented in the polar North Atlantic region during glacial times (e.g., *Broecker and Denton*, 1989). Some of the coldest intervals (H events) are closely related to enhanced discharge of icebergs as a result of instabilities of the large Laurentide ice sheet (*MacAyeal*, 1993). These events seem to have caused a weakening or event shut down of the formation of the North Atlantic Deep Water by the increasing injection of low density fresh waters to the surface ocean in the North Atlantic Region, with a consequently cooling of the ocean and atmosphere and thus, drastically affecting the ocean circulation all around the globe (*Broecker and Denton*, 1990; *Ganopolski and Rahmstorf*, 2001).

In contrast to the pronounced temperature changes recorded in the Northern Hemisphere during the last glacial period, temperature fluctuations in the Southern Hemisphere, best represented by Antarctic ice core records, were more gradual, with temperature changes of the order of 1–3 °C (*Blunier and Brook*, 2001; *EPICA Community Members*, 2006) (Fig. 1-3). Age synchronization between Greenland and Antarctic ice cores through atmospheric methane (CH_4) variations have revealed that Antarctic and Greenland temperatures are linked, but not in phase (e.g., *Blunier and Brook*, 2001; *Steig and Alley*, 2002; *Ahn and Brook*, 2008). A direct relationship between the extent of warming recorded across Antarctica and the surrounding ocean

(known as Antarctic events, A-events, and Antarctic Isotope Maxima, AIM) and the duration of the DO cold phase over Greenland has been observed (*EPICA Community Members*, 2006) (Fig. 1-3). This asynchrony between hemispheres has given support to the concept of a bipolar climate "seesaw", in which cooling in the North is balanced, via the AMOC, by warming in the South Hemisphere and viceversa (*Crowley*, 1992; *Broecker*, 1997; *Blunier et al.*, 1998; *Barker et al.*, 2009).

The traditional bipolar "seesaw" concept assumed that climate changes in the North Hemisphere trigger a response in the South Hemisphere (e.g., *Crowley*, 1992). Some evidence for a northern trigger is provided by modeling studies showing that increases in fresh water discharges into the polar North Atlantic, or close to the areas where deep water forms at high latitudes, produce instabilities of the AMOC and its associated heat transport, causing cooling in the north and warming in the south, following the pattern predicted by the ice-core temperature data (*Knutti et al.*, 2004). However, detailed comparisons between Antarctic and Greenland temperature proxy records in their synchronized age scale show that Antarctic temperature changes precede those in Greenland by about 1,000 to 2,000 years (*Blunier et al.*, 1998), suggesting a southern trigger for abrupt climate changes. Moreover, both model experiments (*Knorr and Lohmann*, 2003; *Weaver et al.*, 2003) and proxy data from the Southern Hemisphere (*Ninnemann and Charles*, 2002; *Peeters et al.*, 2004) suggest that slow climate changes in the SO can influence events in the North Atlantic. These changes included variations in the strength of the SWW and/or changes in the SO stratification as potential southern trigger for abrupt climate changes.

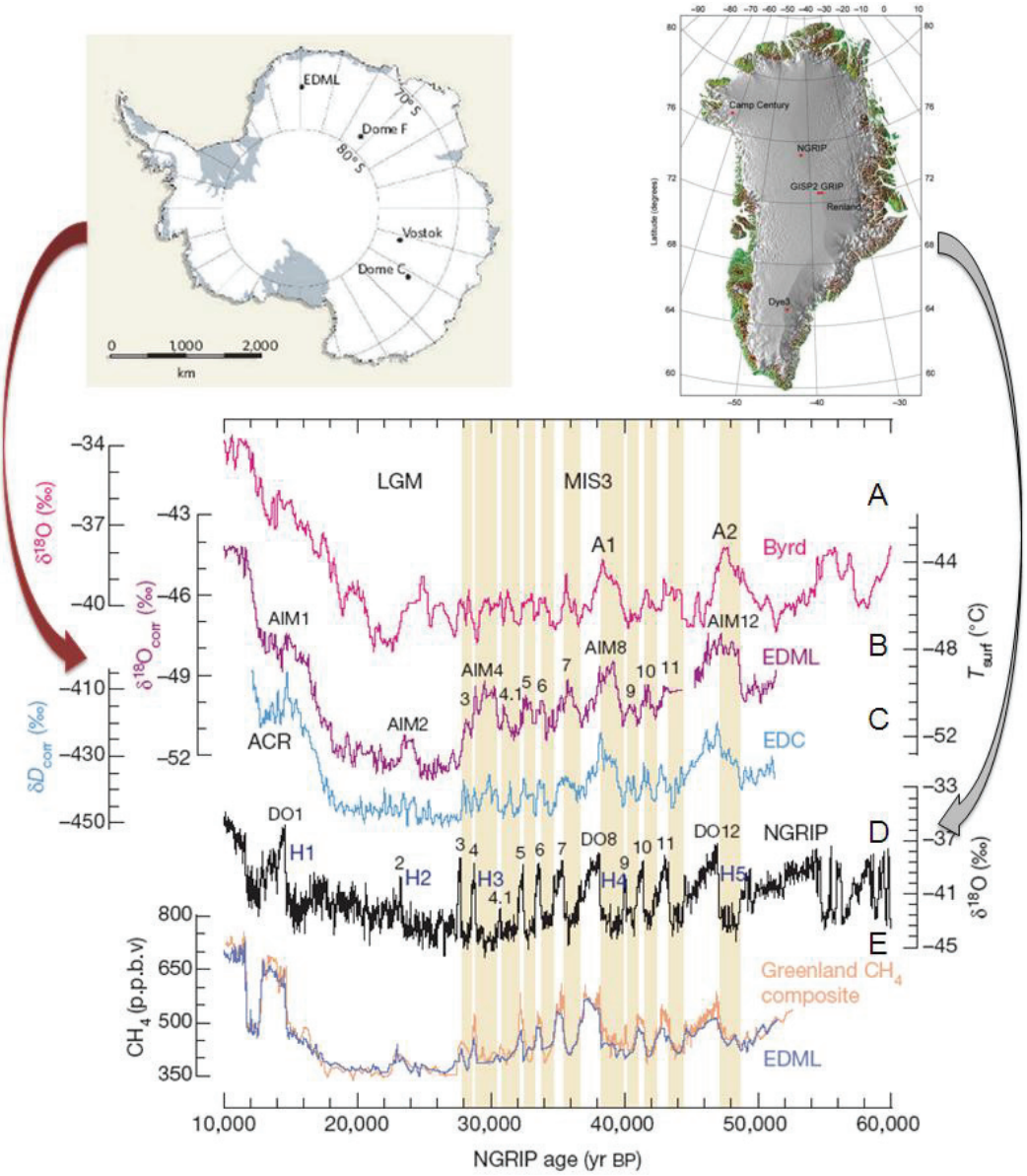

Fig. 1-3: Millennial-scale climate changes during the last glacial period (after *EPICA Community Members*, 2006). Comparison of Antarctic temperature proxy records (or rather, oxygen and deuterium isotope ratios, as proxies for temperature) of Byrd (A), Epica Droning Maud Land (EDML) (B) and Epica Dome C (EDC) (C) ice cores with temperature proxy record of Greenland (NGRIP) (D). Note that the extent of warming in Antarctica (AIMS and A-events) is related to the duration of Dansgaard-Oeschger (DO) cold phase over Greenland.

Direct measurements of CO_2 concentrations in Antarctic ice-cores reaching back in time to about 800 kyr BP suggest a close coupling to Southern Hemisphere temperatures through the climate-carbon feedback (Fig. 1-4a). During the last glacial period, the atmospheric concentration of CO_2 (and of other greenhouse gases) decreased by about 100 parts per million by volume as recorded widely by Antarctic ice core records (Fig. 1-4b) (e.g., *Petit et al.*, 1999; *Ahn and Brook*, 2008) likely

contributing to the global cooling in the Earth. Most theories for lower glacial atmospheric CO_2 concentration rely on one of three mechanisms: (i) a decrease in the exchange of Southern Ocean surface waters with the ocean interior (*Francois et al.*, 1997; *Toggweiler*, 1999); (ii) an increase in the degree to which Southern Ocean surface nutrient is consumed by phytoplankton as a result of increasing atmospheric dust deposition to the surface ocean (*Martin*, 1990), and (iii) an increase in sea-ice coverage, causing a decrease in the ability of CO_2 to escape from supersaturated Southern Ocean surface waters (*Stephens and Keeling*, 2000). However, sources, sinks and regulatory mechanism of atmospheric CO_2 are still under debate (*Fischer et al.*, 2010). Also on millennial time-scale, CO_2 concentrations and Antarctic air temperatures are closely linked (*Ahn and Brook*, 2008) (Fig. 1-4b). This linkage has lead to the notion that glacial atmospheric CO_2 changes depends primarily on marine processes operating in the SO (e.g., *Barker et al.*, 2009).

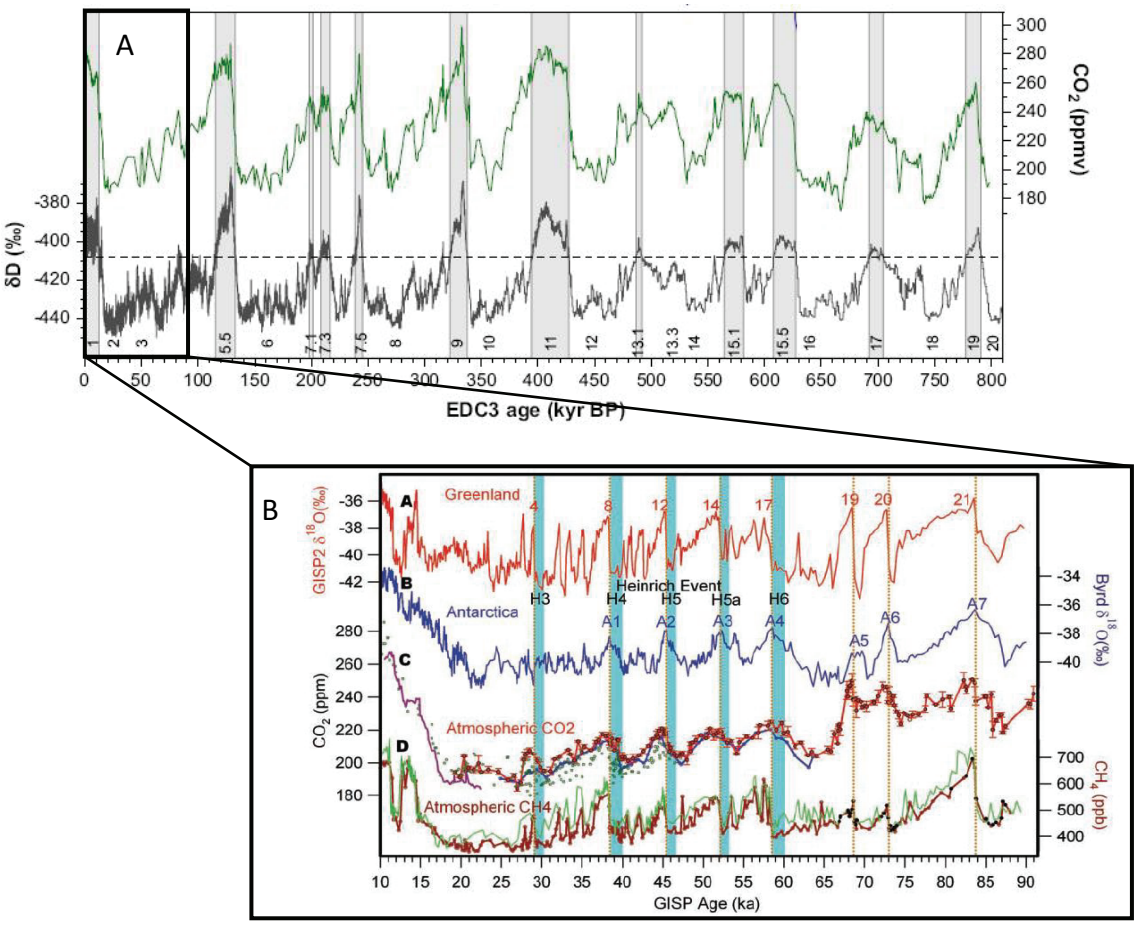

Fig. 1-4: Climate changes over the last 800 yr BP (after *Schilt et al.*, 2010) (panel A) and close up showing in detail millennial-scale variability during the last glacial (panel B). (A) CO_2 and temperature changes over the last 800 kyr recorded by Antarctic EDC ice core. (B) Millennial-scale temperature variability recorded in Greenland and Antarctica and its relationship to changes in atmospheric CO_2.

1.2.2 The last glacial period in southern South America (Chile)

The Chilean continental margin offers a unique platform for studying inter-hemispheric climate changes. But despite being considered a “natural laboratory” for the study of interactions between climate, geology, oceanography and sedimentation processes due to its extraordinary latitudinal gradients in environmental and geological settings, this region still remains one of the least studied paleoceanographic key areas.

Only two high-resolution records for sea surface temperature (SST) variability, covering the major part of the last glacial period, are presently available for the Chilean continental margin (Fig. 1-5a). One of this records is located at central Chile off ~33°S (GIK 17748-2/GeoB 3302-1), spanning the last ~35 kyr BP (*Kim et al.*, 2002), and the longest one at southern Chile off ~41°S (ODP Site 1233) covering the last ~70 kyr BP (*Lamy et al.*, 2004; *Kaiser et al.*, 2005) (Fig. 1-5b-c, respectively). These record show that glacial SST were of the order of ~4 °C and ~5 °C colder than present-day SST values, at ~33°S and ~41°S respectively, without a clear well defined last glacial maximum (LGM; 23–19 kyr BP). Over the last glacial period, pronounced millennial-scale SST variability of the order of 2–3 °C have been noticeably observed in the southernmost record off ~41°S (ODP Site 1233), closely following the millennial-scale temperature fluctuations recorded by the Antarctic ice core records (i.e., the major Antarctic warm events A1 to A4 are characterized by SST increase of up to 3 °C) (Fig. 1-5d).

A northward shift in the SWW of at least 5° latitude (compared to its current core position at ~50°S) linked to the northern margin of the ACC has been considered to be responsible for the glacial SST pattern found off central and southern Chile (*Lamy et al.*, 2004; *Kaiser et al.*, 2005). According to these authors, the couple SWW/ACC might have shifted northwards enhancing the influence of the cold subantarctic water masses and thus, cooling the mid-latitudes of the southeast Pacific. The enhanced glacial northward influence of the ACC up to ~33°S has been also suggested by paleoproductivity reconstructions (e.g., *Mohtadi and Hebbeln*, 2004; *Mohtadi et al.*, 2004). Based on a multi-proxy approach performed on several sediment cores collected between 24°S and 33°S, Mohtadi and co-workers show that marine productivity was higher during the last glacial period in comparison to the Holocene due to the northward advection of the nutrient-rich ACC waters, which are presently the main nutrient source in this region.

The last termination, the rapid transition from the last glacial period into the present interglacial, starts at about 18.5 kyr BP at ~33°S, and 18.8 kyr BP at ~41°S (*Kim et al.*, 2002; *Lamy et al.*, 2004; *Kaiser et al.*, 2005) and was characterized by an abrupt SST warming of ca. 5 °C (Fig. 1-5b-c). At ~41°S (ODP Site 1233), the first warming step was followed by relatively stable SSTs and a cooling event of ~0.8 °C, between ~14.5

and 12.5 kyr BP. This cooling was synchronous with the Antarctic Cold Reversal (ACR) recorded in Antarctic ice core records (Fig. 1-5d). Following the ACR, a second warming of ~2 °C, which falls into the second half of the Northern Hemisphere Younger Dryas cold period (which occurred between 12,900–11,600 yr BP in the Northern Hemisphere; (*Ackert et al.*, 2008), is also recognized. After the second deglacial-warming step, an early Holocene optimum is recorded (~12–9 kyr BP) with SST *ca*. 1–2 °C warmer than modern SST values. Thereafter, SSTs gradually decline to reach modern conditions (Fig. 1-5c).

The strong similarity in timing and direction between the SST record off 41°S and the temperature proxy records in Antarctica i.e. the pronounced millennial-scale variability recorded over the last glacial, the two warming steps over the last deglaciation and the cooling during the ACR (Fig. 1-5d) lead (*Lamy et al.*, 2004) to propose a direct link of the SST changes in the southeast Pacific to climate fluctuations in the southern high latitudes (Antarctic timing).

In Antarctica millennial-scale temperature changes over the last glacial have been consistently explained by the bipolar seesaw concept, which suggests an out-of-phase millennial-scale climate pattern between the northern and southern hemispheres as response to perturbations in the thermohaline circulation and heat transport (*Crowley*, 1992; *Broecker*, 1997; *Blunier et al.*, 1998; *Barker et al.*, 2009). Over the last deglaciation, detailed radiocarbon dating reveals that the SST in the mid-latitude SE Pacific (ODP Site 1233) rose at the same time than the Atlantic meridional overturning circulation (AMOC) decreased (*Lamy et al.*, 2007). Though this timing is largely consistent with Antarctic ice core records, the initial warming in the southeast Pacific was more abrupt, suggesting a direct and immediate response to the slowdown of the Atlantic thermohaline circulation through the bipolar seesaw mechanism. This response requires a rapid transfer of the Atlantic signal to the SE Pacific, without involving the thermal inertia of the Southern Ocean that may contribute to the substantially more gradual deglacial temperature rise, as seen in Antarctic ice cores. As discussed by *Lamy et al*. (2007), the most plausible mechanism is a seesaw-induced change of the coupled ocean-atmosphere system of the ACC and the southern westerly wind belt i.e., northward migration during the last glacial and a poleward displacement during the deglacial.

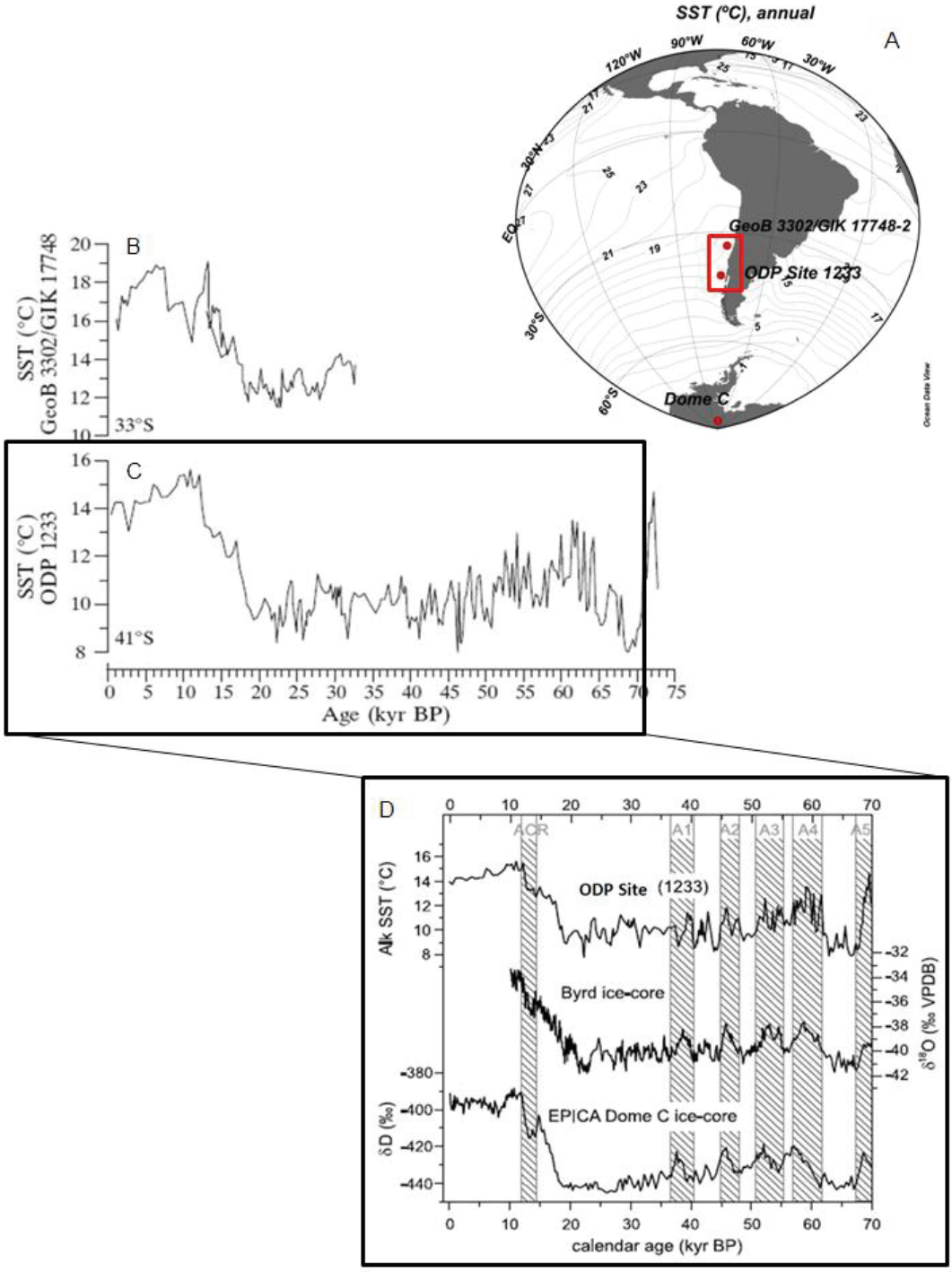

Fig. 1-5: Temperature variability in the southeast Pacific and Antarctica over the last 70 kyr BP. (A) General map showing the present annual SST distribution in the southeast Pacific and location of cores discussed in the text. Alkenone-derived SST records from the Chilean continental margin at ~33°S (B) and ~41°S (C). (D) shows in detail the strong connection of SST variability at ~41°S with those recorded by the temperature proxy record in Antarctica (oxygen isotopes on Byrd ice core and deuterium record on EPICA Dome C ice core, respectively) (after *Kim et al.*, 2002; *Kaiser et al.*, 2005).

There is an ongoing debate on the pattern and timing of millennial-scale climate fluctuations at the Southern Hemisphere. In contrast to the findings of an Antarctic millennial-scale pattern in the SST record off 41°S (Fig. 1-5d), continental, glaciological and palynological data from the Chilean Lake District (~38°–42°S) and on Chiloé island have been used in support for inter-hemispheric asynchrony both, during the last glacial (*Lowell et al.*, 1995) and the last deglaciation, i.e., cooling during the Younger Dryas cold phase (*Denton et al.*, 1999; *Moreno et al.*, 2001). The Younger Dryas (11,000–10,000 ^{14}C yr BP; 12,900 and 11,600 cal. yr BP) was a rapid return to near-glacial conditions during the transition from the LGM to the current Holocene warm period (*Ackert et al.*, 2008) in the North Atlantic region which has nonetheless shown expression in other region of the globe. The mechanisms that cause the Younger Dryas in the Northern Hemisphere are not yet fully understood but they seem related to the drainage of fresh water to the North Atlantic region. For southern Chile at 41°S (directly onshore of the position of the ODP Site), the expansion of cold-resistant forest taxa and the decline of thermophilous tree species between 12,500 and 9,000 ^{14}C yr BP has been interpreted in terms of a cooling during the North Hemisphere Younger Dryas, whereas the alkenone record off 41°S reveal a clear warming at this time. However, it has been recently suggested that the deglacial cold reversal in NW Patagonia started earlier (at ~14.7–13.4 kyr BP), and that the Younger Dryas interval was rather characterized by fire disturbance (*Hajdas et al.*, 2003; *Moreno*, 2004) that may not necessarily imply cooling.

1.3 The Holocene

1.3.1 Global pattern

The Holocene, the last ~11 thousand years before present, has been traditionally considered as a period of relatively stable climate conditions when compared to the last glacial period (Fig. 1-6a). However, paleoclimatic and paleoceanographic studies over the last decades have suggested that the Holocene warm climate has experienced substantial climate variability on a large range of timescales (e.g., *O'Brien et al.*, 1995; *Bianchi and McCave*, 1999; *deMenocal et al.*, 2000; *Mayewski et al.*, 2004).

In the subpolar North Atlantic region, significant millennial-scale cooling episodes, documented by an increase of ice-rafted detritus (in the form of hematite-stained grains, Icelandic volcanic glass and lithics; Fig. 1-6b) (*Bond et al.*, 1997) have been described as the main example of climate instability occurring throughout the Holocene. These Holocene cooling events, occurring with a periodicity of *ca*. 1500 years (*Bond et al.*, 1997) may have been caused by changes in solar activity (*Bond et al.*, 2001). Although a similar 1500-yr periodicities have been reported by several proxy records (e.g., *O'Brien et al.*, 1995; *Bianchi and McCave*, 1999), implying that Dansgaard-Oeschger-type cycles, although attenuated, may have occurred in the North Atlantic region throughout the Holocene, the existence of such periodicity has been discussed controversially (*Schulz and Paul*, 2002).

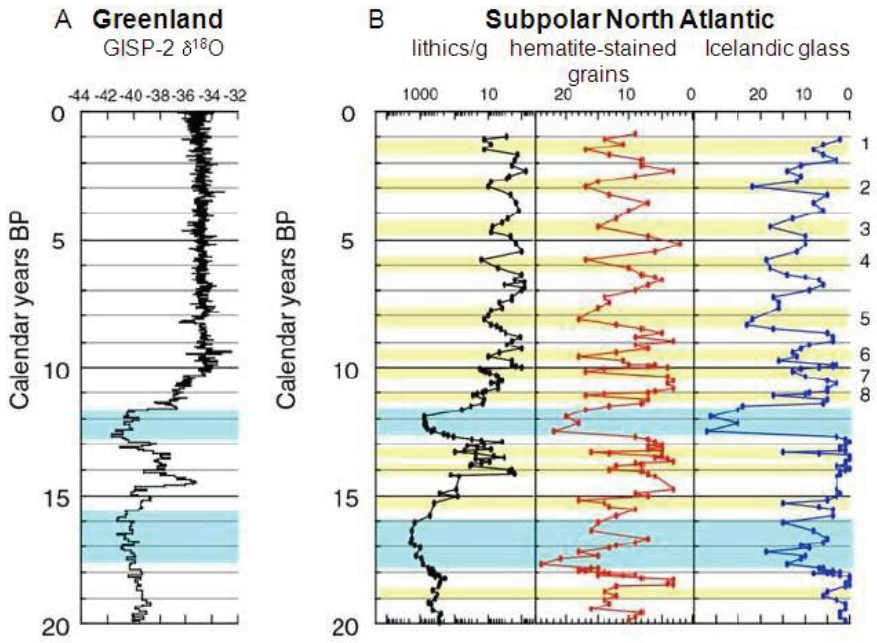

Fig. 1-6: Holocene climate variability in the Northern Hemisphere. (A) Temperature proxy record of Greenland ice core. (B) Proxies for ice rafted detritus recorded in the subpolar North Atlantic region. Note that the Holocene cooling events 1-8 are listed on the right (after *Bond et al.*, 1997).

Superimposed to the 1500 yr of climate variability, high resolution multi-proxy records from the polar North Atlantic region have described the general Holocene climate as a period of cooling aligned with the decreasing insolation at the Northern Hemisphere (e.g., *Birks and Koc*, 2002; *Marchal et al.*, 2002). An early Holocene thermal maximum (or Holocene climate optimum) lasting from 9.5 kyr until ~6.5 kyr is followed by a Holocene transition period from ~6.5–3.0 kyr during which the climate was deteriorating (*Andersen et al.*, 2004a, 2004b). This gradual cooling was suddenly intensified when two North American glacial lakes flooded into the North Atlantic, slowing the formation of North Atlantic Deep Water and its associated northward heat transport for several centuries. The resulting multi-century cold event has now been recognized throughout the Northern Hemisphere as the "8.2-kyr event" (e.g., *Alley et al.*, 1997 and references therein). During the late Holocene the cooling continued. This continuous cooling starting at 3.0 kyr presented a 1–2 °C variability superimposed. Although the dominant forcing factor for the early Holocene thermal maximum was the Northern Hemisphere summer insolation via strong seasonality at high northern latitudes (*Andrews et al.*, 1997; *Calvo et al.*, 2002; *Andersen et al.*, 2004a), the trigger for the onset of relatively unstable climate conditions beginning about 3 kyr is less clear.

In the Southern Hemisphere, paleoclimate archives from Antarctica and the Southern Ocean reveal contrasting results pointing to a complex temperature evolution throughout the Holocene (*Ciais et al.*, 1992; *Masson et al.*, 2000; *Masson-Delmotte et al.*, 2004; *Nielsen et al.*, 2004; *Bentley et al.*, 2009; *Moros et al.*, 2009; *Divine et al.*, 2010). An early Holocene Climatic Optimum (11.5–9 kyr BP) has been widespread documented in Antarctic ice core records, with temperatures up to ~2 °C warmer than present (e.g., *Masson et al.*, 2000). Thereafter, long-term trends in the ice core records partly deviate as large-scale Antarctic cooling during the Holocene, which is locally compensated by a decrease in the ice-sheet elevation in response to ice-sheet dynamics (*Masson-Delmotte et al.*, 2004). However, a secondary mid-Holocene temperature maximum between ~8 and 6 kyr BP seems to be important in the Ross Sea area whereas in eastern Antarctica some records show a weak secondary warming between ~6 and 3 kyr BP (*Masson et al.*, 2000). Furthermore, the ice-core records suggest a consistent multi-centennial-scale temperature pattern in Antarctica over the Holocene with a cyclicity of ~830 years (*Masson et al.*, 2000; *Masson-Delmotte et al.*, 2004).

Marine and lacustrine records around the Antarctic Peninsula confirm the complexity of the Holocene temperature evolution as maximum warming was registered during different time intervals in the early to middle Holocene (e.g., *Bentley et al.*, 2009). Further offshore Antarctica, marine records from the South Atlantic sector of the Southern Ocean (50°–53°S) reveal an early Holocene temperature

optimum and the onset of cooling and sea-ice expansion between ~9 and 7 kyr BP (*Bianchi and Gersonde*, 2004; *Nielsen et al.*, 2004). Earlier work in this region suggested increased ice-rafted detritus to the subantarctic South Atlantic starting abruptly at ~5.5 kyr BP interpreted in terms of the onset of the so-called Neoglacial phase coinciding with a further advance of sea-ice cover around Antarctica (*Hodell et al.*, 2001; *Iizuka et al.*, 2008).

1.3.2 The Holocene climate in southern Chile

The Holocene climate history of southern Chile (south of 41°S) is still not well documented due to the lack of records covering the complete Holocene. In contrast, detailed paleoceanographic reconstructions have been obtained along the Chilean margin up to 41°S.

At ~41°S (ODP Site 1233) an early Holocene climate optimum has been recorded from ~12 to 9 kyr BP with SSTs *ca*. 1–2 °C warmer than modern SST values (*Kaiser et al.*, 2005). Thereafter, temperatures gradually declined reaching modern values in the latest Holocene. The early Holocene optimum was not documented in the higher resolution SST record from core GeoB 3313-1 (same location as ODP Site 1233) (*Lamy et al.*, 2002) since it only covered the past ~8 kyr. In this record, a secondary middle Holocene warming is observed at 5–6 kyr BP with SSTs generally declining afterwards towards the late Holocene in a similar fashion as the comparatively lower resolution SST record off ~41°S (ODP Site 1233). Further north, a SST record located at ~30°S (*De Pol-Holz et al.*, 2006; *Kaiser et al.*, 2008) displays a slightly delayed optimum warming that lasted longer, i.e. into the middle Holocene and cooling thereafter. Off central Chile at ~33°S, the warmest Holocene SST was found between ~7.5 and 6 kyr BP. This warm phase was preceded by an early Holocene cold interval that ended with a pronounced warming of ~2.5 °C between 8 and 7.5 kyr BP (*Kim et al.*, 2002). The reason for this early Holocene cold phase remains unclear.

The early to middle-Holocene temperature maximum appears to coincide with widespread more arid conditions onshore, as recorded in various terrestrial and marine records from central Chile (32°–35°S) (*Villagrán and Varela*, 1990; *Lamy et al.*, 1999; *Jenny et al.*, 2002; *Maldonado and Villagran*, 2002; *Villa-Martinez et al.*, 2003). Since these areas are located at the northern influence zone of the SWW, the main source of precipitation of Chile, a southward displacement of the SWW during this period has been proposed. New precipitation reconstructions of the SWW core zone in the southern Chilean Fjord Region suggest enhanced SWW in the early Holocene that then decreases during the middle and late Holocene (*Lamy et al.*, 2010). Taken

together these reconstructions show an antiphase behavior between the core of the SWW and its northern margin.

2 Description of the Study Area

The sediment cores analyzed in this study were recovered along the southern Chilean coastal margin between ~50°S and ~53°S. To understand the magnitude of the climate changes throughout the late Quaternary, first the modern climate, oceanography, vegetation and tectonic characteristics are described.

2.1 Present-day oceanography

The large-scale surface circulation along the coast of the Chilean margin is dominated by the strong interaction of atmospheric forcing over the ocean (Fig. 2-1). The Subtropical high pressure belt (subtropical Anticyclone (STA) gyre) induces persistently southerly winds favorable to upwelling conditions along the central and northern Chilean margin (e.g., *Muñoz and Garreaud*, 2005) while the SWW drive the Antarctic Circumpolar Current (ACC) that brings cold and nutrient-rich Subantarctic Surface Waters (SAAW) originating north of the Subantarctic Front (*Strub et al.*, 1998).

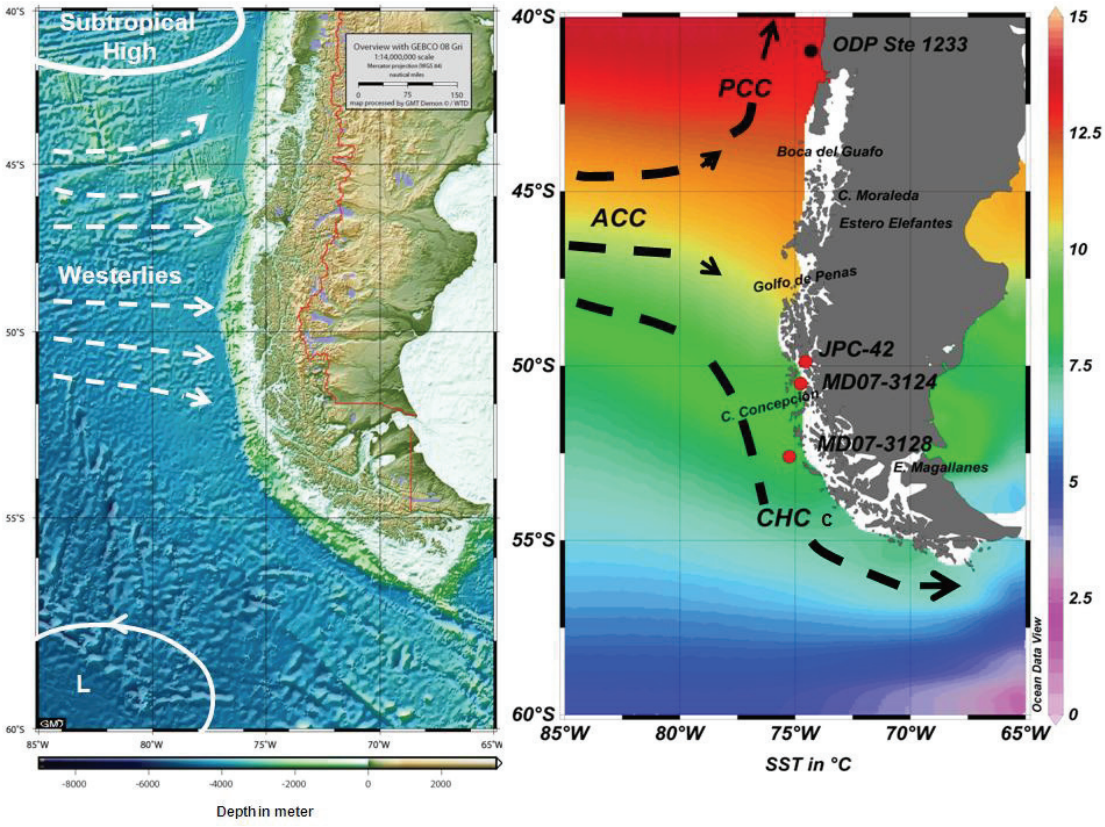

Fig. 2-1: Map of the SE Pacific showing modern atmospheric (left) and oceanic (right) circulation pattern. Major surface currents off southern Chile are discussed in the text.

The surface circulation off southern Chile is entirely influenced by the northern margin of the ACC. It splits around ~45°S into two branches, the Perú-Chile or Humboldt Current (PCC) flowing equatorward, and the Cape Horn Current (CHC) flowing poleward (Fig. 2-1). Both currents transport SAAW along the Chilean coastal margin (*Shaffer et al.*, 1995; *Strub et al.*, 1998).

Adjacent to the Chilean Fjord Region, three water masses have been identified: SAAW (up to 150 meter depth), remnants of Equatorial Subsuperficial Water (ESSW; between ~150 and 300 meter depth) and the Antarctic Intermediate Water (AAIW; below 300 meter depth). The first two water masses penetrate into the Chile Fjord Region through various channels located in the Pacific margin and spread as far as the bathymetry of the gulfs and channels allow them (Fig. 2-2) (*Silva et al.*, 1997, 1998; *Sievers and Silva*, 2008). The SAAW, having salinities between 33 and 34 psu, mixes with fresh waters in different proportions according to the contributions from rivers, glaciers, coastal runoff and rainfall and produce modified SAAW (MSAAW) and Estuarine Water (EW) (*Silva et al.*, 1998; *Sievers and Silva*, 2008). The interaction between SAAW and the diluted waters from the fjords define a coastal salinity front occurring between 42° and 56°S (Fig. 2-2). This front is present during the whole year with strongest gradients during summer.

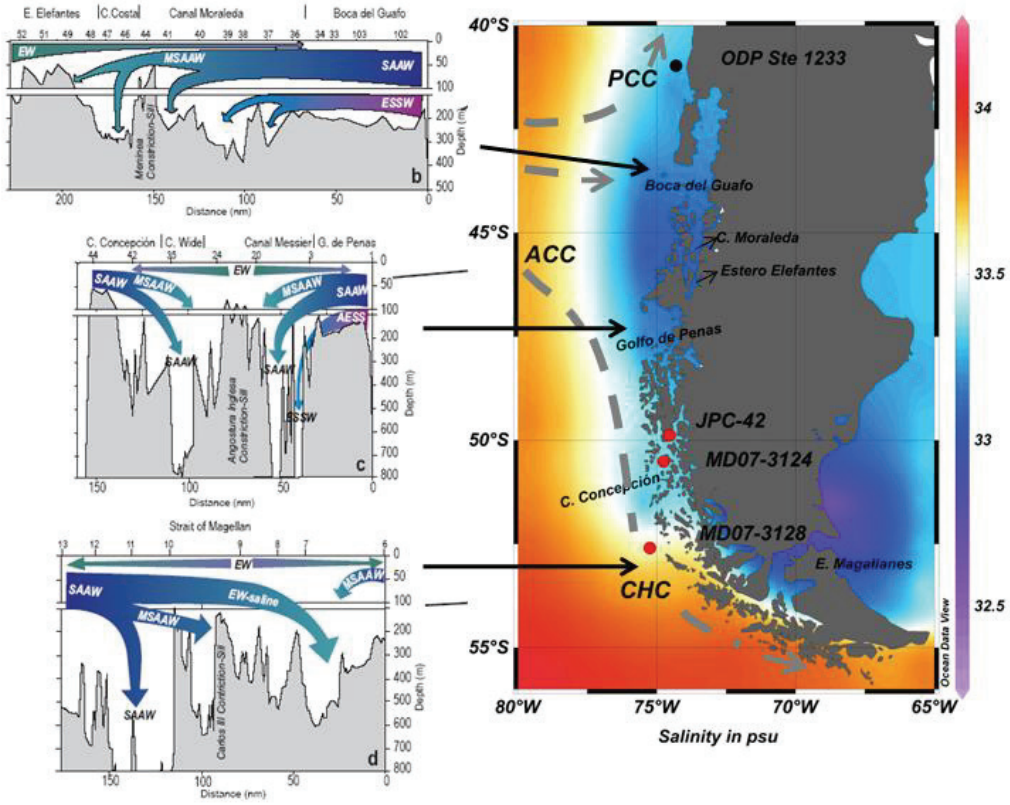

Fig. 2-2: Map of southern Chile showing modern sea surface salinity distribution and water circulation in the interior fjords (after *Sievers and Silva*, 2008). Water masses are discussed in the text.

The water circulation in the fjords is generally described as a two-layer positive circulation (e.g., *Silva et al.*, 1995). The top layer with low salinity and low density flows offshore; while a more stable oceanic bottom layer, characterized by relatively high salinity and high density, flows toward the fjords (*Silva et al.*, 1995; *Sievers and Silva*, 2008). The estuarine waters are usually devoid of nutrients other than dissolved silicon derived from river runoff, while the oceanic SAAW is the main source of nitrate and orthophosphate. Strong vertical gradients (pycnocline, oxycline, nutricline) separate the upper layer from the deep layer (*Sievers and Silva*, 2008) and mixing is necessary to bring nutrients up into the euphotic zone (*Montecino et al.*, 2004).

2.2 Present-day climate

Currently, there are three main climate controls along the Chile continental margin: the quasi-permanent STA, the SWW and the north-south trending mountain barrier of the Andes Cordillera (*Aceituno*, 1988). As result, Chile that spreads over a wide latitudinal range from ~18°S to ~55°S has one of most pronounced climate gradients of the world, from extreme aridity in the north, where precipitation is measured in millimeter per decade, through Mediterranean-type precipitation regime in its central part, with hot and dry summers and mild and wet winters due to seasonal shifts of the SWW, to all year rainy temperate climate in the south (*Miller*, 1976; *Latorre et al.*, 2007) (Fig. 2-3). Consequently, sea surface temperature along the Chilean coast decreases also almost linearly from north to south. The mean annual thermal amplitude varies from ~20 °C in the north to ~7 °C in the south (as seen in Fig. 2-1).

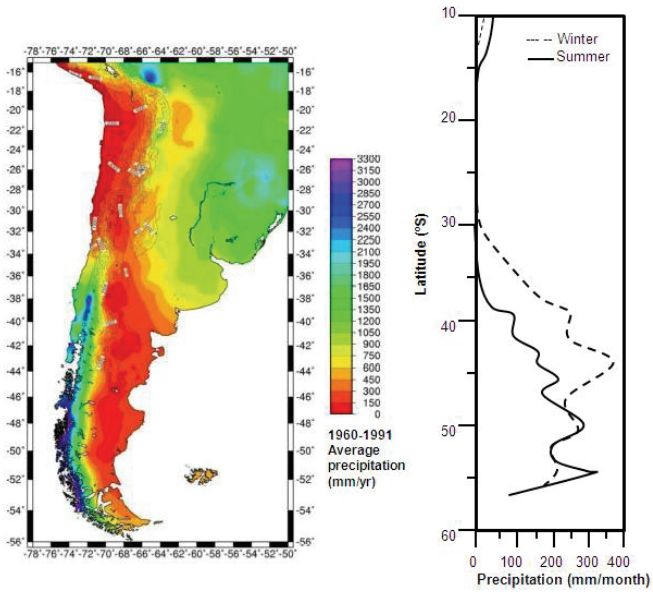

Fig. 2-3: Map of Chile and Argentina showing climate and precipitation regimen (after *New et al.*, 2001). Note that during austral winter (right panel), the SWW extent northward, providing

rainfall to central Chile (33–44°S) while in austral summer, the SWW are confined over southernmost Chile.

Southern Chile is characterized by the permanent influence of the humid and cold SWW, which constitute the primary meteorological element on regional climate changes (*Moreno et al.*, 2009). The SWW are the strongest time-average oceanic winds in the middle latitudes of the earth, blowing from west to east, between the high-pressure areas of the subtropics and the low-pressure areas over the poles (*Toggweiler*, 2009) (Fig. 2-1). The SWW are an important feature of the global atmospheric circulation, not only because they influence the amount and distribution of precipitation on the South America continent, but the westerlies play a major role in carbon cycling in the SO drawing deep water rich in CO_2 directly up to the atmosphere (*Moreno*, 1997; *Moy et al.*, 2008 and references therein).

At present, seasonal shifts of the westerly stormtracks cause important changes in the precipitation regimen at the western coast of South America (*Garreaud*, 2007). These variations are deeply related to seasonal shifts of the quasi-permanent STA. During austral winter, the STA is weak and the SWW extend northward providing rainfall to central Chile (~33°–44°S) while zonal winds are reduced in its core zone in southernmost Chile (50°–55°S) (Fig. 2-3). Contrary, during austral summer, the SA became stronger and the zonal wind pattern shows a latitudinally more confined and intensified SWW with maxima over southernmost Chile (e.g., *Villa-Martinez and Moreno*, 2007; *Lamy et al.*, 2010).

Moreover, the SWW have a deep influence on the hydrological regimen over the Chilean Fjord Region. South of ~40°S, the SWW deliver an average of 4,000 mm of precipitation per year increasing to up to 7,000 mm per year at the core of the SWW which is presently located at *ca*. 50°S (*Aravena and Luckman*, 2008; *Moreno et al.*, 2009) (Fig. 2-4). The precipitation declines rapidly north and south from ~50°S latitude, reflecting the average position of the westerly cyclonic storm tracks.

The Andes Cordillera intersects the SWW in a perpendicular position creating a marked climatic contrast between the Pacific (windward side) and the Atlantic slopes (leeward side) in terms of precipitation (Fig. 2-4) (e.g., *Villa-Martinez and Moreno*, 2007). On the west side of the Andes, the total rainfall can be 100–300% higher than that on the eastern side. The most extreme contrast is between Isla Guarello (7,220 mm yr^{-1}) and Lago Argentino (290 mm yr^{-1}) following the 49°S parallel (*Aravena and Luckman*, 2008).

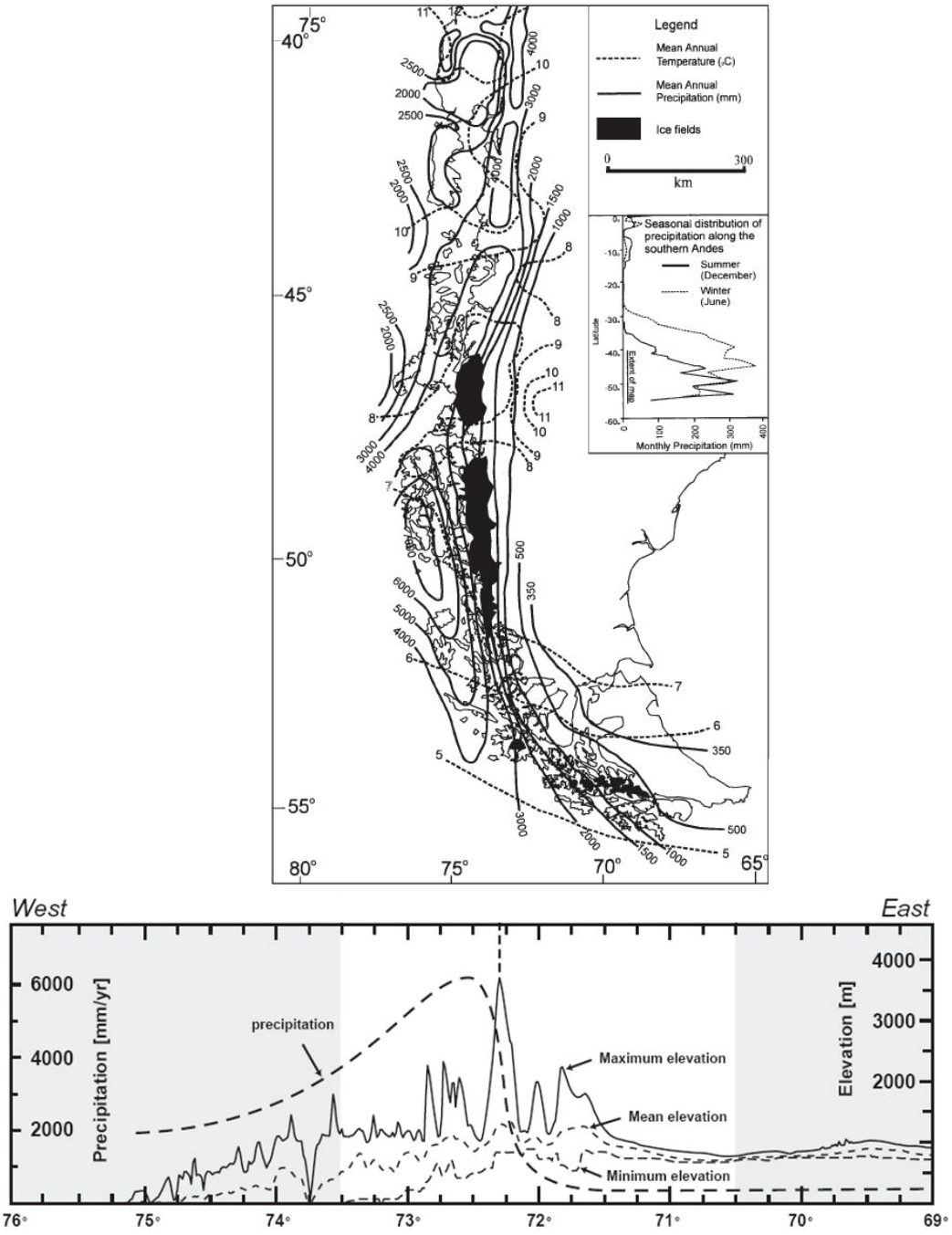

Fig. 2-4: Map of the Chilean Fjord Region showing the precipitation gradient (top panel) and the present-day rain shadow effect across the southern Patagonia Andes (low panel) (after *McCulloch et al.*, 2000; *Blisniuk et al.*, 2005).

2.2.1 Past behavior of the SWW

The SWW play a fundamental role in the climate system at continental, hemispheric, and global scales. Previous discussion on the last glacial-interglacial history of the SWW at the Pacific coast of South America has centered on paleoclimatic records located at or near its northern margin (*Lamy et al.*, 2001; *Jenny et al.*, 2002; *Villa-Martinez et al.*, 2003; *Moreno*, 2004). These works infer a more northward location of the SWW by *ca*. 5–6° of latitude (compared to its current core position at ~50°S) during the last glacial period, generating substantial changes in the precipitation regimen in northern-central Chile (*Lamy et al.*, 1998), as well as significant changes in the surface ocean properties, i.e. decreasing SST for about 4–5 °C [*Lamy et al.*, 2004; *Kaiser et al.*, 2005). The northward migration of the SWW seem to have occurred synchronously with a northward shift of the ACC, as revealed by the increasing marine productivity observed at 33°S (*Hebbeln et al.*, 2002; *Mohtadi et al.*, 2004). As the main nutrient source in this region is currently associated to the advection of the nutrient-rich SAAW, the increasing glacial marine productivity up to 33°S has been interpreted in term of increasing advection of the ACC-derived nutrient-rich SAAW waters.

Modeling studies, on the other hand, show that the westerlies were stronger and shifted equatorward during glacial times [*Toggweiler et al.*, 2006; *Williams and Bryan*, 2006) strongly consistent with the sedimentary record off northern and central Chile. Furthermore, a close dependence between the large Patagonia Ice Sheet (PIS, which covers the entire southern Andes during the last glacial) and the SWW have been also suggested (*Hulton et al.*, 1994; *Sugden et al.*, 2002). These climate/ice mass continuity models identified the climate input required to reproduce the extension reached by the large PIS during the LGM. They argued that the configuration of the icefield implies an overall reduction in air temperature by a minimum of 3 °C and a northward migration of the humid westerly precipitation belt by ~5°S latitude relative to its present average position (e.g., *Kaiser et al*., 2005; *Lamy et al*., 2004).

Contrary to the glacial times, a poleward migration of the SWW seems to have occurred during warm periods (*Toggweiler*, 2009). The prevailing view has been that westerlies shifted toward Antarctica as part of a feedback: a small CO_2 increase or small warming initiated a shift of the westerlies toward Antarctica; the shifted westerlies then caused more CO_2 to be vented up to the atmosphere, which led to more warming, a greater poleward shift of the westerlies, more CO_2 and still more warming (*Toggweiler et al.*, 2006; *Toggweiler*, 2009). Modeling studies show that during the last termination, the southward migration of the westerlies reduced polar stratification and enhanced upwelling of deepwater masses around Antarctica, which would then have released large amount of the stored CO_2 to the atmosphere.

Finally, during the present Holocene warm climate, pollen record and sedimentological data from southernmost Chile at ~53°S have documented changes in

the latitudinal position of the SWW (*Lamy et al.*, 2010). These records show antiphased intensity changes of the SWW in the core area and its northern margin between the early and late Holocene analogous to the changes observed over the present seasonal cycle (during the austral winter, the belt expand northward and the wind intensity in the core decrease; while during austral summer, the belt contracts, and the intensity within the core strengthened). This analogy suggests that the early Holocene was characterized by mean more summer-like conditions of the westerlies versus a more winter-like pattern in the late Holocene.

2.3 Present-day vegetation

The modern vegetation distribution of southern Chile reflects latitudinal and altitudinal gradients of temperature and precipitation of westerly origin (e.g., *Abarzúa et al.*, 2004; *Heusser and Heusser*, 2006) (Fig. 2-5). This gradient is established mainly by the intersection of the SWW with the Andes Cordillera producing one of the most extreme sharper vegetation contrasts in the world between the Pacific and Atlantic slopes.

Adjoining and mixing with the sclerophyllous, subtropical vegetation of central Chile at ~38°S, Lowland Deciduous Beech Forest occurs on lower mountain slopes and is composed of several *Nothofagus* species. In the central valley, it extends to ~41°S, where it merges with Valdivian Evergreen Forest. At ~43°S, North Patagonian and Subantarctic Evergreen Forests, floristically impoverished and structurally simpler version of Valdivian Evergreen Forest develop. These are replaced by Subantarctic Deciduous Forest at higher latitudes (e.g., *Heusser et al.*, 2006 and references therein). From ~47°S toward the southern coast of Tierra del Fuego at ~55°S, the temperate Magellanic rain forest becomes dominant (Fig. 2-5). This landscape is known as Magellanic moorland and consists of blanket mires and large cushion bogs of *Astelia pumila* and *Donatia fascicularis* (*Fesq-Martin et al.*, 2004 and references therein). In the coastal zone of the western Fjord Region, *Nothofagus* trees are only present in wind protected and better drained locations. In the area of the Magellanic rain forest itself, blanket mires from enclaves of up to a few hectares in size within the *Nothofagus* forest.

Altitudinal vegetation zonation of the coastal cordillera on the western slopes of the Andes is similar, ranging upward from low-land evergreen beech forest to evergreen conifer forest, and to deciduous beech forest at higher elevation in the Andes (~900–1200 m) (e.g., *Heusser et al.*, 2006 and references therein). Above treelines, shrubby steppe yields to vegetation dominated by cushion plants and grasses (*Cavieres et al.*, 2000).

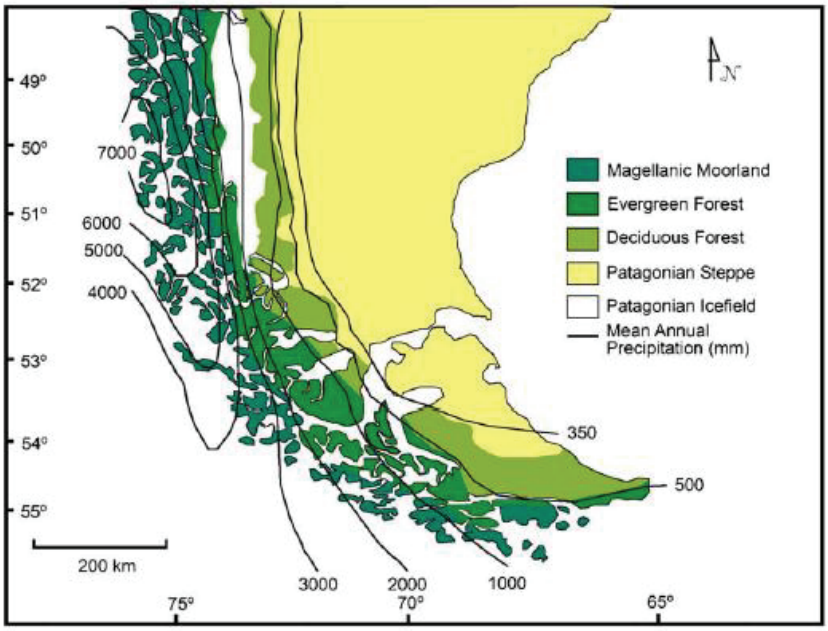

Fig. 2-5: Map of southern Chile showing modern distribution of plant communities (after *Moreno et al.*, 2009). Note, the western slope of the Andes are wetter and more densely vegetated with temperate forest, whereas the eastern flanks are dominated by rainshadow vegetation (Patagonian Steppe).

2.3.1 Past vegetation distribution

Palynological and stratigraphic studies of the temperate region of southern Chile have recognized important changes in the vegetation pattern in phase with major climate fluctuations throughout the late Quaternary (*Denton et al.*, 1999; *Moreno et al.*, 2001; *Villagran*, 2001). According to *Villagran* (2001) four major phases in vegetation development are evident in the temperate region of southern Chile: glacial, deglacial, early-mid and late Holocene. During the glacial phase, cold-resistant North Patagonian taxa along with Magellanic Moorland expanded northward and downslope into the lowlands of latitudes ~40°–43°S suggesting colder and wetter conditions up to 43°S. During the deglacial phase, the "glacial vegetation" expanded into the newly deglaciated regions between 43° and 50°S, and the mountain tops of the Coastal and Andean ranges between 40° and 43°S. This migration is paralleled by a southward movement of thermophilous Valdivian and deciduos forest occupying the region between ~40° and 43°S. Important warming pulses and decline in precipitation are evident during this time (*Villagrán*, 1990; *Moreno et al.*, 1999; *Moreno and León*, 2003). Thermophilous taxa characteristics of Valdivian rainforest became dominant during the subsequent warm-dry interval of the early –mid Holocene. Finally, during

the late Holocene, an opposite trend leads to cooler/wetter conditions characteristic of the modern climate regimen (*Villagrán*, 1988).

2.5 Geological and tectonic settings

The Chilean Fjord Region shows one of the longest and most complete sequences of glacigenic deposits and landforms in the Southern Hemisphere outside Antarctica and, perhaps, of the entire world (*Casassa et al.*, 2007). The landscape morphology of the region shows many erosional and depositional features of glacier origin. Many of these features are related to ancient glaciations, although most of them represent the more recent Quaternary glacial events (*Coronato et al.*, 2004). In all cases, the glaciers that formed this landscape were derived from the larger Patagonian Ice Sheet, which maximum size was reached during the LGM (23–19 kyr BP) (e.g., *Benn and Clapperton*, 2000).

From a geological point of view, the Chilean Fjord Region extends over a basement of varied lithology, structure and age. It is an ancient, buoyant fragment of the Gondwana super-continent, which merged with the South America shield core sometime in the Paleozoic (*Coronato et al.*, 2008; *Rabassa*, 2008).

The Andes Cordillera is the main geographic feature in Chile. Whereas the northernmost Andes are segmented, the southernmost Andes are topographically and structurally continuous, curving through 90°, from the Patagonian cordillera in the North to the Fueguian cordillera in the south. As the Andes Cordillera do so, the amount of crustal thickening decrease and the amount of wrenching increase (*Diraison et al.*, 2000). Compositionally, Andes bedrock consists mostly of volcanics and sediments of upper Jurassic-lower Tertiary age, intruded by plutonic rock of the Andean batholith. From ~52°S southward, structural changes reveal the presence of a prominent geosyncline consisting of sediments mostly of Cretaceous-Terciary age; older plutonic rock parallel younger metamorphic and sedimentary formations lying to the east (*Rabassa and Clapperton*, 1990 and references therein).

Regarding the tectonic settings, southernmost Andes line the margin of the continental South America plate next to three oceanic plates: Nazca, Antarctica and Scotia (Fig. 2-6). Nazca and Antarctica both subduct under the South America plate, but at different rates and direction (*Diraison et al.*, 2000). Southern Chile is mostly located within the continental South American plate, but the southernmost part of the Patagonian Andes and the Fuegian Archipelago is included in the oceanic Scotia plate, south of the major Magallanes-Fagnano fault zone, an active margin cutting across the southern part of the Estrecho de Magallanes (Fig. 2-6) (Singer *et al*., 2004).

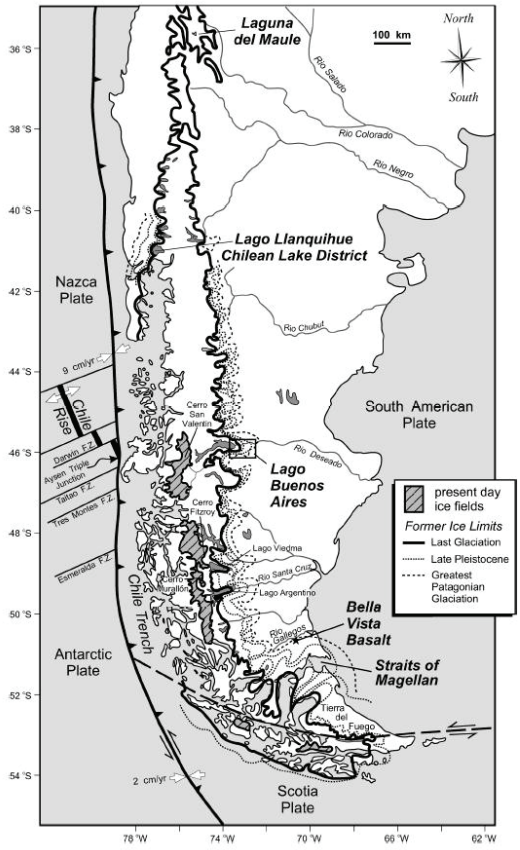

Fig. 2-6: Generalized map of southern Chile showing the present location of the principal tectonic features: South America, Nazca, Antarctic and Scotia plates. The map also shows the present-day size of icefields in Patagonia (Northern and Southern Icefields and Darwin Cordillera) and its maximum extention reached during the LGM (after *Singer et al.*, 2004).

As previously discussed, the southern Andes Cordillera intercepts the humid SWW causing a drastic orographic rain shadows. Geologic data imply that this climatic pattern has been established or significantly enhanced during the Cenozoic uplift of the southern Patagonia Andes (*Diraison et al.*, 2000; *Blisniuk et al.*, 2005). On the basis of plate geometry reconstructions, Cenozoic uplift in this region has been related to two episodes of oceanic ridge subduction beneath the South America plate, (1) the subduction of the Aluk-Farallon spreading center during the Paleogene, and (2) the subduction of several segments of the Chile Ridge since ~15 Ma. The main factor controlling uplift of the southern Patagonia Andes, however, appears to have been a strong increase in the convergence rate along with a decrease in convergence obliquity between the Nazca and South America plates at 26–28 Ma (e.g., *Diraison et al.*, 2000).

2.6 Icefields

The Chilean Fjord Region is characterized by the presence of the "Hielos Patagónicos" which are the largest temperate glaciers in the Southern Hemisphere and the most extensive outside polar latitudes (e.g., *Marden and Clapperton*, 1995; *Aniya*, 1999; *Rignot et al.*, 2003). The Hielos Patagónicos comprise the Hielo Patagónico Norte and Sur (Northern and Southern Patagonian icefields, respectively) covering a total area of ~18,000 km^2 (Fig. 2-6). They are nourished by the SWW and its storm-tracks causing high ablation rates and step mass-balance gradients [*Casassa et al.*, 2002; *Rignot et al.*, 2003; *Glasser et al.*, 2004; *Glasser et al.*, 2008).

Currently, the Hielo Patagónico Norte extends over a distance of *ca*. 100 km in a north-south direction between ~46° and 47°S along 73°30´W. This covers an area of ~4,200 km^2 [*Aniya and Enomoto*, 1986; *Aniya*, 1988). The Hielo Patagónico Sur, on the other hand, is the most extensive icefield in the southern end of the Andes Cordillera between ~48° and ~51°S. It has a length of about 350 km in a north-south direction and an area of roughly 13,000 km^2 (*Aniya et al.*, 1996, 1997). In the south, the Darwin Mountain Icefield in Tierra del Fuego constitutes the smaller and the third main glacier in southern Chile, covering an area of ~2,300 km^2 at latitudes between 54° and 55°S (*Casassa et al.*, 2002 and references therein).

There is considerable evidence that glaciers and icefields in the Patagonian Andes have expanded and contracted during the Quaternary in response to variation in the climate system (*Glasser et al.*, 2004; *Sugden et al.*, 2009). Modeling studies as well as glacigenic deposits indicate that during the last glacial period, the Patagonian Icefields coalesced to form the much larger Patagonian Ice Sheet (PIS) of 1,800 km length, covering the entire southern Andes between ~36° and 55°S (Fig. 2-6) (e.g., *Rabassa*, 2008). Modeling studies also suggest that PIS reach its maximum size during the LGM (23–19 kyr BP) with a volume of ~500,000 km^3 and extended along the crest of the Andes into areas with present-day strong temperatures gradients i.e., from 12 °C at latitude 40°S until 5 °C at latitude 55°S (*Hulton et al.*, 2002 and references therein).

A strong link between the dynamic of the PIS and the amount of dust delivered to Antarctica has been recently suggested (*Sugden et al.*, 2009; *Kaiser and Lamy*, 2010). Based on extensive dating of terrestrial records located on the eastern side of the Andes, *Sugden* and co-workes (2009) show that the expansion and retreat of the Patagonian glacier controlled the amount of dust that was delivered and transported to Antarctica during the last ice age. They show that the maximum dust recorded by ice cores in Antarctica coincide with glacier advances or periods in eastern Patagonia when rivers of glacier meltwater deposited sediment directly onto easily mobilized outwash plain. In contrast, the retreat of the outlet glacier intro pro-glacial lakes

occurred around 21,000 years ago, coinciding with the drop of dust in Antarctic ice cores. They propose that the variable sediment supply resulting from Patagonian glacial fluctuations may have acted as an on/off switch for Antarctic dust deposition. However, the maximum glacier position along much of the western side of the Andes, south of 42°S, has been difficult to determine because of the limited land there and it is assumed that most of the glaciers had a maritime termini (*Glasser and Jansson*, 2008).

3 Material and Methods

3.1 Sampling

This study incorporated the analysis of three long-sediment cores, i.e. MD07-3124, JPC-42 and MD07-3128 recovered from the Chilean continental margin between ~49°S and ~52°S (Fig. 3-1, Table 1). These cores were analyzed to study past sea surface temperature variation and its relationship with climate changes over the last glacial period and the Holocene. In addition, surface sediments collected along the Patagonian margin were analyzed in order to investigate the potential seasonality registered in the modern alkenone-derived SSTs signal (Table 2).

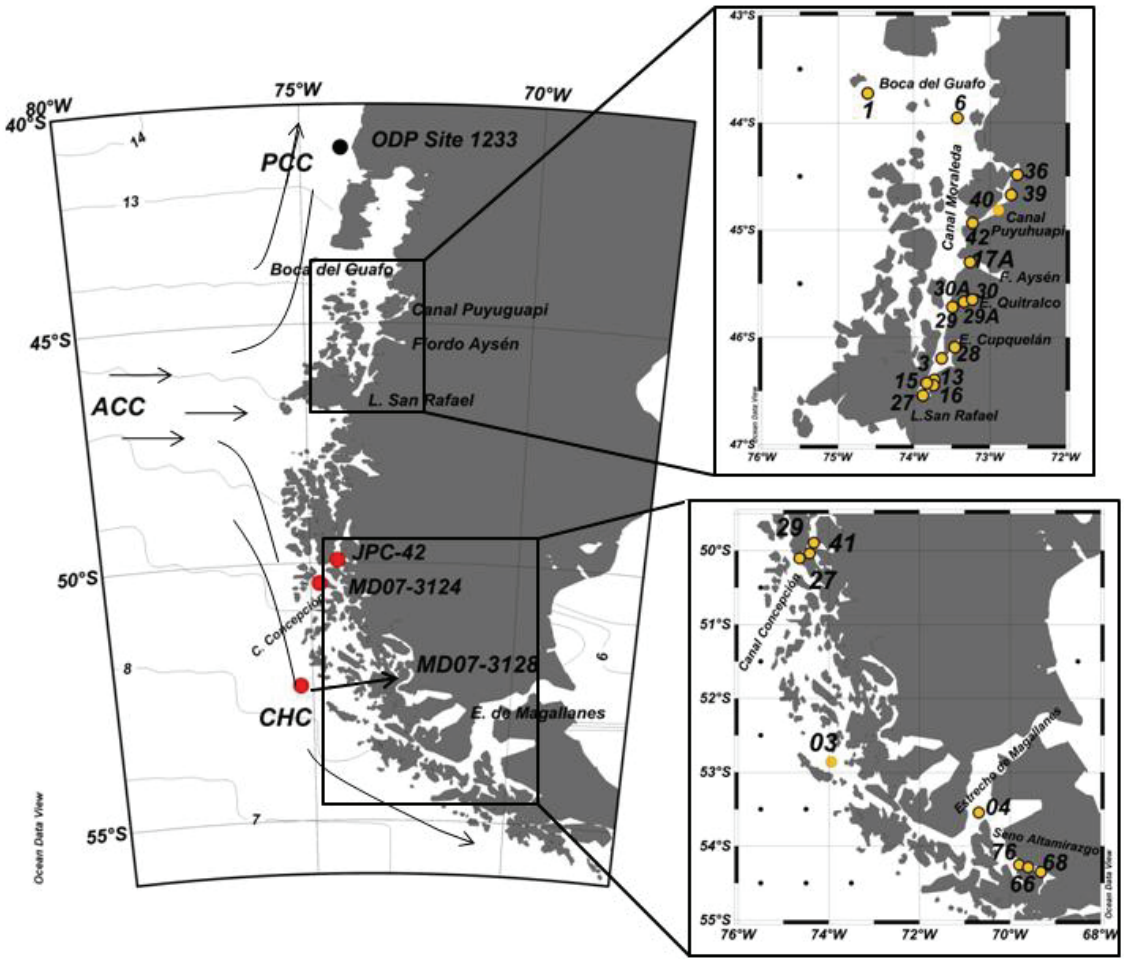

Fig. 3-1: Map of the study area showing the sediment cores (red dots) and surface sediment samples (yellow dots) analyzed in this study. Black arrow represents the main surface currents in the study area: Antarctic Circumpolar (ACC); Perú-Chile (PCC) and Cape Horn (CHC) Currents.

Table 1. Geographic position of long-cores collected from the Chilean Fjord Region.

Core	Type	Area	Lat	Long	Length (m)	Water Depth (m)
JPC-42	Jumbo PC*	Canal Wide	49°54.90´S	74°22.65´W	11.48	904
MD07-3124	Calypso PC	Canal Concepción	50°30.96´S	74°58.33´W	22.25	564
MD07-3128	Calypso PC	E. de Magallanes	52°39.57´S	75°33.97´W	30.33	1,032

* PC: piston core.

Core JPC-42, with a length of ~11.5 meters, was recovered between the Europa and Penguin fjords, in the Canal Wide at ~50°S (Fig. 3-1; Table 1). This core covers the last ~12 thousand years before the present and was obtained using a Jumbo piston corer in July of 2005 during the NBP05-05 Nathaniel B. PALMER cruise onboard the EE.UU RVIB Palmer.

The 22.25 meters-long MD07-3124 core was recovered from the Canal Concepción at ~51°S in the southwestern part of a wide fjord that is presently under comparatively strong marine influence (Fig. 3-1). Core MD07-3124 was obtained using a Calypso piston corer in February of 2007, during the XV-MD159 PACHIDERME cruise on board the R/V *Marion-Dufresne* and covers the entire Holocene.

The 30.33 meters core MD07-3128, on the other hand, was recovered from the continental slope just northwest of the mouth of the Estrecho de Magallanes at ~52°S (Table 1). This core, covering the last ~60 kyr, was recovered during the XV-MD159 PACHIDERME cruise carried on February of 2007 on board the R/V *Marion-Dufresne*.

The surface sediments samples obtained by means of multi-corer, kasten corer and piston corer were extracted from 27 sites along the Chilean Fjord Region (Table 2). These include: 13 cores collected in November of 2001 during the Chilean CIMAR FIORDO (CF) 7 Expedition on board the R/V AGOR Vidal Gormáz; 7 cores collected in July of 2005 during the NBP05-05 Nathaniel B. PALMER cruise, onboard the RVIB Palmer; and 2 cores collected in November of 2003 during the Japanese BEAGLE cruise on board R/V Mirai.

Table 2. Location of surface sediment samples collected from the Chilean Fjord Region

Core	Area	Lat	Long	Water depth (m)
Northern Patagonia				
CF7-BC01*	Boca del Guafo	43.7356°S	74.5836°W	240
CF7-BC06	Boca del Guafo	43.9878°S	73.3654°W	176
CF7-BC36	Canal Puyuguapi	44.4433°S	72.6173°W	219
CF7-BC39	Canal Puyuguapi	44.7279°S	72.714°W	160
CF7-BC40	Canal Puyuguapi	44.8248°S	72.9342°W	260
CF7-BC42	Canal Puyuguapi	44.9108°S	73.3183°W	320
CF7-BC17A	Fiordo Aysén	45.363°S	73.2919°W	330
CF7-BC30	Estero Quitralco	45.7430°S	73.4077°W	269
CF7-BC30A	Estero Quitralco	45.7542°S	73.5099°W	110
CF7-BC29A	Estero Quitralco	45.7602°S	73.4667°W	112
CF7-BC29	Estero Quitralco	45.7812°S	73.5087°W	114
CF7-BC28	Estero Quitralco	46.144°S	73.4958°W	239
Palmer-KC03	Laguna San Rafael	46.165°S	73.6679°W	52
Palmer-KC13	Laguna San Rafael	46.449°S	73.797°W	30
Palmer-KC15	Laguna San Rafael	46.434°S	73.7932°W	112
Palmer-KC16	Laguna San Rafael	46.434°S	73.8012°W	112
CF7-BC27	Laguna San Rafael	46.4852°S	73.8026°W	112
Central Patagonia				
Palmer-KC41	Fiordo Penguin	49.915°S	74.3774°W	711
Palmer-KC29	Fiordo Europa	50.013°S	74.4019°W	350
Palmer-KC27	Fiordo Europa	50.057°S	74.4307°W	414
MD07-3124	C. Concepción	50.516°S	74.9721°W	564
Southern Patagonia				
Palmer-KC76	Seno Altamirazgo	54.26°S	69.7941°W	290
Palmer-KC66	Seno Altamirazgo	54.322°S	69.4571°W	110
Palmer-KC68	Seno Altamirazgo	54.324°S	69.5535°W	117
Beagle-MC03	E. de Magallanes	52.867°S	74.0876°W	528
Beagle-MC04	E. de Magallanes	53.572°S	70.6746°W	428

*Box core (CB), kasten cores (KC) and multi-cores (MC).

3.2 Dating Method

The age model of core MD07-3124 (~51°S) is based on fifteen accelerator mass spectrometer (AMS) radiocarbon dates (^{14}C) and a linear interpolation between the age control points. ^{14}C-AMS dates were measured on a mixture of planktonic foraminifera. All ^{14}C ages were converted to calibrated ages before the present (kyr BP) using the InCal09 software (*Reimer et al.*, 2009), after applying a marine reservoir age of 780 years. This new marine reservoir age was obtained from AMS-^{14}C ages of core JPC-42 located just ~0.5° northeast from the Canal Concepcion site (see manuscript 4.2). According to the age model, core MD07-3124 covers the last ~11 kyr BP. It was sub-sampled at 8-cm interval, resulting in an average temporal resolution of ~100 years.

The chronology for core JPC-42 (~50°S) was established based on seven AMS-^{14}C ages, measured on shell fragments at Woods Hole Oceanographic Institution (WHOI), and a linear interpolation between the data points. The comparison of two AMS-^{14}C ages on shell and wood fragments from the same core depth (at 1.75 meters) resulted in a new local marine reservoir age for Canal Wide of 780 years (see manuscript 4.2). This age was older than the only published local reservoir age for the Chilean Fjord Region, i.e. 530 years at Puerto Natales (*Ingram and Southon*, 1996). After the correction of the AMS-^{14}C ages for the new marine reservoir age, these were converted to kyr BP using InCal09 software. Core JPC-42, covering the last ~12 kyr BP, was sub-sampled at continuous 3-cm intervals, resulting in an average temporal resolution of ~110 years.

The chronology for core MD07-3128 was established by different techniques. The age control of the upper ~18.5 m was based on 13 AMS-^{14}C ages performed on mixed planktonic foraminifera. Below ~18.5-m core depth, the radiometric chronology was supplemented by the record of the Laschamp magnetic field excursion located between 19.65 m (top) and 21.5 m (base). We defined the Laschamp excursion as the directional maximum shift centered at 41.25 kyr (*Laj et al.*, 2009) and used the mid-point at ~20.6 meter as an age control point. Below the Laschamp excursion, we extended the age-scale to the base of the core by tuning our alkenone SST record to that of ODP Site 1233 on its latest age model (*Kaiser and Lamy*, 2010) using only two correlation points (see manuscript 4.1). ^{14}C ages were converted to calendar ages using IntCal09 (Reimer et al., 2009) with a local marine reservoir deviation of 221 ± 40 years (*Ingram and Southon*, 1996). Core MD07-3128, covering the last ~60 kyr, was sub-sampled every 12 cm, resulting in an average temporal resolution of ~2.8 kyr for the intervals corresponding to the Holocene, ~200 years for the period covering Marine Isotope Stage (MIS) 2, and ~230 years for the interval comprising MIS 3.

Calendar ages for all core depths from which measurement were performed were interpolated using the computer program AnalySeries 1.1.

3.3 Reconstruction of paleotemperature

Sea surface temperature (SST) reconstruction was based on the unsaturated index of alkenones. Alkenones are long chain methyl ketones with 37 carbon atoms and 2–4 double bonds or unsaturation that are ubiquitous in the sediment of the world's ocean (*Prahl and Wakeham*, 1987; *Prahl et al.*, 1988; *Müller et al.*, 1998). Alkenones are exclusively produced by only a few species of haptophyte algae, the most common source organism is the abundant and cosmopolitan *Emiliania huxleyi* (e.g., *Rosell-Melé*, 1998 and references therein).

The alkenone unsaturation index $U^{K'}_{37}$ was used to estimate past SST (*Prahl et al.*, 1988). This index measures the relative abundances of the di, and tri- unsaturated C_{37} alkenones as follows:

$$U^{K'}_{37} = \frac{[C_{37:2}]}{[C_{37:2} + C_{37:3}]}$$

The close linkage between the relative abundance of $C_{37:2}$ and $C_{37:3}$ alkenones and the water temperature in which these algae grow has been confirmed by several culture, surface sediments and water column particulate organic matter studies (*Prahl et al.*, 1988; *Müller et al.*, 1998; *Prahl et al.*, 2000; *Bendle and Rosell-Mele*, 2004).

The equation proposed by *Prahl et al*. (1988), which is based on cultures of *Emiliana huxleyi*, was applied to convert $U^{K'}_{37}$ unit to SST values:

$$T = \frac{[U^{K'}_{37} - 0.039]}{0.034}$$

Alkenones were extracted from 3 to 5 g aliquots of freeze-dried and homogenized sediments (*Müller et al.*, 1998). We use UP 200H ultrasonic disruptor probes (200W, amplitude 105 mm, pulse 0.5s) and three successively less polar mixture of methanol and dichloromethane (CH_3OH, CH_3OH:CH_2CL_2 1:1; CH_2CL_2) each for 5 minutes. After centrifugation, the three extracts were combined, washed with demineralized water, dried over $NaSO_4$ and concentrated to dryness with a rotary evaporator. Additionally, the extracts were saponified to avoid interferences with co-eluting C_{36}-fatty acid methyl esters using 300 mL 0.1 M KOH in CH_3OH/H_2O (90:10) at 80ºC for 2 hours. The neutral fractions was partitioned into hexane and separated in two fractions by liquid chromatography using silica gel as an absorbent (Varian Bond

Elut SI). The separation was achieved using solvents of increasing polarity. CH_2Cl_2 was used to obtain the alkane and ketone fractions while CH_3OH was used to recover the alcohol fraction. Finally, the ketone fractions were dried under N_2 and taken up into 25 µL of a mixture of CH_3OH/CH_2Cl_2 (1:1).

The relative abundances of the di-, tri-, and tetraunsaturated C_{37} alkenones were quantified using gas chromatography equipped with a fused silica capillary column (60 m x 0.32 mm, DB-5 MS, Agilent J&W) and flame ionization detector (FID). 2-nanodecanone added to the samples before extraction was used as an internal standard for the calculation of alkenones concentration (in ng/g dry sediment weight). Helium was employed as carrier gas with a constant pressure of 150kPa. After sample injection at 50 °C, the oven temperature was programmed to 250 °C at a rate of 25 °C/min, and then to 290 °C at a rate of 1 °C/min, held for 26 minutes, and finally to 310°C at a rate of 30 °C/min, where the final temperature was maintained for 10 minutes. Alkenone measurements on core MD07-3124 and MD07-3128 were performed at the University of Bremen in Germany while the measurements on core JPC-42 were done in the laboratory of Marine Organic Chemistry at the University of Concepción, Chile. Procedural and analytical reproducibility for the analysis was determined with a homogenous sediment standard analyzed once for every 5 samples. The relatively analytical error was below 1 °C.

3.4 Biogenic components in the bulk sediment using a geochemical approach

The biogenic components in sediments such as the alkenone concentrations (as a proxy for coccoliths), the calcium carbonate (as a proxy for calcareous microorganisms, coccolithophorids and foraminifera), and the biogenic opal contents (as a proxy for siliceous microorganisms, mainly diatoms) were used to reconstruct the calcareous and siliceous productivity of core MD07-3128.

The total alkenone concentrations (converted to µg/g dry sediment weight) were calculated as the sum of di, tri and tetra-unsaturated C_{37} alkenones normalized to total organic carbon (TOC) and are expressed as µg/gTOC. Since alkenones are biomarkers for some haptophyte (coccoliths) algae, and the coccoliths have an exoskeleton composed of numerous calcite platelets that are readily preserved in the sedimentary record, we compared the alkenone concentration with that of the content of calcium carbonate and elemental calcium in the same core.

The content of calcium carbonate ($CaCO_3$) in the sediment was determined according to the formula:

$$\%CaCO_3 = (\%TC - \%TOC) * 8.333$$

where

TC= total carbon content of untreated samples
TOC= total organic carbon content of HCl-treated samples
8.333= constant factor

The TC was determined with a CNS elemental analyzer (Vario EL III) at the Alfred Wegener Institute (AWI) in Bremerhaven. The measurements were done on 5 mg of freeze-dried and homogenized sediment placed on tin capsules. In the Vario EL III analyzer, the samples were first oxidized and then reduced to generate a gaseous mixture of elemental nitrogen, carbon dioxide and sulfur dioxide. The mixture of gases passed though a gas chromatography column at a constant temperature of 70 °C in which the gaseous products were separated. The concentrations of the separated gases were detected as a function of their thermal conductivity. During the measurement, the content of TC and TN of blank tin capsules and different working standards were analyzed to test the reproducibility of the measurements.

The TOC, on the other hand, was determined with a LECO Carbon Sulfur Analyzer (LECO-CS 125) at AWI, Bremerhaven. Prior to the measurement, the freeze-dried and homogenized sediments were acidified by direct addition of 1M HCl and dried overnight at 150 °C.

To obtain a high-resolution calcium record we further measured Ca elemental concentration (unit = total elemental counts) using an Avaatech^{TM} X-Ray Flourescence (XRF) Core Scanner at AWI, Bremerhaven. Ca intensities were measured at 1 cm resolution with an exposure time of 30s. This non-destructive measuring technique allows a rapid semi-quantitative geochemical analysis on split sediment cores.

The content of biogenic opal in the bulk sediment was determined at UDEC following the procedure first described by *Mortlock and Froelich*, (1989) and later modified by *Müller and Schneider*, (1993). The opal content of marine sediment has often been used to infer past changes in surface water productivity (e.g., *Charles et al*., 1991). For the analysis, approximately 25 mg freeze-dried and homogenized sediments were mixed with 10 mL peroxide (H_2O_2) and 5 mL 1N hydrochloric acid (HCl) in polypropylene centrifuge tubes and sonicated for 30 minutes to remove both the inorganic carbon and organic matter fractions. After sonication, 20 mL of Milli-Q water was added to each tube and centrifuged at 4300 rpm for 5 min. The supernatant was removed and the sediments were dried overnight at 60 °C. A 40 mL aliquot of 1M NaOH was added to each tube and sonicated at 85 °C for 5 hours. Finally, samples were centrifuged again at 4200 rpm for 5 minutes before being measured in an Agilent spectrophotometer at 812 nm. Biogenic opal data are reported as $\%Si_{opal}$ according to the formula:

$$\%Si_{opal} = 112.4*(Cs/M)$$

where

112.4= molecular weight of Si (28.9)*the extraction volume of NaOH (0.04 L)*100.
Cs= silica concentration in the sample
M=sample mass in mg

As large and variable amounts of siliciclastics strongly affect the contents of $CaCO_3$, opal, and organic matter, we calculated the concentrations of opal and carbonate relative to the total biogenic fraction (as the sum of the three major biogenic components opal, $CaCO_3$, and organic matter). Organic matter contents were calculated by multiplying TOC contents with a constant factor of 1.5. Furthermore, we used the opal/carbonate ratio for illustrating siliceous versus carbonate component, independent of changes on sedimentation rate.

3.5 Oxygen and Carbon Isotope composition

A Finnigan MAT 253 mass spectrometer coupled to an automated Kiel device was used to measure the oxygen and carbon isotope composition of the planktic foraminifera *Neogloboquadrina pachyderma* sinistral (NPS). The stable isotope analysis of core MD07-3128 was performed at the University of Bergen in Norway, on specimens of NPS selected from the >150–250 µm size fraction. The data are reported in ‰ on the V-PDB scale calibrated with NBS-19 standard calcite. The long-term analytical precision of the system as defined by the reproducibility of carbonate standards between 6–60 mg was ±0.08‰ and ±0.03‰ for $\delta^{18}O$ and $\delta^{13}C$, respectively.

In order to derive the temperature and salinity related signal in the $\delta^{18}O$ record of NPS, an ice-volume correction was performed based on the global Holocene and deglacial sea-level record of *Fairbanks* (1989) (0–22 kyr BP) and the global sea-level record from the Red Sea (*Arz et al.*, 2007), for the earlier part of the record. A 1.2‰ ice-effect for the last termination was assumed.

3.6 Ice Rafted Debris

Ice rafted detritus (IRD) was used to infer the dynamics of the large Patagonian Ice Sheet that covered the southern Andes between ~40°S and ~55°S (e.g., *Hulton et al.*, 2002; *Glasser et al.*, 2008) during the last glacial. The transport of land-derived sediment by icebergs, and the release of that sediment during iceberg melting, has been widely accepted as the primary mechanism for supplying anomalously large (sand-sized and larger) land-derived grains (knows as IRD) to marine settings away

from a continental margin. The temporal distribution of IRD in marine sediments can be interpreted as a history of glacial extension to the sea level, whereas the geographic distribution and the composition of the IRD can be used to identify the glaciated source areas.

The relative percentage of the >150 µm carbonate-free fraction and manual particle counts were used as proxies for ice rafted debris (IRD). In order to separate the fraction >150 µm of core MD07-3128, the sediments were wet sieved after removing both carbonates and organic matter by direct addition of 10% acetic acid and 3.5% hydrogen peroxide. IRD was counted from the >150 µm carbonate-free fraction, assuming that coarser-grained terrigenous sediment can only reach the core location through iceberg transport. Volcanic particles are not a significant component at Site MD07-3128 most likely because ash plumes originating from volcanoes of the Southern Andes are typically transported and deposited eastward due to the prevailing strong westerly winds (e.g. *Kilian et al*., 2003). Opal has not been resolved, but the opal contents are far too low to significantly contribute to the >150 µm carbonate-free fraction record. This assumption is confirmed by microscopic inspection of a number of selected samples.

3.7 Determination of $C_{37:4}$ alkenone as proxy for low salinity waters

The relative abundance of $C_{37:4}$ alkenones was used as a proxy to infer past changes in low salinity waters. It has been proposed that these particular alkenones ($C_{37:4}$ alkenones) are linked to low-salinity water masses and that a $C_{37:4}$ increase of about 5 to 10% corresponds to a freshening of one practical salinity unit (PSU) (*Rosell-Melé*, 1998; *Rosell-Melé et al.*, 2002). It is still unclear if indeed salinity has a direct effect on the $C_{37:4}$ biosynthesis or if the observed pattern is due to a metabolic difference of coccolithophorids endemic of cold or coastal water masses (*Schulz et al.*, 2000). However, according to *Bard et al.* (2000), even if metabolic processes are involved, $C_{37:4}$ abundances may still be used to study the advection of low salinity waters.

The relative abundances of $C_{37:4}$ alkenone were measured on core MD07-3128 using a gas chromatography equipped with a fused silica capillary column and flame ionization detector (FID) (see 3.3, materials and methods) and were calculated as:

$$\%C_{37:4} = 100 * [C_{37:4}]/[C_{37:2} + C_{37:3} + C_{37:4}]$$

The relative abundances of $C_{37:4}$ alkenones were compared to IRD estimates in order to constrain their applicability as a paleosalinity proxy (see chapter 4.1).

4 Manuscripts

4.1 Millennial-scale surface water changes in the Southeast Pacific off southernmost Chile (52°S) over the past ~60 kyr

A. M. Caniupán[1,*], F. Lamy[1], C. B. Lange[2], U. Ninnemann[3], R. Kilian[4], O. Baeza Urrea[4], H. Arz[5], C. Aracena[2], D. Hebbeln[6], J. Kaiser[7], C. Kissel[8], C. Laj[8], G. Mollenhauer[1], R. Tiedemann[1]

[1]Alfred Wegener Institute for Polar and Marine Research, Bremerhaven, Germany
[2]Department of Oceanography and Center for Oceanographic Research in the eastern South Pacific (COPAS), University of Concepción, Concepción, Chile.
[3]Bjerknes Centre for Climate Research, University of Bergen, Bergen, Norway.
[4]Lehrstuhl für Geologie, Universität of Trier, Trier, Germany.
[5]Leibniz Institute for Baltic Sea Research Warnemünde, Seestraße 15, 18119 Rostock-Warnemünde, Germany
[6]Center for Marine Environmental Sciences (MARUM), University of Bremen, Bremen, Germany
[7]UMR 7159 LOCEAN, Université Pierre et Marie Curie, Paris, France
[8]Laboratoire des Sciences du climat et de l'Environnement (LSCE), Gif-sur-Yvette, France.
*to whom correspondence should be addressed. Email: Magaly.caniupan@awi.de

Paleoceanography, in review

Abstract

Glacial millennial-scale paleoceanographic changes in the Southeast Pacific and the adjacent Southern Ocean are only poorly known due to the scarcity of well-dated and high resolution sediment records. Here we present new surface water records from sediment core MD07-3128 recovered at 53°S off the Pacific entrance of the Strait of Magellan. The alkenone-derived sea surface temperature (SST) record reveals a very strong warming of ca. 8˚C over the last Termination and substantial millennial-scale variability in the glacial section largely consistent with our planktonic foraminifera oxygen isotope ($\delta^{18}O$) record of *Neogloboquadrina pachyderma* (sin). The timing and structure of the Termination and some of the millennial-scale fluctuations are very similar to those observed in the well-dated SST record from ODP Site 1233 (41ºS) and the temperature record from EPICA Antarctic ice core. Differences in our new SST

record include a long-term warming trend over Marine Isotope Stage (MIS) 3 followed by a cooling towards the Last Glacial Maximum (LGM). We suggest that these differences reflect regional cooling related to the proximal location of the southern Patagonian ice sheet and related melt-water supply at least during the LGM. This proximal ice-sheet location is documented by generally higher contents of ice rafted debris (IRD) and tetra-unsaturated alkenones, and a slight trend towards lighter planktonic $\delta^{18}O$ during late MIS 3 and MIS 2. On millennial-scales opal contents are generally higher whereas carbonate contents and alkenone concentrations are lower during cold intervals, suggesting SST-related shifts in the siliceous and calcareous plankton communities. These changes may be interpreted in terms of a northward shift of the Southern Ocean fronts and the opal belt during cold periods and/or changes in the nutrient advection consistent with lower planktonic foraminiferal $\delta^{13}C$. Comparatively low opal contents around the LGM are interpreted as reduced productivity due to enhanced melt-water input and resulting surface water stratification.

Keywords: Southeast Pacific, millennial-scale changes, alkenones, ice rafted debris, biogenic silica, calcium carbonate, Patagonian ice sheet.

1. Introduction

Past changes in surface ocean properties in the Southeast Pacific including the Southeast Pacific sector (SEPS) of the Southern Ocean (SO) just north of the modern Subantarctic Front are only poorly known primarily because high resolution sediment records from this region are very scarce (*Gersonde et al*., 2005; *MARGO Project Members*, 2009). In the SEPS, a few records have been retrieved around the Subantarctic Front (SAF) between ~100°W and ~120°W (*Gersonde et al*., 2005; *Mashiotta et al*., 1999). Further north, high-resolution paleoceanographic records are available from the coastal ocean at the mid-latitude Chilean margin between ~27°S and ~41°S (*Kaiser et al*., 2005; *Kaiser et al*., 2008).

The presently available SST data suggest a relatively weak LGM (19–23 kyr BP) cooling of generally less than ~2 °C (based on diatoms transfer function SST; (*Gersonde et al*., 2005) and ~2.5 °C (based on Mg/Ca SST; (*Mashiotta et al*., 1999) in the subantarctic SEPS. In contrast, alkenone-derived SST records from the mid-latitude Chilean margin between ~30°S and ~41°S indicate substantially reduced LGM SSTs of the order of 4–6 °C compared to modern values (5–7 °C compared to early Holocene values) (*Kaiser et al*., 2005; 2008; *Mohtadi et al*., 2008; *Romero et al*., 2006). The large SST changes along the Chilean margin have been related to a ~5–6° northward shift of the northern margin of the Antarctic Circumpolar Current system (ACC) (e.g., *Kaiser et al*., 2005; *Lamy et al*., 2004). It has been speculated that this northward extension of

cold subantarctic water masses could be connected to an expansion of the sea ice cover around Antarctica and a northward displacement of the southern westerly winds (SWW). Such interpretation would be consistent with winter sea ice reconstructions in the Atlantic and Indian Ocean sectors of the SO whereas the few records available suggest a more modest sea ice expansion in the Pacific sector during the LGM (*Gersonde et al*., 2005).

In the SO, the extraction of nitrate and phosphate by phytoplankton is currently incomplete, and phytoplankton in large regions is iron-limited. High nutrient concentrations in surface waters occurring today around Antarctica reflect that the biological pump is running at less than maximum efficiency (*Anderson et al*., 2002). Changes in the efficiency of the SO's biological pump and a more/less efficient uptake of upwelled nutrients has been long recognized to be a potential source of variability in atmospheric CO_2 through glacial/interglacial cycles (e.g., *Sarmiento and Toggweiler*, 1984), as changes in SO productivity may have contributed to glacial atmospheric CO_2 drawdown (*Fischer et al*., 2010; *Petit et al*., 1999). One often cited mechanism to increase relative effiiciency of the biologic pump and draw down CO_2 is iron fertilization (*Martin*, 1990). This concept suggests that enhanced glacial dust supply to the SO decreased the present iron limitation and strengthened the export of organic matter to the deep ocean. Most evidence for enhanced glacial productivity comes from the Atlantic and Indian Ocean sectors of the SO where glacial productivity was enhanced in the subantarctic zone and reduced south of the modern Polar Front (PF) (e.g., *Kohfeld et al*., 2005) although there are indications that glacial diatom productivity was also higher south of the PF (*Abelmann et al*., 2006). Recent productivity records from a sediment core located south of the PF in the Atlantic sector (that resolves millennial-scale variations with reasonable age uncertainties) suggest, for example, that enhanced siliceous productivity associated with the last Termination and Antarctic warm events was induced by upwelling and increased ventilation of deep-waters paralleling the CO_2 rises (*Anderson et al*., 2009). Today, upwelling processes occur just south of the present Antarctic PF being principally determined by wind stress. The Antarctic PF represents an area of massive biogenic silica export (mainly diatoms) and a major oceanographic boundary, south of which water with high dissolved silicon contents are dominant. It clearly demarcates the area where the biological pump is driven by $CaCO_3$ to the north and biogenic SiO_2 particle export to the south (*Honjo*, 2004). The "diatom ooze belt" is located just south of the Antarctic PF where biogenic opal contents may reach 75 wt.% and opal accumulation may be as high as 20g cm^{-2} kyr^{-1} (e.g., *Charles et al*., 1991). Yet, the pattern of productivity in the Pacific sector, by far the largest of the SO sectors, remains poorly defined hindering firm conclusions regarding the role of the SO in past ocean nutrient cycling and CO_2 changes on glacial-interglacial and even less on millennial time-scales.

There is an ongoing debate on the pattern and timing of millennial-scale climate fluctuations in the Southern Hemisphere. In Antarctica, millennial-scale temperature changes over the last glacial have been consistently explained by the bipolar seesaw concept that suggests an out-of-phase millennial-scale climate pattern between the Northern and Southern hemispheres (e.g., *EPICA Community Members*, 2006; *Stocker and Johnsen*, 2003). This Antarctic millennial-scale pattern seems to extend into the Southern Hemisphere mid-latitudes (40–46°S) as indicated by high-resolution SST records from the Chilean margin (ODP Site 1233; (*Kaiser et al.,* 2005; *Lamy et al*., 2004); New Zealand (*Pahnke et al*., 2003) and the SW Indian Ocean (*Barrows et al*., 2007a). Millennial-scale SST amplitudes in these records are of the order of 2–3 °C and are similar to Antarctic temperature changes at these time-scales (*Jouzel et al*., 2007). In the SO south of the SAF, however, high-resolution SST records with sufficient age control for analyzing the timing of millennial-scale pattern are still missing.

In contrast to the findings of Antarctic millennial-scale pattern in SST records, continental glaciological and palynological data from the Chilean Lake District (~40°S; directly onshore of ODP Site 1233) have been used in support for inter-hemispheric synchrony both during the last glacial (*Lowell et al*., 1995) and the deglaciation (e.g., cooling during the Younger Dryas (YD) cold phase; (*Denton et al*., 1999; *Moreno et al*., 2001). However, new glaciological data from the southern Patagonian ice-sheet (PIS, south of ~50°S) suggest glacier advances more in phase with Antarctic climate pattern (*Kaplan et al*., 2008; *Moreno et al*., 2009; *Sugden et al*., 2009) and consistent with data from New Zealand (*Barrows et al*., 2007b; *Kaplan et al*., 2010).

Here we present new surface water records including alkenone-based SST, planktonic foraminifera oxygen isotope, marine productivity, and IRD records from the southernmost continental Chilean margin based on core MD07-3128 retrieved from the Pacific entrance of the Strait of Magellan (53°S) covering the past ~60 kyr. We discuss millennial-scale and longer term SST pattern and compare them to the well-dated SST record from ODP Site 1233 at 41°S and to temperature changes in Antarctic ice core. We show that glacial SSTs were partly influenced by the presence of the large PIS located close to the site, at least during the LGM. Furthermore, we infer significant millennial shifts in calcareous and siliceous plankton communities (based on the contents of biogenic opal, calcium carbonate and total alkenones) documenting northward (southward) movements of the opal belt during cold (warm) periods related to changes in the dynamics of SO circulation.

2. Study Area

Modern surface circulation in the Southeast Pacific off southernmost Chile (~53°S) is dominated by the Cape Horn Current (CHC) a coastal branch of the Antarctic

Circumpolar Current (ACC) (*Antezana*, 1999; *Chaigneau and Pizarro*, 2005; *Strub et al*., 1998) (Figure 1a). The CHC originates from the bifurcation of the northern ACC approaching South America between 40° to 45°S. The northern branch forms the Peru-Chile (or Humboldt) Current flowing equatorward whereas the CHC flows poleward along the southernmost Chilean continental margin towards the Drake Passage and transports Subantarctic Surface water (SAAW) (*Shaffer et al*., 1995; *Strub et al*., 1998). The area off the Strait of Magellan is located ~5° latitude north of the present SAF (*Orsi et al.*, 1995). Modern mean annual SST in this area is ~8 °C and the seasonal range is ~3 °C (World Ocean Atlas 2009).

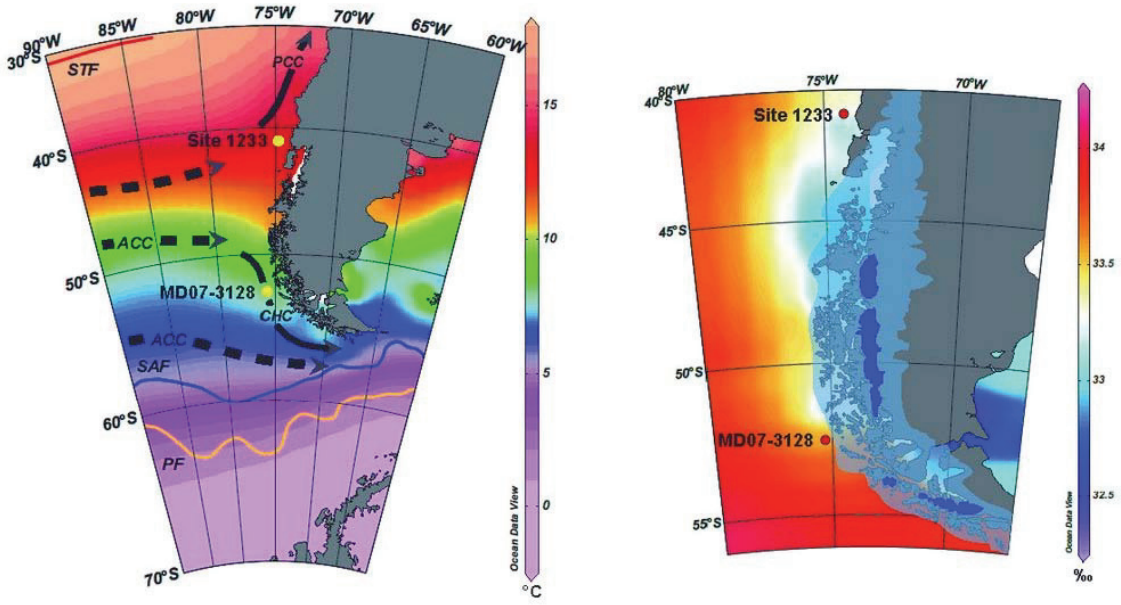

Figure 1. Core location maps. (a) Schematic illustration of the modern surface circulation in the Southeast Pacific after *Strub et al*. (1998) with mean annual SST (World Ocean Atlas 2009); PCC: Peru–Chile Current, ACC: Antarctic Circumpolar Current, CHC: Cape Horn Current. Location of major Southern Ocean fronts after *Orsi et al*. (1995); STF= Subtropical Front (red), SAF= Subantarctic Front (blue), PF= Polar Front (yellow). (b) Annual sea surface salinity (color bar) off southern South America (World Ocean Atlas 2009). Extension of the modern ice fields in Patagonia and maximum extent of the PIS during the LGM (based on (*Hollin and Schilling*, 1981; *McCulloch et al*., 2000) is shown in dark gray and light blue, respectively.

Within the southern Chilean fjord region, the relatively saltier Pacific surface waters progressively mix with fresher waters from melting glaciers, precipitation, and river runoff to produce a positive estuarine circulation characterized by strong density, temperature and salinity gradients (*Pickard*, 1971; *Sievers and Silva*, 2008; *Silva and Calvete*, 2002). However, the exchange between fjord waters and open Pacific water masses is quite restricted due to very shallow sill depths on the continental shelf off

southernmost Chile (30–40 m; (*Antezana*, 1999). Slightly reduced salinities originating from the outflow of fjord waters occur along the continental margin and are restricted to a thin surface layer of up to ~50 m thickness (*Antezana*, 1999; *Kilian et al*., 2007).

At present, Patagonia has three main glacier systems: the Northern and Southern icefields (46º–52ºS) and the Darwin Mountain icefield in Tierra del Fuego (54–55ºS) that greatly expanded during the last glacial and formed the much larger PIS covering the entire Andean part of southern South America between ~38° S and 56°S (e.g., *Glasser and Jansson*, 2008) (Figure 1b). Though little is known about the extent of this ice sheet on the Pacific continental margin, it is assumed that glaciers advanced towards the continental shelf edge and terminated in iceberg-calving fronts (*DaSilva et al*., 1997). This would bring the ice sheet very proximal to our coring site and we thus expect a much larger meltwater influence on surface water salinities and possibly also on SSTs in the study area. Furthermore, glacial advances of the southern PIS have been recently linked to dust content changes as recorded in Antarctic ice-cores, as glacier advances into the eastern Andean foreland largely enhance the availability of fine-grained material in the assumed Patagonian dust source areas (*Kaiser and Lamy*, 2010; *Sugden et al*., 2009). However, an IRD-based record of southern PIS changes on the Pacific side of the ice-sheet is still missing.

3. Material and Methods

The 30.33m-long Calypso piston core MD07-3128 was retrieved in 2007 from the continental slope off the Strait of Magellan, southern South America, at 52°39.57'S, 075° 33.97'W (1,032 m water depth) during the IMAGES (International Marine Past Global Changes Studies) XV-MD159-Pachiderme cruise on board R/V Marion Dufresne.

The top 50 cm of the core (Holocene sediments) consist of olive yellow foraminifera ooze with >40% CaCO3 content. The rest of the sequence is mainly composed of silt-bearing clay with m-scale variations in color between grey and grayish olive. Drop-stones were visually observed in particular in the upper 10 m of the core (except for the Holocene foraminifera ooze interval) and to a lesser amount deeper in the core.

For this study, core MD07-3128 was sub-sampled every 12 cm resulting in an average temporal resolution of ~2.8 kyr for the intervals corresponding to the Holocene, ~200 years for the period covering Marine Isotope Stage (MIS) 2, and ~230 years for the interval comprising MIS 3 (the oxygen isotope records are of lower resolution during this interval). All samples were stored frozen until chemical analysis. We further measured elemental concentrations with a resolution of 1 cm (see below).

3.1 Chronology

The age control of the upper core section of core MD07-3128 (0.3 to 18.51 m) was based on 13 accelerator mass spectrometry (AMS) ^{14}C dates performed on mixed planktonic foraminifera (Table 1). Below ~18.5 m-core-depth, the radiometric chronology was supplemented by the record of the Laschamp magnetic field excursion located between 19.65 m (top) and 21.5 m (base). We define the Laschamp excursion as the directional maximum shift centered at 41.25 kyr (*Laj et al*., 2000, 2009) and use the mid-point at ~20.6 m core depth as an age control point. Below the Laschamp excursion, we extended the age-scale to the base of the core by tuning our alkenone SST record to that of ODP Site 1233 on its latest age model (*Kaiser and Lamy*, 2010) (Figure 2a) using a minimum of only two correlation points (Table 1). This age model is consistent with the low resolution planktonic $\delta^{18}O$ record from our core (Ulysses Ninnemann, unpublished data; Figure 3). All ^{14}C ages were converted to calendar ages using IntCal09 and Marine09 calibration curves (*Reimer et al*., 2009) with a local marine reservoir deviation of 221 ± 40 years (*Ingram and Southon*, 1996). We are aware that pre-Holocene reservoir ages might have been larger at our site. However, to the best of our knowledge, there is presently no information on regional changes in reservoir ages in the study area available. We believe that our present age model is sufficient for the purpose of discussing glacial/interglacial and millennial-scale changes.

Table 1. Age control points for core MD07-3128.

Lab.-ID	Core depth (m)	^{14}C AMS age (kyr B.P.)	±Err (kyr)	Calibrated age (cal. kyr B.P.)	Calibration method
KIA 34252	0.03	3.405	0.025	2.99	IntCal09
KIA 36388	0.3	9.490	0.045	10.11	IntCal09
KIA 34253	0.35	9.945	0.045	10.58	IntCal09
KIA 36390	0.94	13.040	0.06	14.42	IntCal09
KIA 34255	1.55	15.460	0.07	17.99	IntCal09
KIA 36391	2.5	16.100	0.07	18.69	IntCal09
KIA 34256	3.93	17.330	0.13	19.93	IntCal09
KIA 36392	7	19.560	0.1	22.48	IntCal09
KIA 36393	9.52	22.760	0.15	26.53	IntCal09
KIA 36394	13.96	23.610	0.15	27.86	IntCal09
KIA 39462	16.01	26.400	0.24	30.6	IntCal09
KIA 36395	17.96	31.540	0.465	35.28	IntCal09
KIA 39463	18.51	33.660	0.540	37.76	IntCal09
	20.58			41.25	Laschamp excursion
	27.0			49.93	Based on SST tuning to ODP Site 1233
	30.12			59.66	Based on SST tuning to ODP Site 1233

3.2 Alkenone-sea surface temperatures (SSTs)

We determined SST by alkenone paleothermometry in continuous 12 cm intervals. Long-chain alkenones were extracted from 3 to 5 g of powdered freeze-dried sediments according to *Müller et al.* (1998).

The relative abundances and concentrations (in ng/g dry sediment weight) of di-, tri-, and tetra-unsaturated C_{37} alkenones were measured using gas chromatography equipped with a fused silica capillary column (60 m x 0.32 mm, DB-5 MS, Agilent J&W) and flame ionization detection (FID). 2-nanodecanone added to the samples before extraction was used as internal standard. Helium was employed as carrier gas with a constant pressure of 150kPa. After injection at 50 °C, the oven temperature was programmed to 250 °C at a rate of 25 °C/min to 290 °C at a rate of 1 °C/min, held for 26 min, and finally to 310 at a rate of 30 °C/min, where the final temperature was maintained for 10 min.

The $U^{K'}_{37}$ index, based on the concentration of di- and tri-unsaturated ketones with 37 carbon atoms ($U^{K'}_{37}$ =$[C_{37:2}]/[C_{37:2} + C_{37:3}]$) produced by some Haptophyte (coccolithophorids) algae was used to estimate SST (*Prahl and Wakeham*, 1987). To translate $U^{K'}_{37}$ values to an estimation of SST we applied the calibration of *Prahl et al*. (1988) (SST= ($U^{K'}_{37}$–0.039)/0.034)) that has been widely used for paleotemperature estimations. The reproducibility of the procedure was evaluated using a homogeneous sediment standard extracted every batch of 5 samples. The relatively analytical error was below 1 ºC.

We used $U^{K'}_{37}$ in preference to the original index because U^{K}_{37} includes the tetra-unsaturated C37 alkenone ($C_{37:4}$) that, although present in high abundances in cold regions (*Rosell-Melé*, 1998), is affected by other parameters in addition to temperature such as salinity (*Bendle et al*., 2005; *McClymont et al*., 2008; *Sikes et al*., 1997). The abundances of $C_{37:4}$ alkenone were compared to IRD estimates in order to constrain their applicability as a paleosalinity proxy.

3.3 Oxygen and carbon isotopes

Stable isotope ($\delta^{18}O$ and $\delta^{13}C$) analyses were performed at the University of Bergen on specimens of the planktonic foraminifera *Neogloboquadrina pachyderma* sinistral (NPS) selected from the >150–250 µm size fraction. Samples were analyzed using a Finnigan MAT 253 mass spectrometer coupled to an automated Kiel device. The data are reported on the VPDB scale calibrated with NBS-19. The long-term analytical precision of the system as defined by the reproducibility of carbonate standards between 6-60mg is ±0.08‰ and ±0.03‰ for $\delta^{18}O$ and $\delta^{13}C$, respectively.

In order to derive the temperature and salinity related signal in the $\delta^{18}O$ record of NPS, we performed an ice-volume correction based on the global Holocene and deglacial sea-level record of *Fairbanks*, (1989) (0–22 kyr BP) and the global sea-level record from the Red Sea (*Arz et al*., 2007) for the earlier part of the record. We assume 1.2‰ ice-effect for the last termination.

3.4 Biogenic Components

We use biogenic components such as alkenone concentrations (derived from coccolithophorids), calcium carbonate ($CaCO_3$, as a proxy for calcareous microorganisms, coccolithophorids and foraminifera), and biogenic opal (as a proxy for siliceous microorganisms, mainly diatoms) contents as proxies to reconstruct calcareous and siliceous productivity off the Strait of Magellan.

Total alkenone concentrations (converted to µg/g dry sediment weight) were calculated as the sum of di, tri and tetra-unsaturated C_{37} alkenones normalized to total organic carbon (TOC) and are expressed as µg/gTOC.

Calcium carbonate was calculated according to the formula $CaCO_3$= (TC-TOC)*8.333, where TC is the total carbon contents on untreated samples and TOC is the total organic carbon contents on HCl-treated samples. TC and TOC were measured in a vario EL III CHNOS Elemental Analyzer at the Alfred Wegener Institute (AWI-Bremerhaven). Organic matter contents were calculated by multiplying TOC contents with a constant factor of 1.5. Previous to the analysis, all the samples were freezer-dried and homogenized using an agate mortar and pestle. To obtain a high-resolution carbonate record we further measured Ca elemental concentration (unit = total elemental counts) with an AvaatechTM X-Ray Flourescence (XRF) Core Scanner (AWI-Bremerhaven). This non-destructive measuring technique allows rapid semiquantitative geochemical analysis of split sediment cores (Richter and Weering, 2006). Measuring resolution was 1 cm.

For biogenic opal, we followed the procedure described by *Mortlock and Froelich*, (1989) modified by *Müller and Schneider* (1993). Approximately 0.25 g dry sediments were transferred into 50-mL polypropylene centrifuge tubes, and after removal of carbonates and organic matter using peroxide (H2O2) and hydrochloric acid (HCl), 40mL 1M NaOH was added. The samples were then placed in a water bath and heated to 85 °C for 5 hours. Finally samples were read in an Agilent spectrophotometer at 812 nm, and values refer to wt-% Si_{OPAL}.

As large and variable amounts of siliciclastics strongly affect the contents of $CaCO_3$, opal, and organic matter, we calculated the concentrations of opal and carbonate relative to the total biogenic fraction (as the sum of the three major biogenic components opal, $CaCO_3$, and organic matter).

3.5 Ice rafted debris

We use the relative percentage of the >150µm carbonate-free fraction and manual particle counts as proxies for ice rafted debris (IRD). The >150µm was separated by wet-sieving after removal of carbonate with 10% acetic acid and organic matter with 3.5% hydrogen peroxide. IRD was counted from the >150µm carbonate-free fraction, assuming that coarser-grained terrigenous sediment can only reach the core location through iceberg transport. Volcanic particles are not a significant component at Site MD07-3128 most likely because ash plumes originating from volcanoes of the Southern Andes are typically transported and deposited eastward due to the prevailing strong westerly winds (e.g., *Kilian et al*., 2003). Opal has not been resolved, but the opal contents are far too low to significantly contribute to the >150µm carbonate-free fraction record. This assumption is confirmed by microscopic inspection of a number of selected samples.

4. Results

4.1 Chronology

According to our age model, sediment core MD07-3128 records the last ~60 kyr BP covering most of the last glacial (MIS 3 to MIS 2) to the early Holocene (Table 1; Figure 2). Variable sedimentation rates along the core were recorded (Figure 2b), reaching mean values of ~60 cm kyr-1 during almost all MIS 3 with exceptionally high values >350 cm kyr-1 between ~28 kyr and ~27 kyr BP. Mean sedimentation rates were ~125 cm/kyr around the LGM and drastically decrease to ~10 to 18 cm/kyr during the deglaciation, and were even less (~4 cm/kyr) during the Holocene.

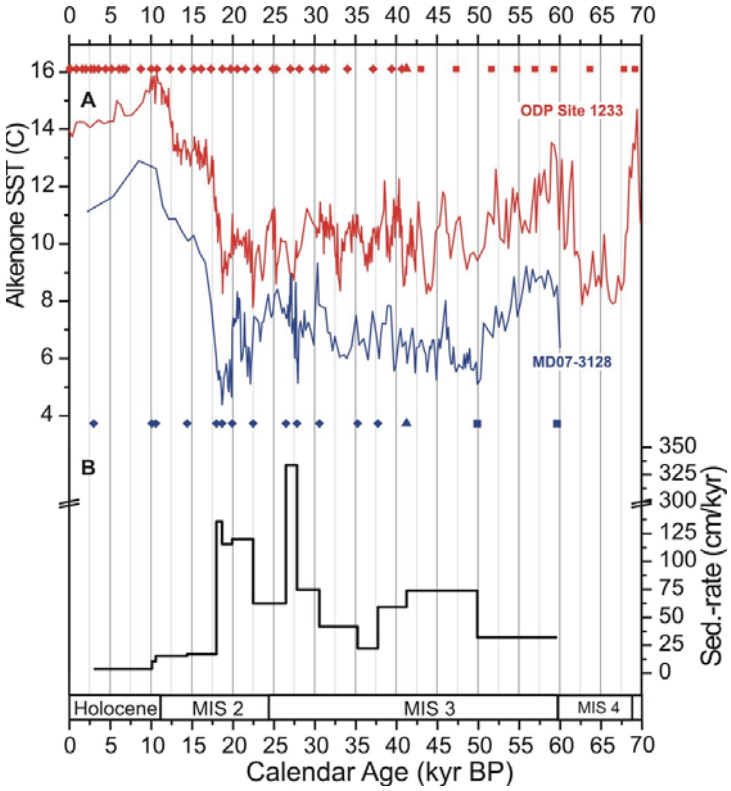

Figure 2. Age model for core MD07-3128. (a) Well-dated alkenone SST record of ODP Site 1233 (red curve; (*Kaiser and Lamy*, 2010)) compared to our SST record of MD07-3128 (blue curve). Diamonds represent radiocarbon dates, triangles the location of the Laschamp paleomagnetic excursion, and squares tuning points. (b) Sedimentation-rates of core MD07-3128.

4.2 Alkenone SST and planktonic foraminiferal $\delta^{18}O$

We reconstructed a continuous alkenone-derived SSTs record for the past ~60 kyr BP (Figure 3a). The SSTs oscillated between a minimum of 4.4 ºC at 18.8 kyr B.P and a maximum of 13 ºC at 9.6 kyr BP. The record exhibits an overall pattern of low temperatures, on average close to 7 °C during the glacial period from ~60 kyr BP to ~19 kyr BP. Relatively warm temperatures (up to ~9 °C) occur during early MIS 3 followed by a minimum of ~5 °C close to 50 kyr BP. Thereafter, a long-term warming trend of ~2 °C persists until ~25 kyr BP which is followed by a cooling trend of the order of ~3 °C leading to the LGM with minimum SSTs around ~19 kyr BP. From 50 kyr BP to 19 kyr BP, pronounced millennial-scale variability is observed. The amplitudes of these short-term variations are mostly ~2–3 ºC with a few larger amplitude oscillations of about 4 °C in the younger half of this period.

After the coldest temperatures at ~19 kyr BP, a drastic increase in the SST of ca. 8 °C is observed; this marks the beginning of Termination 1. Two warming steps characterized the deglacial period at 53ºS: the first one displayed an increase of 4 ºC

and lasted ca. 3 kyr and occurred between ~18.6 and ~15.3 kyr BP. The second step, with a duration of ca. 1.5 kyr, started at about 12.2 kyr BP and had an amplitude of ~2 °C (Figure 3a). Finally, after a brief warm period most likely representing the Holocene Climate Optimum as observed in many records of the Southern Hemisphere (e.g., *Bianchi and Gersonde*, 2004; *Kaiser et al*., 2005), alkenone-derived SSTs progressively declined toward cooler temperatures, reaching values close to 11 °C in the early Holocene.

We compare our alkenone-based SST data to the ice-volume corrected planktonic $\delta^{18}O$ record of NPS (Figure 3b). Although the resolution of the $\delta^{18}O$ record is lower than that of the alkenone SSTs (during MIS 3 and early MIS 2), both records share common millennial-scale variations. These short-term variations in the NPS $\delta^{18}O$ record have amplitudes between ~0.4 and ~~0.7‰. At Termination 1, $\delta^{18}O$ values rise by ~1‰ between ~18.3 and ~15.3 kyr BP, an interval in which alkenone SSTs increase by ~4 °C. Thereafter, the record has very low resolution. Higher $\delta^{18}O$ values occur at ~12 kyr BP (three data points) and at ~5.6 kyr BP (only one data point). There is a slight long-term trend towards lower $\delta^{18}O$ values from late MIS 3 towards the LGM.

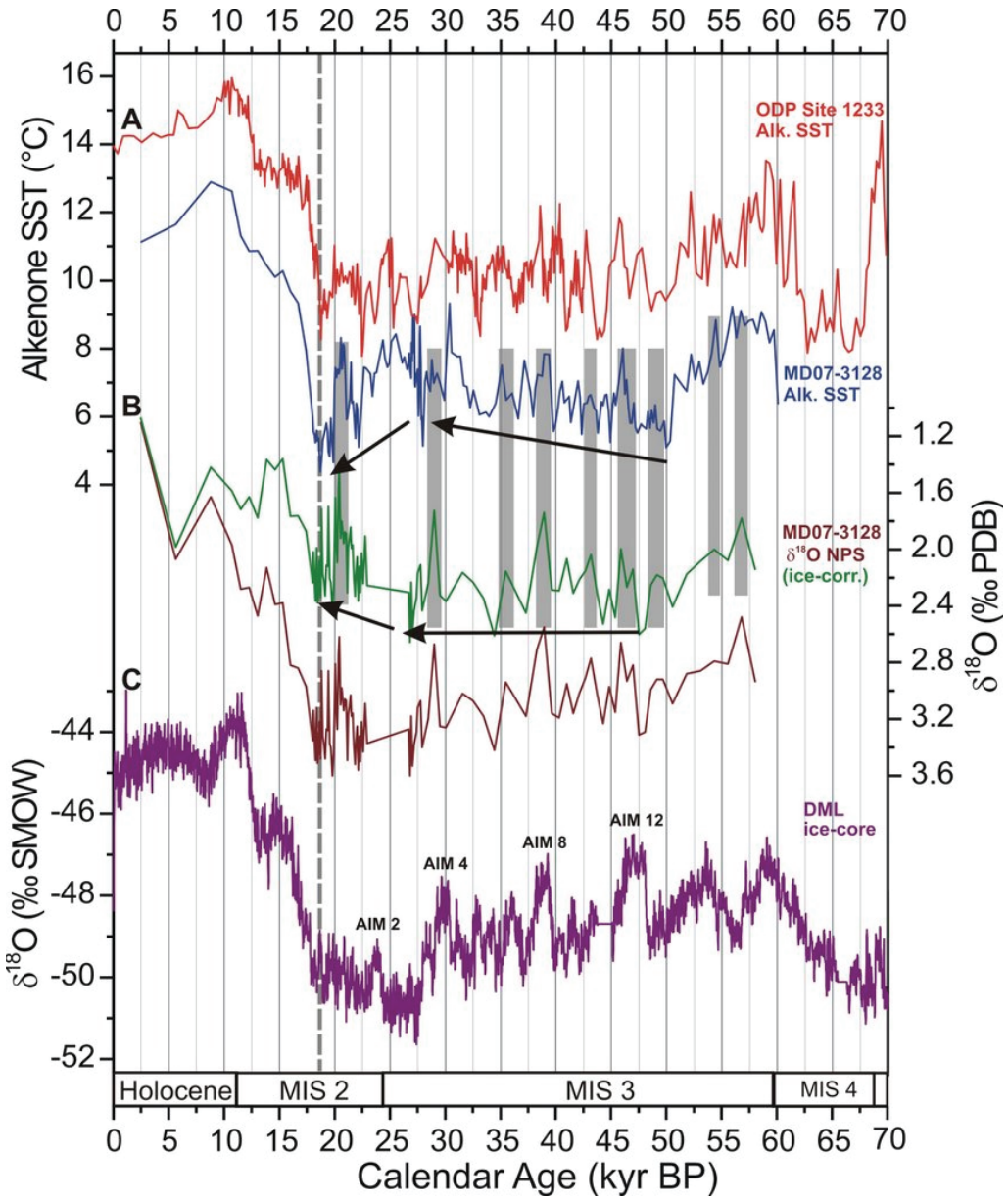

Figure 3. Comparison of SST proxy data from the Southeast Pacific to Antarctic ice core data for the past 70 kyr BP. (a) Alkenone-SST record from ODP Site 1233 located at 41°S (*Kaiser and Lamy*, 2010) and core MD07-3128 (53°S; this study). Black arrows mark the long-term warming trend observed over MIS 3 followed by a cooling trend to the LGM in our record. (b) $\delta^{18}O$ record of *Neogloboquadrina pachyderma* sinistral from core MD07-3128 (brown curve shows uncorrected data; green curve is ice-corrected). Black arrows mark long-term trends. Gray bars between A and B visualize common millennial-scale variability in the alkenone SST and the ice-corrected $\delta^{18}O$ record. (c) $\delta^{18}O$ record from the EPICA Dronning Maud Land (DML) ice core (EPICA Community Members, 2006) on the new Lemieux-Dundon time-scale (*Lemieux-Dudon et al.*, 2010). Vertical dashed line refers to the beginning of the deglacial warming.

4.3 Ice rafted debris and paleosalinity

The IRD count record largely parallels the relative percentages of the >150µm carbonate-free fraction (Figure 4). Most IRD consists of sand-sized particles with generally minor amounts of gravel. Both records show highest values during late MIS 3 and MIS 2 (~18 and 30 kyr BP) with several centennial to millennial-scale pulses reaching values of up to ~8% (>150µm fraction) and counts of up to ~30,000 grains. The most pronounced pulses occur at ~27, 23–25, 21, 19.5–20, and 18 kyr BP. In the earlier part of the records, a number of smaller IRD peaks are present, the most pronounced occurring at ~41.5 and 52.5–54 kyr BP (Figure 4b, c).

The relative abundances of $C_{37:4}$ alkenone were compared to IRD estimates in order to constrain their applicability as a paleosalinity proxy. $C_{37:4}$ alkenones are a by-product of the alkenone analysis. It has been proposed that these particular alkenones are linked to low-salinity water masses and that a $C_{37:4}$ increase of about 5 to 10% corresponds to a freshening of one practical salinity unit (PSU) (*Rosell-Melé*, 1998; *Rosell-Melé et al*., 2002). It is still unclear if indeed salinity has a direct effect on the $C_{37:4}$ biosynthesis or if the observed pattern is due to a metabolic difference of coccolithophorids endemic of cold or coastal water masses (*Schulz et al*., 2000). $C_{37:4}$ alkenone relative abundances in core MD07-3128 are very low (<5%) during the Holocene and during some intervals of MIS 3 (Figure 4d). Values are substantially higher during the last glacial in particular during late MIS 3 and MIS 2 with mean relative abundances in the range of 10 to 20%. A number of short-term (centennial to millennial-scale) spikes in $C_{37:4}$ alkenone relative abundance (up to 40%) occur between ~18 and 30 kyr BP. These partly coincide with higher coarse fraction and IRD contents (Figures 4b, 4c, 4d). In contrast to the IRD proxies that abruptly decreases at ~18 kyr BP, $C_{37:4}$ alkenone relative abundance remains high into the deglaciation until the beginning of the Holocene.

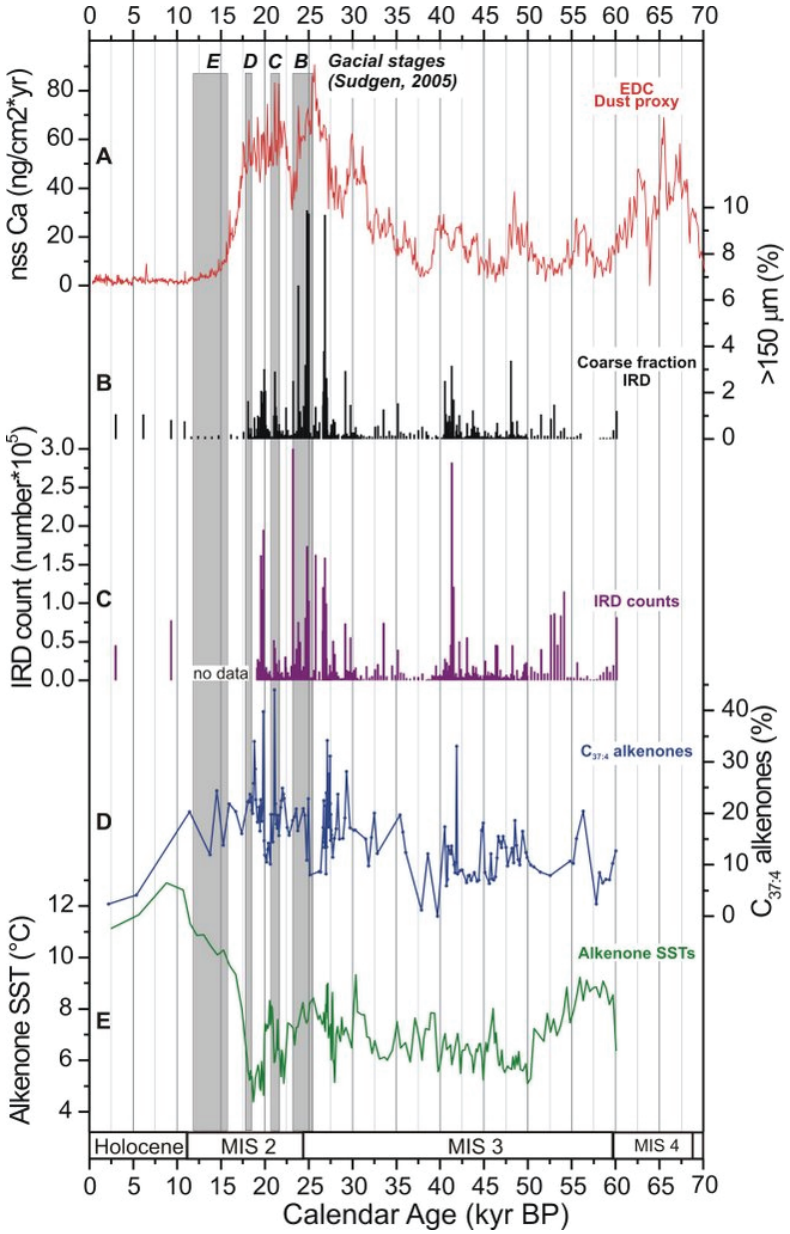

Figure 4. Proxies related to the dynamics of the PIS as recorded in core MD07-3128 compared to an Antarctic dust proxy record. (a) Non-sea-salt calcium from EPICA Dome C (EDC) (a proxy for dust content changes in Antarctic ice-cores) (*Fischer et al.*, 2007). (b) Percentage of >150 µm carbonate-free sediment fraction. (c) IRD counts. (d) Percentage of tetra-unsaturated C_{37} alkenones to total alkenones as a proxy for low-salinity water. (e) Alkenone-derived SST record from our site MD07-3128. Gray bars mark glacial stages as reconstructed from terrestrial records in Southern Patagonia (*Sugden et al.*, 2009).

4.4 Alkenone concentrations, organic matter, opal and carbonate contents

Total C_{37} alkenone concentrations varied greatly throughout the last ~60 kyr BP, ranging from 9 µg/gTOC to 116 µg/gTOC (Figure 5b). A clear millennial-scale pattern in the distribution of alkenones is recognized in our record. In general terms, higher

concentrations characterized warmer intervals while lower concentrations were typical during colder periods (Figures 5a, 5b). Major peaks (when concentrations were higher than the overall average of 40 μg/gTOC) were restricted to very distinct warm phases during the last glacial centered at ~60 to 52, 46, 39, 26 and ~20 kyr BP. A steady increase in alkenone content (albeit highly variable) was observed since the start of the deglacial warming through the early Holocene.

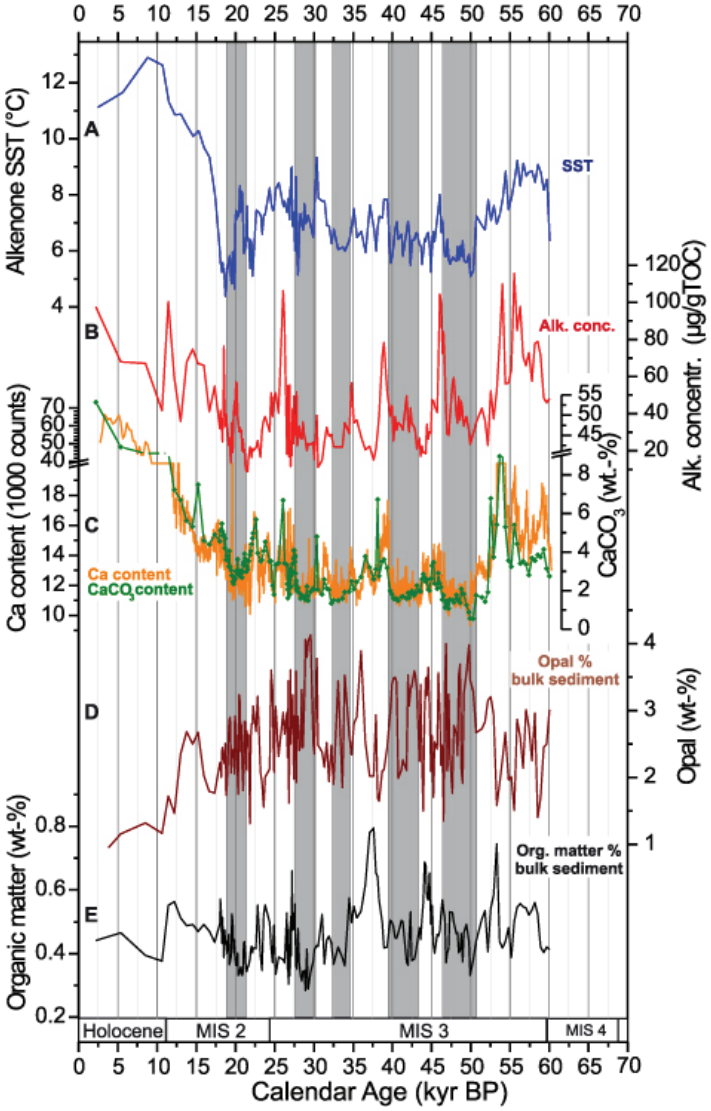

Figure 5. Summary of bulk biogenic proxy records from core MD07-3128 and their relationship to alkenone-SST. (a) Alkenone-SST record. (b) Total C37 alkenone concentrations normalized to total organic carbon (μg alkenone/gTOC). (c) XRF-Ca intensity (in counts*1000) and $CaCO_3$ content (wt-%). (d) Opal contents of the bulk sediment. (e) Organic matter contents of the bulk sediment. Gray bars mark cold periods with high opal and reduced calcareous contents at Site MD07-3128.

Since alkenones are biomarkers for some haptophyte (coccolithophorid) algae, and coccolithophores have an exoskeleton composed of numerous calcite platelets

that are readily preserved in the sedimentary records (e.g., *Marlowe et al*., 1984; *Young et al*., 1999), we compared our alkenone abundance record with that of calcium in the same core (Figures 5b, 5c). Fluctuations in the XRF Ca profile were similar to the changes recorded in the $CaCO_3$ content (Figure 5c) and this strong similarity suggests that almost all the calcium preserved in the sediments derives from biologically produced carbonate. Carbonate contents reach >50 wt-% during the Holocene and much lower values during the glacial (~1–9 wt-%). As was the case for the alkenone concentrations (Figure 5b), substantial increase in Ca and $CaCO_3$ contents coincided with warmer intervals (in particular during MIS 3) as well as the increasing trend since the start of the deglacial through the Holocene (Figure 5c).

Opal contents are very low during the Holocene (<1 wt-%) and range between ~1.5 and 4.5 wt-% in the glacial section (Figure 5d). Organic matter contents are relatively low throughout the core and fluctuate between ~0.3 and 0.8 wt-% (Figure 5e). As the glacial section is largely dominated by terrigenous material, we calculated opal and carbonate contents relative to the biogenic fraction as well as opal/carbonate ratios for illustrating siliceous versus carbonate components, independent of changes in sedimentation rates. The carbonate content in the biogenic fraction reaches >90 % during the Holocene and fluctuates between 20 and 80% in the glacial (Figure 6a). Minima occur during millennial-scale cold phases (gray bars in Figure 6). Contrary to the carbonate profile, the opal content of the biogenic fraction and the opal/carbonate ratio show higher values during relatively colder phases of the glacial section (Figures 6b and 6c). The maxima in opal in the biogenic fraction reach ~60–80% during MIS 3 and ~30–50% during MIS 2. The opal/carbonate ratio was three to four times greater during millennial-scale cold phases than during warmer ones with the exception of the LGM when the ratio was only about two times higher (Figure 6c).

Taken together, the biogenic components in our core point to millennial-scale shifts in the phytoplankton community (siliceous versus calcareous organisms) throughout the last ~60kyr BP at 53°S, apparently in line with fluctuations in SSTs (Figures 5 and 6).

4.5 Planktonic foraminiferal $\delta^{13}C$

The planktonic $\delta^{13}C$ record of NPS is characterized by high amplitude changes ranging from ~0.5‰ during the Holocene and early MIS 3 to minima of ~-1.5‰ in MIS 2 (Figure 6d). Superimposed on a pronounced long-term trend towards lower values from early MIS 3 to late MIS 2, substantial millennial-scale fluctuations can be observed. These changes have amplitudes ranging generally between ~0.5 and 0.8‰ during the earlier part of the record and are more than 1‰ during late MIS 3 and MIS 2.

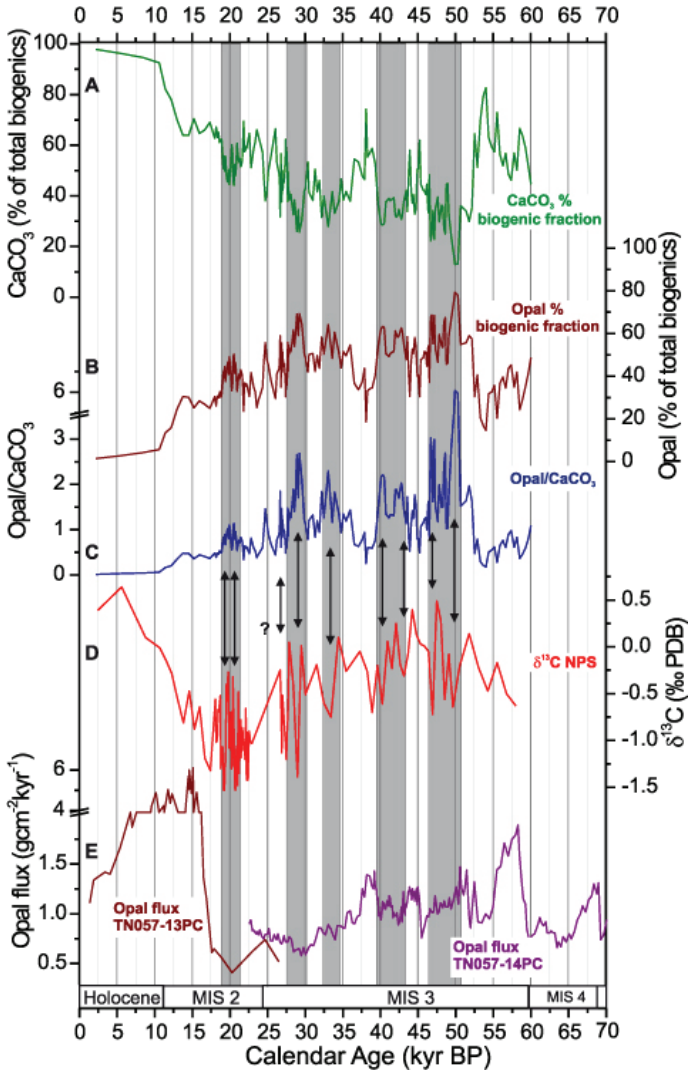

Figure 6. Comparison of biogenic proxy records between core MD07-3128 (a-d) and cores from the Southern Ocean (e). (a) Carbonate content of the biogenic fraction. (b) Opal content of the biogenic fraction. (c) Opal/carbonate ratio. (d) $\delta^{13}C$ record of *Neogloboquadrina pachyderma* sinistral. (e) Opal flux from two Southern Ocean cores located south of the Polar Front (*Anderson et al.*, 2009), cores TN057-13PC and TN057-14PC. Black arrows between C and D visualize antiphased pattern between the $\delta^{13}C$ record and the opal/carbonate ratio.

5. Discussion

5.1 Sea surface temperatures, ice rafted debris, and paleosalinity – Antarctic timing with regional overprint

Despite age uncertainties, alkenone-derived SSTs and planktonic $\delta^{18}O$ in core MD07-3128 generally follow an "Antarctic timing" as also observed in ice cores and marine records further north along the Chilean margin, at ODP Site 1233 (*Kaiser et al.*, 2005; *Lamy et al.*, 2004; *Lamy et al.*, 2007) (Figure 3). Although this pattern is particularly

evident for the deglacial warming, it also includes the millennial-scale variations during the last glacial. The "Antarctic timing" is consistent with the bipolar seesaw concept of anti-phased temperature changes on the Northern and Southern hemispheres that applies for the last glacial (*EPICA Community Members*, 2006) and extends into Termination 1 (e.g., *Lamy et al*., 2007).

The relatively large SST amplitude both over Termination 1 and, on millennial time-scales, during the last glacial suggests an exceptionally strong SST sensitivity at site MD07-3128. The SST changes are even larger than at ODP Site 1233 (Figure 3a) where ~6 °C glacial SST cooling has been interpreted in terms of a ~5–6° northward shift of the northern margin of the ACC system in connection with an expansion of the sea ice cover around Antarctica and a northward displacement of the SWW (e.g., *Kaiser et al*., 2005; *Lamy et al*., 2004). Considering that our study area off the Strait of Magellan is presently located ~5° latitude north of the present SAF (*Orsi et al*., 1995), our study area could have been in the vicinity or even south of the SAF during the coldest times of the last glacial if substantial northward movements of the SO fronts occurred. This interpretation would imply that latitudinal shifts of the SO fronts in the SE-Pacific were much more pronounced than those occurring further west in the central Pacific (*Gersonde et al*., 2005) (see also 5.2). Strong latitudinal shifts of the SO fronts have also been derived from a dinoflagellate cyst record of ODP Site 1233 (*Verleye and Louwye*, 2010). The authors interpret a ~7–10º northward shift of the system and even positioned the LGM Polar Front Zone (PFZ) at the latitude of ODP Site 1233. However, these results are inconsistent with the coccolithophore assemblages at the same site (*Saavedra-Pellitero and Sierro*, submitted), which suggest a more limited northward movement of the assemblages (fronts) of the order of ~5° latitude.

Despite the general "Antarctic timing" of our new southernmost Chilean margin SST record at millennial-time scales and during Termination 1, long-term temperature trends in our record differ from those observed at ODP Site 1233 and in EPICA Antarctic ice core (Figures 3a and 3c). We infer that these diverging long-term trends reflect regional differences in the SST evolution off the Strait of Magellan most likely due to the impact of meltwater and icebergs originating from the southern PIS located close to site MD07-3128, at least during the LGM. An updated view of glacial and deglacial changes in the extension of the southern PIS has been recently presented by *Sugden et al*. (2009) based on extensive dating of terrestrial records on the eastern side of the ice sheet. These data suggest five major advances of the southern PIS and/or stagnation phases of the deglacial ice retreat, named Stages A-E (Figure 4a). The oldest Stage A has been tentatively correlated to MIS 4 and is thus beyond the reach of our marine record. During stages B and C (23.1–25.6 kyr BP, and 20.4–21.7 kyr BP) glaciers were at their maximum extent and discharged directly onto outwash plains east of the Andean crest. Particularly Stage B correlates with three pulses of IRD (Figure 4) whereas stage C is only reflected by a relatively minor IRD peak in our

record. The same applies to advance D at ~17.7 kyr BP during which glaciers where more restricted and terminated in lakes (*Sugden et al*., 2009).

This consistency of our IRD changes with the independently dated terrestrial record provides not only confidence in our age model but also suggests that both the Atlantic and the Pacific sides of the southern PIS reacted, within age uncertainties, in phase. Further evidence that the extent changes of the PIS were coherent over large-scales comes from the terrigenous sediment input (Ti and Fe content maxima) at ODP Site 1233 related to northern PIS activity (*Kaiser and Lamy*, 2010; *Lamy et al*., 2004). Maxima in glaciogenic sediment input from the northern PIS generally correlate with IRD maxima in our record suggesting coeval millennial-scale variations of the complete PIS during the last glacial. Both ODP Site 1233 and the continental Patagonian records have been compared to dust input changes in Antarctic ice cores (*Kaiser and Lamy*, 2010; *Sugden et al*., 2009) suggesting a mechanistic link of PIS advances to dust maxima in Antarctica involving the ice sheet derived supply of fine-grained sediment to the Patagonian dust source areas. Our new IRD record is largely consistent with this interpretation and extends the terrestrial record of ice sheet advances back into MIS 3 (Figure 4). Although the comparison to the terrestrial record suggests that our IRD record primarily documents ice sheet advances, we are aware that wind changes were probably likewise important. Strong SWW would reduce the offshore movement of icebergs from the southern PIS. However, it is likely that during glacier advances (primarily cold phases during the glacial) the SWW intensities would have been slightly reduced off southernmost Chile as the core of the SWW moved northward (*Lamy et al*., 2004; 2007). Thus, the offshore advection of icebergs would have been facilitated during intervals of southern PIS advances.

Furthermore, the proximal location of our site MD07-3128 to the PIS may also explain the long-term SST cooling trend from ~25 kyr to 19 kyr BP (Figure 3a). Our IRD record and the continental evidences (*Sugden et al*., 2009) suggest that the ice sheet extension was at its maximum during this time interval. It is likely that the supply of meltwater induced a locally enhanced SST cooling close to the ice sheet margin consistent with the fact that no similar long-term cooling is observed at ODP Site 1233 (or any other high resolution SST records from the Chilean margin) nor is it seen in Antarctic ice-core records (Figure 3). Furthermore, the ice sheet likely supplied large amounts of meltwater thus reducing sea surface salinities at our site. Reduced paleosalinity at Site MD07-3128 during the glacial are coherent with higher relative abundances of $C_{37:4}$ alkenones (Figure 4d). Higher relative abundances of $C_{37:4}$ alkenones have been related to reduced surface ocean salinities in particular in the Nordic Seas (*Rosell-Melé*, 1998; *Rosell-Melé et al*., 2002) although other studies suggest that the relationship to paleosalinity is not straightforward (*Sikes and Sicre*, 2002). Relative abundances of $C_{37:4}$ alkenones appear to be higher during most but not all of the millennial to centennial-scale IRD events (Figure 4) implying a strong link

between ice sheet extent and regional paleosalinity, also on shorter scales. Interestingly, the $C_{37:4}$ alkenone relative abundance remains comparatively high during the deglaciation suggesting that relatively fresh surface water conditions persist, perhaps due to a continuous supply of meltwater during ice sheet retreat (*Sugden et al*., 2009).

Our ice-volume corrected planktonic $\delta^{18}O$ record of NPS generally follows the alkenone-derived SST changes during the Termination and the glacial millennial-scale variations (Figure 3) suggesting that paleosalinity changes induced by meltwater supply did not penetrate deep enough into the water column to be recorded by the deep-dwelling foraminifera NPS. However, the long-term baseline trends between both records differ. Particularly, the slight trend towards lighter $\delta^{18}O$ from late MIS 3 to the LGM might be interpreted in terms of a freshening of sub-surface water masses or a shallower depth habitat of NPS during the coldest intervals around the LGM.

5.2 Carbonate versus siliceous sedimentation pattern over the past ~60 kyr

The overall pattern of our biogenic proxies shows substantially higher opal abundances in the biogenic fraction during the last glacial while a marked and continuous decreasing trend characterized the period from the deglacial to the early Holocene (Figure 6b). This pattern is opposite to the ones of total C_{37} alkenones and $CaCO_3$ (Figures 5b, 5c, 6a). Superimposed on this overall trend, large fluctuations in both the siliceous and carbonate proxies on millennial time-scales were recorded in our core, intimately related to fluctuations in alkenone-derived SST (Figures 5 and 6). Although we recognize that the biogenic proxies can be affected by preservational/diagenetic factors or sediment focussing that may complicate their interpretation, taken together they strongly point to shifts in phytoplankton composition over the past ~60 kyr BP. Based on the oversimplified picture given by the opal and carbonate contents in the biogenic fraction and the opal/carbonate ratios (Figure 6a, 6b and 6c), we suggest that increased opal contents during colder intervals through the last glacial imply an increase in the contribution of siliceous (diatoms) versus calcareous organisms (coccoliths and foraminifera).

Although many factors can affect the opal preservation in marine sediments, i.e. the rate of opal production, sinking rate through the water column, temperature both in surface and bottom waters (*Bradtmiller et al*., 2009; *Nelson et al*., 1995), and ecological properties of the species must be taken into account when studying opal accumulation in the sediments (e.g., *Abelmann et al*., 2006), modern sediments in the Chilean fjords (41º–55ºS), including the western entrance of the Strait of Magellan, reveal high contents of biogenic opal ($\%Si_{OPAL}$ ~1–13) strongly associated with high diatom productivity in the water column (*Aracena et al*., in press). Presently, chain-

forming diatoms dominate the phytoplankton community in the Strait of Magellan region, recording maximum abundances during austral spring (*Iriarte et al*., 1993; 2001; *Magazzu et al*., 1996). Both biomass and primary production are influenced by exchange mechanisms with the open ocean at the western opening of the Magellan Strait and are strongly associated with the entrance of SAAW, which carries macronutrients such as nitrate and orthophosphate that fertilize the area (*Sievers and Silva*, 2008; *Silva and Calvete*, 2002) while silicates are mainly delivered from rivers (*Silva and Calvete*, 2002). The SWW play an important role in mixing the water column and breaking up the strong stratification (*Montecino et al*., 2006).

There is no available data concerning primary productivity dynamics during the last glacial period off southern South America (south of 50°S). However, there is widespread evidence for an increase in diatom export production in the glacial SO north of the modern SAF (*Anderson et al*., 1998; *Charles et al*., 1991; *Kumar et al*., 1995) that is in good agreement with our paleoproductivity results (Figures 5 and 6). In the modern SO south of the Antarctic PF, diatoms are key players in exporting organic carbon to the seafloor (*Honjo*, 2004) and the "opal belt" is located within and just south of the Antarctic PF (*Kumar et al*., 1995), while in the sub-Antarctic Zone north of the PF, the biological pump is driven by calcareous organisms dominated by coccolithophorids (*Honjo*, 2004; *Kumar et al*., 1995). Sediments accumulated in the Atlantic sector of the SO revealed that opal burial rates increased several-fold north of the modern SAF during the glacial compared to the Holocene (e.g., *Anderson et al*., 1998; *Kumar et a*l., 1995) while just south of the present Antarctic PF this pattern was reversed.

The glacial pattern found north of the modern SAF has been used to argue for a northward migration of the frontal systems, with a concomitant northward shift of the siliceous-ooze belt by ~5º latitude during the glacial (*Kumar et al*., 1993; *1995*). Taking into consideration that our record is presently located ~5º north of the modern SAF (Figure 1a), the increased opal contents of the biogenic fraction at our core site during colder intervals through the last glacial (Figure 6) suggests that the siliceous-ooze belt reached the core site as a result of its northward migration, at least during the last glacial. Perhaps the simplest way to accomplish this is by a northward shift in the SAF related to equatorward extending SWW. This agrees with previously published high-resolution multi-proxy data from mid-latitudes (*Kaiser et al*., 2005; *Lamy et al*., 1999) and off northern Chile (*Mohtadi and Hebbeln*, 2004), as well as with modelling studies (e.g., *Toggweiler et al*., 2006). Although we have not performed detailed diatom species analyses, shipboard data based on a few smear-slides showed the presence of Antarctic/Subantarctic diatoms such as *Fragilariopsis kerguelensis* and *Eucampia antarctica* during most parts of the glacial confirming the strong SO influence. These species were completely absent from deglacial and Holocene sediments.

An increase in diatom export production during glacial times has been suggested as one possible cause for the marked decrease in atmospheric CO_2 concentrations (*Anderson et al*., 1998; *Sarmiento and Toggweiler*, 1984), as recorded in Antarctic ice cores (*Petit et al*., 1999). Alternative mechanisms suggest however, that variations in sea ice extent (*Francois et al*., 1997; *Stephens and Keeling*, 2000), and changes in the SO stratification along with a latitudinal shifts of the SWW are responsible for glacial/interglacial CO_2 variability (see review in *Toggweiler et al*., 2006). Enhanced glacial productivity has also been associated with an increase in the supply of iron to the surface ocean, from increased atmospheric dust deposition (*Martin*, 1990). Changes in dust flux to Antarctica were associated with an expansion/retreat of the PIS, east of the Andes (*Sugden et al*., 2009). Considering that our core is located to the west of the Andes Cordillera, an increase in iron-rich dust cannot explain the increase in siliceous content recorded during the last glacial period in our study area (Figures 6b and 6c).

The glacial-interglacial shift in the species composition of phytoplankton over the past ~60 kyr BP, as strongly suggested by our biogenic proxies (diatoms over coccoliths) (Figure 6), could be a response to a combination of processes, such as a glacial northward migration/expansion of the frontal systems and/or changes in the supply of silica delivered to the surface ocean, promoting the growth of diatoms at the expenses of coccolithophorids. Because the contribution of diatoms to the total phytoplankton community largely depends on the silica supplied to the euphotic layer (to build up their siliceous frustules), an excess of silica supply during glacial times would have strongly favored the growth of diatoms over coccolithophorids, increasing the sequestration of carbon into the deep ocean and lowering atmospheric pCO_2 level (*Harrison*, 2000). This excess of silica supply could have been transported by the SAAW to lower latitudes and reached our core site via circulation pathways. Evidence for enhanced glacial nutrient supply to site MD07-3128 comes from our planktonic $\delta^{13}C$ record (Figure 6d). In general terms, this record is characterized by large glacial-interglacial amplitudes as previously observed in the subantarctic Atlantic sector (*Ninnemann and Charles*, 1997). Substantially lower $\delta^{13}C$ during MIS 2 points to strongly increased availability of nutrients in (sub) surface waters (depth habitat of NPS).

On millennial time-scales, low $\delta^{13}C$ values closely correlate to maxima in opal content in the biogenic fraction and opal/carbonate ratios and minima in alkenone concentrations, carbonate, and SST (Figures 5 and 6). This pattern suggests pronounced variations in nutrient supply paralleling the temperature and paleoproductivity changes likewise on shorter time-scales. *Anderson et al*. (2009) observed important changes in opal fluxes in the SO south of the PF (Figure 6e) with enhanced productivity during Antarctic warm phases (A-events). Within age uncertainties, our opal record and opal/carbonate ratio are anti-phased to their record

consistent with reduced opal sedimentation in the subantarctic zone during warm intervals (Figure 6). This anti-phased siliceous productivity pattern in the Antarctic and Subantarctic zones has been previously described primarily for glacial/interglacial changes (e.g., *Anderson et al*., 1998) and appears to be present also on millennial time-scales and is, as our SST record, fully consistent with the bipolar seesaw concept of anti-phased temperature changes on the Northern and Southern hemispheres.

The substantially higher opal content of the biogenic fraction at our core site during relatively colder phases of MIS 3 (Figure 6b) seems to respond to large-scale processes involving basin-wide changes in SO oceanography. However, local processes can also be invoked. If we look in detail, a period of comparatively less opal was detected between ~25 and ~19 kyr BP (Figures 6b and 6c), closely connected with the long-term cooling period recorded in our paleotemperature record (Figure 5a) which we may associate with variations in the extent of the southern PIS (Figure 4). During this interval, the large size reached by the southern PIS, as strongly suggested by the high abundances of IRD in the >150 µm size fraction and tetra-unsaturated C_{37} alkenone maxima, should have freshened the surface waters around the Strait of Magellan by melting of icebergs inducing a strong water column stratification that would have deepened the nutricline, limiting the nutrient renewal at the surface and thus reducing diatom productivity. Apparently, this water column stratification did not reach the depth habitat of NPS since the strongest minima in our $\delta^{13}C$ record occur during MIS 2 (Figure 6d).

Following this period of comparatively lower opal contents that seem to be related to local processes involving PIS's fluctuations, the opal levels diminished even further (Figures 6b and 6c) coinciding with the deglacial increase in the alkenone-derived SST (Figure 5a). Based on this decrease we infer a poleward displacement of the circumpolar frontal system that lead to a poleward shift of the siliceous-ooze belt, resulting in decreased diatom productivity in the study area. This assumption is also supported by model studies (*Toggweiler et al*., 2006) and is consistent with the strong enhancement of opal sedimentation south of the PF (*Anderson et al*., 2009) (Figure 6e) that showed that the poleward shift of the SWW occurred at the beginning of the deglaciation and was part of a chain of events that led to the early warming of Antarctica and the Southeast Pacific (e.g., *Lamy et al*., 2007).

6. Conclusions

Our multi-proxy paleoceanographic records from the southernmost Chilean margin (53°S) allow resolving millennial-scale pattern in the Southeast Pacific sector. The timing and structure of these millennial-scale patterns and of Termination 1 is

consistent with an “Antarctic timing”, as observed in ice-cores and SST records further north off Chile as well as in the SW Pacific. We find that anti-phased siliceous productivity pattern in the Antarctic and Subantarctic zones previously primarily described for glacial/interglacial changes (*Anderson et al*., 1998) appear to be present at millennial time-scales.

Our data show large amplitude SST changes and connected shifts in siliceous and calcareous plankton communities on both glacial/interglacial and millennial time-scales. Perhaps the simplest way to accomplish this is by substantial latitudinal shifts of the SO fronts and the opal belt and /or changes in the nutrient advection, as suggested by pronounced variations in planktonic foraminiferal $\delta^{13}C$.

We provide the first continuous IRD record of the Pacific margin of the PIS. Generally higher contents of IRD during late MIS 3 and the LGM can be interpreted as advances of the ice sheet or reduced westward migration of icebergs due to a northward displacement and/or regional weakening of the Southern Westerlies. Superimposed millennial-scale IRD variations correlate (within age uncertainties) with dust input changes recorded in Antarctic ice cores implying a causal link between ice advances and dust availability, as previously suggested (*Sugden et al*., 2009). Furthermore, meltwater input during southern PIS advances is at least partly documented by higher relative abundances of $C_{37:4}$ alkenones.

Whether the large amplitude oceanographic changes off the Strait of Magellan are a regional feature of the easternmost Pacific sector or whether they extend to other parts of the Pacific SO remains to be shown by additional high resolution paleoceanographic records from this region in the future.

Acknowledgements

Funding was provided by the Deutsche Forschungsgemeinschaft (DFG) through grants LA 1273/3-2, LA1273/5-1, and KI-456/9-1. C.L. acknowledges support from the COPAS Center (Project FONDAP # 15010007) and the Hanse Wissenschaftskolleg, Delmenhorst (Germany). We thank the captain and crew of IMAGES R/V Marion Dufresne cruise MD159/PACHIDERME.

References

Abelmann, A., R. Gersonde, G. Cortese, G. Kuhn, and G. V. Smetacek (2006), Extensive phytoplankton blooms in the Atlantic sector of the glacial Southern Ocean, *Paleoceanography*, *21*, PA1013, doi:10.1029/2005PA001199.

Anderson, R. F., Z. Chase, M. Q. Fleisher, and J. Sachs (2002), The Southern Ocean's biological pump during the Last Glacial Maximum, *Deep Sea Res. Part II Top. Stud. Oceanogr.*, *49*, 1909-1938.

Anderson, R. F., S. Ali, L. I. Bradtmiller, S. H. H. Nielsen, M. Q. Fleisher, B. E. Anderson, and L. H. Burckle (2009), Wind-Driven Upwelling in the Southern Ocean and the Deglacial Rise in Atmospheric CO2, *Science*, *323*(5920), 1443-1448.

Anderson, R. F., N. Kumar, R.A. Mortlock, P.N. Froelich, P. Kubik, B. Dittrich-Hannen , and M. Suter (1998), Late-Quaternary changes in productivity of the Southern Ocean, *J. Marine Syst.*, *17*(1-4), 497-514.

Antezana, T. (1999), Hydrographic features of Magellan and Fuegian inland passages and adjacent Subantarctic waters, *Sci. Mar.*, *63*, 23-34.

Aracena, C., C. B. Lange, J. Iriarte, L. Rebolledo, and S. Pantoja (in press), Latitudinal pattern of export production recorded in surface sediments of the Chilean Patagonian fjords (41-55° S) as a response to water column productivity, *Cont. Shelf Res.*, doi: 10.1016/j.csr.2010.08.008.

Arz, H. W., F. Lamy, A. Ganopolski, N. Nowaczyk, and J. Patzold (2007), Dominant Northern Hemisphere climate control over millennial-scale glacial sea-level variability, *Quat. Sci. Rev.*, *26*(3-4), 312-321, 10.1016/j.quascirev.2006.07.016.

Barrows, T. T., S. Juggins, P. De Deckker, E. Calvo, and C. Pelejero (2007a), Long-term sea surface temperature and climate change in the Australian-New Zealand region, *Paleoceanography*, *22*, PA2215, doi:10.1029/2006PA001328.

Barrows, T. T., S. J. Lehman, L. K. Fifield, and P. De Deckker (2007b), Absence of cooling in New Zealand and the adjacent ocean during the Younger Dryas chronozone, *Science*, *318*(5847), 86-89, doi:10.1126/science.1145873.

Bendle, J., A. Rosell-Mele, and P. Ziveri (2005), Variability of unusual distributions of alkenones in the surface waters of the Nordic seas, *Paleoceanography*, *20*, PA2001, doi:10.1029/2004PA001025.

Bianchi, C., and R. Gersonde (2004), Climate evolution at the last deglaciation: The role of the Southern Ocean, *Earth Planet. Sci. Lett.*, *228*(3-4), 407-424.

Bradtmiller, L. I., R. F. Anderson, M. Q. Fleisher, and L. H. Burckle (2009), Comparing glacial and Holocene opal fluxes in the Pacific sector of the Southern Ocean, *Paleoceanography*, *24*, PA2214, doi:10.1029/2008PA001693.

Chaigneau, A., and O. Pizarro (2005), Surface circulation and fronts of the South Pacific Ocean, east of 120 degrees W, *Geophys. Res. Lett.*, *32*(8), L08605, doi:10.1029/2004GL022070.

Charles, C. D., P. N. Froelich, M. A. Zibello, R. A. Mortlock, and J. J. Morley (1991), Biogenic opal in southern ocean sediment over the last 450,000 years: Implicactions for surface water chemistry and circulation, *Paleoceanography*, *6*, 697-728.

DaSilva, J. L., J. B. Anderson, and J. Stravers (1997), Seismic facies changes along a nearly continuous 24 degrees latitudinal transect: the fjords of Chile and the northern Antarctic peninsula, *Mar. Geol.*, *143*(1-4), 103-123.

Denton, G. H., C. J. Heusser, T. V. Lowell, P. I. Moreno, B. G. Andersen, L. E. Heusser, C. Schluchter, and D. R. Marchant (1999), Interhemispheric linkage of paleoclimate during the last glaciation, *Geogr. Ann. Ser. A*, *81A*(2), 107-153.

EPICA Community Members (2006), One-to-one coupling of glacial climate variability in Greenland and Antarctica, *Nature*, *444*(7116), 195-198.

Fairbanks, R. G. (1989), A 17,000-year glacio-eustatic sea-level record -Influence of glacial melting rates on the Younger Dryas event and deep-ocean circulation, *Nature*, *342*(6250), 637-642.

Fischer, H., F. Fundel, U. Ruth, B. Twarloh, A. Wegner, R. UdiSti, S. Becagli, E. Castellano, A. Morganti, M. Severi, E. Wolff, G. Littot, R. Rothlisberger, R. Mulvaney, M. A. Hutterli, P. Kaufmann, U. Federer, F. Lambert, M. Bigler, M. Hansson, U. Jonsell, M. de Angelis, C. Boutron, M. L. Siggaard-Andersen, J. P. Steffensen, C. Barbante, V. Gaspari, P. Gabnelli, and D. Wagenbach (2007), Reconstruction of millennial changes in dust emission, transport and regional sea ice coverage using the deep EPICA ice cores from the Atlantic and Indian Ocean sector of Antarctica (vol 260, pg 340,

2007), *Earth Planet. Sci. Lett.*, *262*(3-4), 635-635, doi:10.1016/j.epsl.2007.08.016.

Fischer, H., J. Schmitt, D. Luthi, T. F. Stocker, T. Tschumi, P. Parekh, F. Joos, P. Kohler, C. Volker, R. Gersonde, C. Barbante, M. Le Floch, D. Raynaud, and E. Wolff (2010), The role of Southern Ocean processes in orbital and millennial CO2 variations - A synthesis, *Quat. Sci. Rev.*, *29*(1-2), 193-205, doi:10.1016/j.quascirev.2009.06.007.

Francois, R., M. A. Altabet, E. F. Yu, D. M. Sigman, M. P. Bacon, M. Frank, G. Bohrmann, G. Bareille, and L. D. Labeyrie (1997), Contribution of Southern Ocean surface-water stratification to low atmospheric CO2 concentrations during the last glacial period, *Nature*, *389*(6654), 929-935.

Gersonde, R., X. Crosta, A. Abelmann, and L. Armand (2005), Sea-surface temperature and sea ice distribution of the Southern Ocean at the EPILOG Last Glacial Maximum - a circum-Antarctic view based on siliceous microfossil records, *Quat. Sci. Rev.*, *24*, 869-898.

Glasser, N., and K. Jansson (2008), The glacial map of southern South America, *Journal of Maps*, 175-196.

Harrison, K. G. (2000), Role of increased marine silica input on paleo-pCO2 level, *Paleoceanography*, *15*(3), 292-298.

Hollin, J. T., and D. H. Schilling (1981), Late Wisconsin-Weichselian mountain glaciers and small ice caps, in *The Last Great Ice Sheets*, edited by G. H. Denton and T. J. Hughes, pp. 179-220, Wiley, New York.

Honjo, S. (2004), Particle export and the biological pump in the Southern Ocean, *Antarct. Sci.*, *16*(4), 501-516, doi:10.1017/s0954102004002287.

Ingram, B. L., and J. R. Southon (1996), Reservoir ages in eastern Pacific coastal and estuarine waters, *Radiocarbon*, *38*(3), 573-582.

Iriarte, J. L., Kusch, A., Osses, J., Ruiz, M. (2001), Phytoplankton biomass in the sub-Antarctic area of the Straits of Magellan (53 degrees S), Chile during spring-summer 1997/1998, *Polar Biol.*, *24*(3), 154-162.

Iriarte, J. L., Uribe, J. C., Valladares, C. (1993), Biomass of size-fractionated phytoplankton during the spring-summer season in southern Chile, *Botánica Marina*, *36*(5), 443-450.

Jouzel, J., V. Masson-Delmotte, O. Cattani, G. Dreyfus, S. Falourd, G. Hoffmann, B. Minster, J. Nouet, J. M. Barnola, J. Chappellaz, H. Fischer, J. C. Gallet, S. Johnsen, M. Leuenberger, L. Loulergue, D. Luethi, H. Oerter, F. Parrenin, G. Raisbeck, D. Raynaud, A. Schilt, J. Schwander, E. Selmo, R. Souchez, R. Spahni, B. Stauffer, J. P. Steffensen, B. Stenni, T. F. Stocker, J. L. Tison, M. Werner, and E. W. Wolff (2007), Orbital and millennial Antarctic climate variability over the past 800,000 years, *Science*, *317*(5839), 793-796.

Kaiser, J., F. Lamy, and D. Hebbeln (2005), A 70-kyr sea surface temperature record off southern Chile (ODP Site 1233). *Paleoceanography*, *20*, doi:10.1029/2005PA001146.

Kaiser, J., E. Schefuss, F. Lamy, M. Mohtadi, and D. Hebbeln (2008), Glacial to Holocene changes in sea surface temperature and coastal vegetation in north central Chile: high versus low latitude forcing, *Quat. Sci. Rev.*, *27*(21-22), 2064-2075.

Kaiser, J., and F. Lamy (2010), Links between Patagonian Ice Sheet fluctuations and Antarctic dust variability during the last glacial period (MIS 4-2), *Quaternary Sciece Reviews*, *29*, 1464-1471.

Kaplan, M. R., C. J. Fogwill, D. E. Sugden, N. Hulton, P. W. Kubik, and S. Freeman (2008), Southern Patagonian glacial chronology for the Last Glacial period and implications for Southern Ocean climate, *Quat. Sci. Rev.*, *27*(3-4), 284-294, 10.1016/j.quascirev.2007.09.013.

Kaplan, M. R., J. M. Schaefer, G. H. Denton, D. J. A. Barrell, T. J. H. Chinn, A. E. Putnam, B. G. Andersen, R. C. Finkel, R. Schwartz, and A. M. Doughty (2010), Glacier retreat in New Zealand during the Younger Dryas stadial, *Nature*, *469*(194-197), doi:10.1038/nature09313.

Kilian, R., M. Hohner, H. Biester, H. J. Wallrabe-Adams, and C. R. Stern (2003), Holocene peat and lake sediment tephra record from the southernmost Chilean Andes (53-55 degrees S), *Revista Geologica De Chile*, *30*(1), 23-37.

Kilian, R., O. Baeza, T. Steinke, M. Arevalo, C. Rios, and C. Schneider (2007), Late Pleistocene to Holocene marine transgression and thermohaline control on sediment transport in the western Magellanes fjord system of Chile (53 degrees S), *Quat. Int.*, *161*, 90-107.

Kohfeld, K. E., C. Le Quere, S. P. Harrison, and R. F. Anderson (2005), Role of marine biology in glacial-interglacial CO2 cycles, *Science*, *308*(5718), 74-78.

Kumar, N., R. Gwiazda, R. F. Anderson, and P. N. Froelich (1993), Pa-231/Th-230 ratios in sediments as a proxy for past changes in Southern-Ocean productivity, *Nature*, *362*(6415), 45-48.

Kumar, N., R. F. Anderson, R. A. Mortlock, P. N. Froelich, P. Kubik, B. Dittrichhannen, and M. Suter (1995), Increased biological productivity and export production in the glacial Southern-Ocean, *Nature*, *378*(6558), 675-680.

Laj, C., C. Kissel, A. Mazaud, J. E. T. Channell, and J. Beer (2000), North Atlantic palaeointensity stack since 75 ka (NAPIS-75) and the duration of the Laschamp event, *Philosophical Transactions of the Royal Society of London Series a-Mathematical Physical and Engineering Sciences*, *358*(1768), 1009-1025.

Laj, C., C. Kissel, R. Leonhardt, M. Winklofer, A. Ferk, K. Fabian, and U. Ninemann (2009), Towards a global view of the laschamp excursion, *Geophy. Res. Abstr.*, *11, EGU General Assembly, 2009*.

Lamy, F., D. Hebbeln, and G. Wefer (1999), High-resolution marine record of climatic change in mid- latitude Chile during the last 28,000 years based on terrigenous sediment parameters, *Quat. Res.*, *51*(1), 83-93.

Lamy, F., J. Kaiser, U. Ninnemann, D. Hebbeln, H. Arz, and J. Stoner (2004), Antarctic Timing of Surface Water Changes off Chile and Patagonian Ice Sheet Response, *Science*, *304*, 1959-1962.

Lamy, F., J. Kaiser, H. W. Arz, D. Hebbeln, U. Ninnemann, O. Timm, A. Timmermann, and J. R. Toggweiler (2007), Modulation of the bipolar seesaw in the southeast pacific during Termination 1, *Earth Planet. Sci. Lett.*, *259*(3-4), 400-413.

Lemieux-Dudon, B., E. Blayo, J. R. Petit, C. Waelbroeck, A. Svensson, C. Ritz, J. M. Barnola, B. M. Narcisi, and F. Parrenin (2010), Consistent dating for Antarctic and Greenland ice cores, *Quat. Sci. Rev.*, *29*(1-2), 8-20, doi:10.1016/j.quascirev.2009.11.010.

Lowell, T. V., C. J. Heusser, B. G. Andersen, P. I. Moreno, A. Hauser, L. E. Heusser, C. Schlüchter, D. R. Marchant, and G. H. Denton (1995), Interhemispheric correlation of Late Pleistocene glacial events, *Science*, *269*, 1541-1549.

Magazzu, G., S. Panella, and F. Decembrini (1996), Seasonal variability of fractionated phytoplankton, biomass and primary production in the Straits of Magellan, *J. Marine Syst.*, *9*(3-4), 249-267.

MARGO Project Members (2009), Constraints on the magnitude and patterns of ocean cooling at the Last Glacial Maximum, *Nature Geoscience*, *2*(411), 127-132.

Marlowe, I. T., J. C. Green, A. C. Neal, S. C. Brassell, G. Eglinton, and P. A. Course (1984), Long-chain (n-C37-C39) alkenones in the prymnesiophyceae -distribution of alkenones and other lipids and their taxonomic significance, *British Phycological Journal*, *19*(3), 203-216.

Martin, J. H. (1990), Glacial-Interglacial CO2 change: The Iron Hypothesis, *Paleoceanography*, *5*(1), 1-13.

Mashiotta, T. A., D. W. Lea, and H. J. Spero (1999), Glacial-interglacial changes in Subantarctic sea surface temperature and delta O-18-water using foraminiferal Mg, *Earth Planet. Sci. Lett.*, *170*(4), 417-432.

McClymont, E. L., A. Rosell-Mele, G. H. Haug, and J. M. Lloyd (2008), Expansion of subarctic water masses in the North Atlantic and Pacific oceans and implications for mid-Pleistocene ice sheet growth, *Paleoceanography*, *23*(4), PA4214, doi:10.1029/2008PA001622.

McCulloch, R. D., M. J. Bentley, R. S. Purves, N. R. J. Hulton, D. E. Sugden, and C. M. Clapperton (2000), Climatic inferences from glacial and palaeoecological evidence at the last glacial termination, southern South America, *J. Quat. Sci.*, *15*(4), 409-417.

Mohtadi, M., and D. Hebbeln (2004), Mechanisms and variations of the paleoproductivity off northern Chile (24°S-33°S) during the last 40,000 years, *Paleoceanography*, *19*, PA2023, doi:10.1029/2004PA001003.

Mohtadi, M., P. Rossel, C. B. Lange, S. Pantoja, P. Boning, D. J. Repeta, M. Grunwald, F. Lamy, D. Hebbeln, and H. J. Brumsack (2008), Deglacial pattern of circulation and marine productivity in the upwelling region off central-south Chile, *Earth Planet. Sci. Lett.*, *272*(1-2), 221-230, doi:10.1016/j.epsl.2008.04.043.

Montecino, V., T. Strub, F. Chavez, A. Thomas, J. Tarazona, and T. Baumgartner (2006), Bio-physical interactions off Western South-America, in *The Sea. The global coastal ocean: interdisciplinary regional studies and synthesis*, edited by A. R. K. Brink, Harvard Press, USA.

Moreno, P. I., G. L. Jacobson, T. V. Lowell, and G. H. Denton (2001), Interhemispheric climate links revealed by a late-glacial cooling episode in southern Chile, *Nature*, *409*(6822), 804-808.

Moreno, P. I., M. R. Kaplan, J. P. Francois, R. Villa-Martinez, C. M. Moy, C. R. Stern, and P. W. Kubik (2009), Renewed glacial activity during the Antarctic cold reversal and persistence of cold conditions until 11.5 ka in southwestern Patagonia, *Geology*, *37*(4), 375-378.

Mortlock R., and P. N. Froelich (1989), A simple method for the rapid determination of biogenic opal in pelagic marine sediments, *Deep Sea Res.*, *36*(9), 1415-1426.

Müller, P. J., and R. Schneider (1993), An automated leaching method for the determination of opal in sediments and particulate matter, *Deep Sea Res. Part I*, *40*(3), 425-444.

Müller, P. J., G. Kirst, G. Ruhland, I. von Storch, and A. Rosell-Mele (1998), Calibration of the alkenone paleotemperature index UK'37 based on core-tops from the eastern South Atlantic and the global ocean (60°N-60°S). *Geochim. Cosmochim. Acta*, *62*, 1757-1772.

Nelson, D. M., P. Treguer, M. A. Brzezinski, A. Leynaert, and B. Queguiner (1995), Production and dissolution of biogenic silica in the ocean - revised global estimates, comparison with regional data and relationship to biogenic sedimentation, *Global Biogeochem. Cycles*, *9*(3), 359-372.

Ninnemann, U. S., and C. D. Charles (1997), Regional differences in Quaternary Subantarctic nutrient cycling: Link to intermediate and deep water ventilation, *Paleoceanography*, *12*(4), 560-567.

Orsi, A. H., T. Whitworth, and W. D. Nowlin (1995), On the meridional extent and fronts of the Antarctic Circumpolar Current, *Deep Sea Res. Part I*, *42*(5), 641-673.

Pahnke, K., R. Zahn, H. Elderfield, and M. Schulz (2003), 340,000-year centennial-scale marine record of Southern Hemisphere climatic oscillation, *Science*, *301*(5635), 948-952.

Petit, J. R., J. Jouzel, D. Raynaud, N. I. Barkov, J. M. Barnola, I. Basile, M. Bender, J. Chappellaz, M. Davis, G. Delaygue, M. Delmotte, V. M. Kotlyakov, M. Legrand, V. Y. Lipenkov, C. Lorius, L. Pepin, C. Ritz, E. Saltzman, and M. Stievenard (1999), Climate and atmospheric history of the past 420,000 years from the Vostok ice core, Antarctica, *Nature*, *399*(6735), 429-436.

Pickard, G. L. (1971), Some physical oceanographic features of inlets of Chile, *Journal of the Fisheries Research Board of Canada*, *28*(8), 1077-1106.

Prahl, F. G., and S. G. Wakeham (1987), Calibration of unsaturation patterns in long-chain ketone compositions for paleotemperature assessment, *Nature*, *330*, 367-369.

Prahl, F. G., L. A. Muehhausen, and D. L. Zahnle (1988), Further evaluation of long-chain alkenones as indicators of paleoceanographic conditions, *Geochim. Cosmochim. Acta*, *52*, 2303-2310.

Reimer, P. J., M. G. L. Baillie, E. Bard, A. Bayliss, J. W. Beck, P. G. Blackwell, C. B. Ramsey, C. E. Buck, G. S. Burr, R. L. Edwards, M. Friedrich, P. M. Grootes, T. P. Guilderson, I. Hajdas, T. J. Heaton, A. G. Hogg, K. A. Hughen, K. F. Kaiser, B. Kromer, F. G. McCormac, S. W. Manning, R. W. Reimer, D. A. Richards, J. R. Southon, S. Talamo, C. S. M. Turney, J. van der Plicht, and C. E. Weyhenmeye (2009), IntCal09 and Marine09

radiocarbon age calibration curves, 0-50,000 years cal BP, *Radiocarbon*, *51*(4), 1111-1150.

Richter, T. O., S. van der Gaast, B. Koster, A. Vaars, R. Gieles, H.C. de Stigter, H. de Hass, and T. C. E. v. Weering (2006), The Avaatech XRF Core Scanner: technical description and applications to NE Atlantic sediments, in *New Techniques in Sediment Core Analysis, R.G. Rothwell (ed.), Geological society of London Special Publication, 267*, edited, pp. 39-50.

Romero, O., J. H. Kim, and D. Hebbeln (2006), Paleoproductivity evolution off central Chile from the Last Glacial Maximum to the Early Holocene, *Quat. Res.*, *65*, 519-525.

Rosell-Melé, A. (1998), Interhemispheric appraisal of the value of alkenone indices as temperature and salinity proxies in high-latitude locations, *Paleoceanography*, *13*(6), 694-703.

Rosell-Melé, A., E. Jansen, and M. Weinelt (2002), Appraisal of a molecular approach to infer variations in surface ocean freshwater inputs into the North Atlantic during the last glacial, *Global Planet. Change*, *34*(3-4), 143-152.

Saavedra-Pellitero, M., J.A. Flores, F. Lamy, and F. J. Sierro (submitted), Coccolithophore estimates of paleotemperature and paleoproductivity changes in the Southeast Pacific over the past ~27 kyr.

Sarmiento, J. L., and J. R. Toggweiler (1984), A new model for the role of the oceans in determining atmospheric pCO2, *Nature*, *308*(5960), 621-624.

Schulz, H.-M., A. Schöner, and K.-C. Emeis (2000), Long-chain alkenone patterns in the Baltic Sea -an ocean-freshwater transition, *Geochim. Cosmochim. Acta*, *64*(3), 469-477,.

Shaffer, G., S. Salinas, O. Pizarro, A. Vega, and S. Hormazabal (1995), Currents in the deep ocean off Chile (30°S). *Deep Sea Res. Part I*, *42*, 425-436.

Sievers, H. A., and N. Silva (2008), Water masses and circulation in austral Chilean channels and fjords, in *Progress in the oceanographic knowledge of Chilean interior waters, from Puerto Montt to Cape Horn*, edited by N. Silva and S. Palma, pp. 53-, Comité Oceanográfico Nacional - Pontificia Universidad Católica de Valparaíso.

Sikes, E. L., J. K. Volkman, L. G. Robertson, and J.-J. Pichon (1997), Alkenones and alkenes in surface waters and sediments of the Southern Ocean: Implications for paleotemperature estimation in polar regions, *Geochim. Cosmochim. Acta*, *61*, 1495-1505.

Sikes, E. L., and M. A. Sicre (2002), Relationship of the tetra-unsaturated C-37 alkenone to salinity and temperature: Implications for paleoproxy applications, *Geochem. Geophys. Geosyst.*, *3*(11), 1063, doi:10.1029/2002GC000345.

Silva, N., and C. Calvete (2002), Physical and chemical oceanographic features of southern Chilean inlets between Penas Gulf and Magellan Strait (CIMAR-FIORDO 2 CRUISE), *Ciencia y Tecnología del Mar*, *25*(1), 23-28.

Stephens, B. B., and R. F. Keeling (2000), The influence of Antarctic sea ice on glacial-interglacial CO_2 variations, *Nature*, *404*(6774), 171-174.

Stocker, T. F., and S. J. Johnsen (2003), A minimum thermodynamic model for the bipolar seesaw, *Paleoceanography*, *18*(4), 1087, doi:10.1029/2003PA000920.

Strub, P. T., J. M. Mesias, V. Montecino, J. Ruttlant, and S. Salinas (1998), Coastal ocean circulation off Western South America., in *The global coastal ocean. Regional studies and syntheses*, edited by A. R. Robinson and K. H. Brink, pp. 273-315, Wiley, New York.

Sugden, D. E., R. D. McCulloch, A. J. M. Bory, and A. S. Hein (2009), Influence of Patagonian glaciers on Antarctic dust deposition during the last glacial period, *Nature Geoscience*, *2*(4), 281-285, doi:10.1038/ngeo474.

Toggweiler, J. R., J. L. Rusell, and S. R. Carson (2006), Midlatitude westerlies, atmospheric CO2, and climate change during ice ages, *Paleoceanography*, *21*, PA 2005, doi:10.1029/2005PA001154.

Verleye, T., and S. Louwye (2010), Late Quaternary environmental changes and latitudinal shifts of the Antarctic Circumpolar

Current as recorded by dinoflagellate cyst from offshore Chile (41°S), *Quat. Sci. Rev.*(29), 1025-1039.

Young, J. R., S. A. Davis, P. R. Bown, and S. Mann (1999), Coccolith ultrastructure and biomineralisation, *Journal of Structural Biology*, *126*(3), 195-215.

4.2 Holocene sea surface temperature variability in the Chilean Fjord Region

A. M. Caniupán[1], F. Lamy[1], C. B. Lange[2], H. W. Arz[3], J. Kaiser[3], R. Kilian[4], T. León[2], G. Mollenhauer[1], S. Pantoja[2], R. Tiedemann[1] and Julia Wellner[5]

[1]Alfred Wegener Institute for Polar and Marine Research, Columbustraβe, D-27568 Bremerhaven, Germany
[2]Department of Oceanography and Center for Oceanographic Research in the eastern South Pacific (COPAS), University of Concepción, Casilla 160-C, Concepción, Chile
[3]Leibniz Institute for Baltic Sea Research Warnemünde, Seestraβe 15, 18199 Rostock-Warnemünde, Germany
[4]Lehrstuhl für Geologie, University of Trier, Trier, Germany
[5]Department of Earth and Atmospheric Sciences, University of Houston, Houston, Texas 77204, USA
*to whom correspondence should be addressed. Email: magaly.caniupan@awi.de

To be submitted at The Holocene

Abstract

The Chilean fjords offer unique opportunities to study Southern Hemisphere paleoenvironmental changes during the Holocene. Here we provide new high-resolution alkenone-derived sea surface temperature (SST) data from sediment cores collected within the core zone of the southern westerly wind belt (MD07-3124, 51°S and JPC-42, 50°S) covering the past ~11 thousand years (kyr). Our continuous, ^{14}C-dated alkenone-based SST records show consistently warmer than present-day temperatures except for the past ~0.6 kyr. However, the records do not exhibit a particular early Holocene climate warming as previously described for the continental margin further north off Chile. Only the inner fjord core JPC-42 shows slightly warmer average temperatures during the middle Holocene. Both records reveal pronounced short-term variations of up to 2.5 °C in the middle Holocene with a prominent cooling centered at ~5 kyr BP. We attribute the absence of an early Holocene warm phase to a combination of factors including decreased inflow of open marine waters due to lower sea-level, enhanced advection of colder and fresher inner fjord water, stronger westerly wind, and reduced local summer insolation. A strong decrease in SST of ca. 2 °C toward modern temperatures characterizes the latest Holocene. Our comparison with previously published high-resolution SST records from the Chilean margin and Northern Patagonia fjords shows that this cooling was not a local event but a regional

feature affecting an area of ca. 10° latitude from ~41°S to ~51°S. In the offshore records (GeoB 3313-1; 41°S and GeoB 7186; 44°S) this cooling has a substantially lower amplitude compared with the highest amplitude recorded in the Jacaf fjord (PC33; ~44°S) and in our new records at ~50° and ~51°S, suggesting an amplification of the SST signal in the interior of the Chilean fjords and corroborating the high sensitivity of the fjord system for tracking regional climate change.

Keywords: Holocene, alkenone, temperature, fjords, Chile.

1. Introduction

The Holocene (since ~11.6 ka BP) has been traditionally considered as a period characterized by relatively stable climate conditions when compared to the last glacial period (*Denton and Karlen*, 1973). However, more recent work suggests substantial Holocene climate variability on a large range of timescales (e.g., *Mayewski et al.*, 2004; *Wanner et al.*, 2008), including quasi-cyclic fluctuations as for example shown by the Holocene "Bond cycles" in the North Atlantic region (*O'Brien et al.*, 1995; *Bond et al.*, 1997; *Bond et al.*, 2001).

In the Southern Hemisphere, paleoclimate archives from Antarctica and the Southern Ocean reveal contrasting results pointing to a complex temperature evolution throughout the Holocene (*Ciais et al.*, 1992; *Masson et al.*, 2000; *Masson-Delmotte et al.*, 2004; *Nielsen et al.*, 2004; *Bentley et al.*, 2009; *Moros et al.*, 2009; *Divine et al.*, 2010). An early Holocene Climatic Optimum (11.5–9 kyr BP) has been widespread documented in Antarctic ice core records, with temperatures up to ~2 °C warmer than present (e.g., *Masson et al.*, 2000)). Thereafter, long-term trends in the ice core records partly deviate as large-scale Antarctic cooling during the Holocene, which is locally compensated by a decrease in the ice-sheet elevation in response to ice-sheet dynamics (*Masson-Delmotte et al.*, 2004). However, a secondary mid-Holocene temperature maximum between ~8 and 6 kyr BP seems to be important in the Ross Sea area whereas in eastern Antarctica some records show a weak secondary warming between ~6 and 3 kyr BP (*Masson et al.*, 2000). Furthermore, the ice-core records suggest a consistent multi-centennial-scale temperature pattern in Antarctica over the Holocene with a cyclicity of ~830 years (*Masson et al.*, 2000; *Masson-Delmotte et al.*, 2004).

Marine and lacustrine records around the Antarctic Peninsula confirm the complexity of the Holocene temperature evolution as maximum warming was registered during different time intervals in the early to middle Holocene (e.g., *Bentley et al.*, 2009). Further offshore Antarctica, marine records from the South Atlantic

sector of the Southern Ocean (50°–53°S) reveal an early Holocene temperature optimum and the onset of cooling and sea-ice expansion between ~9 and 7 kyr BP (*Bianchi and Gersonde*, 2004; *Nielsen et al.*, 2004). Earlier work in this region suggested increased ice-rafted detritus to the subantarctic South Atlantic starting abruptly at ~5.5 kyr BP interpreted in terms of the onset of the so-called Neoglacial phase coinciding with a further advance of sea-ice cover around Antarctica (*Hodell et al.*, 2001; *Iizuka et al.*, 2008).

The expression of these Holocene climate fluctuations in the Chilean fjord region (~42°–55°S), the closest land mass to Antarctica, is still not well documented due to the lack of records covering the complete Holocene. In contrast, detailed paleoceanographic reconstructions have been obtained from the Southeast Pacific off mid-latitude Chile (~30°–41°S). At ODP Site 1233 (41°S) located close to the Northern Patagonia fjord region, maximum warm conditions occurred in the early Holocene (~12 to 9 kyr BP) (*Kaiser et al.*, 2005); SSTs during this interval were generally ~1–2 °C above modern values. Thereafter, temperatures gradually declined reaching modern values (~14°C) in the late Holocene. The early Holocene optimum was not documented in the higher resolution SST record from core GeoB 3313-1 (same location as ODP Site 1233) (*Lamy et al.*, 2002) since it only covered the past ~8 kyr. In this record, a secondary middle Holocene warming is observed at 5–6 kyr BP with SSTs generally declining afterward towards the late Holocene in a similar fashion as the comparatively lower resolution SST record from Site 1233. Further north, a SST record located at ~30°S (*De Pol-Holz et al.*, 2006; *Kaiser et al.*, 2008) displays a slightly delayed optimum warming that lasted longer, i.e. into the middle Holocene and cooling thereafter. Off central Chile at ~33°S, the warmest Holocene SST was found between ~7.5 and 6 kyr BP. This warm phase was preceded by an early Holocene cold interval that ended with a pronounced warming of ~2.5 °C between 8 and 7.5 kyr BP (*Kim et al.*, 2002). The reason for this early Holocene cold phase remains unclear.

The early to middle-Holocene temperature maximum appears to coincide with widespread more arid conditions onshore, as recorded in various terrestrial and marine records from central Chile (32°–35°S) (*Villagrán and Varela*, 1990; *Lamy et al.*, 1999; *Jenny et al.*, 2002; *Maldonado and Villagran*, 2002; *Villa-Martinez et al.*, 2003) and further south in the island of Chiloé (*Abarzúa et al.*, 2004). Since these areas are located at the northern influence zone of the southern westerly wind belt (SWW), the main source of precipitation, a southward displacement of the coupled SWW/Antarctic Circumpolar Current (ACC) during this period has been proposed (e.g., *Kaiser et al.*, 2005). New precipitation reconstructions of the SWW core zone in the southern Chilean fjord region suggest enhanced SWW in the early Holocene that decrease during the middle and late Holocene (*Lamy et al.*, 2010).Taken together, these reconstructions point to an antiphase behavior between the core and the northern margin of the SWW.

Here we provide new high-resolution records of SST variability covering the complete Holocene in the Chilean fjord region (Canal Concepción at ~51°S and Canal Wide at ~50°S, both sites located within the core of the SWW) that will help fill the gap of paleoclimate information between high and mid-latitudes of South America. In order to describe regional patterns of paleoclimate changes and identify common forcing mechanisms, our new alkenone-derived SST data are compared with previously published paleotemperature records from the Chilean margin and Northern Patagonia fjords covering from ~41° to ~51°S.

2. Study area

The Chilean fjord region, located between ~42° and 55°S on the western side of the Andes Cordillera, is a key area to study high-resolution climate changes as it is the only land mass intersecting the SWW, which are a key element in regional climate change. Maximum precipitation of westerly origin is recorded between ~50° and 55°S and diminishes northward and southward of these latitudes (e.g., *Schneider et al.*, 2003; *Garreaud*, 2007). Furthermore, a very strong west to east rainfall gradient is observed due to the rain shadow of the Andes (e.g., *Villa-Martinez and Moreno*, 2007). On the western side of the Andes the total rainfall can be 100–300% higher than that on the eastern flank, the most extreme contrast being between Isla Guarello (7,220 mm y^{-1}) and Lago Argentino (290 mm y^{-1}) at ca. 49°S (*Aravena and Luckman*, 2008).

Currently, the oceanic surface circulation is dominated by the northern part of the ACC that bifurcates at ~45°S into the Peru-Chile Current (PCC) flowing equatorward and the Cape Horn Current (CHC) flowing southward, both transporting Pacific subantarctic waters (SAAW) (e.g., (*Strub et al.*, 1998; *Sievers and Silva*, 2008) (Fig. 1). Large latitudinal SST gradients (>5 °C) characterize the oceanic area adjacent to the Chilean fjord region (Fig. 1). Annual SSTs (World Ocean Atlas 2009; (*Locarnini et al.*, 2010) increase from 8 °C at ~50°S (offshore Canal Concepción) to 13 °C at ~42°S (offshore Isla Grande de Chiloé), making this area very sensible to study past changes in SST distribution.

Strong temperature and salinity gradients are observed in the interior zone of the fjord region, due to the permanent confluence of fresh and marine waters. Prevailing strong SWW constantly supply Pacific SAAW (0–100 m) that penetrates into the fjords (*Palma and Silva*, 2004). Depending on the continental shelf bathymetry, deeper water masses such as Equatorial Subsurface Water (100–300 m) may only enter the interior fjords north of ~48°S. Further south sill depths at the entrances of the major channels that connect to the open ocean are generally too shallow (i.e., in the range of 60–70 m). High freshwater supply due to the extreme amounts of rainfall and input from numerous rivers and glaciers produces a thin surface layer (20–30 m),

the Estuarine Water (EW; (*Silva et al.*, 1998)) with salinities of less than 32 psu. EW and SAAW constitute a two-layer circulation, with fresh waters flowing towards the ocean and saltier Pacific SAAW into de fjords (*Dávila et al.*, 2002; *Silva and Calvete*, 2002; *Sievers and Silva*, 2008). Mixing of SAAW and EW forms modified SAAW (MSAAW) with salinities of ~32 to 33 psu that dominates below ~100 m water depth (*Palma and Silva*, 2004). Details on the water masses in the Chilean fjord region and schematic models of general circulation patterns can be found in (*Sievers and Silva*, 2008).

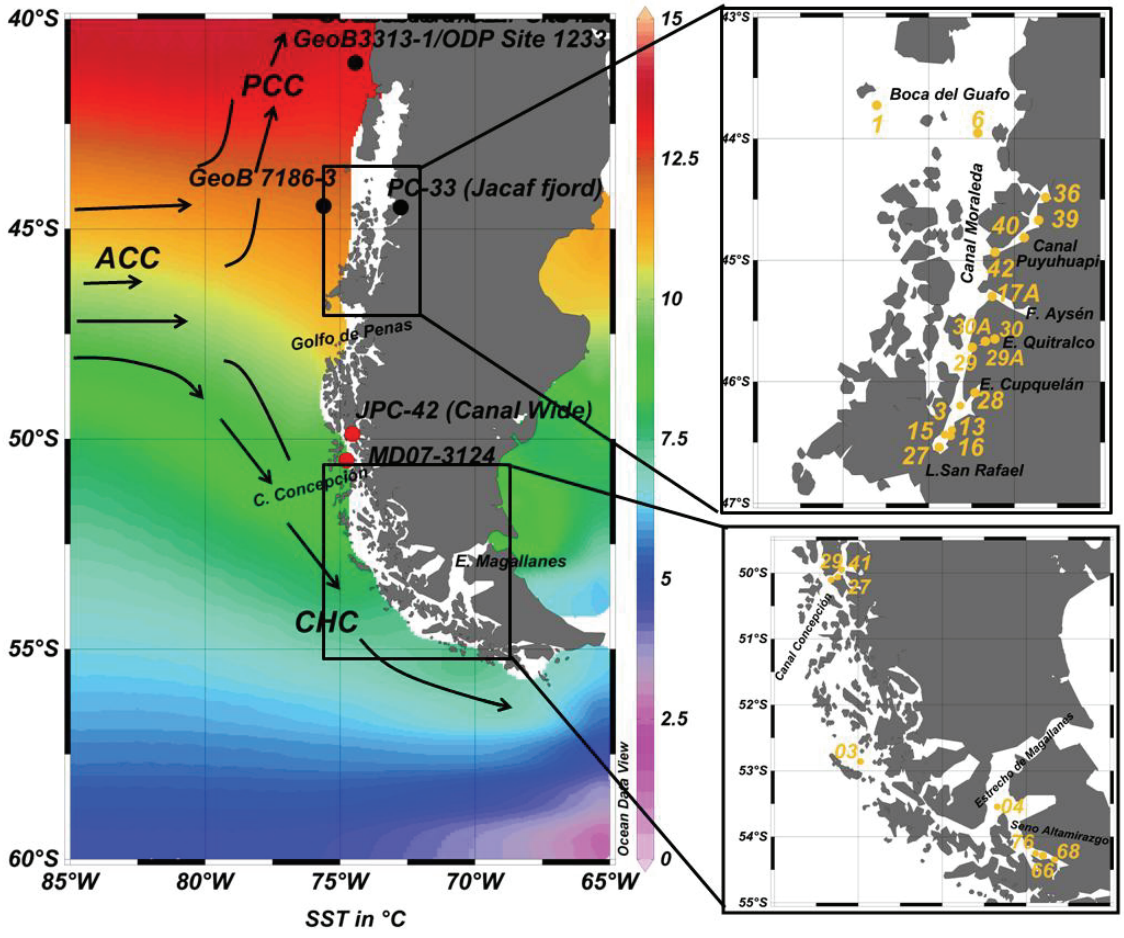

Figure 1. Map of study area showing modern annual SST off southern Chile (World Ocean Atlas, 2009). Black arrows represent the oceanic surface circulation: the Perú-Chile Current (PCC) flowing equatorward and the Cape Horn Current (CHC) flowing poleward, both transporting Pacific subantarctic water (SAAW). Red dots (left panel) indicate the sediment cores analyzed in this study (MD07-3124 and JPC-42), and the black ones refer to previously published records used for comparison. Surface sediment samples used in this study are marked by yellow dots (right panel).

Little information is available on modern SST pattern within the fjord region. In the northern Patagonian fjords, *in situ* SST measurements have been performed during

several Chilean cruises in austral spring, summer, and winter within the CIMAR Program (Cruceros de Investigación Marina en Áreas Remotas; Marine Research Cruises in Remote Areas) whereas farther south only austral spring data are available (http://www.shoa.cl/n_cendhoc/index.html). Compared to SST data in the adjacent open ocean (Table 2), temperatures in the fjords are generally colder with an increasing offset towards the interior fjords. These colder temperatures reflect the increasing contribution of EW and the influence of colder air temperatures inland (e.g. *Schneider et al.*, 2003). Annual SST ranges within the fjords can only be estimated in the northernmost region where they appear to be lower than at the same latitude offshore reflecting the cold summer SSTs in the fjord most likely due to enhanced glacier melt-water input.

Although overall the Chilean fjord region is characterized by downwelling conditions due to the permanent influence of the SWW, a strong temporal variability in phytoplankton productivity has been recorded, with a dominance of chain-forming diatoms during austral spring (October/November) (*Iriarte et al.*, 1993; *Iriarte et al.*, 2001; *Alves-de-Souza et al.*, 2008; *González et al.*, 2010). This spring phytoplankton bloom has been related to an increase in solar radiation resulting in an extended photoperiod during the spring months which promotes the growth of diatoms in a nutrient-replete water column (*González et al.*, 2010).

Our paleo-records are based on two sediment cores: Core MD07-3124 was retrieved from the Canal Concepción (at ~51°S) and is characterized by a comparatively strong marine influence. The second core (JPC-42) is located to the east of the Europa fjord (~50°S) in the Canal Wide and is located relatively close to the Southern Patagonian ice-field (Fig. 1).

3. Material and methods

We reconstructed alkenone-derived SST from two sediment cores retrieved from the Chilean fjord region. Core MD07-3124 (22.25 m length) was retrieved from Canal Concepción (50°30.96'S; 74°58.33'W; 564 m water depth) in 2007 during the XV-MD-159-PACHIDERME cruise on board R/V Marion Dufresne. The second core, JPC-42 (12.5 m length), was recovered between the Europa and Penguin fjords in the Canal Wide (49°54.901'S; 74°22.646'W; 904 m water depth) in 2005 during the NBP05-05 Palmer Cruise with RVIB N.B. Palmer. Core MD07-3124 was sampled at 8-cm intervals, which are equivalent to a mean temporal resolution of ~100 years and core JPC-42 was sampled at continuous 3-cm intervals corresponding to a mean resolution of ~110 years.

In addition, surface sediments collected during previous expeditions in the Chilean fjord region were analyzed in order to detect the potential seasonality in the

signal of alkenone-derived SST. These include: 13 core-top samples (box core; BC) collected in austral spring (12–25 November, 2001) during the Chilean CIMAR FIORDO (CF) 7 Expedition on board R/V AGOR Vidal Gormáz; 7 core-top samples (Kasten core; KC) collected in austral winter (June 23–July 14, 2005) during the PALMER cruise; and 2 core-top samples (multi-core; MC) collected in austral spring (October 19–November 2, 2003) during the Japanese BEAGLE cruise on board R/V Mirai (Table 2).

3.1 Chronology

The chronology of core MD07-3124 is constrained by 15 accelerator mass spectrometer (AMS) radiocarbon dates (^{14}C) (Fig. 2; Table 1) on mixed samples of planktonic foraminifera. ^{14}C-ages were converted to calibrated calendar years before present (kyr BP) using the IntCal09 software (*Reimer et al.*, 2009). ^{14}C-ages were corrected for a local reservoir age of 780 years obtained from core JPC-42 (see below). Sedimentation rates reach an average of 4.6 m/kyr during the early Holocene decreasing to ~1.3 m/kyr in the middle and late Holocene. The age model for core JPC-42 is based on 7 AMS-^{14}C dates on shell fragments (Fig. 2; Table 1). Sedimentation rates in core JPC-42 fluctuate between 1.0 and 1.6 m/kyr during the early Holocene, then decrease to 0.9 m/kyr in the mid- and late Holocene, and increase again to ~1.6 m/kyr during the latest Holocene. The comparison of two AMS-^{14}C dates on shell and wood fragments obtained from the same core depth (1.75 m) allowed us to obtain a local marine reservoir for the Canal Wide of 780 years. This age is older than the only published local reservoir age for the Chilean fjord region of 530 years at Puerto Natales (*Ingram and Southon*, 1996).

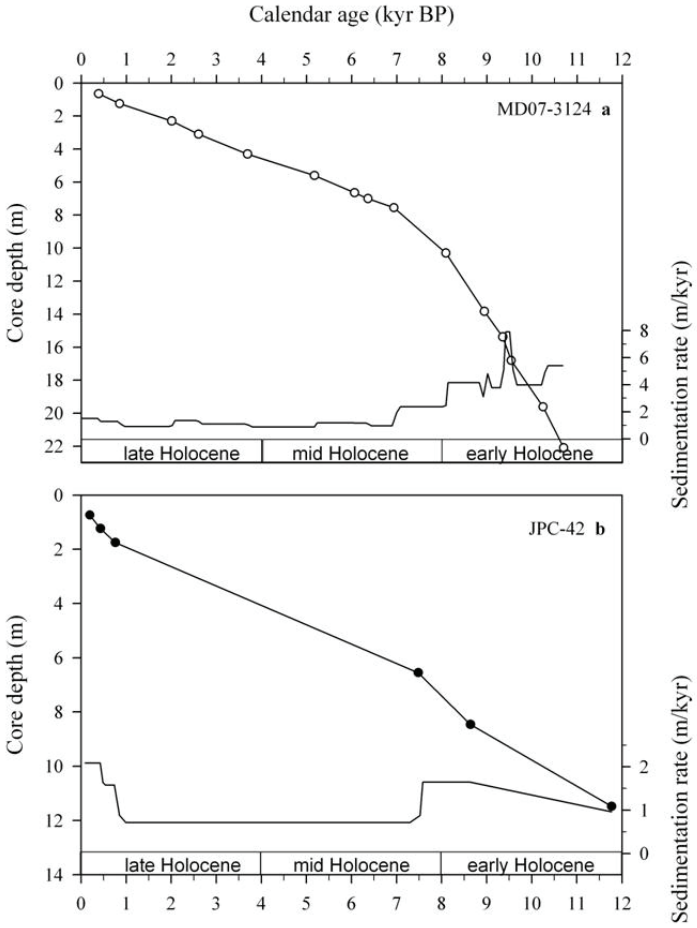

Figure 2. Age-depth relationship and sedimentation rate for cores MD07-3124 (Canal Concepción; ~51°S) and JPC-42 (Canal Wide; ~50°S) based on 15 AMS ^{14}C dates and 6 AMS ^{14}C dates, respectively (see also Table 1).

Table 1

Age control points for cores MD07-3124 and JPC-42. Calibration ages after applying the local marine reservoir of 780 years (*) obtained from core JPC-42.

Core depth (m)	^{14}C age (years)	St. deviation (± years)	Marine reservoir (years)	^{14}C (after applying local marine reservoir)	CALPAL (kyr BP)
MD07-3124					
0.65	1110	30	780	330	0.38
1.25	1690	30	780	910	0.85
2.30	2830	35	780	2050	2,01
3.10	3295	30	780	2515	2.60
4.30	4230	40	780	3450	3.69
5.60	5280	35	780	4500	5.17
6.65	6050	30	780	5270	6.06
7.0	6380	40	780	5600	6.36
7.55	6850	35	780	6070	6.93

10.30	8040	60	780	7260	8.09
13.83	8840	55	780	8060	8.94
15.38	9090	45	780	8310	9.35
16.38	9360	45	780	8580	9.53
19.62	9880	45	780	9100	10.24
22.10	10250	50	780	9470	10.70
JPC-42					
0.74	995	90	780	215	0.195
1.23	1150	35	780	370	0.43
1.75 (shell)	840*	75	0	840	0.76
1.75 (wood)	1620*	90	780	840	0.76
6.55	7370	40	780	6590	7.48
8.46	8620	65	780	7840	8.64
11.48	10900	60	780	10120	11.77

3.2 Alkenone-derived sea surface temperature (SST)

For core MD07-3124 (Canal Concepción), long-chain alkenones (C_{37}) were extracted from 3–5 g of powdered freeze-dried sediment using solvent of decreasing polarity (MeOH, MeOH/CH_2Cl_2, CH_2Cl_2). Organic extracts were saponificated to avoid interferences with co-eluting C_{36}-fatty acid methyl esters using 0.1 N KOH and then partitioned into Bond silica column using CH_2Cl_2 (alcanes and ketones's fraction). The fraction containing the alkenones was analyzed by gas chromatography with flame ionization detection (GC-FID). GC-FID quantification was done by an internal standard method using 2-nanodecanonce ($C_{19}H_{38}O$). Alkenone measurements on core MD07-3124 were performed at the University of Bremen, Germany.

For core JPC-42 (Canal Wide) and the surface sediments, alkenone analyses were done in the laboratory of marine organic chemistry of the University of Concepción, Chile, according to the methodology described by *Prahl and Wakeham* (1987) and *Prahl et al.* (1988). About 3 g of wet sediment were extracted with dichloromethane-methanol. Prior to extraction, a recovery standard (*n*-heptacosanone) was added to the sediment. The lipid fraction was subjected to column chromatography. The fractions containing C_{37} alkenones were concentrated and dissolved in iso-octane and 5α-cholestane, and then an internal standard (C_{27} alkenones) was added; the fractions were analyzed in a Shimadzu Gas Chromatograph equipped with a capillary column (Rtx-5 m, 0.22 µm, 0.32 mm i. d.×30 m, J&W Scientific) and a flame ionization detector.

For all samples, we determined the simplified alkenone unsaturation index ($U^{K'}_{37}$) (*Prahl and Wakeham*, 1987). Using the calibration equation proposed by *Prahl et al.* (1988) we converted the $U^{K'}_{37}$ index into SST values ($U^{K'}_{37}$= 0.034T + 0.039). The robustness of this technique has been demonstrated with hundreds of globally dispersed surface sediment samples (e.g., *Müller et al.*, 1998; *Grimalt et al.*, 2000).

4. Results

4.1 Alkenone-derived SST from surface sediment samples

Alkenone-derived SST was reliably quantified in 19 out of the 26 surface sediment samples analyzed from the Chilean fjord region (Fig. 1; Table 2). No alkenone signal was found near to Laguna San Rafael at 46.5°S (CF7-BC27, 28; Palmer-KC03; 13; 15–16), an area that is presently under strong influence of glacier meltwater and having salinities between 22.2 and 23.2 psu.

Overall, alkenone-derived SSTs decreased from north to south with maximum temperatures of 11.5 °C at ~44°S (CF7-BC01) and minimum of 8.6 °C at ~53°S (Palmer-KC66 and KC68) (Table 2). In northern Patagonia (44°–46°S), the mean SST is 11 °C with higher temperatures at stations with comparatively strong open marine influence, i.e. Boca del Guafo (11.5 °C; CF7-BC01), entrance of Canal Moraleda (11.2 °C; CF7-BC06) and the mouth of Canal Puyuhuapi (11.5 °C; CF7-BC42). SST diminishes slightly to the south of the bathymetric constriction called "Constricción de Meninea" at ~45°S, reaching values of 10.3 °C in the Quitralco fjord (CF7-BC29A). For central Patagonia, we obtained a few alkenone SSTs from Kasten cores in the fjords Penguin and Europa with comparatively cold SST values (9.6–9.7 °C; Palmer- KC27, 29, 41). Further south in the Magallan Strait region, the highest SST corresponds to the sample close to Punta Arenas (10.1 °C, Beagle-MC04) and the coldest SSTs are from the Seno Almirantazgo close to the Marinelli and Ainsworth glaciers (8.6–9 °C; Palmer- KC66, 68, 76). At the Pacific entrance of the strait a value of 9.3°C was determined (Beagle-MC03).

Table 2

Summary of the surface sediment samples analyzed from the Chilean fjord region. Cores were collected during CIMAR FIORDO (CF) 7, Palmer (P) and Beagle (B) cruises. *In situ* seasonal SST data were compared with SST data obtained from the World Ocean Atlas (WOA 2009) and alkenone-derived SST. *In situ* SST data (CTD) were measured during several Chilean CF cruises in northern (CF4 austral summer; CF7 austral winter/spring), central (CF2 austral spring) and southern Patagonia (CF3 austral spring); the temperatures of the upper 30 m of the water column were considered.

Description	Lat (°S)	Long (°W)	Water depth (m)	Winter SST (°C) *in situ*	Spring SST (°C) *in situ*/WOA	Summer SST (°C) *in situ*/WOA	Annual SST (°C) WOA	UK'_{37} SST (°C)
Northern Patagonia								
Boca del Guafo (CF7-BC01)	43.7356	74.5836	240	10.4	11.1/12.4	13.6/14.8	12.0	11.5
Boca del Guafo (CF7-BC06)	43.9878	73.3654	176	9.6	11.8/12.4	12.2/14.8	12.0	11.2

Canal Puyuguapi (CF7-BC36)	44.4433	72.6173	219	8.7	11.4/12.0	/14.0	12.0	10.9
Canal Puyuguapi (CF7-BC39)	44.7279	72.714	160	9.4	11.6/12.0	/14.0	12.0	10.7
Canal Puyuguapi (CF7-BC40)	44.8248	72.9342	260	9.0	11.9/12.0	/14.0	12.0	11.0
Canal Puyuguapi (CF7-BC42)	44.9108	73.3183	320	9.2	11.5/12.0	11.9/14.0	12.0	11.5
Fiordo Aysén (CF7-BC17A)	45.363	73.2919	330	8.7	10.3/11.5	12.7/13.8	11.5	11.3
Estero Quitralco (CF7-BC30)	45.7430	73.4077	269	9.0	10.4/11.5	12.0/13.8	11.5	11.5
Estero Quitralco (CF7-BC30A)	45.7542	73.5099	110	8.6	10.2/11.5	12.0 /13.8	11.5	10.8
Estero Quitralco (CF7-BC29A)	45.7602	73.4667	112	8.7	10.2/11.5	12.0/13.8	11.5	10.3
Estero Quitralco (CF7-BC29)	45.7812	73.5087	114	8.7	10.3/11.5	12.0/13.8	11.5	10.7
Estero Cupquelán (CF7-BC28)	46.144	73.4958	239	8.8	9.7/	/	11.0	n.d
Laguna San Rafael (Palmer-KC03)	46.165	73.6679	52	8.7	9.5/	11.8/	11.0	n.d.
Laguna San Rafael (Palmer-KC13)	46.449	73.797	30	8.3	9.2/	11.4/	11.0	n.d.
Laguna San Rafael (Palmer-KC15)	46.434	73.7932	112	8.1	8.9/	10.9/	11.0	n.d.
Laguna San Rafael (Palmer-KC16)	46.434	73.8012	112	7.2	8.9/	10.9/	11.0	n.d.
Laguna San Rafael (CF7-BC27)	46.4852	73.8026	112	7.2	8.9/	10.9/	11.0	n.d.
Central Patagonia								
Fiordo Penguin (Palmer-KC41)	49.915	74.3774	711		6.3/8.0	/10	9.0	9.7
Fiordo Europa (Palmer-KC29)	50.013	74.4019	350		6.8/8.0	/10	9.0	9.6
Fiordo Europa (Palmer-KC27)	50.057	74.4307	414		6.7/8.0	/10	9.0	9.7
Canal Concepción MD07-3124	50.516	74.9721	564		8.2 /8.0	/10	9.0	10.4
Southern Patagonia								
Seno Altamirazgo (Palmer-KC76)	54.26	69.7941	290		6.1/7.0	7.5/8.5	7.4	9.0
Seno Altamirazgo (Palmer-KC66)	54.322	69.4571	110		5.8/7.0	7.5 /8.5	7.4	8.6
Seno Altamirazgo (Palmer-KC68)	54.324	69.5535	117		5.4/7.0	7.5 /8.5	7.4	8.6
E. de Magallanes (Beagle-MC03)	52.867	74.0876	528		7.0/7.7	10.6 /10.1	8.4	9.3
E. de Magallanes (Beagle-MC04)	53.572	70.6746	428		6.6/8.0	/11.7	9.6	10.1

n.d.= not detected (Laguna San Rafael)

For more detail on *in situ* SST data over the Chilean fjord region see http://www.shoa.cl/n_cendhoc/index.html

4.3 Downcore alkenone-derived SST records

We constructed continuous alkenone-derived SST records that cover the past ~8 kyr and ~11 kyr for core JPC-42 (Canal Wide) and MD07-3124 (Canal Concepción), respectively (Fig. 3). Mean SST over the past ~8 kyr at site JPC-42 is 12.1°C, maximum temperature is 13.8 °C at 5.3 kyr BP (mid-Holocene) and minimum SST is 8.6°C at 0.3 kyr BP (latest Holocene). Alkenones were not detected in samples older than ~8 kyr BP. Generally warmer SSTs occur from ~6 to 4 kyr BP during the mid-Holocene with values mostly ≥13 °C. Intermediate values characterize the early part of the mid-Holocene and the late Holocene from ~4 to 1 kyr BP. A pronounced SST drop of ~2°C is recorded between ~1.1 and 0.6 kyr BP. Thereafter, large short-term fluctuations occur with amplitudes exceeding 2 °C over the past 600 years. A few of such short-term events that are often documented by only one single data point are also present in the earlier part of the record (Fig. 3).

For core MD07-3124 (Canal Concepción), alkenone-SSTs oscillate between a maximum of 12.7 °C at 5.4 kyr BP (mid Holocene) and a minimum of 9.8 °C at 0.3 kyr BP (latest Holocene) (Fig. 3). The SST record does not reveal pronounced long-term trends. SSTs fluctuate around 12 °C during most of the Holocene with a number of multi-centennial scale and shorter-term fluctuations of the order of 1–2 °C. The most important of these high frequency variations is an abrupt SST drop of >2 °C (from 12.7 °C to 10.1 °C) at ~5.4 kyr BP lasting until ~4.7 kyr BP. An additional cold event is recorded at 6.2 kyr BP. In the latest Holocene, since ~0.9 kyr BP we observe a very strong decrease in SST of ca. 2 °C over a period of ~300 years and SSTs remain comparatively low up to the present (10–10.5 °C).

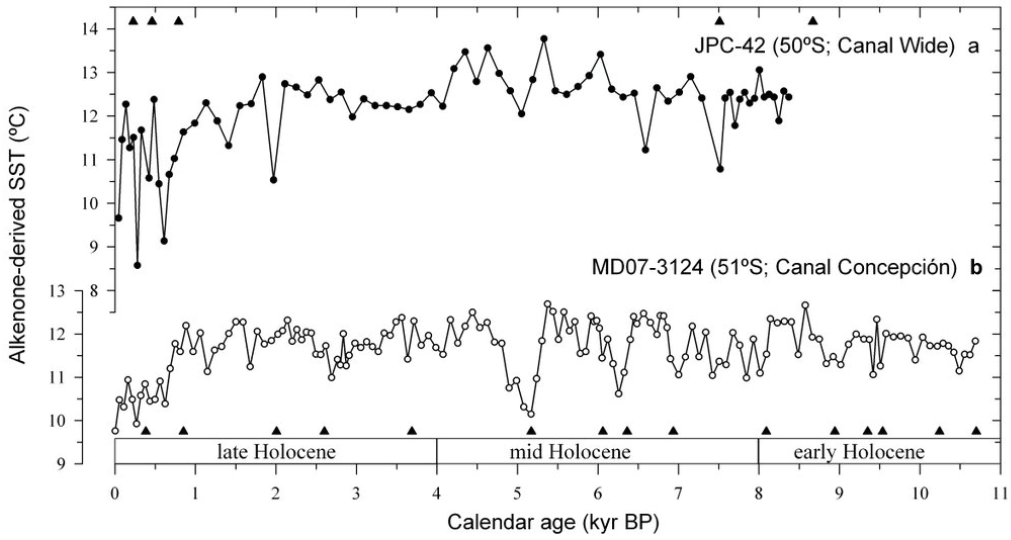

Figure 3. Holocene alkenone-derived SST variability for the Chilean Fjord region. (a) Core JPC-42 (~50°S; Canal Wide) and (b) core MD07-3124 (~51°S; Canal Concepción). Black triangles on X-axes (upper and lower) represent age control points (see Table 1).

5. Discussion

5.1. Seasonal signal of alkenone-derived SST in the Chilean fjord region

Based on a large number of modern sediments from the global ocean, it is generally assumed that alkenone-derived SST represents mean annual SST (*Müller et al.*, 1998). However, there have also been studies that suggested that alkenone paleotemperatures are seasonally skewed, particularly in polar latitudes (e.g., *Sikes et al.*, 1997). Within the Chilean fjord region, no information is available on the preferred productivity season for alkenone-producing haptophytes and modern SST measurements (*in situ* SST) are restricted to the austral spring and winter seasons. We compare our alkenone-derived SST values from surface sediments to the available *in situ* SST data for the different seasons and World Ocean Atlas 2009 data (*Locarnini et al.*, 2010) from the same latitude directly offshore in the open ocean (Table 2). Our comparison shows that in the Northern Patagonia Fjord region, alkenone-derived SST largely corresponds to spring *in situ* temperatures (Table 2). Further south (central and southern Patagonia), alkenone SST are warmer than spring *in situ* temperatures. Unfortunately, there are no summer *in situ* SST data available from this region. Compared to the World Ocean Atlas 2009 data, alkenone SSTs approach summer SST in this region. For our core locations in the Canal Wide at ~50ºS (JPC-42) and Canal Concepción at ~51ºS (MD07-3124), the core-top value for JPC-42 is 9.7 °C which is ca 3 °C warmer than *in situ* austral spring SST, whereas for core MD07-3124 the top of the core is ~2 °C warmer than *in situ* austral spring SST (10.4 °C *versus* 8.2 °C).

Taken together, our surface sediment SST results may be interpreted in terms of a delayed productivity season of alkenone-producing nanoplankton towards the south related to the latitudinal gradients of light and temperature. *Alves-de-Souza et al.* (2008) demonstrated a heterogeneous temporal and spatial phytoplankton distribution in terms of abundance and composition in the Chilean Fjord region. Phytoplankton concentrations were highest (182 cells L^{-1} 10^4) in the area between 48° and 52°S mainly in spring, whereas in the Magellan Strait area (53°S), the highest concentrations (98 cells L^{-1} 10^4) were observed in spring–summer. The nanoflagellates showed the largest spatial differences in the phytoplankton composition with the highest abundances in summer and autumn in the southern area. Although no detailed information is available on the preferred productivity season for alkenone-producing haptophytes in the Chilean fjords, the dominance of nanoplankton during post bloom events during spring in northern Patagonia fjords, and pico- and nanoplankton in summer-autumn in southernmost Patagonia fjords has been previously reported (*Iriarte et al.*, 1993; *Magazzu et al.*, 1996; *González et al.*, 2010).

Recently, *Prahl et al.* (2010) showed that alkenone SSTs in the subarctic NE Pacific are strongly biased towards the summer season and are ~4 °C warmer than

mean annual SSTs. Based on a few samples from the Southeast Pacific off southern Chile, Prahl and co-workers further showed that this summer offset of alkenone SSTs is less pronounced (~1 °C) in the Southern Hemisphere because the seasonal temperature contrast is much less compared to the same latitude in the north. Our data from the Chilean fjords are consistent with these data and suggest an increasing offset to annual mean SST from north to south that is larger than offshore, most likely due to an amplification of the seasonal signal within the fjords.

5.2. Holocene SST changes

There is widespread evidence for the presence of an early Holocene Climatic Optimum (~12–9 kyr BP) from Chilean alkenone-derived SST records at ~30°S (*Kaiser et al.*, 2008) and ~41°S (Fig. 4a) (*Kaiser et al.*, 2005), and from Antarctic ice-core records (e.g., *Masson et al.*, 2000). Furthermore, the early Holocene warming is likewise visible in a low resolution alkenone SST record from the continental margin off southernmost Chile (MD07-3128; ~53°S; (*Caniupán et al.*, submitted)). In contrast, our SST record from core MD07-3124 (Fig. 4e) located relatively close to the Pacific does not reveal a particular early Holocene temperature maximum but shows warmer than present temperatures over most of the Holocene except for the past ~0.6 kyr and a centennial-scale cooling centered at ~5 kyr BP. The alkenone SST record for core JPC-42, on the other hand, only extends to 8 kyr BP because alkenones were not detected in the early Holocene (Fig. 4d).

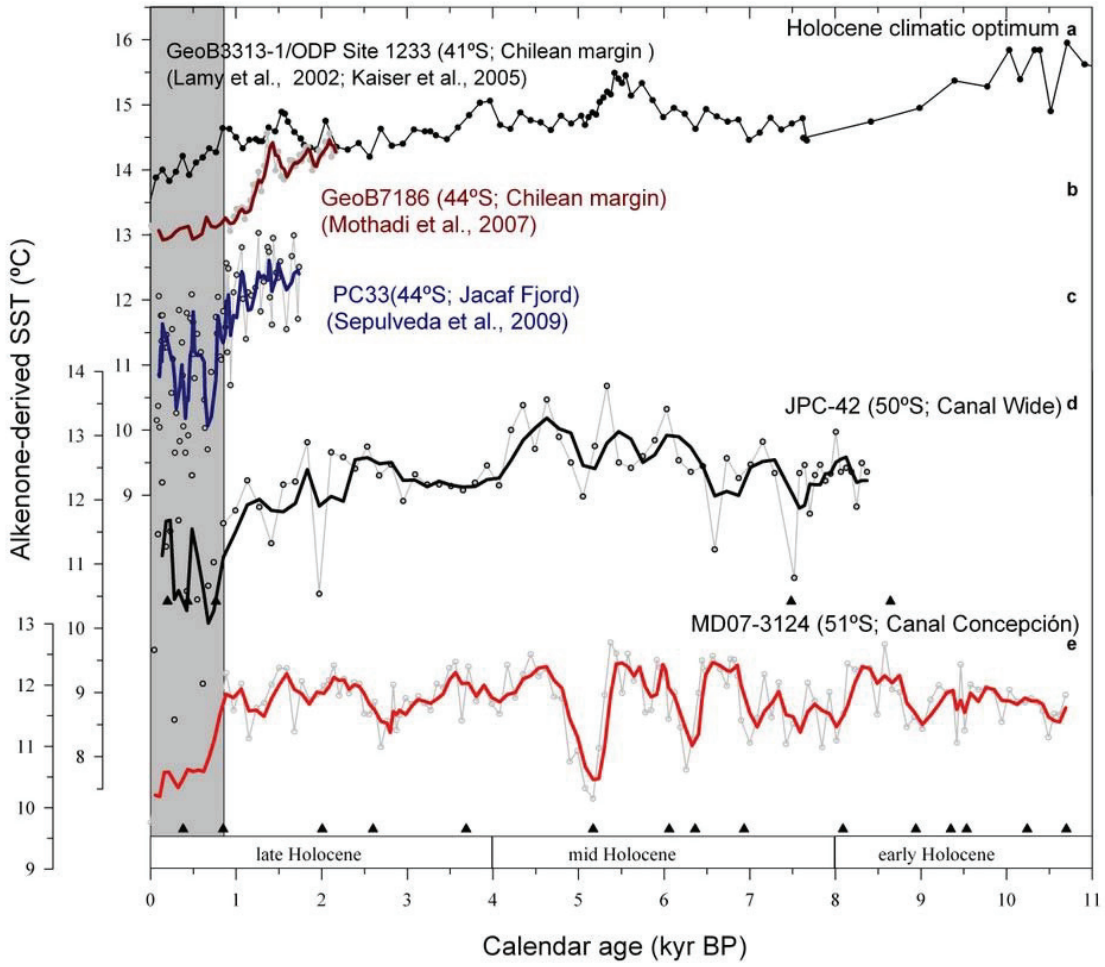

Figure 4. Comparison between Holocene alkenone-SST variability from oceanic sites and sites within the fjord region. (a) GeoB3313-1/ODP Site 1233 at ~41°S (*Lamy et al.*, 2002; *Kaiser et al.*, 2005). (b) GeoB7186 at ~44°S (*Mohtadi et al.*, 2007). (c) PC-33 at ~44°S (*Sepúlveda et al.*, 2009). (d) JPC-42 at ~50°S. (e) MD07-3124 at ~51°S. Dark lines (brown, blue, black and red) represent 3-point running average. Vertical grey bar indicates the general cooling trend observed in all the records from the Chilean margin from ~41° to ~51°S.

The early Holocene temperature maximum in the Southern Hemisphere has been related to changes in the global ocean circulation involving a bipolar seesaw-like temperature pattern (*Masson et al.*, 2000; *Lamy et al.*, 2010). Within the fjords, global open ocean processes are superimposed to local processes, i.e. sea-level changes. The presence of alkenones throughout the past ~11 kyr in Canal Concepción clearly documents marine conditions back to the early Holocene consistent with shelf sill depths of ~60-70 m and a global sea-level of ~-40 m at 11 kyr BP (e.g., *Fairbanks*, 1989). However, due to the lower sea-level, the flow of open ocean water into the fjord system was significantly reduced during the early Holocene. At the same time, the advection of colder and fresher inner fjord water (EW) was probably enhanced

induced by higher precipitation and runoff (*Lamy et al.*, 2010). The enhanced early Holocene precipitation has been related to stronger westerly winds that might additionally have impounded the colder EW insight the fjords. The fact that alkenones in our second more proximal core JPC-42 are only present after ~8 kyr BP points to substantially reduced surface water salinities in the inner fjords during the early Holocene consistent with reduced open marine inflow, higher precipitation and meltwater input, and stronger winds. Glaciers were generally less extended during the early Holocene compared to the Neoglacial starting at ~5.5 kyr BP except for limited advances between ~8 and 9 kyr BP (*Kilian et al.*, submitted) coeval with a cosmogenic nuclide-dated glacier advance at the Northern Patagonian Ice Field (*Douglass et al.*, 2005). This advance does not relate to a particular cooling in our record.

A further factor for the absence of an early Holocene temperature maximum in our records may involve local insolation changes. As discussed above, alkenone SSTs in central and southern Patagonia most likely reflect summer temperatures. Though it has been suggested that local insolation changes are only a minor factor (*Lamy et al.*, 2010), these changes might be more important inside the fjords. Therefore, we suggest that reduced local summer insolation could have been an additional factor for explaining the relatively cold early Holocene SSTs within the fjords compared to the warmer open ocean reconstructions.

Our more inland record from core JPC-42 (Fig. 4d) shows a slightly warmer interval from 6 to 4 kyr BP during the middle Holocene that may partly correspond to the secondary middle Holocene warming observed offshore at 41°S (*Lamy et al.*, 2002) (Fig. 4a). This middle Holocene warming is not apparent in the SST record from core MD07-3124 (Fig. 4e) which is characterized by comparatively large short-term SST variability of the order of 1–2 °C during this time interval. A pronounced cooling of ~2.5°C lasting from ~5.4 to 4.7 kyr BP at Canal Concepción coincides with the first, relatively limited, Neoglacial advance in the Southern Andes (*Glasser et al.*, 2004; *Kilian et al.*, submitted). This advance occurs after sea-ice cover around Antarctica increased at ~5.5 kyr BP (*Hodell et al.*, 2001; *Iizuka et al.*, 2008). Interestingly, the SST cooling during this event is less pronounced in our inner fjord record JPC-42 (~1.4°C) which should document a potential cooling effect of advancing glaciers from the Southern Patagonian ice-field even better. This may suggest a Southern Ocean origin of the first Neoglacial cooling signal consistent with the sea-ice advance around Antarctica. The SST record from core GeoB 3313-1 at 41°S also shows a cooling after the middle Holocene warming which is, however, less pronounced of the order ~1°C (Fig. 4a).

The most striking feature of the latest Holocene in our two SST records is the pronounced cooling of >2 °C starting at around 1.1 kyr BP in core JPC-42 and ~0.9 kyr BP in core MD07-3124 and lasting in both cores until ~0.6 kyr BP. This cooling coincides with the transition from the globally known Medieval Warm Period (MWP) to the Little Ice Age (LIA). A similar cooling has been observed in the late Holocene alkenone-based

SST record from the Jacaf Fjord, located in northern Patagonia at ~44°S (Fig. 4c) (*Sepúlveda et al.*, 2009). Here, the transition from warm and less humid conditions before 0.95 kyr BP to ~2 °C cooler and more humid climates after ~0.75 kyr BP takes place over a short period of ~200 years. Thereafter, SSTs recover rapidly to a maximum at ~0.5 kyr BP followed by a rather cool but highly variable interval that is terminated with a warming around 0.1 kyr BP. While SSTs remain cool in our MD07-3124 record (Fig. 4e), large fluctuations occur in the inner fjord record from core JPC-42. These data point to a stronger SST variability in the inner fjords (Fig. 4c and 4d) compared to the more oceanic location of the Canal Concepción. This pattern is consistent with a quite continuous cooling trend in the continental margin sites GeoB 3313-1 (41°S; Fig. 4a) and GeoB 7186 (44°S; Fig. 4b) (*Lamy et al.*, 2002; *Mohtadi et al.*, 2007) which has however a smaller amplitude of only ~1–1.5 °C. This cooling trend starts at ~0.85 kyr in the northern record but significantly earlier (at ~1.3 kyr BP) at 44°S directly offshore of the Jacaf Fjord record. Taken together, the available SST records from the Chilean fjords and the adjacent continental margin all show a pronounced late Holocene cooling suggesting the cooling was not a local event but a regional feature affecting an area of ca. 10° latitude from ~41° to 51° S. The exact timing and duration of the cooling varies between sites by a few hundred years. Whether this is a consequence of radiocarbon dating uncertainties including local reservoir age changes is difficult to assess. SSTs generally remain cool or cool even further after the main shift in the offshore Pacific records and the comparatively open Canal Concepción. Both more inland located fjord records (Jacaf and Canal Wide) show, on the other hand, major fluctuations over the past 700 years. This feature is more similar to the recent primarily tree-ring-derived continental temperature reconstructions for Southern Patagonia over this time-frame (*Neukom et al.*, 2010) suggesting that these variations are possibly amplified in continental areas. The same applies to the larger amplitude of the cooling in the fjord records compared to those located at the continental margin (Fig. 4).

Recent glacier reconstructions in the Chilean Fjord Region show five major advances during the Neoglaciation since ~5.5 kyr BP. The first advance coincides with a major cooling in our SST records as discussed above. However, the following three glacier advances between ~4.1–3.8 kyr BP, ~2.2–2.3 kyr BP, and ~1.1 to 0.87 kyr BP fall into relatively warm intervals in our SST records suggesting a predominant precipitation control of these advances (*Kilian et al.*, submitted). Only the final advance starting at ~0.65 BP and extending until the last century coincides with our cool interval after the major late Holocene cooling at the transition of the MWP to the LIA. Therefore, *Kilian et al*. (submitted) derive a predominant temperature control for this LIA advance. A recent precipitation reconstruction based on well-dated stalagmites from the Chilean Fjord Region at ~53°S (*Schimpf et al*., in press) support these

interpretations showing for example ~30% higher precipitation during the MWP compared to the cooler interval thereafter.

6. Conclusions

Surface sediment data from the complete latitudinal range of the Chilean fjords show that alkenone SSTs do not represent annual mean temperatures. Instead, they resemble austral spring temperatures in the northern fjords and austral summer further south, suggesting a delayed productivity season of alkenone-producing nanoplankton towards the south.

Alkenone SSTs in our two downcore records from the Canal Concepción and the Canal Wide show warmer than present temperatures over most of the Holocene except for the past ~0.6 kyr and a centennial-scale cooling centered at ~5 kyr BP. There is no evidence of a particular warming in the early Holocene as found in Chilean continental margin records and other Southern Hemisphere temperature-related proxy data. We attribute the absence of an early Holocene warm phase to a combination of factors including decreased inflow of open marine waters due to lower sea-level stands, enhanced advection of colder and fresher inner fjord water, stronger westerly winds, and reduced local summer insolation.

A pronounced cooling of ~2.5°C occurred in the latest Holocene between ~0.9 and 0.6 kyr BP correlating to a similar cooling further north in the Chilean fjords and offshore at the Chilean continental margin. The widespread occurrence of this cooling suggests that is was not a local event but a regional feature affection an area of ~10° latitude. The exact timing, duration, and amplitude vary slightly among the sites. Higher amplitudes in the fjords records points to an amplification of the signal inland.

Acknowledgements

Funding was provided by the Deutsche Forschungsgemeinschaft (DFG) through grants LA 1273/3-2, He3412/6-1, LA1273/5-1, and KI-456/9-1. C.L. acknowledges support from the COPAS Center (Project FONDAP # 15010007). We thank the captains and crews of IMAGES R/V Marion Dufresne cruise MD159/PACHIDERME and RVIB Nathaniel B. Palmer cruise NBP0505. We also would like to thank Lilian Nuñez and Ralph Kreutz for help in the alkenone analysis.

References

Abarzúa, A., C. Villagrán, and P. I. Moreno (2004), Deglacial and postglacial climate history in east-central Isla Grande de Chiloe, southern Chile (43ºS), *Quaternary Research*, *62*(1), 49-59.

Alves-de-Souza, C., M. T. González, and J. L. Iriarte (2008), Functional groups in marine phytoplankton assemblages dominated by

diatoms in fjords of southern Chile, *Journal of Plankton Research*, *30*(11), 1233-1243.

Aravena, J., and B. Luckman (2008), Spatio-temporal rainfall patterns in Southern South America, *International Journal of Climatology*, DOI: 10.1002/joc.1761.

Bentley, M. J., D. A. Hodgson, J. A. Smith, C. Ó. Cofaigh, E. W. Domack, R. D. Larter, S. J. Roberts, S. Brachfeld, A. Leventer, C. Hjort, C.-D. Hillenbrand, and J. Evans (2009), Mechanisms of Holocene palaeoenvironmental change in the Antarctic Peninsula region, *The Holocene*, *19*(1), 51-69.

Bianchi, C., and R. Gersonde (2004), Climate evolution at the last deglaciation: The role of the Southern Ocean, *Earth and Planetary Science Letters*, *228*(3-4), 407-424.

Bond, G., W. Showers, M. Cheseby, R. Lotti, P. Almasi, P. DeMenocal, P. Priore, H. Cullen, I. Hadjas, and G. Bonani (1997), A pervasive millenial-scale cycle in North Atlantic Holocene and Glacial climates, *Science*, *278*, 1257-1266.

Bond, G., B. Kromer, J. Beer, R. Muscheler, M. N. Evans, W. Showers, S. Hoffmann, R. Lotti-Bond, I. Hajdas, and G. Bonani (2001), Persistent solar influence on north Atlantic climate during the Holocene, *Science*, *294*(5549), 2130-2136.

Caniupán, A. M., F. Lamy, C. B. Lange, U. Ninnemann, R. Kilian, C. Aracena, O. Baeza, H. Arz, D. Hebbeln, J. Kaiser, C. Kissel, C. Laj, G. Mollenhauer, and R. Tiedemann (submitted), Millennial-scale surface water changes in the Southeast Pacific off southermost Chile (53ºS) over the past ~60 kyr.

Ciais, P., J.R. Petit, J. Jouzel, C. Lorius, N.I. Barkov, V. Lipenkov, and V. Nicolaïev (1992), Evidence for an early Holocene climatic optimum in the Antarctic deep ice-core record, *Climate Dynamics*, *6*, 169-177.

Dávila, P., D. Figueroa, and E. Müller (2002), Freshwater input into the coastal ocean and its relation with the salinity distribution off austral Chile (35-55ºS), *Continental Shelf Research*, *22*, 521-534.

De Pol-Holz, R., O. Ulloa, L. Dezileau, J. Kaiser, F. Lamy, and D. Hebbeln (2006), Melting of the Patagonian Ice Sheet and deglacial perturbations of the nitrogen cycle in the eastern South Pacific, *Geophysical Research Letters*, *33, L04704, doi:10.1029/2005GL024477*.

Denton, G. H., and W. Karlen (1973), Holocene climate variations - their pattern and possible cause, *Quaternary Research*, *3*, 155-205.

Divine, D. V., N. Koc, E. Isaksson, S. Nielsen, X. Crosta, and F. Godtliebsen (2010), Holocene Antarctic climate variability from ice and marine sediment cores: Insights on ocean-atmosphere interaction, *Quaternary Science Reviews*, *29*, 303-312.

Douglass, D. C., B. S. Singer, M. R. Kaplan, R. P. Ackert, D. M. Michelson, and M. W. Caffee (2005), Evidence of early Holocene glacial advance in southern South America from cosmogenic surface exposure dating, *Geology*, *33*, 237-240.

Fairbanks, R. G. (1989), A 17,000 year glacio-eustatic sea-level record – influence of glacial melting rates on the Younger Dryas Event and deep-ocean circulation, *Nature*, *342*(6250), 637-642.

Garreaud, R. D. (2007), Precipitation and circulation covariability in the extratropics, *Journal of Climate*, *20*(18), 4789-4797.

Glasser, N. F., S. Harrison, V. Winchester, and M. Aniya (2004), Late Pleistocene and Holocene palaeoclimate and glacier fluctuations in Patagonia, *Global and Planetary Change*, *43*(1-2), 79-101.

González, H. E., M. J. Calderón, L. Castro, A. Clement, L. A. Cuevas, G. Daneri, J. L. Iriarte, L. Lizárraga, R. Martínez, E. Menschel, N. Silva, C. Carrasco, C. Valenzuela, C. A. Vargas, and C. Molinet (2010), Primary production and plankton dynamics in the Reloncaví Fjord and the Interior Sea of Chiloé, Northern Patagonia, Chile, *Marine Ecology Progress Series*, *402*, 13-30.

Grimalt, J. O., J. Rullkötter, M. Sicre, R. Summons, J. Farrington, H. R. Harvey, M. Goñi, and K. Sawada (2000), Modifications of the C37 alkenone and alkenoate composition in the water column and sediment: Possible implications for sea surface temperature

estimates in paleoceanography, *Geochemistry, Geophysics, Geosystems*, *1*(11), doi:10.1029/2000GC000053.

Hodell, D. A., S. L. Kanfoush, A. Shemesh, X. Crosta, C. D. Charles, and T. P. Guilderson (2001), Abrupt cooling of Antarctic surface waters and sea ice expansion in the South Atlantic sector of the Southern Ocean at 5000 cal yr B.P., *Quaternary Research*, *56*, 191-198.

Iizuka, y., T. Hondoh, and Y. Fujii (2008), Antarctic sea ice extent during the Holocene reconstructed from inland ince core evidence, *Journal of Geophysical Research*, *113, D15114, doi:10.1029/2007JD009326*.

Ingram, B. L., and J. R. Southon (1996), Reservoir ages in eastern Pacific coastal and estuarine waters, *Radiocarbon*, *38*(3), 573-582.

Iriarte, J. L., J. C. Uribe, and C. Valladares (1993), BIOMASS OF SIZE-FRACTIONATED PHYTOPLANKTON DURING THE SPRING-SUMMER SEASON IN SOUTHERN CHILE, *Botanica Marina*, *36*(5), 443-450.

Iriarte, J. L., A. Kusch, J. Osses, and M. Ruiz (2001), Phytoplankton biomass in the sub-Antarctic area of the Straits of Magellan (53 degrees S), Chile during spring-summer 1997/1998, *Polar Biology*, *24*(3), 154-162.

Jenny, B., B. L. Valero-Garces, R. Villa-Martinez, R. Urrutia, M. Geyh, and H. Veit (2002), Early to Mid-Holocene Aridity in Central Chile and the Southern Westerlies: The Laguna Aculeo Record (34(deg)S), *Quaternary Research*, *58*(2), 160-170.

Kaiser, J., F. Lamy, and D. Hebbeln (2005), A 70-kyr sea surface temperature record off southern Chile (ODP Site 1233). *Paleoceanography*, *20*, PA4009, doi:4010.1029/2005PA001146.

Kaiser, J., E. Schefuss, F. Lamy, M. Mohtadi, and D. Hebbeln (2008), Glacial to Holocene changes in sea surface temperature and coastal vegetation in north central Chile: high versus low latitude forcing, *Quaternary Science Reviews*, *27*(21-22), 2064-2075.

Kilian, R., F. Lamy, H. Arz, O. Baeza, S. Breuer, T. Steinke, M. Caniupán, A. Mangini, C. Schneider, and M. Möller (submitted), Accumulation sensitivity of Holocene glaciers in the superhumid southernmost Andes.

Kim, J. H., R. R. Schneider, D. Hebbeln, P. J. Muller, and G. Wefer (2002), Last deglacial sea-surface temperature evolution in the Southeast Pacific compared to climate changes on the South American continent, *Quaternary Science Reviews*, *21*(18-19), 2085-2097.

Lamy, F., D. Hebbeln, and G. Wefer (1999), High-resolution marine record of climatic change in mid- latitude Chile during the last 28,000 years based on terrigenous sediment parameters, *Quaternary Research*, *51*(1), 83-93.

Lamy, F., C. Ruhlemann, D. Hebbeln, and G. Wefer (2002), High- and low-latitude climate control on the position of the southern Peru-Chile Current during the Holocene, *Paleoceanography*, *17*(2), art. no.-1028.

Lamy, F., R. Kilian, H. W. Arz, J. P. Francois, J. Kaiser, M. Prange, and T. Steinke (2010), Holocene changes in the position and intensity of the southern westerly wind belt, *Nature Geoscience*, *3*, 695-699.

Locarnini, R. A., A. V. Mishonov, J. I. Antonov, T. P. Boyer, and H. E. Garcia (2010), World Ocean Atlas 2009, Volumen 1: Temperature, in *NOAA Atlas NESDIS 68*, edited by S. Levitus, p. 184, U.S. Goberment Printing Office, Washington, D.C., .

Magazzu, G., S. Panella, and F. Decembrini (1996), Seasonal variability of fractionated phytoplankton, biomass and primary production in the Straits of Magellan, *Journal of Marine Systems*, *9*(3-4), 249-267.

Maldonado, A., and C. Villagran (2002), Paleoenvironmental Changes in the Semiarid Coast of Chile (~32(deg)S) during the Last 6200 cal Years Inferred from a Swamp-Forest Pollen Record, *Quaternary Research*, *58*(2), 130-138.

Masson-Delmotte, V., B. Stenni, and J. Jouyel (2004), Common millennial-scale variability of Antarctic and Southern Ocean temperatures during the past 5000 years reconstructed from the EPICA Dome C ice core, *The Holocene*, *14*, 145-151.

Masson, V., F. Vimeux, J. Jouzel, V. Morgan, M. Delmotte, P. Ciais, C. Hammer, S. Johnsen, V. Y.

Lipenkov, E. Mosley-Thompson, J. R. Petit, E. J. Steig, M. Stievenard, and R. Vaikmae (2000), Holocene climate variability in Antarctica based on 11 ice-core isotopic records, *Quaternary Research*, *54*(3), 348-358.

Mayewski, P. A., E. E. Rohling, J. C. Stager, W. Karlén, K. A. Maasch, L. D. Meeker, E. A. Meyerson, F. Gasse, S. van Kreveld, K. Holmgren, L. Lee-Thorp, G. Rosqvist, F. Rack, M. Staubwasser, R. Schneider, and E. Steig (2004), Holocene climate variability, *Quaternary Research*, *62*, 243-255.

Mohtadi, M., O. Romero, J. Kaiser, and D. Hebbeln (2007), Cooling of the southern high latitudes during the Medieval Period and its effect on ENSO, *Quaternary Science Reviews*, *26*, 1055-1066.

Moros, M., P. De Deckker, E. Jansen, K. Perner, and R. Telford (2009), Holocene climate variability in the Southern Ocean recorded in a deep-sea sediment core off South Australia, *Quaternary Science Reviews*, *28*, 1932-1940.

Müller, P. J., G. Kirst, G. Ruhland, I. von Storch, and A. Rosell-Mele (1998), Calibration of the alkenone paleotemperature index UK'37 based on core-tops from the eastern South Atlantic and the global ocean (60°N-60°S). *Geochimica et Cosmochimica Acta*, *62*, 1757-1772.

Neukom, R., J. Luterbacher, R. Villalba, M. Küttel, D. Frank, P. D. Jones, M. Grosjean, J. Esper, L. Lopez, and H. Wanner (2010), Multi-centennial summer and winter precipitation variability in southern South America, *Geophysical Research Letters*, *37*, doi:10.1029/2010GL043680.

Nielsen, S., N. Koc, and X. Crosta (2004), Holocene climate in the Atlantic sector of the Southern Ocean: Controlled by insolation or oceanic circulation?, *Geology*, *32*(4), 317-320.

O'Brien, S. R., P. A. Mayewski, L. D. Meeker, D. A. Meese, M. S. Twickler, and S. I. Whitlow (1995), Complexity of Holocene Climate as Reconstructed from Greenland Ice Core, *Science*, *270*, 1962-1964.

Palma, S., and N. Silva (2004), Distribution of siphonophores, chaetognaths, euphausiids and oceanographic conditions in the fjords and channels of southern Chile, *Deep-Sea Research Part II-Topical Studies in Oceanography*, *51*(6-9), 513-535.

Prahl, F. G., and S. G. Wakeham (1987), Calibration of unsaturation patterns in long-chain ketone compositions for paleotemperature assessment, *Nature*, *330*, 367-369.

Prahl, F. G., L. A. Muehhausen, and D. L. Zahnle (1988), Further evaluation of long-chain alkenones as indicators of paleoceanographic conditions, *Geochimica et Cosmochimica Acta*, *52*, 2303-2310.

Prahl, F. G., J.-F. Rontani, N. Zabeti, S. E. Walinsky, and M. A. Sparrow (2010), Systematic pattern in UK'37 - Temperature residuals for surface sediments from high latitude and other oceanographic settings, *Geochimica et Cosmochimica Acta*, *74*, 131-143.

Reimer, P. J., M. G. L. Baillie, E. Bard, A. Bayliss, J. W. Beck, P. G. Blackwell, C. B. Ramsey, C. E. Buck, G. S. Burr, R. L. Edwards, M. Friedrich, P. M. Grootes, T. P. Guilderson, I. Hajdas, T. J. Heaton, A. G. Hogg, K. A. Hughen, K. F. Kaiser, B. Kromer, F. G. McCormac, S. W. Manning, R. W. Reimer, D. A. Richards, J. R. Southon, S. Talamo, C. S. M. Turney, J. van der Plicht, and C. E. Weyhenmeye (2009), INTCAL09 AND MARINE09 RADIOCARBON AGE CALIBRATION CURVES, 0-50,000 YEARS CAL BP, *Radiocarbon*, *51*(4), 1111-1150.

Schneider, C., M. Glaser, R. Kilian, A. Santana, N. Butorovic, and G. Casassa (2003), Weather observations across the Southern Andes at 53(degrees)S, *Physical Geography*, *24*(2), 97-119.

Sepúlveda, J., S. Pantoja, K. A. Hughen, S. Bertrand, D. Figueroa, T. León, J. Drenzek, and C. Lange (2009), Late Holocene sea-surface temperature and precipitation variability in northern Patagonia, Chile (Jacaf Fjord, 44ºS), *Quaternary Research*, *72*, 400-409.

Sievers, H. A., and N. Silva (2008), Water masses and circulation in austral Chilean channels and fjords, in *Progress in the oceanographic knowledge of Chilean interior waters, from Puerto Montt to Cape Horn*, edited by N. Silva and S. Palma, pp. 53-, Comité Oceanográfico Nacional - Pontificia Universidad Católica de Valparaíso.

Sikes, E. L., J. K. Volkman, L. G. Robertson, and J.-J. Pichon (1997), Alkenones and alkenes in surface waters and sediments of the Southern Ocean: Implications for paleotemperature estimation in polar regions, *Geochimica et Cosmochimica Acta*, *61*(7), 1495-1505.

Silva, N., C. Calvete, and H. A. Sievers (1998), Masas de agua y circulación general para algunos canales australes chilenos entre Puerto Montt y laguna San Rafael (Crucero CIMAR-Fiordo 1), *Ciencia y Tecnologia del Mar*, *21*, 17-48.

Silva, N., and C. Calvete (2002), Physical and chemical oceanographic features of southern Chilean inlets between Penas Gulf and Magellan Strait (CIMAR-FIORDO 2 CRUISE), *Ciencia y Tecnologia del Mar*, *25*(1), 23-28.

Strub, P. T., J. M. Mesias, V. Montecino, J. Ruttlant, and S. Salinas (1998), Coastal ocean circulation off Western South America., in *The global coastal ocean. Regional studies and syntheses*, edited by A. R. Robinson and K. H. Brink, pp. 273-315, Wiley, New York.

Villa-Martinez, R., C. Villagran, and B. Jenny (2003), The last 7500 cal yr BP of westerly rainfall in Central Chile inferred from a high-resolution pollen record from Laguna Aculeo (34 degrees S), *Quaternary Research*, *60*(3), 284-293.

Villa-Martinez, R., and P. I. Moreno (2007), Pollen evidence for variations in the southern margin of the westerly winds in SW Patagonia over the last 12,600 years, *Quaternary Research*, *68*(3), 400-409.

Villagrán, C., and J. Varela (1990), Palynological evidence for increased aridity on the Central Chilean coast during the Holocene, *Quaternary Research*, *34*, 198-207.

Wanner, H., J. Beer, J. Bütikofer, T. Crowley, U. Cubasch, J. Flückiger, H. Goose, M. Grosjean, F. Joos, J. Kaplan, M. Küttel, S. A. Müller, I. Prentice, O. Solomina, T. F. Stocker, P. Tarasov, M. Wagner, and M. Widmann (2008), Mid- to Late Holocene climate change: an overview, *Quaternary Science Reviews*, *27*, 1791-1828.

4.3 Accumulation-sensitivity of Holocene glacier in the superhumid southernmost Andes

R. Kilian[1], F. Lamy[2], M. Caniupán[2], H. Arz[3], O. Baeza[1], S. Breuer[1], M. Möller[4], C. Schneider[4], A. Mangini[5]

[1]Department of Geology, FB VI, University of Trier, 54286 Trier, Germany
[2] Alfred Wegener Institute for Polar and Marine Research, Bremerhaven, Am Handelshafen 12, 27570 Bremerhaven, Germany
[3] Leibniz Institute for Baltic Sea Research Warnemünde (IOW), Seestraße 15, D-18119 Rostock-Warnemünde, Germany
[4] Department of Geography, RWTH Aachen University Wüllnerstraße 5 52056 Aachen, Germany
[5] Heidelberger Akademie of Science der Wissenschaften, Universität Heidelberg Im Neuenheimer Feld 229, D-69120 Heidelberg, Germany
* To whom correspondence should be addressed. E-mail: kilian@uni-trier.de

To be submitted to Nature Geoscience

Abstract

Recent glacier retreat has been primarily ascribed to global warming through enhanced summer ablation. However, the mass balance of glaciers depends also on snow accumulation especially in temperate mountain ranges. For the Holocene, the interplay of these driving mechanisms is still not well understood. We present new terrestrial and marine records for timing and extent of Holocene glacier changes in the superhumid southernmost Andes. Forcing mechanisms were evaluated by applying a simple glacier mass balance model using new regional temperature and precipitation reconstructions. We show that the most extended glacier advances were driven by strongly increased accumulation and only minor temperature changes. Therefore, Holocene glacier advances in superhumid environments may also occur during relatively warm periods with enhanced snow accumulation.

On a global scale, Holocene glacier fluctuations are often ascribed to temperature and related ablation changes (*Anderson and Mackintosh*, 2006), especially during the past few centuries (*Oerlemans*, 2005). However, other studies and glacier mass balance modelling suggests that winter snow accumulation and thus precipitation related to atmospheric circulation changes plays a major role in controlling Late Quaternary glacier advances in temperate regions such as New

Zealand (*Rother and Shulmeister*, 2005; *Schaefer et al.*, 2009) and Norway (*Nesje et al.*, 2008). The interplay of both factors determines the equilibrium line altitude (ELA) above which the glacier catchment is situated. Reconstructions of the ELA and related glacier changes require well dated regional temperature and precipitation records that are often not available (e.g. *Winkler and Matthews, 2010*). In addition, other local non-climatic factors may influence glacier flow dynamics and thus affect glacier lengths. Despite these complex influences, Holocene glacier fluctuations from different mountain regions including the Alps (e.g. *Ivy-Ochs et al.*, 2009), North America (*Clague et al.*, 2009), New Zealand (*Rother and Shulmeister*, 2005; *Anderson and Mackintosh*, 2006; *Schaefer et al.*, 2009), the Peruvian (*Licciardi et al.*, 2009) and Patagonian Andes (*Mercer*, 1982; *Glasser et al.*, 2004; *Douglass et al.*, 2005), and Antarctica (*Hall*, 2009) have been used to depict climate linkages on regional and global scales (Fig. S1). However, a more profound knowledge of the complex glacier-climate linkage is urgently required in order to improve our estimates of future glacier response under global warming scenarios (*Lemke et al.*, 2007), particularly in areas where accumulation changes play an important role.

One such area are the superhumid Southern Andes where little glaciological and paleoclimatological data have been provided so far. Nevertheless, it has been previously hypothesized that glaciers located at the windward side of the Andes are primarily accumulation-driven and glaciers on the leeward, less-humid side are mainly ablation-controlled (*Warren and Sugden*, 1993). Most available glaciological data comes from the less-humid eastern side of the Andes north of 48°S, because very few moraines are preserved on-land in the western fjord system (*Glasser et al.*, 2004). Furthermore, the dating of advances is problematic, since it is based either on ^{14}C minimum ages (through dating of soil or plant relicts on top of moraines) and/or cosmogenic exposure dates with age uncertainties of several hundred years (e.g. *Douglass et al.*, 2005). More exact dendrochronological methods have only been applied for the most recent advances during the Little Ice Age (LIA) (e.g *Koch and Kilian*, 2005; *Masiokas et al.*, 2009; *Neukom et al.*, 2010). Besides the weak age control, the discussion of the driving mechanisms of these regional advances is hampered by few paleoclimatic background information, especially concerning regional temperature and precipitation changes.

Here we present, for the first time, continuous and well-dated Holocene fjord sediment records of glacial clay input as an integrated signal of glacier advances (A1-A6; Fig. 2 and 3) and their duration in the Southern Andes (~50°-53°S). These records are complemented by mapping and dating of individual moraines focusing on the most extended Neoglacial advances over the past ~5.5 thousand years before present (kyr BP). We compare data from three different glacier systems including the Southern

Patagonian Ice Field (SPIF), the Gran Campo Nevado Ice Field (GCN) and smaller glaciers in vicinity of Santa Ines Island (Fig. 1). Our sites are located within the present day core of the Southern Westerly wind belt (SWW) (Fig. 1) characterised by very high whole year-round precipitation (4.0-10.0 m/yr) (*Schneider et al.*, 2003) and extremely high snow accumulation even during summer at elevations of >800–1000 m above sea level (see material and methods; supporting online material) (Fig. S2). Paleoclimatic background information includes a new alkenone-based fjord temperature record and a speleothem-based precipitation reconstruction (*Schimpf et al., 2011*).

Our continuous proxy records for glacier extent changes are based on two well-dated fjord sediment cores (MD07-3124 and PALM-2), situated 90 and 35 km, respectively, west of the present-day glaciers tongues along their discharge pathways of glacial clay (Fig. 1). These sediment cores therefore provide an integrated signal of glacier changes at the western side of the SPIF (~1600 km^2 catchment) (*Casassa et al.*, 2000) and the GCN (200 km^2) (*Schneider et al.*, 2007). We utilize changes in the chemical composition of the predominantly fine-grained terrigenous sediments as proxies for long-distance transport and deposition of glacial clay throughout the Holocene (Figs. 2 and 3). Glacial clay from the granitoid catchment of the SPIF and GCN glaciers is illite-rich and thus characterised by high K/Si ratios. Additionally, allochthonous glacial clay can be distinguished by higher Al/Si ratios mirroring enhanced clay/silt ratios. The timing, extent, and duration of Neoglacial Holocene glacier advances is confirmed through a number of well-dated proximal sediment and speleothem records in four selected areas (Fig. 1) (see material and methods; supporting online material). From north to south, these include the Peel Fjord (located close to the SPIF; Figs. S3 and S4), the western (Figs. S5-S7) as well as eastern (Fig. S8) sides of the GCN, and the smaller Arthuro Mountain glacier system with a ~12 km^2 catchment on the Santa Ines Island at ~53°S (Fig. S9 and S10). In all proximal areas, extensive terrestrial and subaquatic (bathymetrical and echosound data-based) mapping provides detailed information on the distribution of moraines and glacial sediments.

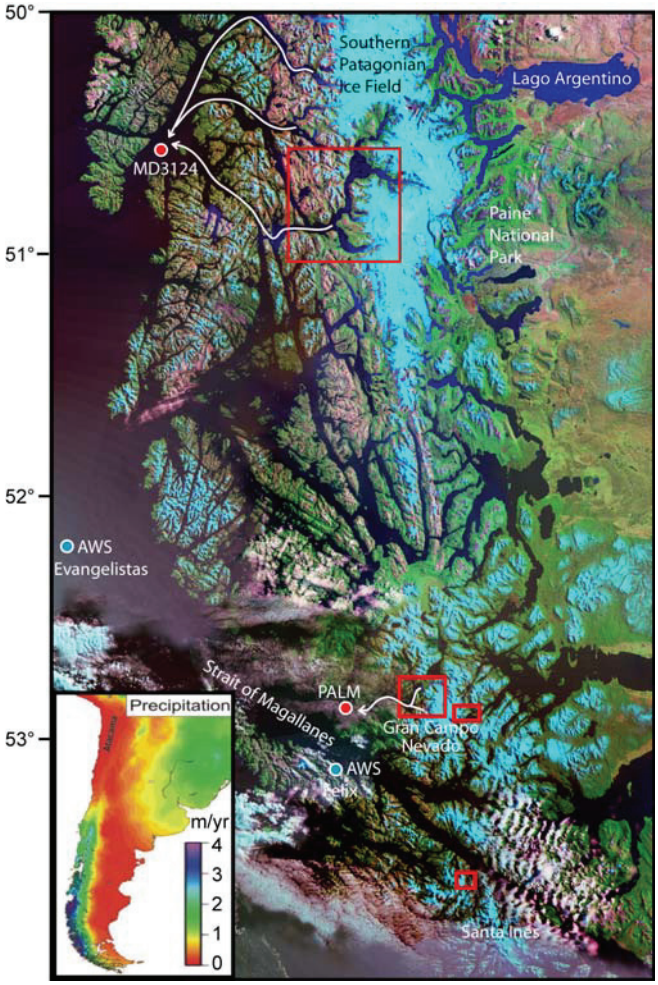

Figure 1. Area of investigation in the southern Andes between 50° to 54°S where the highest present day annual precipitation (inset map after *New et al.*, 2002) marks the core of the Southern Westerly wind belt. The sediment cores MD07-3124 and PALM2 with related possible pathways of Andean glacial clay (white arrows) are indicated. The four areas of detailed investigations including the Holocene moraine belts are marked (Figs. S3, S5, S8, S9). The locations of the Automatic Weather Stations (AWS; Evangelistas and Felix) used to evaluate the glacier-climate relationship of the last 100 years are also shown (Fig. S12).

The best documented and most extended Holocene glacier advance A4 occurred from ~2.3 to 2.2 kyr BP. This advance overran all older less extended Holocene moraines and e.g. abraded the sediments of Lake Arthuro on Santa Ines Island (Fig. S9) and from a shallow fjord basin along the Peel fjord (Fig. S3). The beginning of A4 was precisely dated by the stalagtite GC1, which was removed from the roof of an open cave within the GCN moraine belt when an advancing glacier entered the cave. This stalagtite was growing continuously from 8.0 to 2.35 kyr BP (see material and methods; supporting online material) (Fig. S7). Further evidence comes from sediment core FART1 which has been recovered from a fjord ~6 km east of Arthuro Mountain close to the A4 moraine limit (Fig. S9). This core records organic-rich

sedimentation since at least ~11 kyr BP, only interrupted by a white glacial clay-bearing interval related to the A4 advance (Fig. S10). The end of A4 is documented in sediment core PEEL-1 that shows the transition from coarse glacial detritus and overlain organic-free glacial clay towards more organic-rich sedimentation at ~2.2 kyr BP lasting until the present (Fig. 3A). Our distal sediment cores MD07-3124 and PALM-2 show a sharp and pronounced increase in glacial clay deposition during A4 (Fig. 2A-D and Fig. 3C-D). Coeval advances were recognized at many other southern Andean sites (*Mercer*, 1982; *Glasser et al.*, 2004).

Together with the continuous organic sedimentation at the FART-1 site (Santa Ines Island; Fig. S10), the mapping of moraine belts in all working areas (Figs. S3, S5, S8, and S9), and the continuously growing peat bogs located close the A4 moraines at the GCN (see material and methods; supporting online material) (Fig. S8) clearly show that all earlier Holocene glacier advances were less extended than A4 and probably did not extended much further than modern glaciers. Therefore, we have to rely on our distal glacial clay records (MD07-3124 and PALM-2) in order to derive early Holocene glacier advances. Both cores extend to the early Holocene and reveal a pronounced long-term trend of increasing glacial clay contents culminating in the late Holocene suggesting generally increasing glaciers in the course of the Holocene (Fig. 2) (see material and methods; supporting online material). A first centennial-scale increase in glacial clay contents occurs in both distal cores from ~9 to 8 kyr BP (A1; Fig. 2A-D), coeval with a cosmogenic nuclide-dated glacier advance at the Northern Patagonian Ice Field (*Douglass et al.*, 2005). The Mid-Holocene increase of glacial clay from 5.5 to 4.8 kyr BP marks A2, the first relatively limited Neoglacial glacier advance. This advance probably caused the bursting of moraines which dammed the proglacial Lake Lengua at eastern GCN (dated to 5.4 kyr BP (see material and methods; supporting online material). A2 was registered also at several other glaciers of Patagonia (Fig. 3B) (*Glasser et al.*, 2004) and Antarctica (*Hall*, 2009). Thereafter, a second Neoglacial advance (A3) is indicated in both distal fjord sediment cores from ~4.1 to 3.8 kyr BP, probably corresponding to glacier advances minimum ages of 3.6 kyr BP reported elsewhere in the Southern Andes (*Glasser et al.*, 2004).

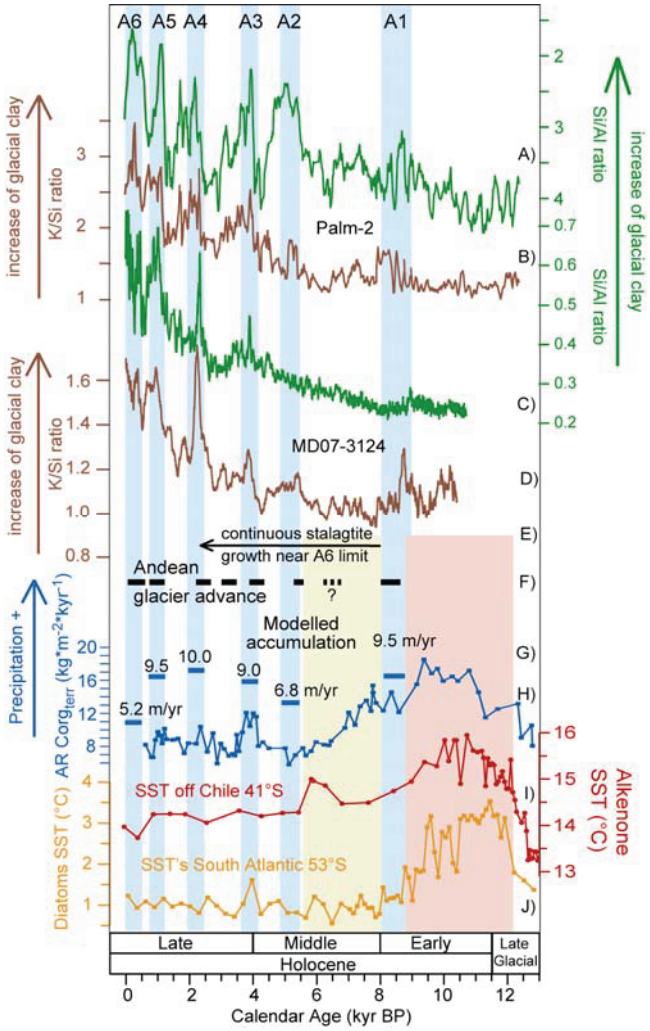

Figure 2. Holocene glacier fluctuations in the Southern Andes and relevant paleoclimate background information. (A and B) Al/Si and K/Si ratios of core PALM-2. A1 to A6 define Holocene glacier advances. (C and D) Al/Si and K/Si ratios of core MD07-3124. (E) Period of stalagmite growth within the Holocene moraine belt as an indicator for limited glacier extent. (F) Reported advances from other Southern Andean sites (20) (Fig. S1). (G) Modelled accumulation during glacier advances A1-A6. (H) Terrestrial organic carbon record as a proxy for precipitation; core TML1 (53°S) (24). (I) Sea surface temperature record (SST) from the Chilean margin (28). (J) SST record from the South Atlantic (31).

After the most extended Holocene glacier advance A4 (discussed above), two further advances occurred during the past ~2 kyr (A5 and A6; Figs. 2 and 3) that are documented in both distal fjord cores and the proximal sediment record PEEL-1. This core shows an increased glacial clay signature from ~1.1 to 0.87 kyr BP (A5; Fig. 3A) during the globally known Medieval Warm Period (MWP). Moraine minimum ages of around 1.0 to 0.8 kyr BP reported from the SPIF region (*Mercer*, 1982; *Glasser et al.*, 2004; *Masiokas et al.*, 2009) may be related to A5. A second glacial clay peak in PEEL-1 indicates the A6 advance. It starts abruptly at ~0.65 kyr BP, reaches a maximum

between 0.55 to 0.45 kyr BP and ends with a successive retreat until the last century. The A6 maximum and retreat phase coincides with the Little Ice Age (LIA) moraines which have been mapped and dated in the GCN area (*Kilian et al.*, 2007). A similar timing of the LIA advances was found further north in the Southern Andes (*Mercer*, 1982; *Glasser et al.*, 2004; *Douglass et al.*, 2005; *Masiokas et al.*, 2009).

.

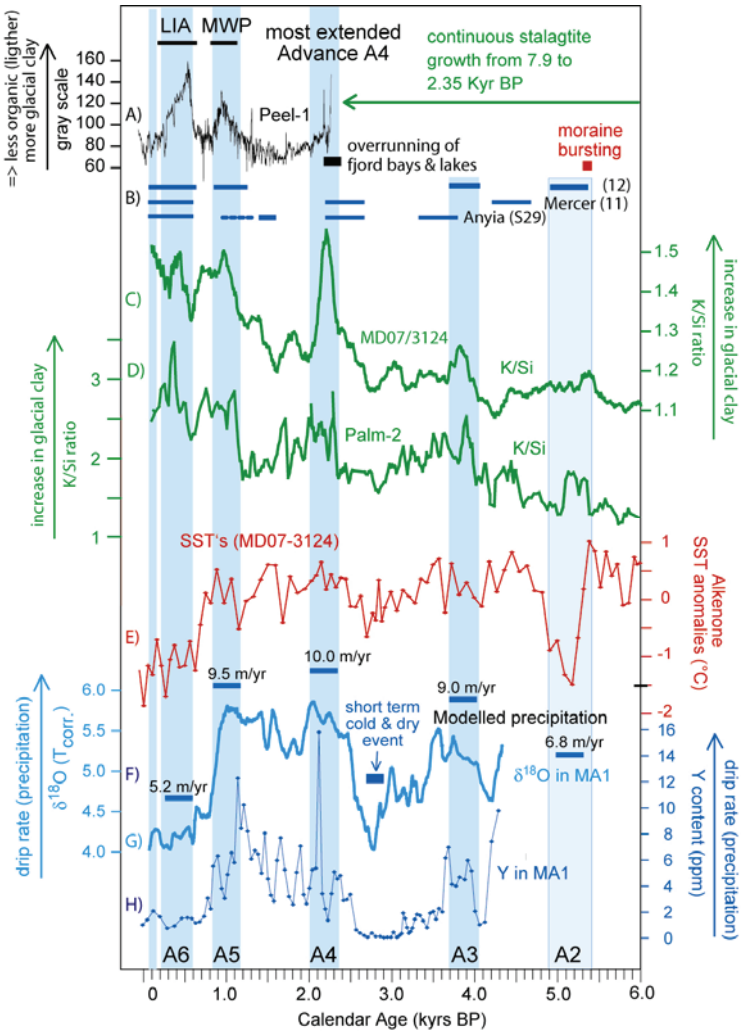

Figure 3. Glacier advances, paleoclimate records, and glacier modelling results for the Neoglacial. (A) Gray-scale record of core PEEL-1 as a proxy for glacial clay input and the period of stalagmite growth within the Holocene moraine belt as an indicator for limited glacier extent. (B) Reported advances from other Southern Andean sites (see material and methods; supporting online material) (Fig. S1). (C) Al/Si ratios in core MD07-3124 and (D) K/Si in core PALM-2. (E) Fjord SST record from core MD07-3124 (deviation from the mean). (F) Modelled accumulation during glacier advances A1-A6. (G and H) Temperature corrected $\delta^{18}O$ and Y records of the MA1 stalagmite (52°S, GCN area) as indicators for paleoprecipitation (*Schimpf et al., 2011*).

Our results from different sized glacial catchments (12, 80 and 1600 km^2) show coeval glacier advances suggesting a similar short response time to changes in the distinct glacier mass balance systems. To evaluate the accumulation versus temperature forcing for the individual Holocene glacier advances (A1-A6), we use a degree-day glacier mass balance model (*Moller and Schneider, 2010*) which was adapted and calibrated using recent glacier fluctuations at the GCN (see material and methods; supporting online material). The model was run with average temperatures over the individual glacier advance periods using the alkenone-based SST record from core MD07-3124 for A2-A6 and ODP Site 1233 (*Kaiser et al.*, 2005) for A1. The paleo summer SST's were linearly adjusted to regional present day summer and average annual air temperatures (see material and methods; supporting online material). The modelled accumulation values for reasonable positive mass balances (see material and methods; supporting online material) are compared to regional precipitation reconstructions using trace element (Y content) and temperature-corrected $\delta^{18}O$ data (*Schimpf et al., 2011*) from the MA1 cave located close to GCN for the Neoglacial advances (Fig. 3) and sedimentological precipitation proxies for A1 (Fig. 2H) (*Lamy et al.*, 2010).

The oldest A1 occurred after the early Holocene warm and more humid period (*Lamy et al.*, 2010) when regional temperature dropped around 2°C (similar to the Neoglacial temperature average; Fig. 3I and 3J) (*Kaiser et al.*, 2005) but precipitation remained comparatively high (Fig. 2H). This is consistent with our mass balance model indicating 9.5 m/yr accumulation (Fig. S11). Between A1 and the first limited Neoglacial advance A2, glaciers retreated due to further decreasing precipitation (*Lamy et al.*, 2010) while temperatures did not change significantly. A2 occurred when the temperature decreased by ~2°C (Fig. 3E) resulting in relatively low model accumulation rates of 6.8 m/yr.

Advances A3 to A5 occurred during relatively warm phases of the Neoglacial which were characterised by extraordinarily high precipitation especially valid for the most extended Neoglacial advance A4 (Fig. 3). The modelled snow accumulation is also very high (9.0-10.0 m/yr compared to present day values of 4-4.5 m/yr). In contrast to these advances, A6 of the LIA is primarily temperature-driven. Our temperature record shows a preceding cooling of ~1.5°C at around 0.75 kyr BP coinciding with a substantial decrease in precipitation (Fig. 3G and 3H). This is consistent with the lowest modelled precipitation of 5.2 m/yr. A further decrease in precipitation after 0.55 kyr and lasting until the last decades (Fig. 3G and S2) is paralleling a systematic glacier retreat (*Koch and Kilian*, 2005; *Masiokas et al.*, 2009), whereas Northern Hemisphere (NH) LIA advances mostly culminate around AD 1850 (e.g. *Oerlemans*, 2005; *Ivy-Ochs et al.*, 2009). In contrast to NH glacier reconstructions (*Oerlemans*, 2005; *Nesje et al.*, 2008; *Ivy-Ochs et al.*, 2009) , LIA advances in southern Chile were not the most extended of

the Holocene and show distinct internal pattern on a centennial scale (Fig. S6). A distinct behaviour is also obvious for the second globally important Neoglacial advance period of ~3.3-2.5 kyr BP (*Bond et al.*, 2001; *Nesje et al.*, 2008; *Clague et al.*, 2009; *Ivy-Ochs et al.*, 2009). Though a slight temperature depression is recorded in core MD07-3124 and cold perturbations have been reported elsewhere in Patagonia (*van Geel et al.*, 2000), glacier advances did not occur due to significantly reduced precipitation.

A high precipitation-related sensitivity of the glaciers in our study area is also obvious from more precise weather and glacier length records of the last 100 years: A continuous ~20 % decrease in precipitation was registered from AD 1900 to 1980 at regional weather stations and in our proxy records (Fig. 1; Fig. S12) (see material and methods; supporting online material) which is correlated with a significant glacier retreat around the GCN (*Koch and Kilian*, 2005; *Schneider et al.*, 2007) while the temperature did not change significantly until AD 1960. However, from 1960 to 2005, a temperature increase of 0.2 to 0.5 °C contributed to the glacier retreat. After AD 1990, a significant increase in precipitation as e.g. registered at station Evangelistas (Fig. S12) can explain the recent glacier growth at higher elevations of the GCN Ice Cap (see material and methods; supporting online material) and glacier advances in the Cordillera Darwin since AD 2007 (*Masiokas et al.*, 2009).

Taken together, our results show that the glacier mass balance of very humid and westerly wind-influenced maritime mountain ranges is highly sensitive to accumulation changes. The overall positive correlation of Neoglacial temperature and precipitation shown in Fig. 3 for the Southern Andes indicates that future global warming with enhanced precipitation could cause regional re-advances, similar to those observed during warm phases such as the MWP.

Acknowledgements

M. Arevalo is acknowledged for technical and logistic support during various campaigns with RV Gran Campo II. Analytical support was given by Birgit Plessen and Norbert Nowaczyk. Financial support was obtained by DFG grants AR 367/6-1, Ki-456/9-1; K-456/10-1, La1273/3-2, and La1273/5-1, the GFZ-Potsdam, and the AWI-Bremerhaven.

References

Anderson, B., and A. Mackintosh (2006), Temperature change is the major driver of late-glacial and Holocene glacier fluctuations in New Zealand, *Geology*, *34*(2), 121-124.

Bianchi, C., and R. Gersonde (2004), Climate evolution at the last deglaciation: The role of the Southern Ocean, *Earth and Planetary Science Letters*, *228*(3-4), 407-424.

Bond, G., B. Kromer, J. Beer, R. Muscheler, M. N. Evans, W. Showers, S. Hoffmann, R. Lotti-Bond, I. Hajdas, and G. Bonani (2001), Persistent solar influence on north Atlantic climate during the Holocene, *Science*, *294*(5549), 2130-2136.

Casassa, G., A. Rivera, M. Aniya, and R. Naruse (2000), Características glaciológicas del campo de Hielo Patagónico Sur, *Anales del Instituto de la Patagonia, Serie Ciencias Naturales*, *28*, 5-22.

Clague, J. J., B. Menounos, G. Osborn, B. H. Luckman, and J. Koch (2009), Nomenclature and resolution in Holocene glacial chronologies, *Quaternary Science Reviews*, *28*(21-22), 2231-2238.

Douglass, D. C., B. S. Singer, M. R. Kaplan, R. P. Ackert, D. M. Mickelson, and M. W. Caffee (2005), Evidence of early Holocene glacial advances in southern South America from cosmogenic surface-exposure dating, *Geology*, *33*(3), 237-240.

Glasser, N. F., S. Harrison, V. Winchester, and M. Aniya (2004), Late Pleistocene and Holocene palaeoclimate and glacier fluctuations in Patagonia, *Global and Planetary Change*, *43*(1-2), 79-101.

Hall, B. L. (2009), Holocene glacial history of Antarctica and the sub-Antarctic islands, *Quaternary Science Reviews*, *28*(21-22), 2213-2230.

Ivy-Ochs, S., H. Kerschner, M. Maisch, M. Christl, P. W. Kubik, and C. Schluchter (2009), Latest Pleistocene and Holocene glacier variations in the European Alps, *Quaternary Science Reviews*, *28*(21-22), 2137-2149.

Kaiser, J., F. Lamy, and D. Hebbeln (2005), A 70-kyr sea surface temperature record off southern Chile (ODP Site 1233). *Paleoceanography*, *20, PA4009*, doi:10.1029/2005PA001146.

Kilian, R., C. Schneider, J. Koch, M. Fesq-Martin, H. Biester, G. Casassa, M. Arevalo, G. Wendt, O. Baeza, and J. Behrmann (2007), Palaeoecological constraints on late Glacial and Holocene ice retreat in the Southern Andes (53 degrees S), *Global and Planetary Change*, *59*(1-4), 49-66.

Koch, J., and R. Kilian (2005), 'Little Ice Age' glacier fluctuations, Gran Campo Nevado, southernmost Chile, *Holocene*, *15*(1), 20-28.

Lamy, F., R. Kilian, H. W. Arz, J. P. Francois, J. Kaiser, M. Prange, and T. Steinke (2010), Holocene changes in the position and intensity of the southern westerly wind belt, *Nature Geoscience*, *3*, 695-699.

Lemke, P., J. Ren, R. B. Alley, J. Allison, J. Carrasco, G. Flato, Y. Fuji, G. Kaser, P. Mote, R. H. Thomas, and T. Zhang (2007), Observations: Changes in Snow, Ice and Frozen Ground, in *Climate Changeg 2007: The Physical Science Basis. Contribution of Working Group I to the Fourth Assessment Report of the Intergovermental Panel on Climate Change*, edited by S. Salomon, D. Qin, M. Manning, Z. Chen, M. Marquis, K. B. Averyt, M. Tignor and H. L. Miller, Cambridge, University Press, Cambridge, United Kingdon and New York, NY, USA.

Licciardi, J. M., J. M. Schaefer, J. R. Taggart, and D. C. Lund (2009), Holocene Glacier Fluctuations in the Peruvian Andes Indicate Northern Climate Linkages, *Science*, *325*(5948), 1677-1679.

Masiokas, M. H., A. Rivera, L. E. Espizua, R. Villalba, S. Delgado, and J. C. Aravena (2009), Glacier fluctuations in extratropical South America during the past 1000 years, *Palaeogeography Palaeoclimatology Palaeoecology*, *281*(3-4), 242-268.

Mercer, J. H. (1982), Holocene glacier variations in southern South America, *Striae*, *18*, 35-40.

Moller, M., and C. Schneider Calibration of glacier volume-area relations from surface extent fluctuations and application to future glacier change, *Journal of Glaciology*, *56*(195), 33-40.

Nesje, A., J. Bakke, S. O. Dahl, O. Lie, and J. A. Matthews (2008), Norwegian mountain glaciers in the past, present and future, *Global and Planetary Change*, *60*(1-2), 10-27.

Neukom, R., J. Luterbacher, R. Villalba, M. Küttel, D. Frank, P. D. Jones, M. Grosjean, H. Wanner, J. C. Aravena, D. E. Black, D. A. Christie, R. D'Arrigo, A. Larra, M. Morales, C. Soliz-Gamboa, A. Srur, R. Urrutia, and L. von Gunten (2010), Multiproxy summer and winter surface air temperature field reconstructions for southern South America covering the past centuries, *Climate Dynamics*, doi:10.1007/s00382-00010-00793-00383.

New, M., D. Lister, M. Hulme, and I. Makin (2002), A high-resolution data set of surface climate over global land areas, *Climate Research*, *21*(1), 1-25.

Oerlemans, J. (2005), Extracting a climate signal from 169 glacier records, *Science*, *308*(5722), 675-677.

Rother, H., and J. Shulmeister (2005), Synoptic climate change as a driver of late Quaternary glaciations in the mid-latitudes of the Southern Hemisphere, *climate of the Past Discussions*, *1*, 231-253.

Schaefer, J. M., G. H. Denton, M. Kaplan, A. Putnam, R. C. Finkel, D. J. A. Barrell, B. G. Andersen, R. Schwartz, A. Mackintosh, T. Chinn, and C. Schluchter (2009), High-Frequency Holocene Glacier Fluctuations in New Zealand Differ from the Northern Signature, *Science*, *324*(5927), 622-625.

Schimpf, D., R. Kilian, A. Kronz, K. Simon, C. Spotl, G. Worner, M. Deininger, and A. Mangini The significance of chemical, isotopic, and detrital components in three coeval stalagmites from the superhumid southernmost Andes (53 degrees S) as high-resolution palaeo-climate

proxies, *Quaternary Science Reviews*, *30*(3-4), 443-459.

Schneider, C., M. Glaser, R. Kilian, A. Santana, N. Butorovic, and G. Casassa (2003), Weather observations across the Southern Andes at 53(degrees)S, *Physical Geography*, *24*(2), 97-119.

Schneider, C., M. Schnirch, C. Acuna, G. Casassa, and R. Kilian (2007), Glacier inventory of the Gran Campo Nevado Ice Cap in the Southern Andes and glacier changes observed during recent decades, *Global and Planetary Change*, *59*(1-4), 87-100.

van Geel, B., C. J. Heusser, H. Renssen, and C. J. E. Schuurmans (2000), Climatic change in Chile at around 2700 BP and global evidence for solar forcing: a hypothesis, *Holocene*, *10*(5), 659-664.

Warren, C. R., and D. E. Sugden (1993), The Patagonian Icefields - A glaciological review, *Arctic and Alpine Research*, *25*(4), 316-331.

Winkler, S., and J. A. Matthews Holocene glacier chronologies: Are 'high-resolution' global and inter-hemispheric comparisons possible?, *Holocene*, *20*(7), 1137-1147.

Supporting Online Material

1. Material and methods

Sediment coring as well as sampling and mapping of Holocene glacial moraines in the fjord system of the southernmost Andes was done during twelve cruises with R/V Gran Campo II between 2002 and 2009 and during the PACHIDERME cruise in February 2007 with R/V Marion Dufresne.

Sediment echo sounding and bathymetry

Possible sites for sediment cores as well as sediment structures and thickness were investigated with the Parametric Echo Sounding System SES96 from Innomar operated on board of RV Gran Campo II. Between 2002 and 2009 various seismic profiles have been recorded in the research areas which are shown in Figs S3, S5, S8 and S9. Based on local CTD depth profiles a sound velocity correction has been applied to the seismic data. In addition, high resolution bathymetry focusing on possible subaquatic moraine systems was obtained from a multi-beam echo sounder (ELAC Seabeam 1180 provided by GEOMAR, Kiel) in the fjords to the west and east of the Gran Campo Nevado (GCN) (Figs. S5 and S8).

Sedimentological proxies

TC, TN and TOC were measured on a vario EL III CHNOS Elemental Analyzer at the Alfred Wegener Institute (AWI-Bremerhaven) and a CarloErba Elementar Analysator NC2500 at the GeoForschungsZentrum Potsdam (GFZ). Previous to the analysis, all samples were freeze-dried and homogenized using an agate mortar and pestle. Calcium carbonate was calculated according to the formula $CaCO_3$= (TC-TOC)*8.333, where TC is the total carbon content on untreated samples and TOC is the total organic carbon content on HCl-treated samples. Due to a good correlation of Corg content and sediment color in the PEEL1 core, a grey scale analyses was done from the planed sediment surface of the split cores.

The chemical composition (major elements) of the sediment cores MD07/3124 and PALM-2 was measured in situ with an Avaatech^{TM} X-Ray Flourescence (XRF) Core Scanner at the AWI-Bremerhaven. This non-destructive measuring technique allows semiquantitative geochemical analysis of split sediment cores with a resolution of 1 cm (S1). Measurements were carried out with a rhodium anode and a voltage of 10 kV and current range at 0.3 mA. No filter was used.

Alkenone-derived SST's

Long-chain alkenone (C_{37}) were extracted from 3–5 g of powdered freeze-dried sediment using solvent of decreasing polarity (MeOH, MeOH/CH_2Cl_2, CH_2Cl_2). Organic

extracted were saponificated to avoid interferences with co-eluting C_{36}-fatty acid methyl esters using 0.1 N KOH and then partitioned into Bond silica column using CH_2Cl_2 (alcanes and ketones's fraction). The fraction containing the alkenones was analyzed by gas chromatography with flame ionization detection (GC-FID). GC-FID quantification was done by an internal standard method using 2-nanodecanonce ($C_{19}H_{38}O$). Alkenone measurements on core MD07-3124 were performed at the University of Bremen, Germany.

For all samples, we determined the simplified alkenone unsaturation index ($U^{K'}_{37}$) defined by *Prahl and Wakeham* (1987). Using the calibration equation proposed by *Prahl et al*. (1988) we converted the $U^{K'}_{37}$ index into SST values ($U^{K'}_{37}$= 0.034T + 0.039). The robustness of this technique has been demonstrated with hundreds of globally dispersed surface sediment samples (*Müller et al*., 1998).

Sediment cores

MD07-3124 core

The 22.25 m long sediment core MD07/3124 was retrieved with the R/V Marion Dufresne (50°30.96'S; 74°58.33'W; 564 m water depth; site location in Fig. 1) during the PACHIDERME cruise in 2007. The site is located in the Concepción fjord around 90 km west of the southern Patagonian Ice field and it receives glacial clay from the large glaciers Eyre, Falcon, Penguin, Europa, Andres and Peel (~3500 km^2 catchment) (S5), depending especially on their glacier lengths and velocity. The age model is based on 16 ^{14}C ages obtained from benthic shell fragments (Table S1). The given ages are based on the SHcal04 curve considering a reservoir age of 780 years due to inflow of relatively old pacific waters to the fjord bottom. SST's were determined from alkenones as described above and represent spring to early summer paleotemperatures. We can not exclude that the paleotemperatures were slightly influenced by glacier calving and melting, since at this site melting of westward migrating ice bergs could cause lower fjord surface temperatures. However, this effect on the SST's may appear especially during winter when the westerly winds are weaker and enable a better westward migration of icebergs.

High K/Si ratios indicate high amounts of illite-rich glacial clay from the granitoid catchment of the Andean glaciers. Such clay types have been analysed along the possible sediment pathways and in Peel fjord sediments (Rolf Kilian; unpublished data). High Al/Si ratios correlate with high clay/silt ratios (and high K/Si; Fig.S1) and therefore also indicate allochthonous glacial clay. This is also documented in the very good correlation of both proxies.

The assumed reservoir age 780 years is consistent with a coeval strong temperature decrease in the well-dated alkenone-record of the Jacaf Fjord at 44°S (S6). In the MD07-3124 record the lower alkenone temperatures determined from 3.5 to 2.5 kyr BP are also consistent with a pronounced climate perturbation in the precisely U/Th-dated speleothem record from the same area (Fig. 3g, h) (S7). Furthermore, the 4.1 to 3.8 kyr BP glacial clay peak appears at the same time as in the more southern PALM-2 record where it is well-dated by the 4.18-kyr Mt. Burney tephra which has an independent age control (S8).

PALM-2 core

The 8.86 m PALM-2 core (52°47.4'S, 73°38.9'W) was retrieved with R/V Gran Campo II at 43.5 m water depth in a coastal basin between Parlamento and Merino Island around 35 km SSW of the Gran Campo Nevado (GCN) from where Holocene glacial clay plumes merge towards this site (Fig. 1). The age scale is based on the determination of four tephra layers (S8, S9, S10) and, additionally, three ^{14}C ages (Table S1). With respect to the 4.18–kyr Mt. Burney tephra layer a low reservoir age of 200 years was considered for this shallow and freshwater-rich (14-26 salinity) (S11) core site. XRF core scanning was performed at the AWI Bremerhaven in the same way as it described above for core MD07-3124 core. The autochtonous sediment component is also characterised by low clay/silt ratios, low K/Si and Al/Si ratios similar to that of core MD07-3124. Investigated sediments from the Andean glacial clay plumes derived from the GCN glaciers are characterised by relatively high K/Si and Al/Si ratios. A sharp and prominent peak in K/Si and Al/Si ratios from 2.3 to 2.2 kyr BP is consistent with the most extended Holocene glacier advance A4 documenting that glacier lengths are related to the intensity of the allochthonous glacial clay signal.

PEEL-1 core

The 6.5 m long sediment core PEEL-1 (50°50'127 S; 74°00'540 W) was retrieved with RV Gran Campo II in a 40 m deep rounded fjord basin which is connected only by a small channel with the large Peel fjord (Fig. S3, inset A). The 300 m wide bay receives terrestrial plant and siliciclastic detritus from a 4 km^2 catchment (up to 500 m elevation) as well as glacial clay which comes from glaciers (e.g. Amalia glacier), which enters the eastern Peel fjord. Eight ^{14}C ages of macroplant remains give a very good age control and a well defined age-depth relationship for core PEEL-1 (Fig. S4; Table S1). The record starts with a basal coarse clastic glacial detritus which is overlain by organic free glacial clay (Fig. S4). This documents that the bay was overrun and abrased by glacial advance A4. The ^{14}C ages indicate that this glacier retreat and the start of organic-bearing sedimentation occurred at around 2.2 kyr BP. Overlapping of surface sediments (retrieved by a 70 cm long gravity core) and two sections of a 5 m

long piston corer were controlled by highly resolved magnetic susceptibility. The C_{org} content and a highly correlated gray-scale record as well as magnetic susceptibility document changes between the autochthonous organic-rich sediment supply and the allochthonous glacial clay which is especially controlled by the extent and dynamics of the glaciers in the more eastern Peel fjord (Fig. S3). The 70 cm PEEL-2 gravity core (site position in Fig. S3) was retrieved from outside of the bay in 70 m water depth at the shore of the up to 350 m deep Peel fjord. The sediment composition of this gravity core represents the organic poor glacial clay which is derived from five large calving glaciers the eastern Peel fjord and partly entered the fjord bay of the PEEL-1 site.

FART-1 core

The FART-1 core (53°30'052 S; 72°55'421 W) was retrieved from 57 m water depth in a 700 m wide fjord bay, located around 3 km to the west of the Arthuro Mountain (Fig. S9). The site is only 1 km to the SW of lake Arthuro which was overrun by the glacier advance A4 (from 2.3 to 2.2 Kyr BP; Fig. S10). Sediments are dominated by organic- and biogenic carbonate-bearing olive-dark grey clays and silts since at least 10.6 kyr BP, only interrupted by a 10 cm thick light-grey glacial clay-rich band which is related to the nearby overrunning of lake Arthuro during advance A4 (Fig. S10).

ART-1 gravity core

Sediment echo sounding profiles across Lake Arthuro show very low sediment thicknesses (~0.5 m) above either coarse clastic glacial detritus or basement rocks (Fig. S9 Inset map). Four gravity cores were taken in this lake, all of them showing 35 to 60 cm thick organic-rich sediments above organic-free glacial clay (Fig. S10). The ART-1 core (53°29'775 S; 72°55'806 W) from 42 m water depth shows a very small tephra layer at 20.5 cm core depth which could be related to the 0.93 kyr BP eruption of Reclus volcano (Fig. S10; Moy et al 2008), consistent with calibrated radiocarbon age of a plant remain in 28 cm core depth. This indicates an approximate extrapolated age of 2.0 to 2.2 kyr BP for the basal transition from organic-rich sediment to glacial clay at 36 cm core depth.

LO-1 core

The 8.17 m long LO-1 core (52°44'59 S; 73°16'06 W; Site in Fig. S5) was retrieved with RV Gran Campo II from 83 m water depth in a 3 x 0.8 km wide fjord bay which receives frequently glacial clay/silt-bearing melt water plumes and sometimes smaller ice bergs from the large northeastern Glacier of the GCN. The complete core consists of silty-clayey sediment with very little organic material (Fig. S6: LO-1 core). A calibrated radiocarbon age of 0.73 kyr BP was obtained from macro plant remnants at 761 cm core depth indicating very high sedimentation rates of ~10 mm/yr during the LIA. Silty

to sandy layers occur from 0.5 to 0.3 kyr BP indicating more coarse clastic material which was probably introduced by advance A6.

MD07/3126-QASQ and SG1 gravity core

A 48 cm long QASQ core (MD07-3126/QASQ; 52°46.3737'S and 73°24.0606'W, obtained with R/V Marion Dufresne) and a 56 cm long gravity core (SG1; 52°46'743 S and 73°23'289 W; obtained with R/V Gran Campo II) were retrieved from a 520 m deep basin ~20 km west of the present day glacier tongues on the western side of GCN (Site locations in Fig. S5). The silty to clayey sediment is underlain by coarse clastic ice-rafted debris (IRD; visible in the echo sounding) which prohibited a deeper sediment penetration (Fig. S6). ^{210}Pb ages for the past 75 years indicate average sedimentation rates of 1.2 mm/yr (Tab. S1) and suggest that the massive IRD was deposited during the early maximum of the LIA advance A6 from 0.6 to 0.5 kyr BP, when our PEEL-1 record and other regional glacier reconstructions indicate a maximum of this advance phase (Fig. S6) (e.g. S13 and S14). Due to the strong influence of the SWW on the drift ice distribution in the fjords, frequent periods of reduced westerly winds are required to allow a westward migration (>10 km) of icebergs in order to produce the comparatively thick IRD layers. A period with weak westerlies was especially detected at around 0.55 kyr BP in sediment cores from a lake at the Paine National Park (S12).

LU1 gravity core

The 1.63 m long gravity core LU1 was retrieved from 320 m water depth in the Swett Channel (52°45'950 S; 73°19'515 W; Fig. S5) with R/V Gran Campo. The uppermost 20 cm of the clayey sediment was dated by six ^{210}Pb-ages covering the past 160 years (Tab. S1). These ages give sedimentation rates between 0.7 and 1.4 mm/yr (on average 1.2 mm/yr). Extrapolating these average sedimentation-rates down-core gives a basal age of ~1.2 kyr BP. Between 1.2 and 0.8 kyr BP, significantly increasing C/N ratios indicate higher precipitation than during the following 0.7 kyr BP (Fig. S6) which is consistent with the nearby precipitation record of the MA1 stalagmite (S7).

Modelling of glacier mass balance

A degree-day glacier mass balance model was applied in order to relate paleo-air temperatures (deduced from alkenone-based SST reconstructions for the Concepción fjord site MD07-3124 for advances A2-A6 and core ODP Site 1233 for advance A1; Fig. 1) and glacier extents of the Glaciar Noroeste, the major outlet glacier of the GCN, to plausible precipitation sums (Figs. S11 and S13). The model architecture follows Möller & Schneider (S15) who were using this model for volume-area scaling of Glaciar Noroeste. It considers glacier changes over recent decades by calculating a monthly

resolved snow/ice melt and snow accumulation for each pixel of the glacier surface. The model includes the effect of altitude by assuming constant lapse rates for temperature (-0.63 K (100 m)$^{-1}$) and precipitation (+5% /100 m^{-1}). Degree-day factors for ice (7.0 mm w.e. K^{-1} day^{-1}) and for snow (3.5 mm w.e. K^{-1} day^{-1}) are set according to Möller et al. (S16) who modeled glacier mass balance for recent decades for the complete GCN Ice Cap.

Data processing and model setup

Based on multi-temporal remote sensing data (S15 and S17) the linear relation between changes of glacier length (L) and changes of glacier area (A) based on 6 data pairs was determined to

$$A = 1.67*L \qquad (1)$$

with an explained variance of 93% (r^2=0.93). This relation also holds for Holocene glacier advances A4 and A6 as determined from the location of terminal moraines and mapped outlines of the glacier surface at that time (Fig. S5 and S13). A5 was set to a 2% shorted length compared to A6. Glacier areas of the other advance A1 to A3 can not be reconstructed, since these older moraines were overrun during younger advances A4 to A6. For these older advances reasonable shorter lengths (reduced glacial clay signature) as shown in Fig. 13 were set in equation 1. Compared to the glacier area and thickness in 1984 a moderate glacier thickening was calculated for the Holocene advances A1 to A6.

The model was run by using a five year climate record (09/2000-08/2005) from the automatic weather station Puerto de Bahamondes, approximately 5 km from Glaciar Noroeste (Fig. S5 and S18). The record of air temperature was linearly adjusted according to the temperature difference in summer temperature (DJF) between the original record at AWS Bahamondes for the time period 09/2001 to 08/2005 and the adjusted, reconstructed paleo temperature record. Pre-processing implies that the alkenone paleo-climate record for the year 2000 (-0.05 BP) was adjusted to mean summer air temperature (DJF) from NCEP/NCAR reanalysis data for the period 1998 to 2002 downscaled to the monthly air temperature record of AWS Bahamondes according to S19. A 5 year record of mass balance was modeled simulating steady-state conditions. Therefore, volume-area scaling as used in S15 was not applied. For each Holocene glacier extent the model was run multiple times in order to screen temperature variations of ±0.3 K (typical error for the paleo SST estimates) and varying annual precipitation between 4.0 m and 13.0 m (Fig. S11). Each model run consists of five years of monthly mass balance values. The first year serves as spin-up time. The mean annual sum of the mass balance from year 2 to 5 provide the resulting mass-balance state. Spin-up time is required to allow for snow cover adjustment from a

synthetic initial snow cover at time 0. As shown in S16 differences in initial snow cover does not significantly affect modeled mass balance for later years.

Model uncertainty

Uncertainties related to degree-day factors, glacier area and glacier surface altitude can be estimated by additional model runs using upper and lower limits of these variables as follows: The uncertainty includes possible errors according to S15 by allowing for an uncertainty of the degree-day factors of ±1 mm w.e. K^{-1} day^{-1} for ice surfaces and ±0.5 mm w.e. K^{-1} day^{-1} for snow surfaces. The lower and upper constraint of glacier area was taken into account assuming the 95% confidence interval according to equation 1 as upper and lower limit. Lower and upper constraints of glacier surface altitude were accounted for by distributing additional pixels over altitude in different ways, respectively increasing altitudes compared to the original digital elevation model of 1984. The model uncertainty ranging from about 0.5 to 1 m w.e. per mass balance year is dominated by the uncertainty of the degree-day factors. Therefore, the error estimate increases with higher air temperature and lower precipitation.

Further principal changes in the climate forcing of glacier mass balance cannot be ruled out. Although there are good reasons to assume that changes in radiative forcing, cloud cover, wind speed, and other variables are reflected in the air temperature record (e.g. S20), there is the possibility that fundamentally different climate conditions change the climate forcing of glacier mass balance resulting in changes of either degree day factors or lapse rates beyond the uncertainty accounted for in the error estimate of this study. The remaining uncertainty is impossible to assess in further detail without applying a physically based 3-dimensional coupled climate and glacier model including high resolution modeling of atmosphere and ice dynamics. Such kind of model would need many different precise and high resolution input data that cannot be provided. Therefore, no resilient results can be expected from such an approach.

Further Model discussion

The results show precipitation of approx. 5.2 m/yr for the Little Ice Age (LIA; advance A6) moraines (400 – 500 yr BP) which is about 130% of recent annual precipitation amounts of approx. 4.0 m (annual mean at AWS Bahamondes for the time period September 2001 – August 2005) while air temperatures based on this period were about 0.3 K lower during the formation of the LIA moraines. Lower air temperatures and higher precipitation allowed for a larger glacier area during the LIA. During the 20th century the glacier retreated well behind its LIA terminal moraines and is further retreating back, due to the fact that it is not in steady state with most recent climate forcing. Möller & Schneider (S19) show that in order to obtain zero mass balance (steady state) for the period 2001 to 2005 and for the glacier area of 1998 air

temperatures would need to be 0.2 K lower than they were actually measured at AWS Bahamondes. From these findings it must be concluded that air temperatures during the LIA were slightly lower than during most parts of the 20th century. Consequently, glacier advance during LIA was not only driven by lower air temperatures but also by significantly higher precipitation rates.

Moraines of advance of A2 and A6 can be modeled assuming an annual precipitation of about 6.8 m/yr and 5.2 m/yr, respectively, which is within the range of observed values at AWS Puerto Bahamondes (S18). For all other advances annual precipitation must have been much higher (9.0 – 10.0 m/yr, approx. 200% of the current mean) based on the extensive glacier area and fairly warm atmospheric conditions according to the alkenone fjord temperature record. Overall very large annual precipitation sums during the early and mid Holocene with significantly higher air temperatures but still large glacier extents are plausible given that warmer air masses can carry much larger amounts of precipitable water. This results in overall much higher precipitation sums and possibly higher precipitation lapse rate. Changing strength and location of the major band of west winds responsible for the high precipitation sums in the area may have further contributed to higher levels of precipitation during the Holocene (S10).

2. Supporting text

Comparison of global Holocene glacier advances

A global compilation of Holocene glacier advances is shown in Fig. S1. It includes Norway (S21), the Cascade Range of Canada (S22), Alaska (S23) and the Alps (S24) for the Northern Hemisphere (NH). These advances seem to be partly coeval with Neoglacial North Atlantic drift ice phases (Bond Cycles; S25). Advances in the Southern Hemisphere (SH) including the Peruvian (S26) and Patagonian Andes (S27, S27, S29) as well as New Zealand (S30, S31, S32) and the Antarctic Peninsula (S33) are also shown in Fig. S1. Furthermore, the advances A1 to A6 in the Southernmost Andes (50°S) deduced from our K/Si ratio record of the fjord sediment core MD07/3124 are shown. The SH advances are not so clearly linked to the NH advances. Only the LIA advances (A6) appear synchronously on a global scale. MWP advances (A5) occur also partly in both hemispheres, especially in regions with humid mountain ranges where advances may be more accumulation-driven. In both hemispheres Neoglacial advances started at around 5.5 kyr BP (S34) synchronously with an increased drift ice deposition in the South Atlantic (e.g, S35) and the first Neoglacial advance A6 in our records. In the NH the most extended Holocene advance occurred during the LIA, whereas the most extended one (A4) of the Southernmost Andes appeared from 2.3 to 2.2 kyr BP. Especially during the Bond Cycle 2 from 3.5 to 2.5 kyr BP several advances were

recorded in the NH, whereas no advance occurred in the superhumid southern Andes (probably due to very low precipitation).

Modern regional climate in the research area

At the GCN (52°45'S) mean annual temperature ranged from 5.5 to 6.3 °C between 1999 to 2008 (S18 and S19; and personal communication). Precipitation occurs throughout the year with a slight maximum during the summer months January to March (Supplement Fig. S2). Applying a local determined temperature/elevation gradient of -0.63°K/100 m (S19), >85% of the precipitation is accumulated as snow in the glacier catchment above 800 m elevation. The ELA was estimated to 750 m a.s.l. for the year 2000 (S16).

The 100-year climate records from AWS Evangelistas and Felix at 53°S (AWS locations see Fig. 1) show a continuous decrease in precipitation by about 20% between 1900 and 1980 (Fig. S12). This continuous decrease in precipitation is also indicated by Mg/Ca ratios of MA1 stalagmite (S7) and a decrease in the typically precipitation-controlled terrestrial Corg accumulation in the ^{210}Pb-dated SG-1 gravity core (Fig. S6). Only during the last two decades a significant increase in precipitation is obvious in the Evangelista record. Between latitudes 52°30 and 54°S, temperature records from Evangelistas, Punta Arenas and Fangano do not show a clear change in temperature from 1900 to 1960 (Fig. S12). Afterwards until 2005 a temperature increase of up to 0.5 °C is indicated. Considering these climate data, the successive reduction of glacier lengths at GCN between 1900 and 1960 (S13 and S17) was primarily caused by less accumulation, while afterwards increased ablation may have played also a role. However, Möller & Schneider (S36) show that the uppermost parts the ice cap have recently shown a slight thickening. This can be explained especially by an increased precipitation. Higher precipitation during the last two decades, as indicated by the Evangelistas record from 1980 and 2001, could explain increased glacier thickness of the higher elevated glacier catchment of the GCN (S36) and advancing glacier in the year 2007 in the Cordillera Darwin (14).

Holocene paleoclimate in the western range of the southernmost Andes (49°-50°S).

Pollen and sedimentological records from the superhumid western side of the Andes within the present day core of the Southern Hemispheric Westerlies from 49 to 53°S indicate significant changes in precipitation during the last 12 kyr (S10; Fig. 2H) characterised by a relatively humid period from 12 to 8.5 kyr BP and a variable but less humid Neoglacial after ~5.5 kyr BP. On a millennium scale, these changes in precipitation and westerly strength are correlated positively with the paleotemperatures. The Holocene mid-latitude temperature changes of the southern hemisphere can be deduced from alkenone-based SST's off the Chilean coast at 41°S

(Fig. 2I; S37) and SST reconstructions from the South Atlantic at 53°S (Fig. 2J; S38). In addition, we present regional alkenone-based fjord SST's for the last 5.5 kyr from Concepción channel (51°S; Fig. 3E), consistent with published SST's from Jacaf fjord located in northern Patagonia at around 44°S (S6). However, the alkenone-derived fjord SST's represent the surface water temperatures during the growing season of coccolithophorides in spring and summer. Regional fjord SST's clearly follow a seasonal course (S11) and are used to depict more regional relative atmospheric temperature changes. For the last 0.65 kyr BP and, with less precision, for the last 1.1 kyr BP a tree ring based temperature reconstruction is also available for the research area (S39). These records also indicate a similar strong temperature decrease of 1.0 to 1.5 °C between the MWP and the LIA starting at around 0.55 kyr BP (Fig. S6).

The stalagmite record of the MA cave near to the GCN is the only highly resolved and well dated Neoglacial precipitation record from the western range of the southernmost Andes (Location in Fig. S5; S7). Yttrium as the only drip rate-dependent proxy for deposition of siliciclastic detritus on the flat top of the stalagmite depicts centennials scale changes during the last 4.4 kyr BP (Fig. 3H). On a millennium scale the Y record shows similar changes as a $\delta^{18}O$ record which is controlled by a drip-rate dependent kinetical fractionation (Fig. 3G; S7). This $\delta^{18}O$ record was corrected for relative changes in paleotemperatures, assuming that each 0.1°C lower air temperature lets to a 0.01 higher $\delta^{18}O$ in the rain water. Lighter O isotopes in the rain water during cold periods are expected, since lower temperature cause stronger O isotope fractionation during evaporation in the Pacific. Mg/Ca ratios of the same stalagmite which were calibrated for precipitation with respect to regional 100-year precipitation records indicate Neoglacial variations in precipitation at sea level ranging from 3.5 to 7.0 m/yr (S7). Such precipitation amounts at sea level would be related to 6-12 m annual precipitation at higher elevations (> 800m a.s.l) at the GCN which is consistent with our modelling results for Holocene glacier advances.

Mapping and sampling terrestrial and subaquatic glacial deposits within Holocene moraine belt as well as speleothem implications (50°-53°S)

The selected areas for the Holocene moraine mapping include different large glacial catchments (Fig. 1). The northernmost location at Peel fjord (Fig. S3) is controlled by glacial fluctuations in the southwestern area of the southern Patagonian Ice Field with a glacial catchment of 1600 km^2 and elevations up to 2800 m a.s.l. (S5). Further south glaciers derived from the 200 km^2 ice cap of the GCN with elevations reaching up to 1700 m a.s.l. were investigated on its western side (Fig. S5) and eastern side (Fig. S8; S16 and S17). Its western glaciers include a catchment of 80 km^2, where as its eastern glaciers represent a smaller catchment of 10 km^2. The southernmost area represents

glaciers from the 1250 m high Arthuro mountain (unofficial name) on Isla Santa Ines with a ~12 km^2 catchment (Supplement Fig. S9).

Glacier extents along Peel fjord

Holocene glacier advances left very few deposits of glacial detritus on-land along the deeply incised fjord system. However, some moraine remnants have been mapped along the Peel fjord (Fig. S3). The thickness of glacial clay deposits and the distribution of subaquatic moraines were mapped in this fjord by a grid of systematic parametric echo sounding profiles. Near the present day glacier tongue of the Amalia glacier a limited sediment thickness of 2-3 m reflects areas where the sedimentation first occurred after the retreat of the A5 and A6 advances. Fjord areas with 8-10 m postglacial sediment cover (comparable to the PEEL1 core) represent areas where the deposition started after abrasion of the fjord bottom by advance A4. This area is constricted by a subaquatic moraine belt which was formed during the most extended Neoglacial advance A4 from 2.3 to 2.2 kyr BP (Fig. S3). Outside of this A4 moraine belt the thickness of sediments at the fjord bottom exceeds more than 30 m deposited probably throughout most of the Holocene.

Western Gran Campo Nevado

Several glaciers and related glacial clay plumes enter the fjord system to the west of the GCN (Fig. S5). The MA cave site with continuous speleothem records in an open cave at the coast documents an unglaciated area since at least 6 kyr BP (S7). This speleothem record provides also a precipitation record (Fig. 3G and 3H) for the last 4.5 kyr. Close to the MA cave location, the 8.8 m sediment core BA-1 was retrieved with R/V Gran Campo II from a shallow (5-6 m water depths) and small bay along Swett Channel (Site location in Fig. S5). The sediment record documents a continuous organic-bearing clayey sedimentation throughout the last 5 kyr. The age constraints of this record includes the 4.18-kyr Mt. Burney tephra in 4.2 m core depth and a calibrated ^{14}C age of 1.7 kyr BP obtained from macro plant remnants found at 1.7 m core depth (Tab. S1) indicating relatively constant sedimentation rates of 1 mm/yr. Below 5 m core depth (aprox. 5 kyr BP) a transition towards a more coarse clastic sedimentation is obvious, probably documenting a less elevated coastline near to the core site. The suggested coastline depression by around 15 m after 5 kyr BP may have been caused by isostasy related to the increased Neoglacial glacier load at the GCN.

At the site GC (Fig. S5), a stalagtite was found on the floor of a cave with a wide entrance (6 m wide and 15 m high), exposed towards the Neoglacial glacier pathways. The stalagtite was embedded in glacio-lacustrine sediments. The floor of the cave is about 35 m above the present day sea level. The cave was formed in granodiorites by costal erosion during a higher early Holocene coastline. Five U/Th ages were obtained

from this stalagtite which documents its formation between 8 and 2.35 kyr BP (Fig. S7 and Table S1). This indicates that no glacier has overrun the cave during this period. The youngest extrapolated age of the stalagmite (2.35 kyr BP) indicates that the stalagtite was removed by glacier advance A4 from the roofs of the cave, coeval with the abrasion of the fjord bays along Peel fjord and Lake Arthuro. The stalagite shows a porous section dated between 6 and 4 kyr BP probably indicating distinct hydrous conditions with overall lower precipitation.

Fig. S5 shows the terrestrial and subaquatic moraine belt of the advances A4 to A5. More than 30 m sediment thickness in the Swett channel and sedimentation rates of 1-2 mm/yr for the sediment core LU1 (Fig. S6) indicate that this area was not occupied or abrased during Holocene glacier advances. This is consistent with the above described site information and further regional moraine mapping (S13 and S40).

Eastern Gran Campo Nevado

On the eastern side of GCN a set of moraines formed by the Lengua Glacier documents the systematic glacier retreat during the LIA after the maximum of advance A6 (S13; Fig S8). 1.5 km down-valley outcrops of an older more extended moraine belt does not include the 4.18-kyr Mt. Burney tephra and thus is attributed to the most extended Neoglacial A4 advance. Still more down-valley along the Lengua river an extend forest was devasted and embedded into coarse gravels and blocks at around 5.4 kyr BP (^{14}C age in Tab. S1). This destructive event at the beginning of Advance A2 (5.5 to 4.9 kyr BP) is interpreted as a result of bursting of a moraine dammed proglacial lake below the Lengua glacier. Along the ancient glacier flow path and around 6 km from the present day glacier tongue the core GC-2 shows the transition (14.2 kyr BP) from glacial clay to organic-bearing sediment and peat which accumulated throughout the Holocene. Chandler Lake sediment core CH-1, situated within the Late Glacial glacier pathway, also shows the transition from glacial clay to organic bearing sediment already at ~12 kyr BP. These findings indicate that glaciers retreated very fast during the Late Glacial and earliest Holocene from the above described sites (Fig. S8).

Arthuro mountain, Santa Ines

The Arthuro mountain (unofficial name) on the Santa Ines Island represents the southernmost location at 54°S and includes a ~12 km^2 glacier field which drains towards the investigated sediment cores ART1-4 of lake Arthuro and FART-1 of Fjord Arthuro (core sites in Fig. S9). Reconstructed glacier extents and moraines shown in Fig. S9 are based on on-land mapping as well as sediment core information and parametric echo sounding profiles which depict sediment structures and thicknesses. The advance A4 clearly overran and abraded the bottom of lake Arthuro and reached only a restricted part of the nearby fjord system. At Lake Arthuro four sediment cores

show that organic-bearing sediments of upper core sections were formed after around 2.1 kyr BP on top of the glacial detritus of advance A4. Mapping of the sediment-fill by echosounding indicate that the whole lake was abrased before ~2.2 kyr BP (Fig. S9, inset).

3. Supporting figures:

Fig. S1: Global compilation of Holocene glacier advances compared to North Atlantic and South Atlantic IRD records. (A) North Atlantic drift ice record and Holocene "Bond events" (S25). Dark bars mark glacier advances in Norway (S21), Cascade Range of Canada (S22), Alaska (S23) and the Alps (S24) in the Northern Hemisphere (NH). Southern Hemisphere glacier advances in Peru (S26), New Zealand (S30, S31, S32) and the Antarctic Peninsula (S33) and the Patagonian Andes (27, S28, S29) are shown. (B) K/Si ratios from core MD07/3124 site in the Concepción fjord as an integrated signal for advances A1 to A6 in the western range of the southernmost Andes (this study). (C) South Atlantic IRD record from 53°S (S35) indicating the start of the Neoglacial at around 5.5 kyr BP, coeval with the A2 advance. In the NH the most extended Holocene advance occurred during the LIA, whereas the most extended one of the Southernmost Andes (A4) is dated to ~2.2-2.3 kyr BP (this study). Especially during Bond Cycle 2 (~3.5 to 2.5 kyr BP) several NH advances were recorded, whereas no advance occurred in the superhumid southern Andes (probably due to very low precipitation).

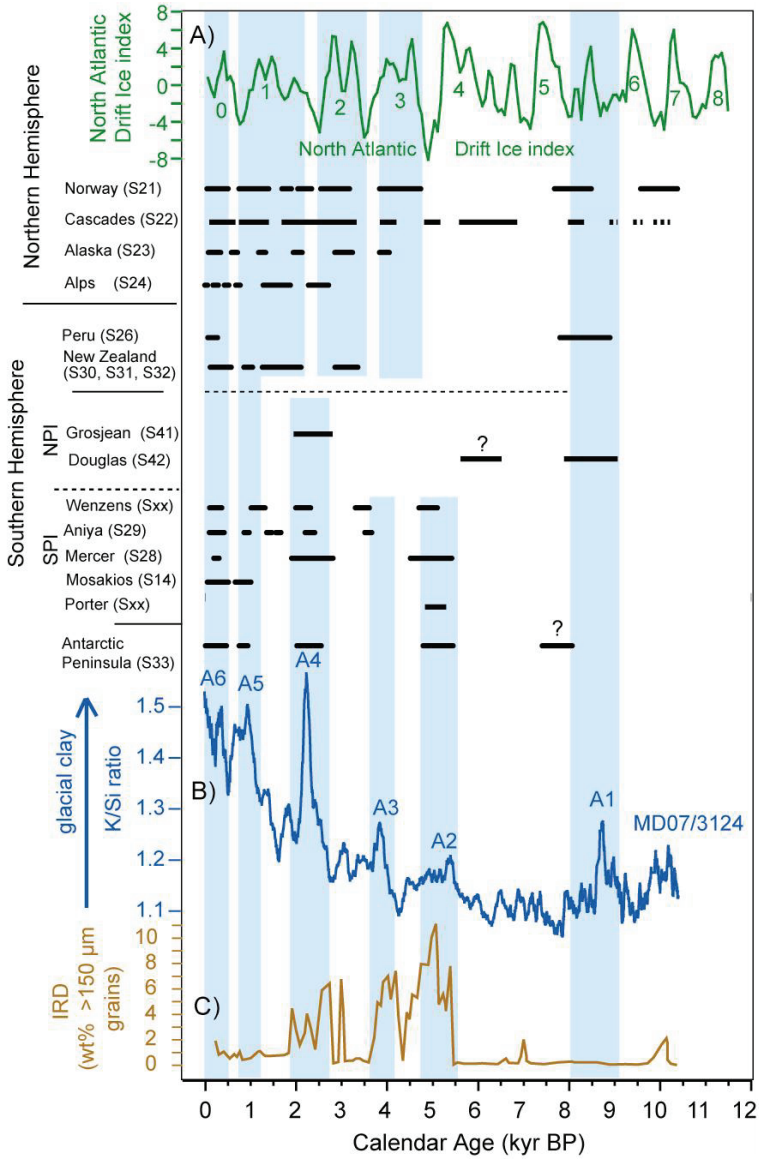

Fig. S2: Monthy average wind velocity and precipitation from the AWS Passo at the GCN between 2001 to 2008 (S18, S19) and calculated snow accumulation above 800 m elevation (using a regional temperature gradient of -0.63°C/100 m elevation). This documents that snow accumulation occurs throughout most of the year at higher elevations.

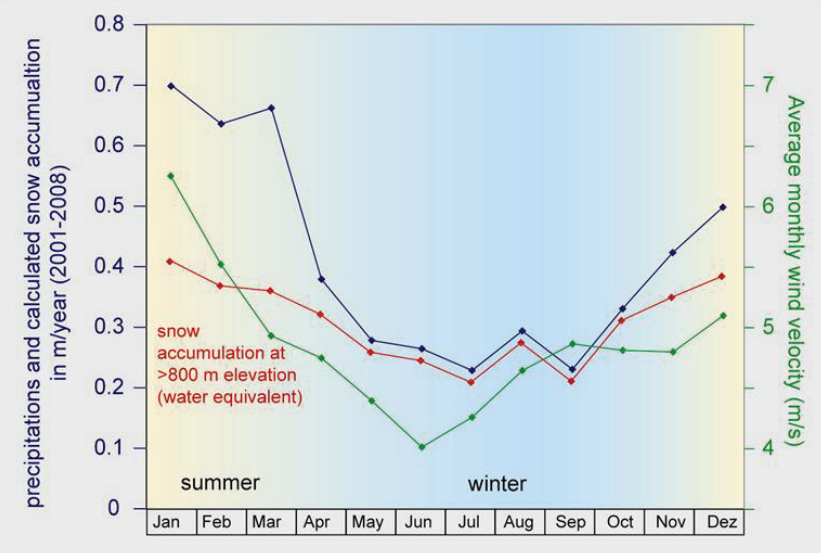

Fig. S3: Peel fjord with nearby Southern Patagonian Ice Field and the location of Peel-1 core in a 40 m deep bay besides the Peel fjord and Peel-2 core at the northern shore of Peel fjord. The bathymetry is based on the Hydrographic Map 1:70000 from SHOA and our echo sounding profiles which gave further information on sediment structures and thicknesses. Deduced limits of moraines from the advance A4 to A6 are shown.

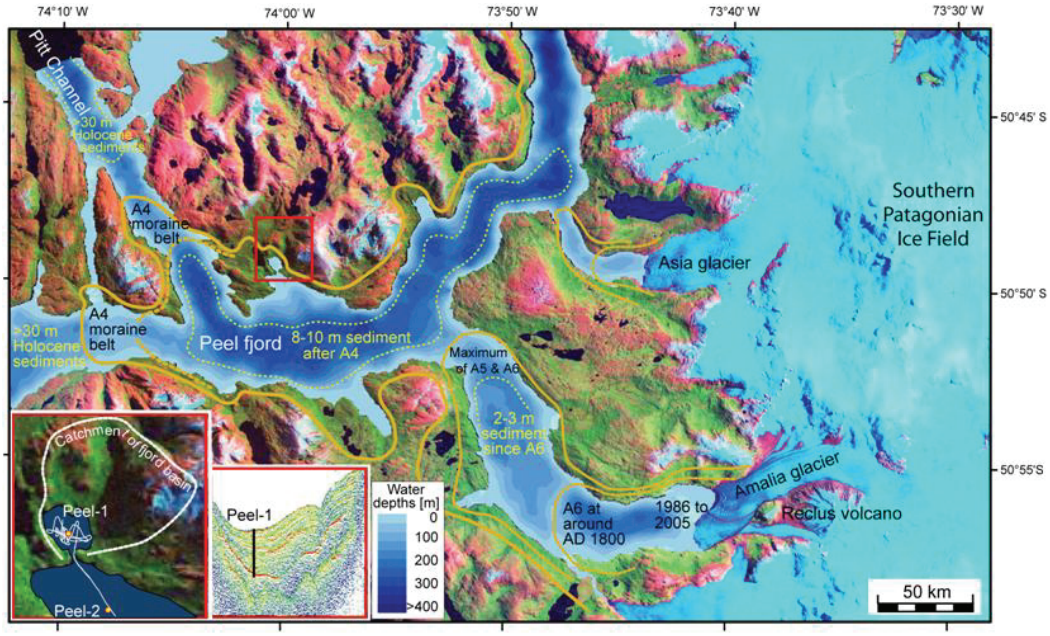

Fig. S4: (A) Depth-age relationship of Peel-1 core; (B) Proposed Neoglacial advances A4 to A6; (C) Tree-ring-deduced temperature anomalies for the southwestern Andes (S39); (D) Sediment core colour variations (gray scale); (E) C_{org} contents of the Peel-1 core.

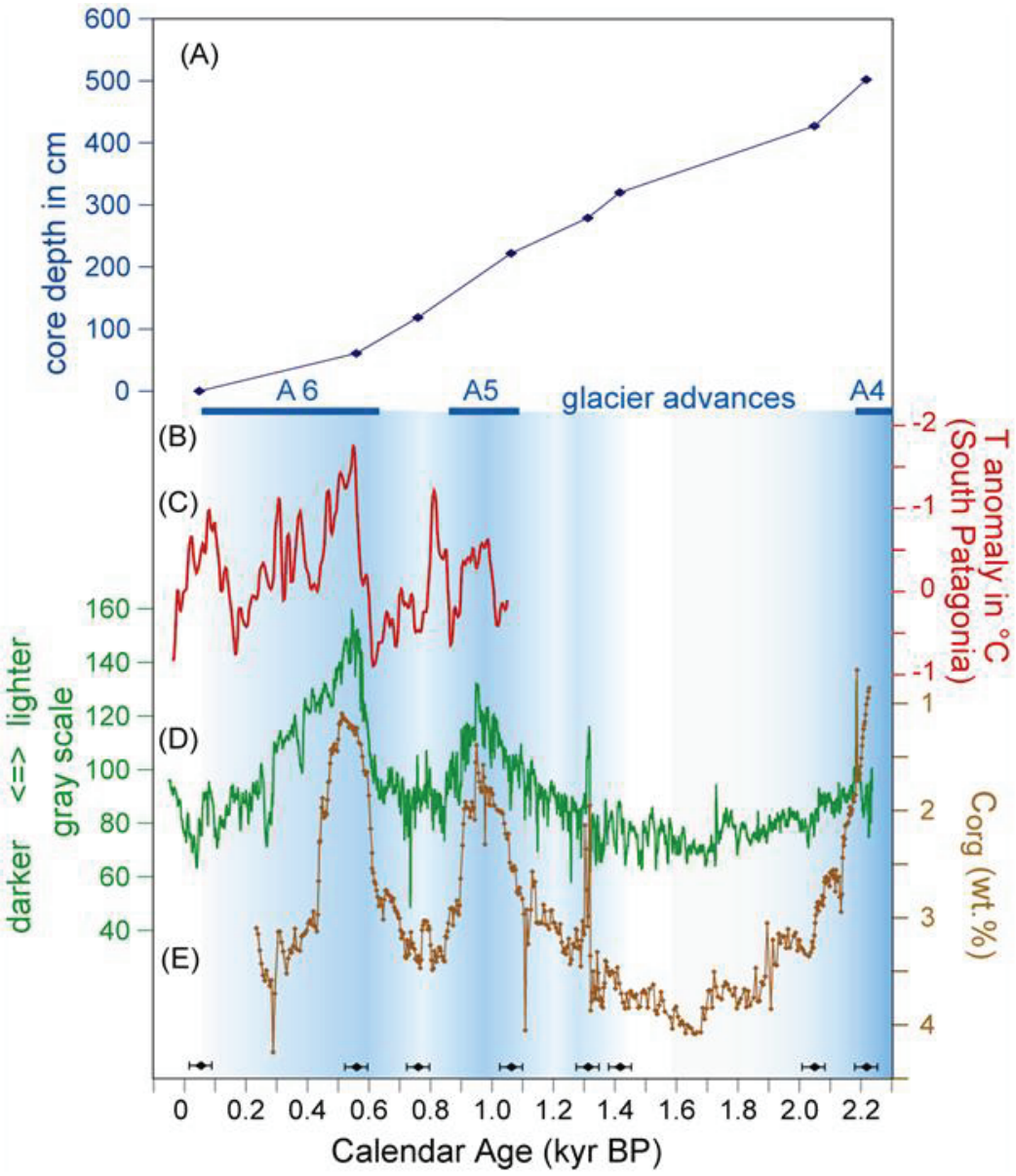

Fig. S5. Detailed map of the western side of the Gran Campo Nevado with fjord bathymetry, results from echo sounding surveys, and deduced sediment thicknesses. In addition, modern glaciers and their recent retreat phases (S13) as well as moraine limits of the advances A4-A6 are shown. The sites of the MA1 and GC1 caves, and the AWS Arevalo as well as the drilling sites of the short gravity cores (SG-1; LU-1, SW1), the 8.8 m long BA-1 and 8.2 m LO-1, and the MD07/3126 cores are shown.

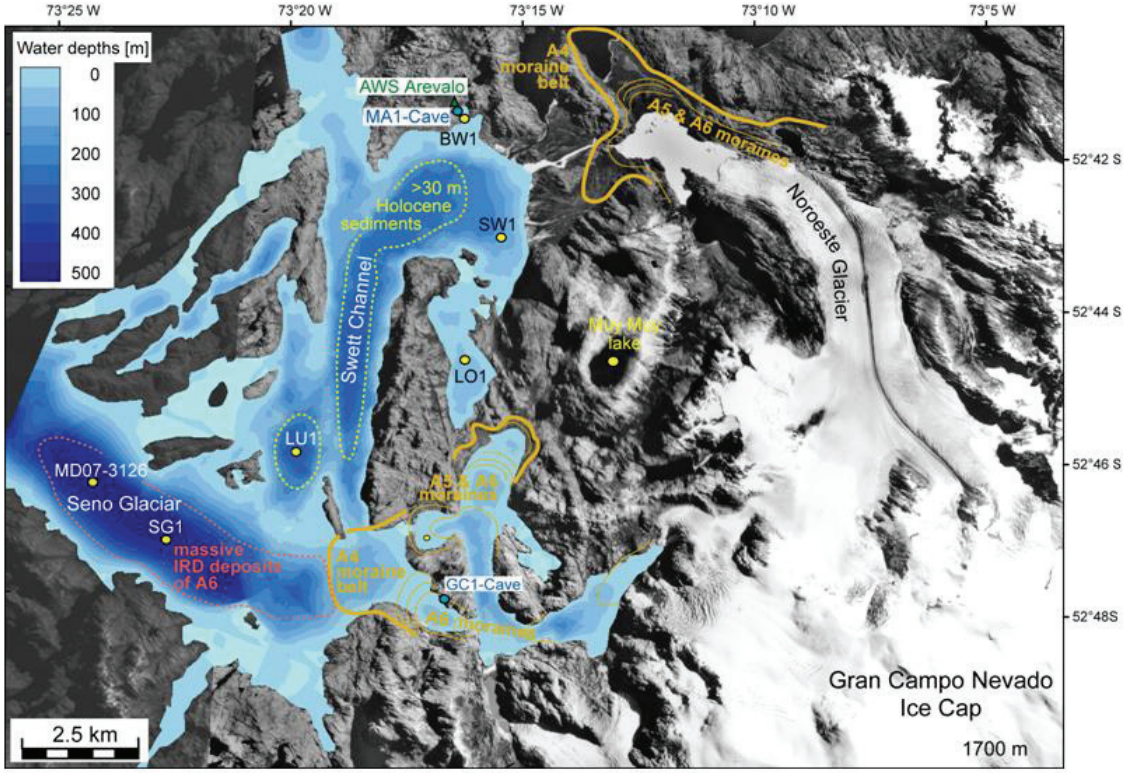

Fig. S6: Age constrains and sediment properties including C_{org} contents and C/N ratios for the SG-1, LU-1 BA-1 and LO-1 cores compared to the well dated Peel-1 core. (Site locations in Fig. S5).

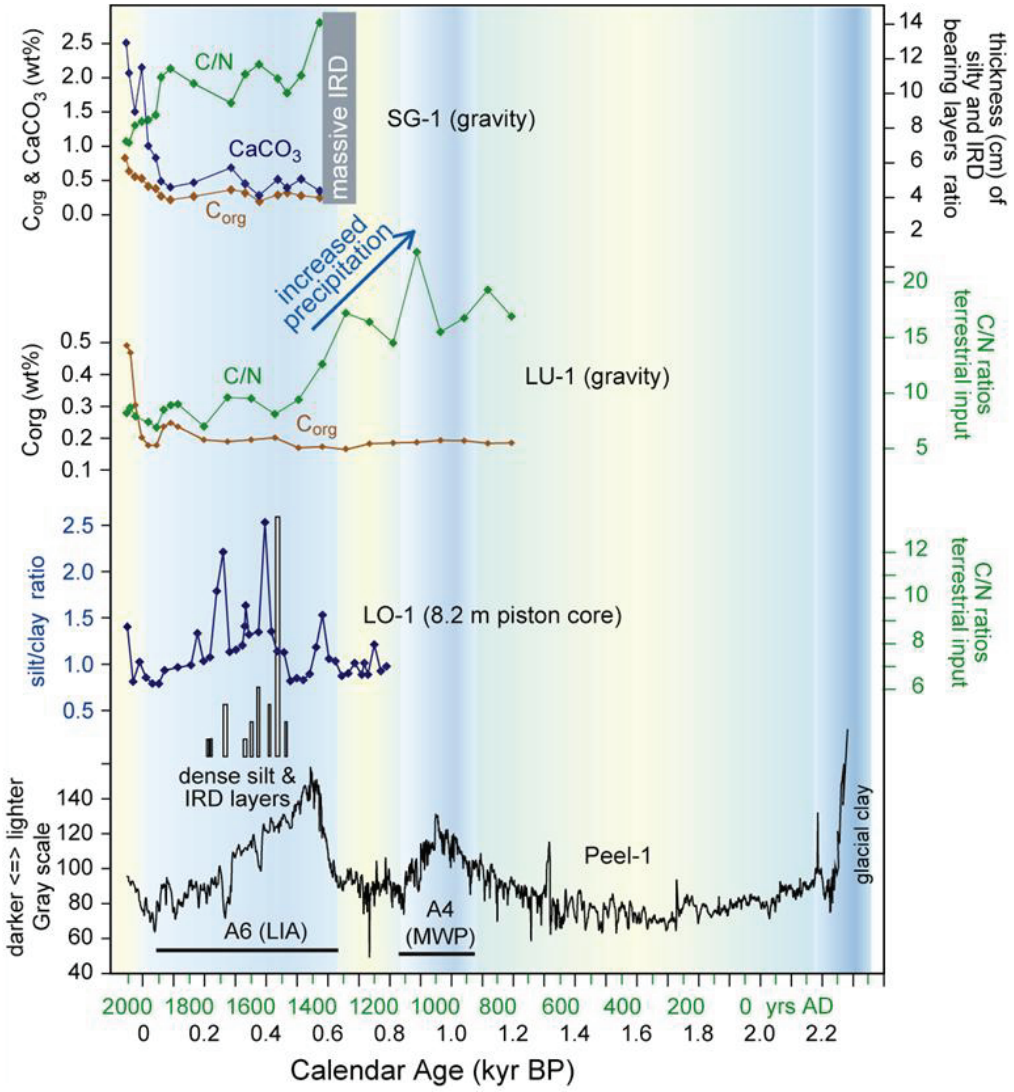

Fig. S7: Stalagtite GC1 from a cave inside of Holocene moraine belt, 6 km to the west of the GCN with U/Th ages and sampling holes.

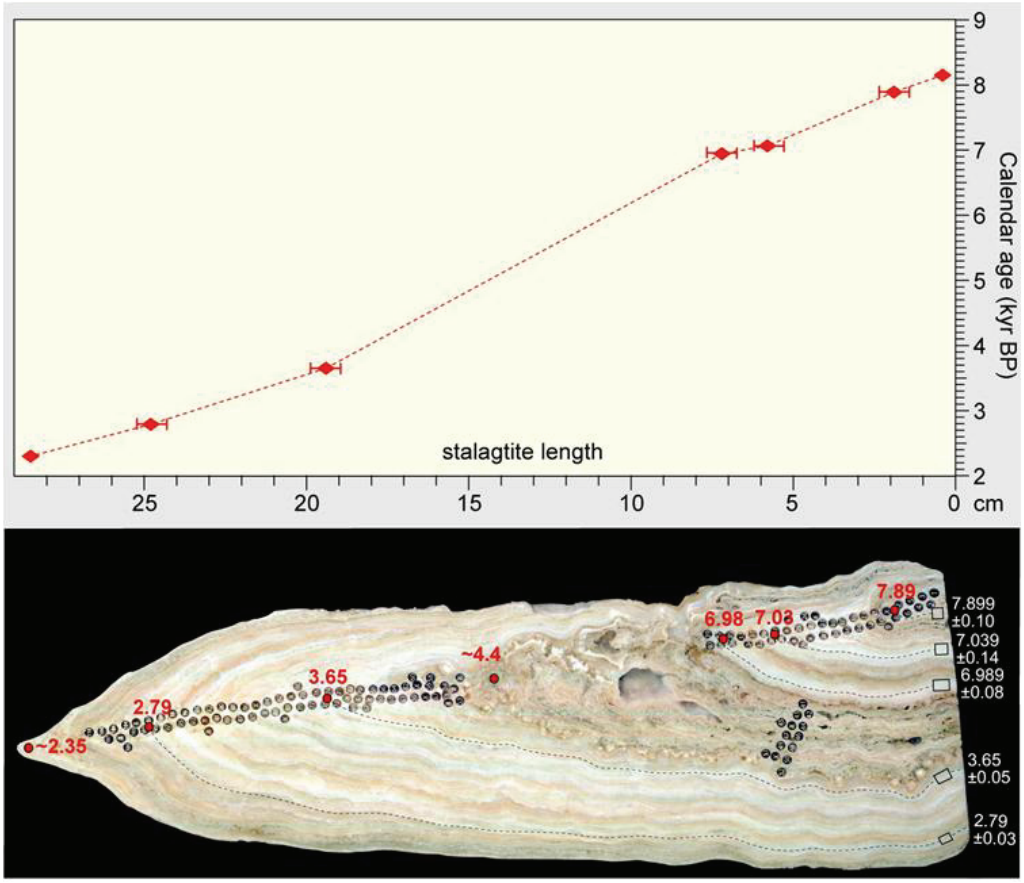

Fig. S8: Western range of Gran Campo Nevado with the Lengua Outlet Glacier, Holocene and Neoglacial moraines as well as dated transitions of glacial clay to organic carbon-bearing sediment in the CH1 and GC2 cores.

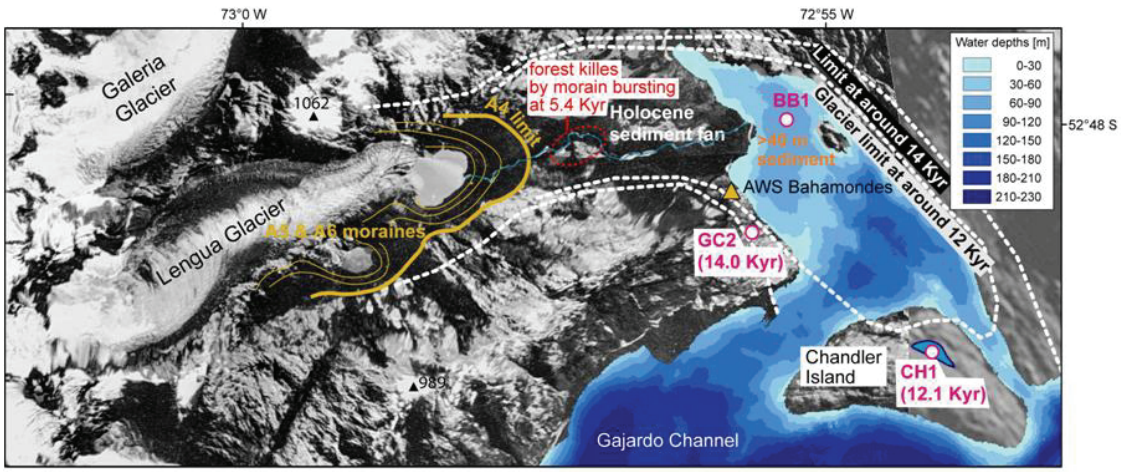

Fig. S9: Lake Arthuro and associated glaciers and fjord bays with drilling sites and moraine limits for the LIA (A6) and the most extended A4 advance (from ~2.3 to 2.2 kyr BP). The sediment structure and thickness (yellow isolines show sediment thicknesses in the fjord above coarse clastic glacial detritus which were mapped with a parametric echosounder. The site of the 7.5 m long FART1 sediment core is indicated. The inset map shows sediment thickness in Lake Arturo deposited after 2.2 kyr BP, deduced from sediment cores ART1-4.

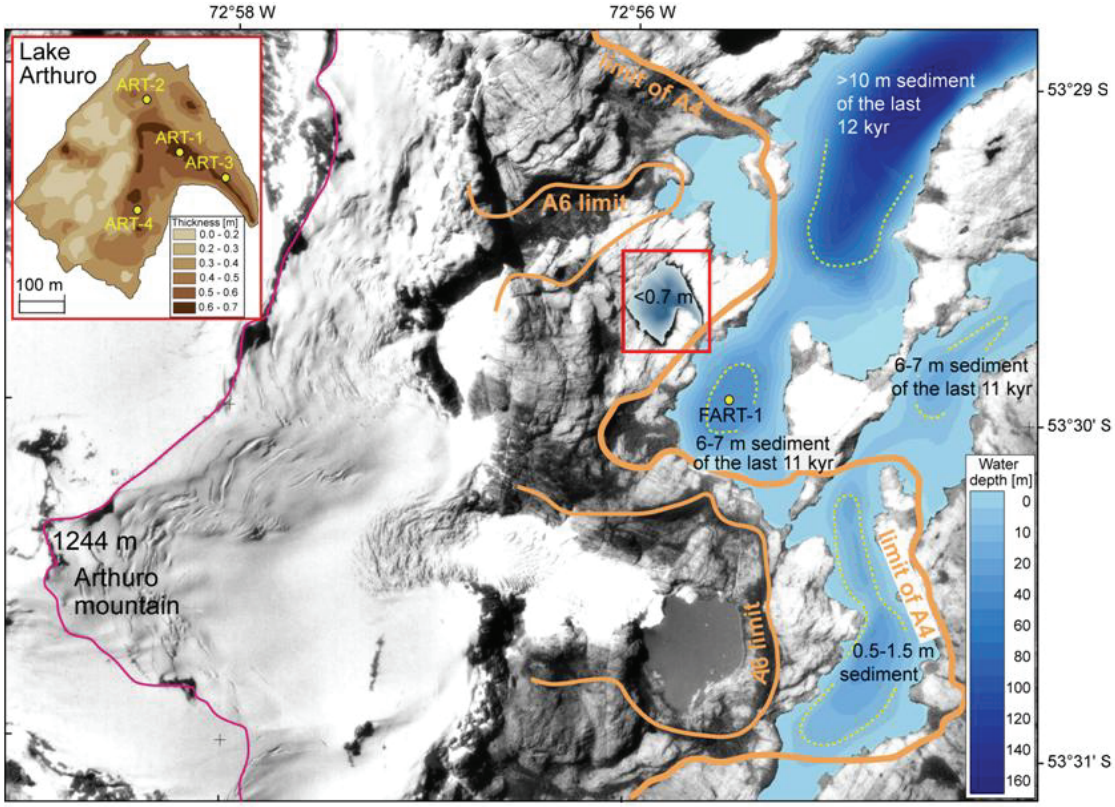

Fig. S10: Sediment gravity core from Lake Arthuro (ART1) and a piston sediment core from Arthuro fjord (FART-1; site locations in Fig. S9) with light grey layers of glacial clay corresponding to advance A4 (~2.2-2.3 kyr BP). Two calibrated ^{14}C ages (numbers in red) and a tephra layer of the Reclus volcano (S12) give preliminary age constrains. Additionally, clayey layers possibly related to the advances A5 and A6 are shown. Linear interpolated ages (numbers in white) are based on a constant mass accumulation considering dry densities of the sediment).

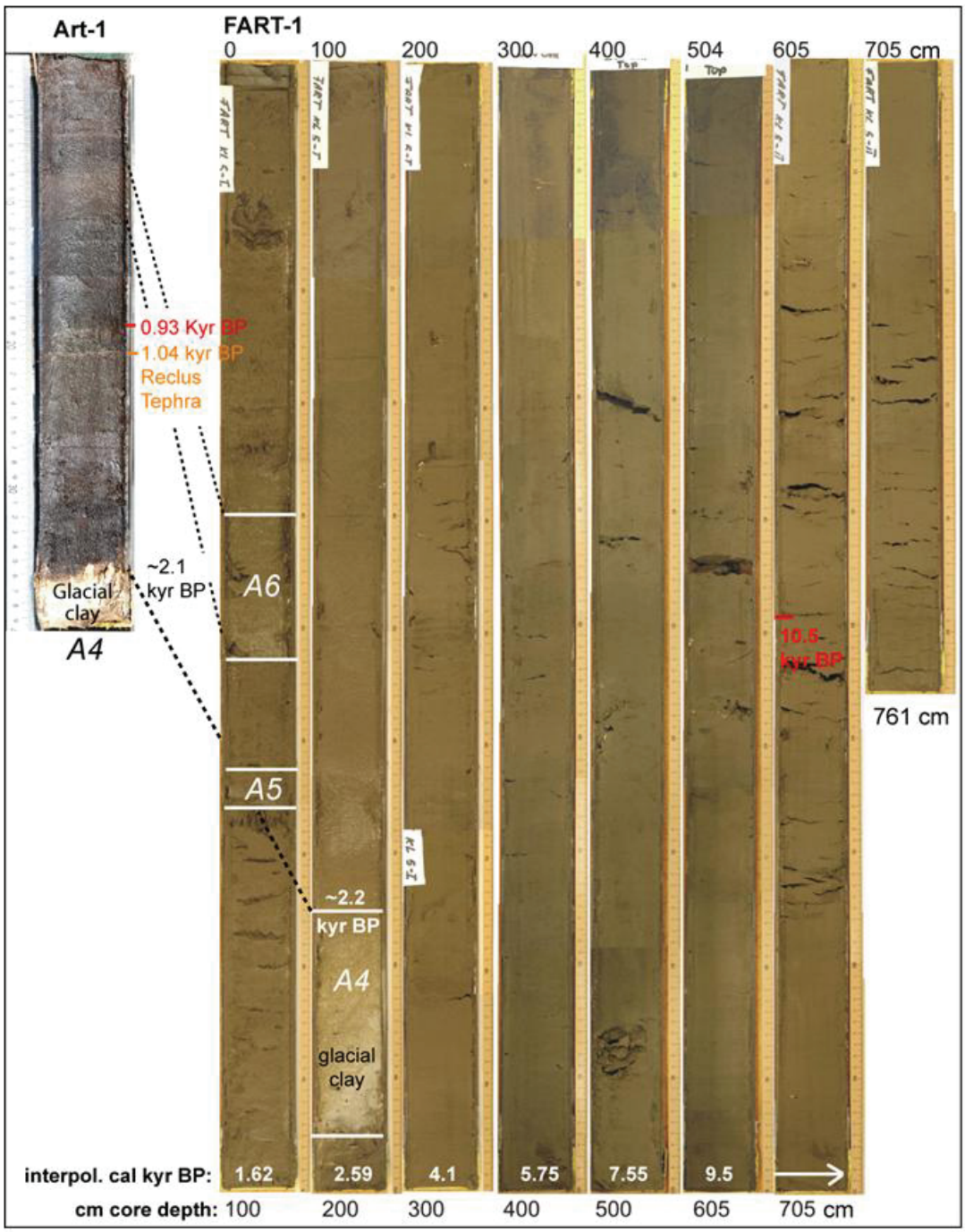

Fig. S11: Mass balance modelling concerning the influence of temperature and accumulation for the determined phases of glacier advance. Further details on the model see descriptions in the supplement text. Dark diagonal lines with numbers denote different positive or negative mass balances (MB). For the Holocene advance positive MB's were chosen (depending on glacier lengths). The stippled yellow lines indicate the required precipitation within the typical temperature error of ±0.3 °C.

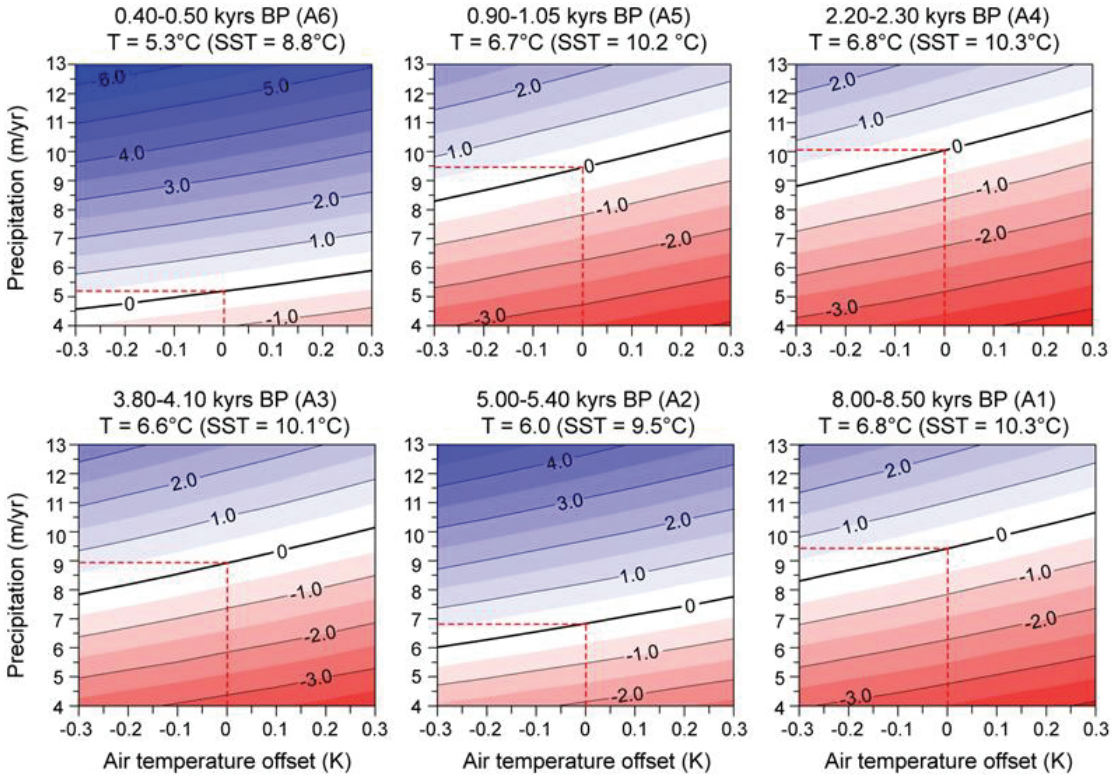

Fig. S12: 100-year temperature and precipitation records from the AWS Evangelistas and Felix, precipitation controlled Mg/Ca ratios of MA1 stalagmite (S7), and precipitation controlled C/N ratios measured in the SG1 gravity core (Fig. S6) compared to length measurements at the Lengua glacier and several western glaciers of the GCN (S13 and S17). ABCD

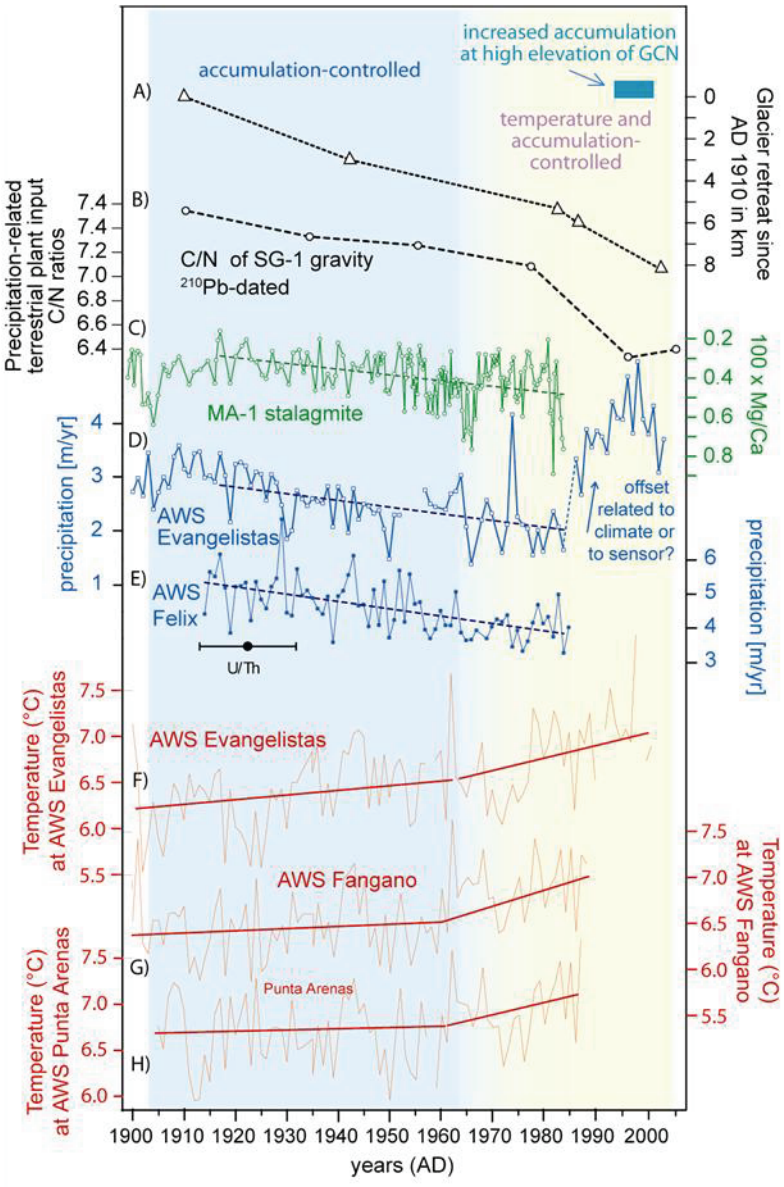

Fig. S13: Observed and reconstructed area-length relations of Glaciar Noroeste. Black triangles mark directly observed (aerial or satellite imagery) glacier extents and black squares mark glacier extents reconstructed according to morain mapping. Black line indicates the linear best fit to observed glacier extents (cf. Equation 1). Dashed lines represent the 95% confidence interval. Grey squares mark modelled glacier extents for estimated glacier lengths according to equation 1.

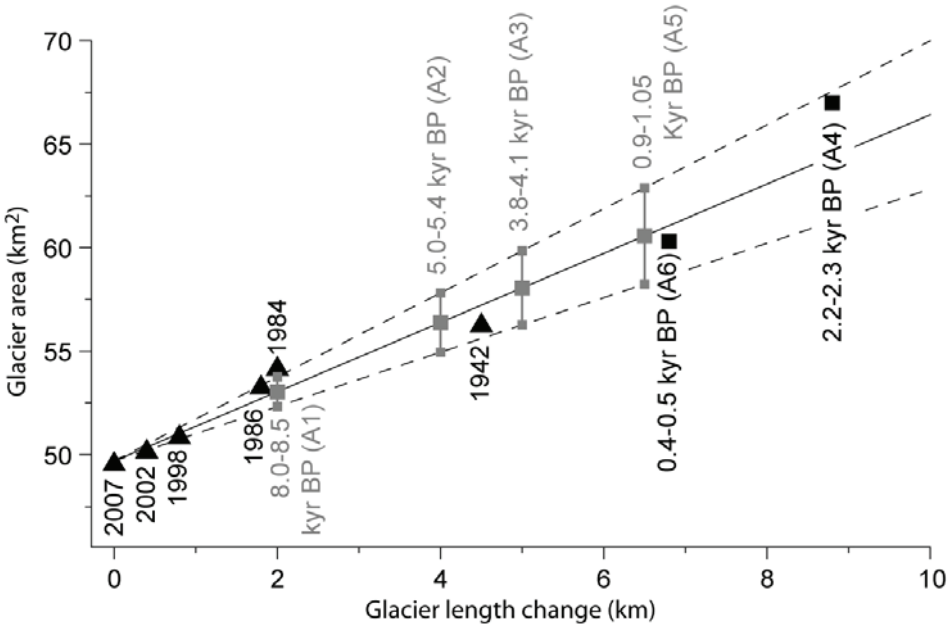

4. Supporting Online Table S1

Table S1. List of ^{14}C ages for the piston cores MD3124, PALM-2, Peel-1, LO-1, BA-1, FART-1, Arthuro 1 and ^{210}Pb ages for the gravity cores SG-1 and LU-1. U/Th ages for the GC1-Stalagite are also given.

Core depth#	Material	^{14}C age (yr BP)	Error (± yr)	Calibrated age (yr BP)*	Sed.-rate (cm/kyr)	References
Palm2						
0				-50		Modern age
185	marine shell	2570	30	2410	75	Lamy et al 2010
292	Mt. Burney tephra	3860	50	4185	60	Lamy et al 2010
351	Mt. Burney tephra			5690	39	Lamy et al 2010
463	Hudson tephra			8090	47	Lamy et al 2010
482	Mt. Burney tephra	7890	45	8610	37	Lamy et al 2010
590	marine shell	10240	60	11690	35	Lamy et al 2010
Peel-1						
0				-50		Modern age
15						This paper
60.8	Plant remain	450	30	480	30	This paper
118.5	Plant remain	790	40	690	40	This paper
222	Plant remain	1150	65	1010	70	This paper
279	Plant remain	1390	30	1270	35	This paper
320	Plant remain	1565	25	1380	30	This paper
427	Plant remain	2130	40	2040	45	This paper
502	Plant remain	2320	30	2210	30	This paper
MD07/3124						
0				-50		Modern age
65	marine shell	1110	30	380	35	This paper
125	marine shell	1690	30	850	30	This paper
230	marine shell	2830	35	2010	40	This paper
310	marine shell	3295	30	2600	35	This paper
430	marine shell	4230	40	3690	40	This paper
560	marine shell	5280	35	5170	30	This paper
665	marine shell	6050	30	6060	35	This paper
700	marine shell	6380	40	6360	45	This paper
755	marine shell	6850	35	6930	40	This paper
1030	marine shell	8040	60	8090	65	This paper
1383	marine shell	8840	55	8940	65	This paper
1538	marine shell	9090	45	9350	45	This paper
1680	marine shell	9360	45	9530	45	This paper
1962	marine shell	9880	45	10240	50	This paper
2210	marine shell	10250	50	10700	55	This paper

FART1						
649	Plant remain	9360	55	10500	60	This paper
0						
ART-3						(*S11*)
28	Plant remain	3280	45	3430	14	This paper
31	Reclus tephra			1035		(*Moy et al 2008*)
Lengua Forest relict	Plant remain	7290	70	8060	46	This paper
	Hudson tephra			8090	33	Interpolated age, this study
LO-1		7635	40	8390	33	
	Mt Plant remain.	7890	45	8610	27	This paper
BA1						
	Plant remain	9660	85	10950	30	This paper
	Plant remain	9740	40	11110	25	This paper
2	Plant remain	12020	200	13890	27	This paper

U/Th ages of stalagite GC1

Depth from drip tipp	**Material**					
0.5	carbonate	8250	25	8250	25	This paper
1.5	carbonate	7950	30	7950	30	This paper
5.7	carbonate	7090	30	7090	30	This paper
7.1	carbonate	7040	25	7040	25	This paper
19.3	carbonate	3710	40	3710	40	This paper
24.8	carbonate	2850	25	2850	25	This paper
28.5	Extrapolated age	2350		2350		This paper

210Pb ages of LU1

210Pb ages of LU1 and CG-1

Depth (cm)	210Pb age	Sed-rate
1	0	
3	4	0,50
5	39	0,06
7	54	0,13
12	82	0,07
	104	0,14
2	**Average Sed rate =**	**0,12**

Depth (cm)	210Pb age	Sed-rate
1,5	0	
4,5	11	0,27
7,5	44	0,09
10,5	81	0,08
14,5	92	0,36
17,5	104	0,25
19,5	162	0,03
		Average Sed rate = 0,12

5. Supporting references and notes

S1 Richter, T. O., S. van der Gaast, B. Koster, A. Vaars, R. Gieles, H.C. de Stigter, H. de Hass, and T. C. E. v. Weering (2006), The Avaatech XRF Core Scanner: technical description and applications to NE Atlantic sediments, in *New Techniques in Sediment Core Analysis, R.G. Rothwell (ed.), Geological society of London Special Publication, 267*, edited, pp. 39-50.

S2 Prahl, F. G., and S. G. Wakeham (1987), Calibration of unsaturation patterns in long-chain ketone compositions for paleotemperature assessment, *Nature*, *330*, 367-369.

S3 Prahl, F. G., L. A. Muehhausen, and D. L. Zahnle (1988), Further evaluation of long-chain alkenones as indicators of paleoceanographic conditions, *Geochimica et Cosmochimica Acta*, *52*, 2303-2310.

S4 Müller, P. J., G. Kirst, G. Ruhland, I. von Storch, and A. Rosell-Mele (1998), Calibration of the alkenone paleotemperature index UK'37 based on core-tops from the eastern South Atlantic and the global ocean (60°N-60°S). *Geochimica et Cosmochimica Acta*, *62*, 1757-1772.

S5 Casassa, G., A. Rivera, M. Aniya, and R. Naruse (2000), Características glaciológicas del campo de Hielo Patagónico Sur, *Anales del Instituto de la Patagonia, Serie Ciencias Naturales*, *28*, 5-22.

S6 Sepúlveda, J., S. Pantoja, K. A. Hughen, S. Bertrand, D. Figueroa, T. León, J. Drenzek, and C. Lange (2009), Late Holocene sea-surface temperature and precipitation variability in northern Patagonia, Chile (Jacaf Fjord, 44ºS), *Quaternary Research*, *72*, 400-409.

S7 Schimpf, D., R. Kilian, A. Kronz, K. Simon, C. Spotl, G. Worner, M. Deininger, and A. Mangini (2011), The significance of chemical, isotopic, and detrital components in three coeval stalagmites from the superhumid southernmost Andes (53 degrees S) as high-resolution palaeo-climate proxies, *Quaternary Science Reviews*, *30*(3-4), 443-459.

S8 Stern, C. R. (2008), Holocene tephrochronology record of large explosive eruptions in the southernmost Patagonian Andes, *Bulletin of Volcanology*, *70*(4), 435-454.

S9 Kilian, R., M. Hohner, H. Biester, H. J. Wallrabe-Adams, and C. R. Stern (2003), Holocene peat and lake sediment tephra record from the southernmost Chilean Andes (53-55 degrees S), *Revista Geologica De Chile*, *30*(1), 23-37.

S10 Lamy, F., R. Kilian, H. W. Arz, J. P. Francois, J. Kaiser, M. Prange, and T. Steinke (2010), Holocene changes in the position and intensity of the southern westerly wind belt, *Nature Geoscience*, *3*, 695-699.

S11 Kilian, R., O. Baeza, T. Steinke, M. Arevalo, C. Rios, and C. Schneider (2007a), Late Pleistocene to Holocene marine transgression and thermohaline control on sediment transport in the western Magellanes fjord system of Chile (53 degrees S), *Quaternary International*, *161*, 90-107.

S12 Moy, C. M., R. B. Dunbar, P. I. Moreno, J. P. Francois, R. Villa-Martinez, D. M. Mucciarone, T. P. Guilderson, and R. D. Garreaud (2008), Isotopic evidence for hydrologic change related to the westerlies in SW Patagonia, Chile, during the last millennium, *Quaternary Science Reviews*, *27*(13-14), 1335-1349.

S13 Koch, J., and R. Kilian (2005), 'Little Ice Age' glacier fluctuations, Gran Campo Nevado, southernmost Chile, *Holocene*, *15*(1), 20-28.

S14 Masiokas, M. H., A. Rivera, L. E. Espizua, R. Villalba, S. Delgado, and J. C. Aravena (2009), Glacier fluctuations in extratropical South America during the past 1000 years, *Palaeogeography Palaeoclimatology Palaeoecology*, *281*(3-4), 242-268.

S15 Möller, M., and C. Schneider (2010), Calibration of glacier volume-area relations from surface extent fluctuations and application to future glacier change, *Journal of Glaciology*, *56*(195), 33-40.

S16 Möller, M., C. Schneider, and R. Kilian (2007), Glacier change and climate forcing in recent decades at Gran campo Nevado, southermost Andes, *Annals of Glaciology*, *46*, 136-144.

S17 Schneider, C., M. Schnirch, C. Acuna, G. Casassa, and R. Kilian (2007), Glacier inventory of the Gran Campo Nevado Ice Cap in the Southern Andes and glacier

changes observed during recent decades, *Global and Planetary Change*, *59*(1-4), 87-100.

S18 Schneider, C., M. Glaser, R. Kilian, A. Santana, N. Butorovic, and G. Casassa (2003), Weather observations across the Southern Andes at 53(degrees)S, *Physical Geography*, *24*(2), 97-119.

S19 Möller, M., and C. Schneider (2008), Climate sensitivity and mass balance evolution of Gran Campo Nevado Ice Cap, southwest Patagonia, *Annals of Glaciology*, *48*(32-42).

S20 Ohmura, A. (2001), Physical basis for the temperature-based melt-index method, *Journal of Applied Meteorology*, *40*(4), 753-761.

S21 Nesje, A., J. Bakke, S. O. Dahl, O. Lie, and J. A. Matthews (2008), Norwegian mountain glaciers in the past, present and future, *Global and Planetary Change*, *60*(1-2), 10-27.

S22 Clague, J. J., B. Menounos, G. Osborn, B. H. Luckman, and J. Koch (2009), Nomenclature and resolution in Holocene glacial chronologies, *Quaternary Science Reviews*, *28*(21-22), 2231-2238.

S23 Barclay, D., G. C. Wiles, and P. E. Calkin (2009), Holocene coastal glaciation of Alaska, *Quaternary Science Reviews*, *28*(21-22), 2034-2048.

S24 Ivy-Ochs, S., H. Kerschner, M. Maisch, M. Christl, P. W. Kubik, and C. Schluchter (2009), Latest Pleistocene and Holocene glacier variations in the European Alps, *Quaternary Science Reviews*, *28*(21-22), 2137-2149.

S25 Bond, G., B. Kromer, J. Beer, R. Muscheler, M. N. Evans, W. Showers, S. Hoffmann, R. Lotti-Bond, I. Hajdas, and G. Bonani (2001), Persistent solar influence on north Atlantic climate during the Holocene, *Science*, *294*(5549), 2130-2136.

S26 Licciardi, J. M., J. M. Schaefer, J. R. Taggart, and D. C. Lund (2009), Holocene Glacier Fluctuations in the Peruvian Andes Indicate Northern Climate Linkages, *Science*, *325*(5948), 1677-1679.

S27 Glasser, N. F., S. Harrison, V. Winchester, and M. Aniya (2004), Late Pleistocene and Holocene palaeoclimate and glacier fluctuations in Patagonia, *Global and Planetary Change*, *43*(1-2), 79-101.

S28 Mercer, J. H. (1982), Holocene glacier variations in southern South America, *Striae*, *18*, 35-40.

S29 Aniya, M. (1995), Holocene glacial chronology in Patagonia -Tyndall and Upsala glaciers, *Arctic and Alpine Research*, *27*(4), 311-322.

S30 Schaefer, J. M., G. H. Denton, M. Kaplan, A. Putnam, R. C. Finkel, D. J. A. Barrell, B. G. Andersen, R. Schwartz, A. Mackintosh, T. Chinn, and C. Schluchter (2009), High-Frequency Holocene Glacier Fluctuations in New Zealand Differ from the Northern Signature, *Science*, *324*(5927), 622-625.

S31 Winkler, S., and J. A. Matthews (2010), Holocene glacier chronologies: Are 'high-resolution' global and inter-hemispheric comparisons possible?, *Holocene*, *20*(7), 1137-1147.

S32 Anderson, B., and A. Mackintosh (2006), Temperature change is the major driver of late-glacial and Holocene glacier fluctuations in New Zealand, *Geology*, *34*(2), 121-124.

S33 Hall, B. L. (2009), Holocene glacial history of Antarctica and the sub-Antarctic islands, *Quaternary Science Reviews*, *28*(21-22), 2213-2230.

S34 Magny, M., and J. N. Haas (2004), A major widespread climatic change around 5300 cal. yr BP at the time of the Alpine Iceman, *Journal of Quaternary Science*, *19*(5), 423-430.

S35 Hodell, D. A., S. L. Kanfoush, A. Shemesh, X. Crosta, C. D. Charles, and T. P. Guilderson (2001), Abrupt cooling of Antarctic surface waters and sea ice expansion in the South Atlantic sector of the Southern Ocean at 5000 cal yr B.P., *Quaternary Research*, *56*, 191-198.

S36 Möller, M., and C. Schneider (2010), Volume change at Gran Campo Nevado in 1984-2000: a reassessment based on new findings, *Journal of Glaciology*, *56*(196), 363-365.

S37 Kaiser, J., F. Lamy, and D. Hebbeln (2005), A 70-kyr sea surface temperature record off southern Chile (ODP Site 1233). *Paleoceanography*, *20, PA4009*, doi:10.1029/2005PA001146.

S38 Bianchi, C., and R. Gersonde (2004), Climate evolution at the last deglaciation: The role of the Southern Ocean, *Earth And Planetary Science Letters*, *228*(3-4), 407-424.

S39 Neukom, R., J. Luterbacher, R. Villalba, M. Küttel, D. Frank, P. D. Jones, M. Grosjean, H. Wanner, J. C. Aravena, D. E. Black, D. A. Christie, R. D'Arrigo, A. Larra, M. Morales, C. Soliz-Gamboa, A. Srur, R. Urrutia, and L. von Gunten (2010), Multiproxy summer and winter surface air temperature field reconstructions for southern South America covering the past centuries, *Climate Dynamics*, doi:10.1007/s00382-00010-00793-00383.

S40 Kilian, R., C. Schneider, J. Koch, M. Fesq-Martin, H. Biester, G. Casassa, M. Arevalo, G. Wendt, O. Baeza, and J. Behrmann (2007b), Palaeoecological constraints on late Glacial and Holocene ice retreat in the Southern Andes (53 degrees S), *Global and Planetary Change*, *59*(1-4), 49-66.

S41 Grosjean, M., M. A. Geyh, B. Messerli, H. Schreier, and H. Veit (1998), A late-Holocene (< 2600 BP) glacial advance in the south-central Andes (29°S), northern Chile, *Holocene*, *8*(4), 473-479.

S42 Douglass, D. C., B. S. Singer, M. R. Kaplan, R. P. Ackert, D. M. Michelson, and M. W. Caffee (2005), Evidence of early Holocene glacial advance in southern South America from cosmogenic surface exposure dating, *Geology*, *33*, 237-240.

S43 Wenzens, G. (1999), Fluctuations of outlet and valley glaciers in the southern Andes (Argentina) during the past 13,000 years, *Quaternary Research*, *51*(3), 238-247.

S44 Porter, S. C. (2000), Onset of Neoglaciation in the Southern Hemisphere, *Journal of Quaternary Science*, *15*(4), 395-408.

4.4 Holocene changes of the Southern Westerlies on centennial to multi-millennial timescales inferred from southern Chilean fjord sediments records

Sascha Serno[a,b,c*], Helge W. Arz[a,d], Frank Lamy[e], A. Magaly Caniupán[e], Rolf Kilian[f].

[a]Helmholtz-Zentrum Potsdam, Deutsches GeoForschungsZentrum (GFZ), Telegrafenberg, D-14473 Potsdam, Germany.
[b]Lamont-Doherty Earth Observatory, 61 Route 9W, Palisades, NY 10964-8000, United States of America.
[c]Institut für Geowissenschaften, Universität Potsdam, Karl-Liebknecht-Strasse 24, D-14476 Potsdam, Germany.
[d]Present address: Leibniz-Institut für Ostseeforschung Warnemünde, Seestrasse 15, D-18119 Rostock, Germany.
[e]Alfred Wegener Institut für Polar- und Meeresforschung, Am Alten Hafen 26, D-27568 Bremerhaven, Germany.
[f]Universität Trier, Fachbereich Geographie/Geowissenschaften (FB VI), Lehrstuhl für Geologie, D-54286 Trier, Germany.
*Corresponding author: sserno@ldeo.columbia.edu

Manuscript in preparation

Abstract

The dynamics of the Southern Westerlies are very important in controlling the Antarctic Circumpolar Current (ACC) and the global thermohaline circulation. Despite that, there are still uncertainties about Holocene changes in the Southern Westerlies because of a lack of studies concerning with Southern Westerlies changes on a wide latitudinal range. Here, we present results of a multi-proxy study of high resolution marine sediment cores from within the southern Chilean fjord system from the Aysén fjord (45°23'S) north of the northern margin of the Southern Westerlies core and Canal Concepción (50°31'S) at the northern margin of the core region, and compare our results with previous reconstructions from north and south of our study area to obtain reliable reconstructions of Holocene changes in the Southern Westerlies on centennial- to multi-millennial timescales.

We support previous findings of a latitudinal antiphasing of the Southern Westerlies on multi-millennial timescales during the Holocene (*Lamy et al.*, 2010). A

wet early Holocene indicated by reconstructions from within the core region is also observed at the northern margin, but not north of the northern margin at the Aysén fjord. This pattern resembles modern austral-summer conditions with the Southern Westerlies more confined and strengthened within the core region. Decreasing precipitation in the core region of the Southern Westerlies during the middle and late Holocene, a small increase from 7 to 5.5 cal kyr BP and constant rainfall amounts at the northern margin of the region at Canal Concepción from 5.5 cal kyr BP to the present and strongly increasing precipitation between 4.5 and 2.5 cal kyr BP and constantly high rainfall amounts after 2.5 cal kyr BP at the Aysén fjord support the idea of a more austral-winter pattern of the Southern Westerlies in the middle and late Holocene with less intense westerly winds in the core region but a more latitudinal extension of the same. This is further supported by rainfall records from north of the southern Chilean fjord system (30-41°S) indicating higher precipitation in the late Holocene. These Southern Westerlies dynamics are probably a result of sea-surface temperature (SST) changes in the mid- and low-latitudes of the southern Pacific Ocean. On centennial to millennial timescales, foraminiferal stable oxygen isotope records are characterized by increased variability after about 7 cal kyr BP. This is probably the result of a more frequent and increasing El Niño-Southern Oscillation (ENSO) activity and thereby indicates the strong influence of precipitation changes as well as a strong control by low-latitude climatic changes on the stable oxygen isotope variability in the middle and late Holocene on shorter timescales.

Keywords: paleoclimate; Holocene; Southern Westerlies; southern Chilean fjord system; ENSO

1. Introduction

Southern South America is ideally located to reconstruct Holocene climatic variability in the Southern Hemisphere. This is due to the well developed Southern Westerlies which play an important role in driving the ACC and in the global thermohaline circulation by inducing upwelling within the ACC (e.g., *Kuhlbrodt et al*., 2007). Despite that the Southern Westerlies are a very important circulation system affecting the global climate system, there are still a lot of open questions about their dynamics, especially during the Holocene.

Most Holocene palaeoenvironmental reconstructions from southern South America are based on continental records, primarily glaciological (e.g., *Hulton and Sugden*, 1997; *Mercer*, 1982; *Rabassa and Clapperton*, 1990), limnological (e.g., *Haberzettl et al*., 2007; *Stine and Stine*, 1990) and palynological studies (e.g., *Ashworth*

et al., 1991; *Heusser*, 1989; *Lumley and Switsur*, 1993; *Mancini*, 2009; *Markgraf*, 1989, 1993; Markgraf et al., 1992; Massaferro et al., 2005; Mayr et al., 2007; McCulloch and *Davies*, 2001; *Villa-Martínez and Moreno*, 2007). Since the age control of these continental records can be problematic, comparisons with marine sediment records are essential. However, marine records from the southeast Pacific and Chilean continental slope are still rare and have just been conducted in great quantities in the last 10 years (*Lamy et al*., 1998), with few of these covering the full Holocene period. Furthermore, most of the Holocene palaeoclimatic studies from the continent and open ocean were carried out north of 43°S and south of 53°S (*Ashworth et al*., 1991). Few studies were performed in the western Magellanes fjord region (~53°S; e.g., *Kilian et al*., 2007; *Lamy et al*., 2010). Palaeoclimatic studies from the northern margin of the core region of the Southern Westerlies between 45°S and 50°S are very sporadic. We performed a multi-proxy study on three marine sediment cores (MD07-3114, MD07-3115 and MD07-3124) from two sites in the southern Chilean fjord system. These cores have been drilled during the MD159 - PACHIDERME IMAGES XV Cruise in February 2007. Fjord sediment cores are perfectly suited for conducting high resolution palaeoenvironmental studies since fjords are highly variable environments with high sedimentation rates (*Syvitski et al*., 1987). Thus, there is the possibility of studying terrestrial-, marine-, atmospheric- and glacial-induced palaeoenvironmental changes of local, regional and even global scale on shorter and longer timescales. The results of the multi-proxy approach from the two study sites are compared with results from previous studies in the core region of the Southern Westerlies (*Lamy et al*., 2010) and with palaeoclimatic reconstructions from other studies from South America to reveal Holocene changes in the behaviour of the Southern Westerly wind belt and the causes for these changes.

2. Regional Settings

2.1 Geography

The two study areas are located at around 45°04’S to 45°38’S in the Aysén fjord region and 50°08’S to 50°55’S in the Canal Concepción region in the southern Chilean fjord system (Fig. 1A-C). This system of fjords, channels and islands characterizes the Chilean coastal zone south of 41°S and extends over 1600 km to Tierra del Fuego (*Syvitski et al*., 1987). Two of the three present ice-fields in southern South America, the Hielo Patagónico Norte (HPN; 46-47.5°S) and Hielo Patagónico Sur (HPS; 48-52°S), are located in the hinterland of the fjord system (Fig. 1A; *Hulton and Sugden*, 1997).

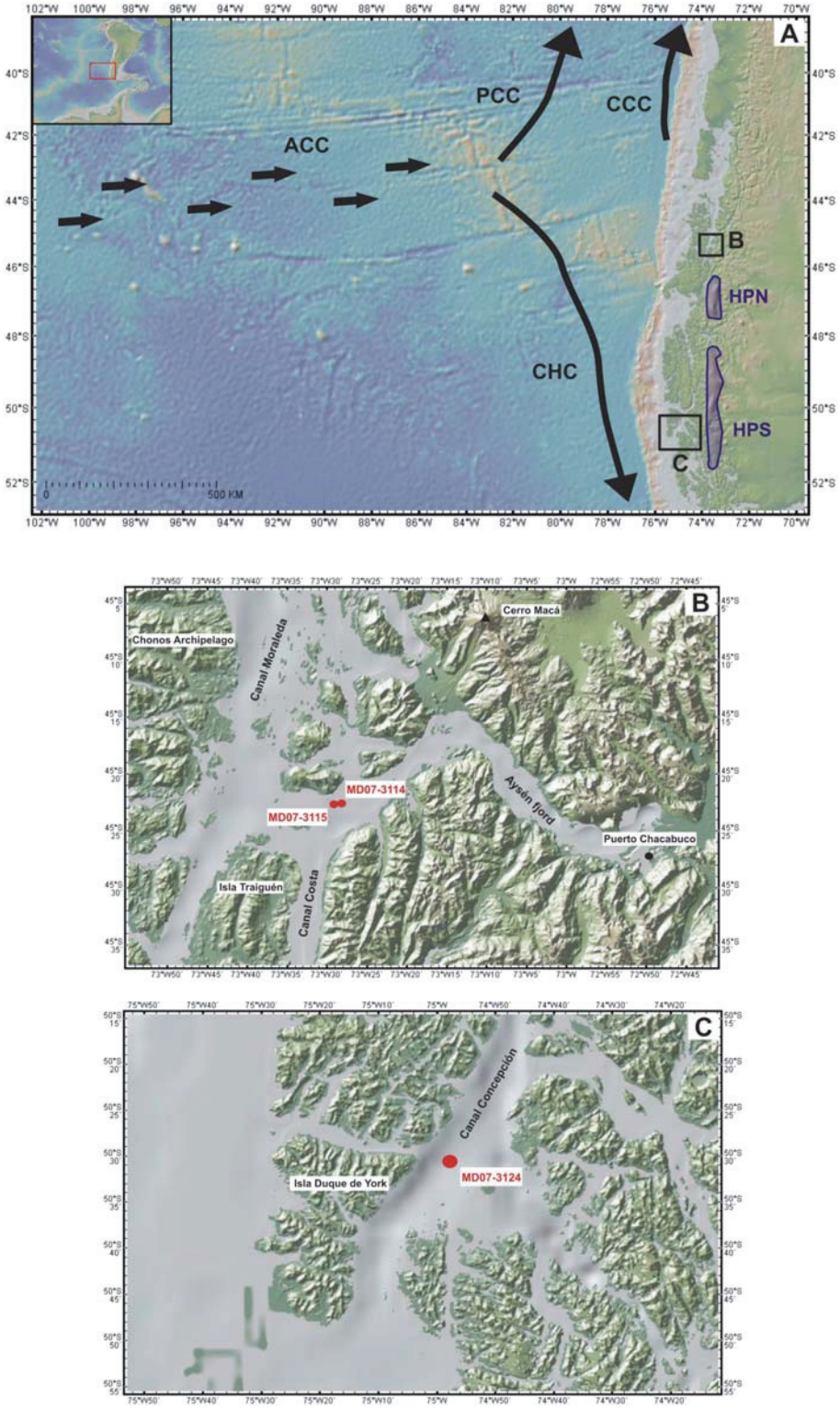

Fig. 1. (A) Regional setting of the broader study area in the northern and central part of the southern Chilean fjord system. Oceanic currents are indicated by black arrows (after *Strub et al*., 1998, and *Tomczak and Godfrey*, 2003). Present Patagonian ice-fields are presented by blue zones (after *Hulton and Sugden*, 1997). The study areas at the mouth of the Aysén fjord (B) and Canal Concepción (C) are indicated by black frames (ACC = Antarctic Circumpolar Current, CCC = Chile Coastal Current, CHC = Cape Horn Current, PCC = Peru-Chile Current, HPN = Hielo

Patagónico Norte, HPS = Hielo Patagónico Sur). (B) Location map of the Aysén fjord cores MD07-3114 and MD07-3115 (after *Kissel and shipboard scientists*, 2007a). The volcano Cerro Macá is indicated by a black triangle. (C) Location map of the Canal Concepción core MD07-3124 (after *Kissel and shipboard scientists*, 2007a).

The Aysén fjord is located east of Canal Moraleda and Canal Costa which separate the Chonos Archipelago and Isla Traiguén to the west from the Chilean mainland to the east (Fig. 1B). The fjord has a length of around 70 km and a mean width of 4.2 km. The maximal water depth is 335 m and the depth of the outer sill is ~70 m, favouring high sedimentation at the fjord bottom (Pickard, 1971). Riverine discharge to the Aysén fjord is dominated by the Aysén River entering the fjord at the head. The fjord is presently not influenced by glaciers.

Canal Concepción is characterised by an average water depth of 405 m (*Pickard*, 1971) and shows no direct river inflow near the study site. This channel is directly connected to the Pacific Ocean and is still under the influence of the Hielo Patagónico Sur located in the hinterland (Fig. 1A, C).

2.2 Present Climate

Chile is characterized by one of the largest latitudinal precipitation gradient. The region north of 31°S is characterized by a present hyper-arid to arid climate. Between 31°S and 42°S, Mediterranean-type climate prevails with dry summers and wet winters due to an increasing influence of the Southern Westerlies. The intensity and latitudinal position of the Southern Westerlies are strongly controlled by the location and strength of the circum-Antarctic low-pressure belt, which is mainly influenced by the extent of the Antarctic sea-ice, and the tropical southeast Pacific high-pressure belt (e.g., *Cerveny*, 1998; *Miller*, 1976). Changing SST and air temperature gradients, as a result of changes in the high- and low-latitude pressure systems, result in latitudinal shifts of the Southern Westerlies, which are annually focused at around 50-55°S (*Schneider et al*., 2003). During austral winters, the Antarctic sea-ice expands. This results in a steeper temperature gradient between pole and equator and an equatorward shift of the southeast Pacific high-pressure belt. This allows a northward expansion of storm tracks associated with the Southern Westerlies. At the same time, zonal winds are reduced in the present core region in southern Chile. During austral summers, the extent of Antarctic sea-ice decreases and the southeast Pacific anticyclone shifts southward, blocking a northward migration and forcing a more poleward position of latitudinally more confined and intensified storm tracks associated with the Southern Westerlies (e.g., *Cerveny*, 1998; *Miller*, 1976).

The latitudes south of ~42°S are penetrated by the Southern Westerlies throughout the year. Consequently, rainfall amounts ranging between 4000 and 10000

mm per year characterize the region between 50°S and 55°S, with an austral summer maximum correlating with stronger westerly winds (*Schneider et al*., 2003). This results in high terrigenous sediment input due to high riverine discharge (e.g., *Cerveny*, 1998; *Markgraf*, 1998; *Miller*, 1976). Besides the latitudinal precipitation gradient, a pronounced meridional precipitation gradient exists south of 34°S due to the presence of the Southern Westerlies and southern Andes as an orographic barrier to the westerly winds (e.g., *Cerveny*, 1998; *Miller*, 1976).

Interannual rainfall variability in central and southern Chile is strongly influenced by the coupled system of ENSO. This is due to a strong influence of ENSO changes on the strength and position of the tropical southeast Pacific high-pressure belt (e.g., *Cerveny*, 1998; *Montecinos and Aceituno*, 2003; *Rutllant and Fuenzalida*, 1991). In contrast to the rainfall variability, ENSO-related SST anomalies just reach south up to 33-36°S (*Strub et al*., 1998). During warm ENSO events (El Niño), the southeast Pacific anticyclone weakens and the Southern Westerly wind belt expands further northward. This results in above-average rainfall amounts in central Chile. During colder phases (La Niña), the southeast Pacific high-pressure belt is strong throughout the year, resulting in reduced precipitation in mid-latitudes due to the Southern Westerly wind belt remaining south of 45°S (e.g., *Cerveny, 1998*; *Montecinos and Aceituno*, 2003; *Rutllant and Fuenzalida*, 1991; *Schneider and Gies*, 2004).

2.3 Oceanography

Central and southern Chile is under the influence of several oceanic currents (*Tomczak and Godfrey*, 2003). The ACC as the southern boundary current of the subtropical gyre is driven by the Southern Westerlies and brings cold, relatively fresh and nutrient-rich subpolar waters to the Chilean coast. At ~43°S, the ACC splits into a northward-flowing branch and the Cape Horn Current (CHC) flowing southward (Fig. 1A). The northward-flowing branch is divided into an oceanic current (Peru-Chile Current; PCC) and a coastal current (Chile Coastal Current; CCC; Fig. 1A) separated north of 35°S by the poleward-flowing Peru-Chile Countercurrent (PCCC). Within 300 km off the coast, the surface waters are underlain by the southward-flowing Peru-Chile Undercurrent (PCU) flowing over the continental slope and outer shelf south to ~48°S. Deeper water masses comprise the northward-flowing Antarctic Intermediate Water (AAIW), the southward-flowing Pacific Deep Water (PDW) and the northward-flowing Antarctic Bottom Water (AABW) in the Chile Trench (*Strub et al*., 1998).

In the southern Chilean fjord system, the water column is typically stratified and characterized by a two-layer estuarine circulation, with the deep-water layer mainly comprising saline waters flowing into and the thin surface layer comprising fresh waters flowing out of the fjord (*Hromic et al*., 2006; *Pickard*, 1971; *Silva et al*.,

1997). The two-layer stratification causes strong physical and chemical gradients in the fjord water column. These gradients differ between distinct fjords as a result of changing fjord and channel physiographies (*Hromic et al*., 2006; *Syvitski et al*., 1987). Canal Concepción waters are characterized by strong marine conditions. Therefore, the deep-water layer comprises saline Pacific surface water masses. In the Aysén fjord, the deep-water layer is primarily dominated by the riverine freshwater entering the fjord. Saline Pacific surface waters do not play an important role in this enclosed fjord basin since shallow sills surrounding the Aysén fjord prevent a pronounced inflow at the bottom. At present, stagnant bottom waters in southern Chilean fjords and channels are uncommon, probably due to an absence of shallow sills (*Pickard*, 1971; *Silva et al*., 1997).

3. Material and Methods

3.1 Marine Sediment Cores from the MD159 - PACHIDERME IMAGES XV Cruise

The three long piston cores MD07-3114, MD07-3115 and MD07-3124 were drilled during the MD159 - PACHIDERME IMAGES XV Cruise in February 2007 (*Kissel and shipboard scientists*, 2007a, b).

The coring sites of the two inner fjord cores MD07-3114 and MD07-3115 at the mouth of the Aysén fjord (~45°23'S; Fig. 1B and Table 1) were selected based on the sediment echography. It indicates a very thick sediment cover of ~60 m (Fig. 2). The outer fjord core MD07-3124 was drilled in the southwestern part of Canal Concepción (~50°31'S; Fig. 1C and Table 1). Based on echosounder profiles, a ~50 m thick post-glacial sediment package characterizes this coring site.

Table 1. Core name, latitude and longitude, location details, water depth and core length of the marine sediment cores used in this thesis.

Core name	Latitude	Longitude	Location details	Depth (m)	Length (m)
MD07-3114	45°23.0107'S	73°28.0342'W	Mouth of Aysén fjord, just north of Isla Traiguén (Figure 1)	294	31.78
MD07-3115	45°23.1451'S	73°29.5896'W	Mouth of Aysén fjord, just north of Isla Traiguén (Figure 1)	319	31.72
MD07-3124	50°30.9616'S	74°58.3325'W	Canal Concepción, northeast of Isla Duque de York (Figure 1)	564	22.25

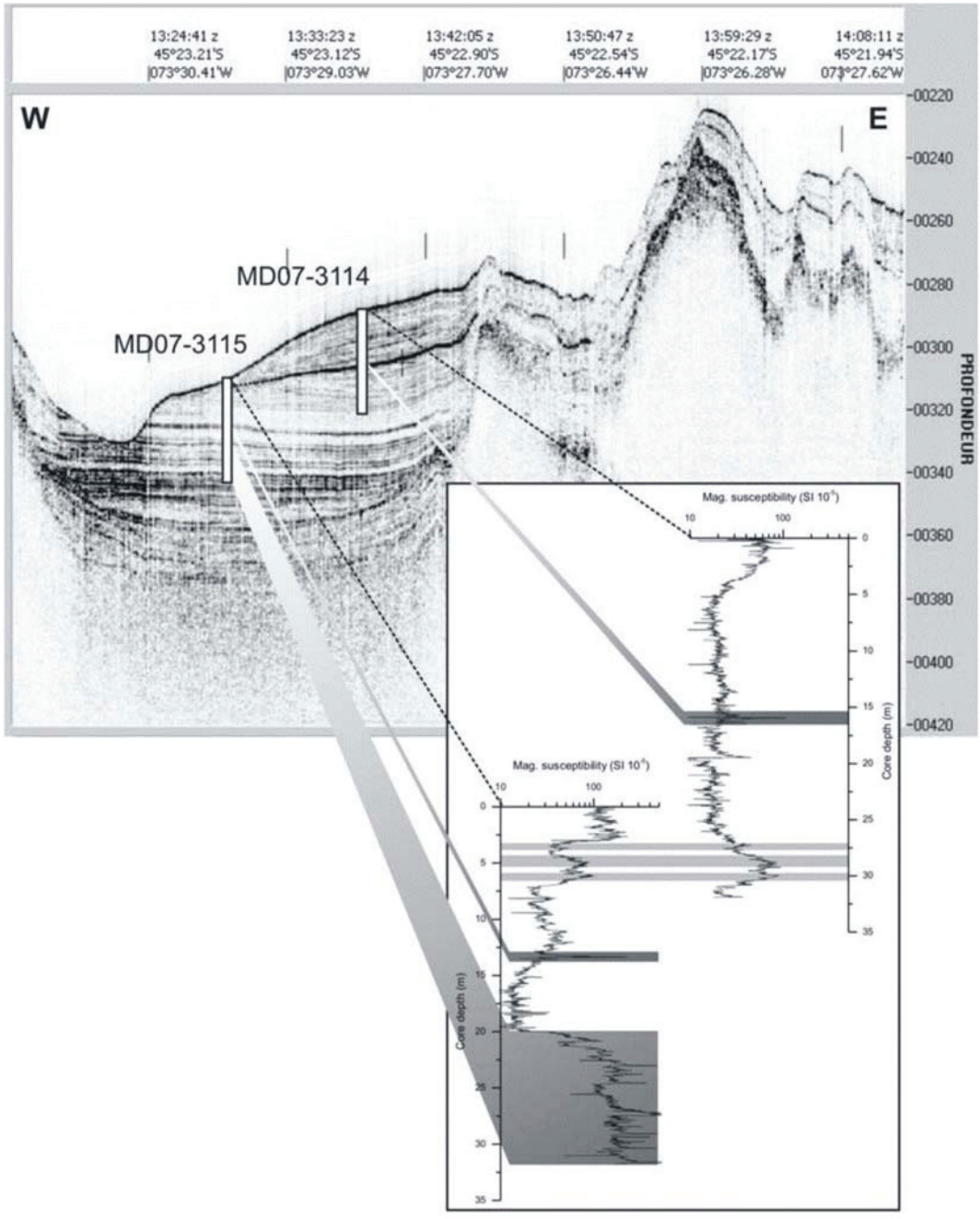

Fig. 2. Sediment echography and magnetic susceptibility data (MD07-3115 on the left, MD07-3114 on the right) measured onboard the R/V Marion Dufresne and used for the combination of the two cores. Very high magnetic susceptibility values are indicated by dark grey bars. Light grey bars indicate the correlation of both cores.

Low field magnetic susceptibility was measured onboard the M/V Marion Dufresne with an interval of 2 cm using a Geotek Multi-Sensor-Core-Logger track. The results were used to combine the marine sediment cores MD07-3114 and MD07-3115 to one long core. An overlap of ~7 m is indicated in which the sedimentation rates are

the same in both cores (Fig. 2). As a result, the cores were combined at a core depth of 30.31 m in core MD07-3114 and 6.49 m in MD07-3115 to create the core MD07-3114/15 with a core length of 55.54 m.

3.2 Dating Method

The age models of the cores are based on ^{14}C-AMS (accelerator mass spectrometer) ages and linear interpolation between the age control points. The age model of MD07-3114/15 is based on 21 radiocarbon ages. 8 plant and 5 mollusc samples were dated in core MD07-3114. In core MD07-3115, 2 plant and 6 mollusc samples were dated. The age model of MD07-3124 is based on 16 mollusc sample ages. All but 7 sample ages were measured at the National Ocean Sciences Accelerator Mass Spectrometer (NOSAMS) facility of the Woods Hole Oceanographic Institution in Woods Hole, Massachusetts (von *Reden et al*., 1992, 1994). The other 7 sample ages were measured at the Leibniz-Labor AMS facility of the Christian-Albrechts University in Kiel, Germany (*Nadeau et al*., 1997). All radiocarbon ages were corrected for 13C. Detailed information about the radiocarbon dating is presented and discussed in Chapter 4.

3.3 Stable Oxygen Isotope Composition of Planktic and Benthic Foraminifera

For the stable oxygen isotope measurements on planktic and benthic foraminifera, MD07-3114 was sampled with a 24 cm interval. The core MD07-3115 was sampled with an interval of 4 cm from 0 to 2 m core depth, 8 cm from 2 to 9.52 m, 12 cm from 9.52 to 18.52 m and 16 cm from 18.52 to 31.64 m core depth. MD07-3124 was sampled with an interval of 5 cm from 0 to 7.8 m and 25 cm on average from 7.8 to 22.2 m core depth.

At the Helmholtz-Zentrum Potsdam (Deutsches GeoForschungsZentrum, GFZ), 4 specimens of the planktic foraminifer *Globigerina bulloides* were measured per sample from MD07-3124 within a size range of 200-300 µm. 2-7 specimens of the benthic foraminifer *Nonionella opima* were measured per sample from core MD07-3124 in every size available. Since test measurements of stable oxygen isotope compositions in MD07-3114/15 on the benthic foraminiferal species *Nonionella opima* and *Nonionella auris* indicated identical stable oxygen isotope ratios, 2-12 specimens of a mixture of both were measured per sample from MD07-3114/15 in every size available. They are not enough planktic foraminifera to perform stable oxygen isotope measurements for this core.

Stable oxygen isotope measurements were performed using a Finnigan MAT 253 IRMS that is directly connected with a Kiel IV Carbonate Device. A working standard CO_2 gas used for the stable oxygen isotope measurements was calibrated

against V-PDB via the NBS-19 working standard. $^{18}O/^{16}O$ ratios are presented in the typical delta notation ($\delta^{18}O$) and in ‰ versus V-PDB (*Coplen*, 1996; *Hut*, 1987). The analytical standard deviation for stable oxygen isotope measurements was <0.06‰ based on replicate measurements on carbonate standards (Laboratory for Stable Isotopes and Elemental Analysis, GFZ Potsdam).

Because of an effect of sea-level changes on the foraminiferal $\delta^{18}O$ composition, the measurement results were further corrected for this effect using the global sea-level curve from *Fleming et al*. (1998). An additional effect due to changing isotopic signature of the precipitation (*Wolff et al*., 1998) is unlikely since the study sites are located within the source area of the Southern Westerlies.

3.4 Organic Geochemical Proxies

Measurements of total organic carbon (C_{org}), total carbon (C_{total}) and total nitrogen (N_{total}) contents were performed at the GFZ Potsdam for core MD07-3114/15 and at the Alfred Wegener Institut für Polar- und Meeresforschung (AWI) at Bremerhaven for MD07-3124. The cores were sampled at the AWI Bremerhaven with a ~50-year interval for MD07-3114/15 and a ~100-year interval for MD07-3124.

C_{org}, C_{total} and N_{total} contents were measured using a Euro EA3000 Series - EuroVector Elemental Analyser. The homogenised sediment samples for C_{org} measurements were treated with hydrochloric acid 3% and 20% prior to the measurements to remove the inorganic carbon fraction (*Meyers and Teranes*, 2001). The measurement results are presented in weight% (weight percentages). The analytical precision was <5% based on repeated measurements of samples and standards (Laboratory for Stable Isotopes and Elemental Analysis, GFZ Potsdam). C_{org} and N_{total} contents were further used to calculate mass C_{org}/N_{total} ratios. These mass C_{org}/N_{total} ratios were multiplied by 1.167 (the ratio of atomic weights of carbon and nitrogen) to obtain atomic C_{org}/N_{total} ratios.

Since the inorganic carbon fraction removed for C_{org} measurements is mainly carbonate (*Holmes et al*., 1999), we calculated the carbonate content $CaCO_3$ using the following equation:

$$CaCO_3 = (C_{total} - C_{org}) \times 8.333$$

Using the calculated $CaCO_3$ contents, we computed the mass accumulation rate of carbonate ($CaCO_3$AR) by multiplying the measured $CaCO_3$ contents, the dry bulk density (DBD) and the sedimentation rate (SR; e.g., *Müller and Suess*, 1979). The results are presented in g m^{-2} yr^{-1}.

The equal number of samples from the same core depths used for C_{org}, C_{total} and N_{total} measurements in core MD07-3114/15 was used for measurements of the

stable carbon isotope composition of organic matter ($\delta^{13}C_{org}$). The sample preparation was the same as for the C_{org} measurements. Stable carbon isotope measurements on organic matter were performed at the GFZ Potsdam using a Finnigan MAT Deltaplus XL IRMS in combination with a CarloErba NC 2500 series elemental analyser and Finnigan MAT Continuous Flow Interface ConFlo III. The working standard gas was calibrated against V-PDB via the USGS24 and IAEA-CH-7 standards. $\delta\ ^{13}C_{org}$ values are presented in ‰ versus V-PDB (*Coplen*, 1996; *Hut*, 1987). The analytical precision was <0.2‰ based on replicate measurements of standards (Laboratory for Stable Isotopes and Elemental Analysis, GFZ Potsdam).

Since there are specific $\delta^{13}C_{org}$ values for C3 land plants (around -27‰) and marine algae (around -20‰; e.g., *Meyers*, 1994, 1997), these two end-members were used to calculate the terrestrial and marine portions of C_{org}. Terrestrial C_{org} accumulation rates ($C_{org}AR_{terr}$) were computed using the same approach as for $CaCO_3AR$.

3.7 Iron and Calcium Measurements

X-ray fluorescence (XRF) measurements of iron and calcium were performed at the AWI Bremerhaven using the Avaatech XRF Core-Scanner. XRF measurements were performed on MD07-3114/15 and MD07-3124 with an interval of 1 cm. The results of Fe and Ca intensities are presented in 1000 cps (measured XRF intensity).

4. Chronology

The age control points of MD07-3114/15 are presented in Table 2. Mollusc ^{14}C ages were corrected for the reservoir effect before conversion to calendar ages using terrestrial calibration curves. Since published reservoir ages for southern Chile are sparse, the difference between the radiocarbon age curves of mollusc and plant samples from MD07-3114 was used to calculate an average total reservoir age of ~550 years (Fig. 3A). This total reservoir age was subtracted from the mollusc ^{14}C ages to obtain “terrestrial” ^{14}C ages. The final result of the correction can be seen in Fig. 3B, with both curves almost identical. Due to only two dated wood samples with almost the same ^{14}C age in MD07-3115 and due to the proximity to the coring site of MD07-3114, the total reservoir age from MD07-3114 was used to correct mollusc sample ages in MD07-3115.

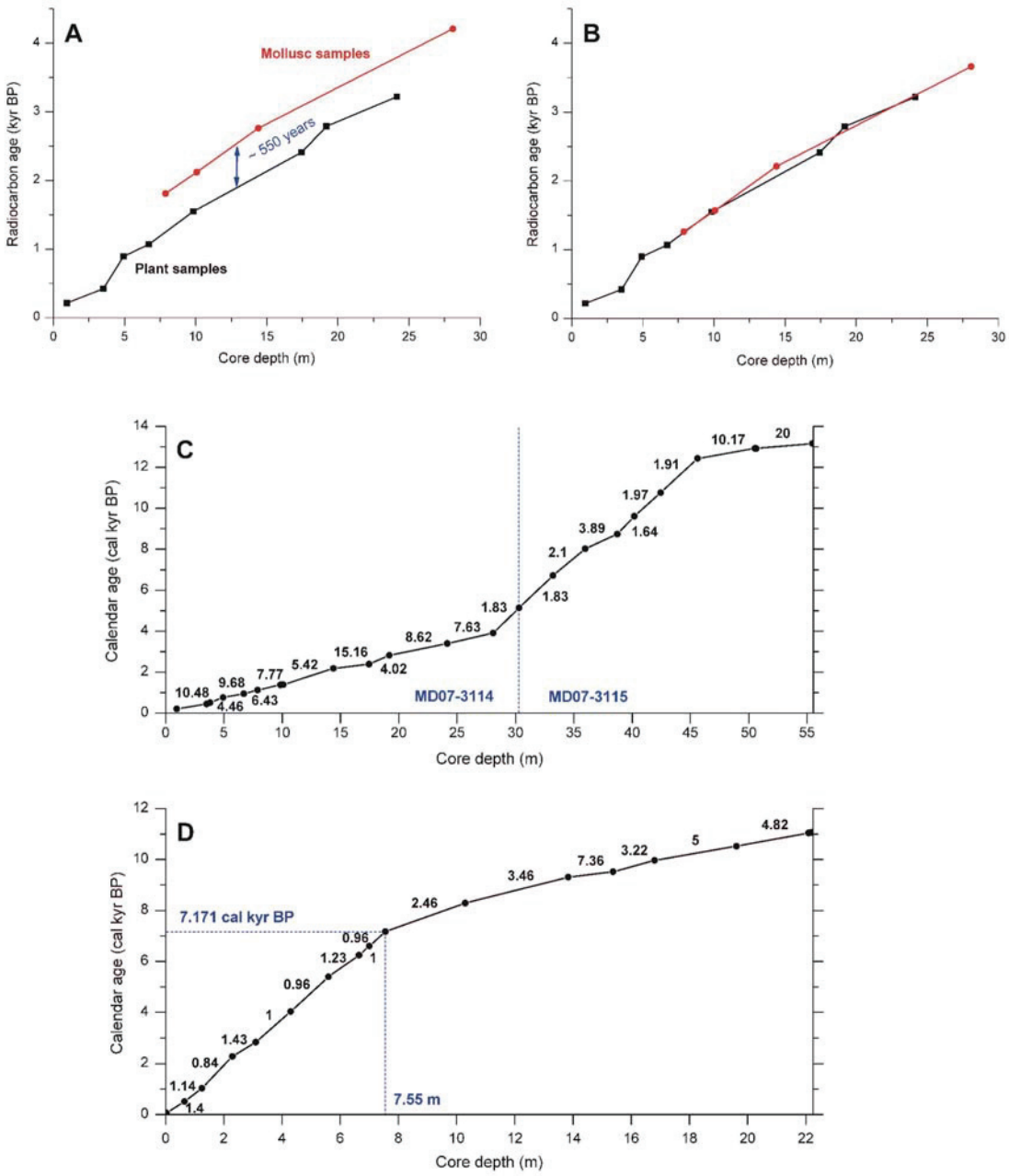

Fig. 3. (A) Reservoir effect correction for mollusc ^{14}C ages in MD07-3114. Depth versus radiocarbon age plot for the samples from MD07-3114 with the plant samples in black and mollusc samples in red. The difference between the two curves is equivalent to the total reservoir age. (B) Depth versus radiocarbon age plot with the reservoir-corrected mollusc sample ages in red and plant samples in black. (C) Age model of core MD07-3114/15. The blue dashed line indicates the core combination depth at 30.31 m in core MD07-3114. (D) Age model of core MD07-3124. The blue dashed line indicates the depth of a pronounced sedimentation rate change at 7.55 m. The numbers above and below the curves indicate the sedimentation rates in m/kyr between two dating points.

The conversion to calendar ages was performed using the Calib 5.0.2 software (*Stuiver et al*., 2005). The mean of the one-sigma value was used for the calendar age of the sample. For all but the three oldest samples in MD07-3114/15 the SHCal04 calibration curve was used for the conversion to calendar ages (*McCormac et al*., 2004). The last three samples have calendar ages older than 11 cal kyr BP. Therefore, their ^{14}C ages were converted using the IntCal04 calibration curve (*Reimer et al*., 2004).

The age model of MD07-3114/15 indicates very high sedimentation rates with an average value of 15.084 m/kyr between the extrapolated core base age of ~13.169 and 12.435 cal kyr BP (Fig. 3C). The period between ~12.435 and 5.128 cal kyr BP, the calendar age of the core combination depth, is the one with the lowest average sedimentation rates with ~2.222 m/kyr.

Since the last age control point of core MD07-3114 at a core depth of 28.08 m and with a calendar age of ~3.91 cal kyr BP is in the overlapping part of MD07-3114 and MD07-3115, in which both cores show the same sedimentation rates, the core depth of this age control point in MD07-3115 was determined at 4.26 m using the magnetic susceptibility data. Using the sedimentation rate between this calculated age control point and the following dating point in MD07-3115, the age of the core combination depth was interpolated at ~5.128 cal kyr BP (Fig. 3C). The mean sedimentation rate for the period from ~5.128 to 3.91 cal kyr BP is 1.831 m/kyr. The last ~3.91 kyr are characterized by very high sedimentation rates with an average of 8.467 m/kyr. An assumption of zero age at the core top was not made because it would require a pronounced change in sedimentation rates compared to the sedimentation rate between the following two age control points. Based on the sedimentation rate between these following dating points, the age of the core top is ~0.108 cal kyr BP. This is most probably due to some sediment loss during the coring procedure or erosion at the sediment surface due to strong bottom currents.

The age control points of MD07-3124 are presented in Table 3. Since there was no terrestrial material available for dating, a published local reservoir age of $\Delta R = 211 \pm 40$ years from the region (*Ingram and Southon*, 1996) was utilized for the conversion of radiocarbon to calendar ages using the Marine04 calibration curve (*Hughen et al*., 2004) and the Calib 5.0.2 software (*Stuiver et al*., 2005).

The age model of MD07-3124 indicates very high sedimentation rates throughout the core and a sudden change in sedimentation rates at a core depth of 7.55 m which is equivalent to a calendar age of ~7.171 cal kyr BP (Fig. 3D). From the core base with an extrapolated calendar age of ~11.071 cal kyr BP to 7.171 cal kyr BP, the average sedimentation rate is very high with 4.388 m/kyr. From 7.171 cal kyr BP to the present, the sedimentation rates are lower, averaging 1.108 m/kyr. An assumption of zero age at the core top was not made, based on the same argumentation as for core MD07-3114/15. Using the mean sedimentation rate of the following age control points, the age of the core top is approximately 0.045 cal kyr BP.

Table 2. Age control points of cores MD07-3114/15

Core name	Sample name[1]	Depth (m)	Corrected depth[2] (m)	^{14}C age[3] (kyr BP)	± Error (kyr)	Calendar age[4] (cal kyr BP)	SR (m/kyr)	Dated material	Calibration curve
MD07-3114	WHOI 69352	0.95	0.95	0.215	0.030	0.199	4.762	leaf fragments	SHCal04
MD07-3114	WHOI 69353	3.51	3.51	0.420	0.030	0.444	10.480	leaf fragments	SHCal04
MD07-3114	WHOI 69360	3.82	3.82	0.490	0.030	0.506	4.981	scaphopods	SHCal04
MD07-3114	WHOI 69354	4.93	4.93	0.895	0.030	0.755	4.456	leaf fragments	SHCal04
MD07-3114	WHOI 69355	6.71	6.71	1.070	0.035	0.939	9.678	leaf fragments	SHCal04
MD07-3114	WHOI 69356	7.89	7.89	1.260	0.035	1.123	6.431	bivalvae	SHCal04
MD07-3114	WHOI 69357	9.84	9.84	1.550	0.035	1.374	7.769	leaf fragments	SHCal04
MD07-3114	WHOI 69363	10.08	10.08	1.570	0.030	1.388	16.970	scaphopods	SHCal04
MD07-3114	WHOI 69364	14.40	14.40	2.210	0.030	2.185	5.417	bivalvae	SHCal04
MD07-3114	WHOI 69357	17.45	17.45	2.410	0.035	2.386	15.163	leaf fragments	SHCal04
MD07-3114	WHOI 69358	19.19	19.19	2.790	0.055	2.820	4.017	leaf fragments	SHCal04
MD07-3114	WHOI 69359	24.16	24.16	3.220	0.035	3.396	8.615	leaf fragments	SHCal04
MD07-3114	WHOI 69365	28.08	28.08	3.660	0.030	3.910	7.630	bivalvae	SHCal04
MD07-3114	combi depth	30.31	30.31			5.128	1.831		
MD07-3115	KIA 33284	9.40	33.22	5.960	0.035	6.717	1.831	bivalvae	SHCal04
MD07-3115	WHOI 69366	12.16	35.98	7.260	0.055	8.031	2.101	bivalvae	SHCal04
MD07-3115	WHOI 69367	14.92	38.74	7.970	0.040	8.741	3.885	bivalvae	SHCal04
MD07-3115	WHOI 69368	16.36	40.18	8.750	0.040	9.620	1.638	bivalvae	SHCal04
MD07-3115	KIA 33285	18.62	42.44	9.555	0.050	10.768	1.968	bivalvae	SHCal04
MD07-3115	WHOI 69369	21.80	45.62	10.450	0.050	12.435	1.908	scaphopods	IntCal04
MD07-3115	WHOI 69370	26.72	50.54	11.000	0.050	12.919	10.168	wood	IntCal04
MD07-3115	KIA 33286	26.83	50.65	11.008	0.050	12.924	20.000	wood	IntCal04
MD07-3115	last sample	31.64	55.46			13.165	20.000		
MD07-3115	core base	31.72	55.54			13.169	20.000		

Table 3. Age control points of core MD07-3124

Sample name[1]	Depth (m)	^{14}C age (kyr BP)	± Error (kyr)	Calendar age[2] (cal kyr BP)	SR (m/kyr)	Dated material
WHOI 69340	0.03	0.685	0.030	0.066		bivalvae
WHOI 69341	0.65	1.110	0.030	0.509	1.401	bivalvae
WHOI 69342	1.25	1.690	0.030	1.033	1.144	bivalvae, scaphopods
WHOI 69343	2.30	2.830	0.035	2.278	0.843	bivalvae, scaphop., benthic foraminifera
KIA 33278	3.10	3.295	0.030	2.836	1.434	echinoderm
WHOI 69344	4.30	4.230	0.040	4.040	0.997	scaphopods
WHOI 69345	5.60	5.280	0.035	5.400	0.956	bivalvae, scaphop., benthic foraminifera
WHOI 69346	6.65	6.050	0.030	6.251	1.234	bivalvae, scaphopods
WHOI 69347	7.00	6.380	0.040	6.600	1.001	scaphopods
KIA 33279	7.55	6.850	0.035	7.171	0.963	bivalvae
WHOI 69348	10.30	8.040	0.060	8.291	2.456	bivalvae, scaphopods
WHOI 69349	13.83	8.840	0.055	9.311	3.459	bivalvae
KIA 33280	15.38	9.090	0.045	9.522	7.363	scaphopods
WHOI 69350	16.80	9.360	0.045	9.963	3.220	scaphopods
KIA 33281	19.62	9.880	0.045	10.526	5.009	bivalvae
WHOI 69351	22.10	10.250	0.050	11.040	4.820	bivalvae, scaphopods
last sample	22.20			11.061	4.820	
core base	22.25			11.071	4.820	

5. Results and Discussion

5.1 Local and regional palaeoenvironmental changes at the Aysén fjord during the late glacial and Holocene

For a discussion of late glacial and Holocene local and regional palaeoenvironmental changes at the Aysén fjord, we obtained $\delta^{18}O_{benthic}$ ($\delta^{18}O$ composition of the mixture of *Nonionella opima* and *Nonionella auris*), Fe and Ca intensity as well as $CaCO_3AR$ and $C_{org}AR_{terr}$ data from core MD07-3114/15 (Figure 4A-E). The $\delta^{18}O$ composition of planktic and benthic foraminiferal shells is controlled by the temperature, global ice volume and salinity (e.g., *Shackleton and Opdyke*, 1973). Due to the correction of the $\delta^{18}O$ ratios for the global ice effect, we were able to reveal local influences on the foraminiferal $\delta^{18}O$ variability due to temperature and/or salinity changes introduced by freshwater influx.

Since there is almost a total absence of planktic foraminifera throughout the late glacial and Holocene in the Aysén fjord core MD07-3114/15 and due to the presence of the benthic species *Nonionella opima* and *Nonionella auris* as indicators for dysoxic conditions (e.g., *Sen Gupta and Machain-Castillo*, 1993; *Tapia et al*., 2008), we propose a constant freshwater lens in the surface water layer of the Aysén fjord. This can be explained by a constant high freshwater influx into the fjord and the proximity of the coring site to river inflows. Since the Aysén fjord is an enclosed fjord basin, the deep-water layer in the fjord is not strongly influenced by saline Pacific waters. The whole circulation system in the enclosed fjord is probably dominated by the fresh surface waters, resulting in constant low ventilation in the deeper waters and resulting dysoxic conditions.

Higher Fe intensities indicate high terrigenous clastic input, either due to changing glacier activity in the hinterland or rainfall-induced freshwater input into the fjords. Ca intensities and carbonate accumulation rates in marine sediments are strongly controlled by the abundance of carbonate skeletal material. Therefore, they are used as proxies for marine productivity (e.g., *Lamy et al*., 1998). An additional effect of terrigenous input of detrital carbonates is possible. The Fe intensity record shows generally high intensities throughout the Aysén fjord core. This indicates a constant high input of terrigenous clastic material by riverine inflow. Highest intensities before 11.5 to 11.3 cal kyr BP indicate still strong glacier retreat and resulting high meltwater input into the fjord (Fig. 4B). The lithology characterised by partly silt-bearing grey clays and several thin silt/sand layers and lenses also provides evidence for mainly glacial-controlled sedimentation before ~11.3 cal kyr BP. After the end of the glacier retreat at ~11.5-11.3 cal kyr BP, the Aysén fjord environment is no longer influenced by glacier activity. This is indicated by the lithology with greyish olive, diatom-bearing to diatomaceous clays with lower siliciclastic contents. During the phase of the strongest and final glacier retreat between 12.5 and 11.3 cal kyr BP, slightly increasing values in the $CaCO_3$ accumulation rate and Ca intensity indicate a first pronounced overflow of marine waters over the sill due to the combined effect of the global sea-level rise and isostatic rebound (Fig. 4C, D). Since there is no information about isostatic rebound rates, the exact timing of the flooding of the fjord basin cannot be determined. The increasing trend in $CaCO_3AR$ and Ca intensity culminates at ~11.2 cal kyr BP. The correlation with a decreasing trend to lowest Fe intensities indicates not only the first pronounced marine signal in the fjord record after the flooding of the basin, but also points to a low influence of detrital carbonate input on the variability of the $CaCO_3AR$ and Ca intensity records in the late glacial and early Holocene (Fig. 4B-D). Low terrestrial C_{org} accumulation rates signify an undeveloped vegetation cover in the Aysén fjord region before 11.3 cal kyr BP (Fig. 4E). After 11.3 cal kyr BP, an increasing trend in $C_{org}AR_{terr}$ culminating at ~8.5 cal kyr BP indicates a developing vegetation cover in the hinterland. This trend correlates with the trend in the Fe intensity record,

thereby indicating the variation of Fe intensities with rainfall-induced freshwater input into the Aysén fjord after the final glacier retreat at 11.5-11.3 cal kyr BP (Fig. 4B). This small higher rainfall event also correlates with low marine productivity, except for a short productivity peak at ~8.2 cal kyr BP (Fig. 4C, D). After ~6 cal kyr BP, the anti-correlation of the $CaCO_3AR$ and Ca intensity records and correlation of the Ca and Fe intensity records indicate a dominant control of detrital carbonate input on the Ca intensity variability (Fig. 4B-D). The $CaCO_3AR$ record still indicates changes in marine productivity. High riverine-induced clastic input between 5.5 and 4 cal kyr BP is probably a result of a short-scale glacier advance in the hinterland since there is no change in the $C_{org}AR_{terr}$ record with very low values between 8 and 4 cal kyr BP indicating constantly low precipitation in the middle Holocene (Fig. 4B, C, E). Therefore, lower temperatures seem to be the determinant on glacier activity between 5.4 and 4 cal kyr BP. The timing of this glacier advance fits perfectly with the timing of known glacier advances between 5.4 and 4.2 cal kyr BP in southern South America (e.g., *Mercer*, 1982; *Rabassa and Clapperton*, 1990).

After 4 cal kyr BP, high $C_{org}AR_{terr}$ values point to high riverine input of terrigenous organic material into the fjord as a result of highest rainfall in the course of the Holocene during the late Holocene in the Aysén fjord region (Fig. 4E). Since the $C_{org}AR_{terr}$ record perfectly correlates with the $CaCO_3AR$ record indicating higher marine productivity in the late Holocene, marine productivity seems to be triggered by riverine-induced nutrient input during the last 4 kyr (Fig. 4D, E). Since the Fe intensity record shows a slightly decreasing trend in the late Holocene (Fig. 4B), marine productivity seems not be limited by micronutrients like iron. It remains uncertain why there are low Fe and Ca intensities in the late Holocene with high precipitation indicated by other proxies. It can be a result of high organic input strongly dominating over clastic input during the late Holocene. This is in contrast to the time period between 5.4 and 4 cal kyr BP with clastic input dominating over organic input.

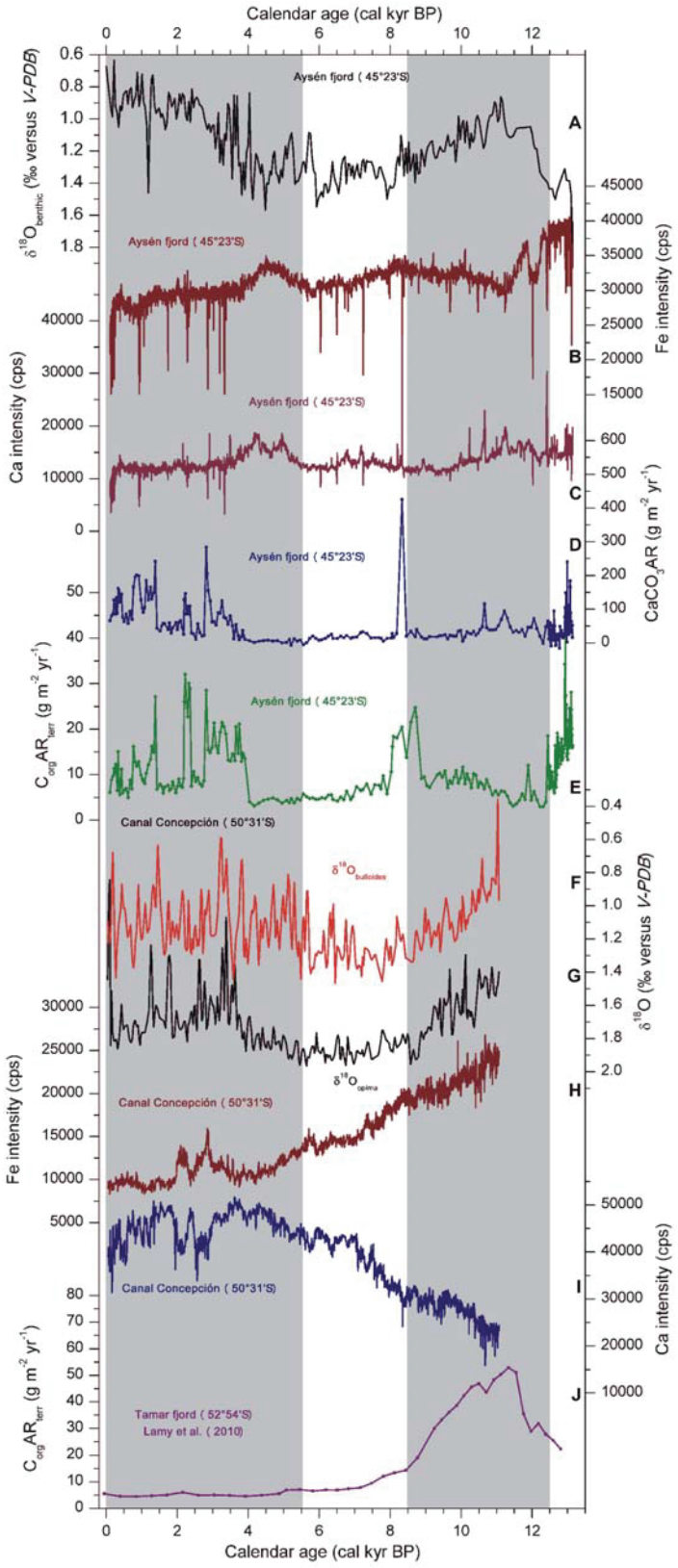

Fig. 4. Records of palaeoenvironmental changes for the Aysén fjord core MD07-3114/15 north of the northern margin of the present Southern Westerlies core region, the Canal Concepción core MD07-3124 at the northern margin and the Tamar fjord just inside the present Southern

Westerlies core region. (A) $\delta^{18}O_{benthic}$ record of MD07-3114/15. (B) Fe intensity record of MD07-3114/15. (C) Ca intensity record of MD07-3114/15. (D) $CaCO_3AR$ record of MD07-3114/15. (E) $C_{org}AR_{terr}$ record of MD07-3114/15. (F) $\delta^{18}O$ bulloides record of the planktic foraminifer *Globigerina bulloides* from MD07-3124. (G) $\delta^{18}O$ opima record of the benthic foraminifer *Nonionella opima* from MD07-3124. (H) Fe intensity record of MD07-3124. (I) Ca intensity record of MD07-3124. (J) $C_{org}AR_{terr}$ record from the Tamar fjord core TM1 (*Lamy et al*., 2010). The first grey bar between 12.5 and 8.5 cal kyr BP indicates the time of enhanced and compressed Southern Westerlies core in the early Holocene (after *Lamy et al*., 2010). The second grey bar between 5.5 cal kyr BP and the present represents the time of reduced precipitation and less intense Southern Westerlies core (after *Lamy et al*., 2010).

Since $CaCO_3$ accumulation rates are very low in the Aysén fjord record during the Holocene (Fig. 4D), except for the late Holocene, the marine influence seems not to be strong in this enclosed fjord. To support this assumption, we measured $\delta^{13}C_{org}$, C_{org} and N_{total} values to differentiate between different sources of organic matter. The values indicate that the fjord basin was dominated by more limnic or brackish conditions with some input of C3 land plant material into the basin before 12.25 cal kyr BP (Fig. 5). A first marine signal between 12.25 and 11.95 cal kyr BP signifies a first flooding of the Aysén fjord basin. Afterwards, the values indicate a mixture of organic matter produced by land plants and marine algae and a small trend to more marine conditions during the early and middle Holocene and stronger marine conditions in the late Holocene (Fig. 5).

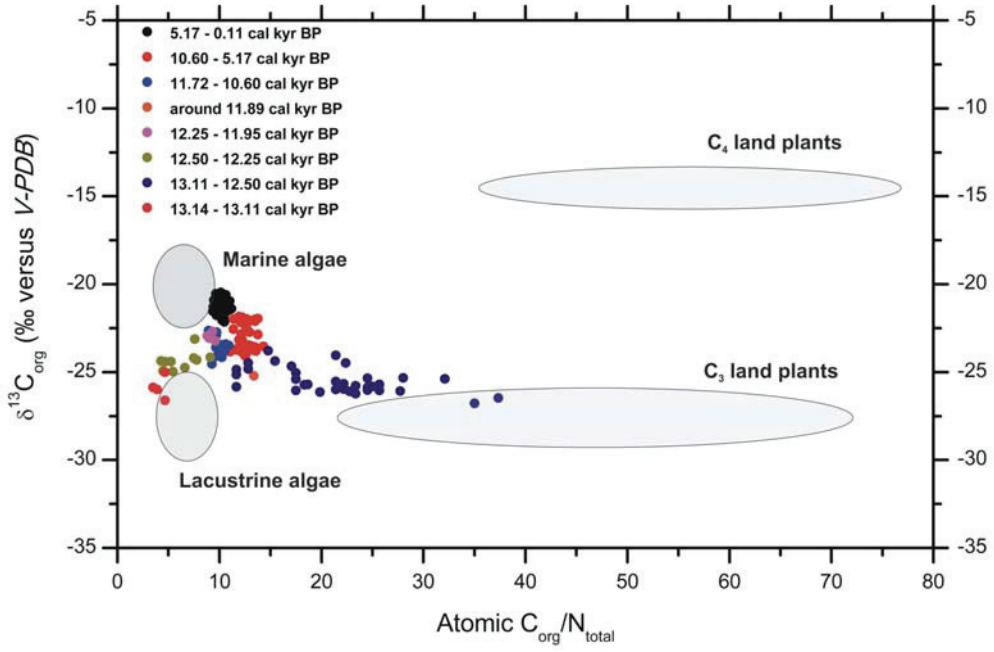

Fig. 5. Atomic C_{org}/N_{total} versus $\delta^{13}C_{org}$ ratios from the Aysén fjord core MD07-3114/15. The ratios are grouped, with the groups indicating different time ranges (signified by differing colours). Marine algae produce organic matter with a $\delta^{13}C_{org}$ composition of about -18 to -22 ‰ versus V-

PDB. C3 land plants and lacustrine algae have typical $\delta^{13}C_{org}$ compositions of around -26 to -28 ‰ versus V-PDB. C4 land plants, on the other side, produce $\delta^{13}C_{org}$ values of circa -14 ‰ versus V-PDB (*Meyers*, 1994, 1997). Since the $\delta^{13}C_{org}$ composition cannot be used to differentiate between organic matter produced by C3 land plants and lacustrine algae or organic matter produced in brackish conditions, atomic C_{org}/N_{total} ratios were calculated. Organic matter produced by algae is characterised by ratios of 4-10. C3 and C4 land plants produce ratios of higher than 20 respectively ~32 (*Meyers*, 1994; *Meyers and Teranes*, 2001).

Lower $\delta^{18}O_{benthic}$ values between ~12 and 8.5 cal kyr BP are probably not a result of lower salinity due to rainfall-induced freshwater input since this time period is characterised by lower precipitation at the Aysén fjord site, as indicated by the $C_{org}AR_{terr}$ record (Fig. 4A, E). However, this period of lower $\delta^{18}O_{benthic}$ values correlates well with the early Holocene climatic optimum between 11.5 and 9 cal kyr BP as observed in 11 Antarctic ice-core records (*Masson et al*., 2000; *Steig et al*., 1998) and other palaeoclimatic records from southern South America (e.g., *Kaiser et al*., 2005, 2008). Therefore, we propose a dominant control of temperature on the $\delta^{18}O_{benthic}$ variability in the early Holocene. Between 8.5 and 4.5 cal kyr BP, highest $\delta^{18}O_{benthic}$ ratios throughout the record indicate either lower temperatures or low precipitation. The decreasing trend in $\delta^{18}O_{benthic}$ values from 4.5 cal kyr BP to the present, with the strongest trend between 4.5 and 2.5 cal kyr BP (Fig. 4A), cannot be explained by temperature changes since palaeoclimatic records from mid-latitudes in South America as well as Antarctica indicate decreasing temperatures after the early Holocene climatic optimum (e.g., *Bianchi and Gersonde*, 2004; *Kaiser et al*., 2005, 2008; *Lamy et al*., 2007; *Steig et al*., 1998). Therefore, this strong decrease in $\delta^{18}O_{benthic}$ values must be a result of increasing precipitation in the late Holocene, with a strong increasing trend in rainfall amounts between 4.5 and 2.5 cal kyr BP and constant high precipitation from 2.5 cal kyr BP to the present (Fig. 4A).

5.2 Local and regional palaeoenvironmental changes at Canal Concepción during the Holocene

For marine sediment core MD07-3124 in Canal Concepción, we measured stable oxygen isotope compositions of the planktic foraminifer *Globigerina bulloides* ($\delta^{18}O_{bulloides}$) and the benthic species *Nonionella opima* ($\delta^{18}O_{opima}$) as well as Fe and Ca intensities (Fig. 4F-I). Since the coring site in this open channel is not in the proximity of a river inflow, we haven't measured organic geochemical proxies to reconstruct precipitation changes.

Since the Hielo Patagónico Sur is still present in the hinterland of the study site and influences the sedimentation at the coring site through iceberg activity, we

interpret changes in the Fe intensity record to primarily reflect changes in iceberg activity. Iceberg activity is controlled by precipitation and temperature changes. Since the Fe intensity record displays a slightly decreasing trend in the late Holocene, we propose a dominant control of precipitation changes on the variability in this record. The strong decreasing trend in the early and middle Holocene and slightly decreasing trend in the late Holocene also signify a secondary effect by temperature changes on the variability in this record since there is an early Holocene climatic optimum and following decreasing temperatures recorded in mid-latitudes of South America (e.g., *Bianchi and Gersonde*, 2004; *Kaiser et al*., 2005, 2008; *Lamy et al*., 2007; *Steig et al*., 1998). Additionally, changes in the sea-level probably had an influence on iceberg activity in this open channel. Because there is an almost perfect antiphasing of the Fe and Ca intensity records (Fig. 4H, I), the Ca intensity is not influenced by input of detrital carbonate and therefore is a proxy of marine productivity. The possibility of measuring δ^{18}O compositions of planktic and benthic foraminiferal shells indicates that this more open and deeper channel has a more established two-layered estuarine circulation with fresh surface waters and a deep-water layer occupied by saline Pacific surface waters. But the presence of the benthic species *Nonionella opima* also indicates dysoxic conditions and signifies a precipitation influence on the deeper-water layer and consequently the δ^{18}Oopima variability.

High values and a decreasing trend in the Fe intensity record during the early and middle Holocene indicate strongest iceberg activity and high rainfall amounts at this site at the northern margin of the Southern Westerlies core in the early Holocene and a trend of decreasing precipitation to ~4 cal kyr BP (Fig. 4H). The late Holocene is characterized by low Fe intensities, except for the time period between 3.7 and 2 cal kyr BP. This time period of higher Fe intensity excursions, with two pronounced peaks, is probably a result of neoglacial glacier advances since there are published glacier advances at ~3.5 and between 2.7 and 2 cal kyr BP (e.g., *Mercer*, 1982; *Rabassa and Clapperton*, 1990). High freshwater input into the channel seems to hamper marine productivity since the Ca and Fe intensity records are antiphased (Fig. 4I). The time period of the glacier advances is also characterized by lower Ca intensities superimposed on generally high intensities in the late Holocene. In comparison to the Aysén fjord record, the high Ca intensities indicate a generally stronger marine influence in Canal Concepción. This is further supported by the general pattern of the Ca and Fe intensity records which show a change in their trends at ~7 cal kyr BP with a more pronounced trend before 7 cal kyr BP (Fig. 4H, I). This correlates well with the pattern of the global postglacial sea-level rise which is characterized by a more pronounced rise before ~7 cal kyr BP and an attenuated global sea-level rise afterwards (e.g., *Fleming et al*., 1998).

The $\delta^{18}O_{bulloides}$ and $\delta^{18}O_{opima}$ records show a similar pattern up to 7 cal kyr BP (Fig. 4F, G). This is probably the result of a common controlling factor, predominantly temperature changes. Higher temperatures during the early Holocene and a decreasing trend thereafter correlate with lower $\delta^{18}O$ ratios in the early Holocene and an increasing trend to ~7.5 cal kyr BP (Fig. 4F, G). An additional effect of precipitation changes on the $\delta^{18}O$ variability in the early Holocene is most likely, as the Fe intensity record indicates high precipitation during this time period (Fig. 4H).

After 7 cal kyr BP, the stable oxygen isotope curves show different patterns. The $\delta^{18}O_{bulloides}$ values decrease from 7 and 5.5 cal kyr BP and then strongly vary around 1.1 ‰ vs. V-PDB to the present (Fig. 4F). This trend cannot be caused by changes in temperatures. Therefore, precipitation is the primary control on the $\delta^{18}O_{bulloides}$ variability in the middle and late Holocene. Since the Fe intensity and $\delta^{18}O_{bulloides}$ records do not correlate in the middle and late Holocene, the Fe intensity should be stronger influenced by temperature changes than in the early Holocene (Fig. 4F, H). In summary, precipitation seems to slightly increase from 7 to 5.5 cal kyr BP and the last 5.5 kyr are characterized by constant high precipitation with pronounced shorter-scale variability.

The $\delta^{18}O_{opima}$ record indicates a decreasing trend from 5.5 to 3.4 cal kyr BP and a slightly increasing trend afterwards (Fig. 4G). The decreasing trend is probably a result of a delayed response to a freshening in the surface-water layer, thereby indicating a remaining connection to surface-water changes. The increasing trend in the late Holocene indicates a predominant control of temperature on the $\delta^{18}O_{opima}$ variability. This is probably a result of a constant fresh surface-water layer and a strong stratification with saline Pacific surface waters dominating the deep-water layer in the channel.

5.3 Multi-millennial-scale changes of the Southern Westerlies during the Holocene

Lamy et al. (2010) propose a distinct latitudinal antiphasing of Southern Westerlies changes on multi-millennial timescales. Based on a multi-proxy approach on sediment cores from the core region of the Southern Westerlies at ~53°S in the westernmost Estrecho de Magellanes, they reconstruct an enhanced and compressed Southern Westerlies core in the early Holocene between ~12 and 8.5 cal kyr BP, intermediate conditions until 5.5 cal kyr BP and reduced precipitation and less intense Southern Westerlies during the late Holocene (Fig. 4J; *Lamy et al*., 2010).

The Southern Westerlies are a result of meridional transport of westerly momentum by transient eddies which are driven by the potential energy available in the meridional temperature gradients (e.g., *Gill*, 1982). In the Southern Hemisphere, where oceans strongly dominate over land surface, eddy activity, momentum flux

convergence and hence strength and position of the Southern Westerlies are primarily controlled by changes in SST. Consequently, the early Holocene climatic optimum in the mid-latitudes, as indicated by warmest SSTs in records from the Pacific (Fig. 6B; *Lamy et al*., 2007) and Atlantic sector (Fig. 6C; *Bianchi and Gersonde*, 2004), resulted in an early Holocene maximum of the Southern Westerlies core. At the same time, SSTs in the eastern tropical Pacific were relatively cold (Fig. 6A; *Koutavas and Sachs*, 2008), thereby reducing the mid- to low-latitude SST gradient in the Pacific. This resulted in weakened westerly winds north of the northern margin of the Southern Westerlies core in the early Holocene.

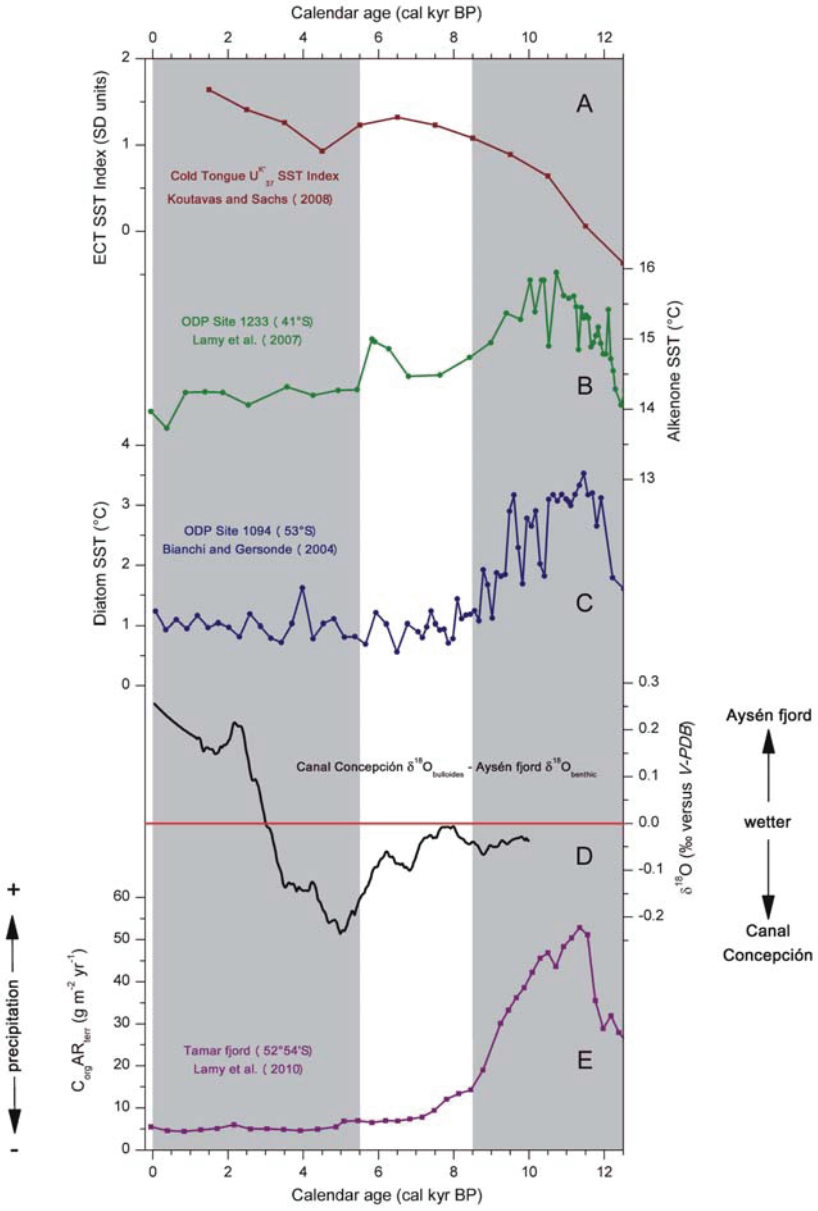

Fig. 6. Palaeoclimatic records to explain Southern Westerlies changes during the Holocene. (A) Composite alkenone SST Index (in SD (= standard deviation) units) based on five records from the eastern Pacific equatorial cold tongue (ECT; *Koutavas and Sachs*, 2008). (B) Alkenone SST record

from the ODP Site 1233 off the Chilean coast (41°S; *Lamy et al*., 2007). (C) Diatom-based summer SST record from the Atlantic sector of the Southern Ocean (53°S; ODP Site 1094; *Bianchi and Gersonde*, 2004). (D) Difference of the $\delta^{18}O_{bulloides}$ values from Canal Concepión and the $\delta^{18}O_{benthic}$ ratios from the Aysén fjord. The red line indicates the perfect similarity of these records. Since these records are interpreted to indicate precipitation changes in the middle and late Holocene, differences higher than 0 ‰ indicate higher precipitation at the Aysén fjord site compared to the Canal Concepción site, and vice versa. (E) $C_{org}AR_{terr}$ record from the Tamar fjord core TM1 (*Lamy et al.*, 2010), interpreted as a proxy for precipitation. The first grey bar between 12.5 and 8.5 cal kyr BP indicates the time of enhanced and compressed Southern Westerlies core in the early Holocene (after *Lamy et al*., 2010). The second grey bar between 5.5 cal kyr BP and the present represents the time of reduced precipitation and less intense Southern Westerlies core (after *Lamy et al*., 2010).

We conducted a multi-proxy palaeoenvironmental study on marine sediment cores from the northern margin of the Southern Westerlies core (Canal Concepción core MD07-3124 at 50°31'S) and from north of the northern margin (Aysén fjord core MD07-3114/15 at 45°23'S) to continue the work of *Lamy et al*. (2010) to cover a wide latitudinal range of palaeoclimatic records for the reconstruction of Southern Westerlies changes in the Holocene. As discussed previously, the rainfall records from Canal Concepción indicate a wet early Holocene and a transitional phase up to 7 cal kyr BP (Fig. 4F-H). Consequently, the northern margin of the core region is still influenced by the more intense Southern Westerlies core in the early Holocene. Precipitation records from the Aysén fjord north of the northern margin of the Southern Westerlies core show drier conditions during the early and middle Holocene (Fig. 4D, E) and therefore support the assumption of a more austral summer-like pattern of the Southern Westerlies during the early Holocene as proposed by *Lamy et al*. (2010).

In the middle and late Holocene, the SST records indicate a cooling trend in the mid-latitudes and an equatorial Pacific warming resulting in a weakened Southern Westerlies core and latitudinal extension of the same (Fig. 6A-C; e.g., *Bianchi and Gersonde*, 2004; *Koutavas and Sachs*, 2008; *Lamy et al*., 2007). The Tamar fjord record from the core region of the Southern Westerlies supports these findings by indicating intermediate conditions from 8.5 to 5.5 cal kyr BP and reduced precipitation within the less intense Southern Westerlies core during the late Holocene (Fig. 6E; *Lamy et al*., 2010). The rainfall records from Canal Concepción display an increase in precipitation from 7 to 5.5 cal kyr BP and constant high rainfall amounts to the present (Fig. 4F and 6D). The rainfall records from the Aysén fjord site MD07-3114/15 indicate a strong increase in precipitation from 4.5 to 2.5 cal kyr BP and high and slightly increasing precipitation afterwards (Fig. 4A). More intense precipitation compared to the Canal Concepción site is indicated after ~3 cal kyr BP (Fig. 6D). These findings verify the assumption of *Lamy et al*. (2010) that the late Holocene and part of the middle Holocene are characterized by a more austral winter-like pattern of the Southern

Westerlies with less intense westerly winds in the core region but a more latitudinal extension of the same. Rainfall records from marine sediment cores north of the southern Chilean fjord system (30-41°S) also signify drier conditions during the early and middle Holocene and increased precipitation during the late Holocene (e.g., *Kaiser et al*., 2008; *Lamy et al*., 1999, 2001, 2002).

As already discussed by *Lamy et al*. (2010), previous reconstructions within the Southern Westerlies core region and the northern margin of the core region were primarily performed on pollen from the lee-side of the Andes in southeast Patagonia and show inconsistencies with our reconstructions (e.g., *Mayr et al*., 2007, at Laguna Potrok Aike (52°S) and *Villa-Martínez and Moreno*, 2007, at Vega Ñandú (51°S)). This is probably due to rainfall sources other than the Southern Westerlies becoming more important lee-side of the Andes (primarily of Atlantic origin; *Wagner et al*., 2007). Additionally, plant communities at the drier lee-side of the Andes respond more indirectly to changes in the Southern Westerlies changes because the wind-induced dry stress is a major ecological factor in this dry region (*Endlicher*, 1991).

Support for our results comes from *Mancini* (2009) who has performed pollen analysis from a peat-bog sequence at 50°24'S. She suggests high precipitation after 5.8 cal kyr BP. This correlates well with the phase of higher precipitation in the Canal Concepción record after 5.5 cal kyr BP (50°31'S). A northward extension of Southern Westerlies influence after ~6 cal kyr BP is also indicated in several pollen records from Australia (*Shulmeister and Lees*, 1995).

5.4 Centennial- to millennial-scale changes in $\delta^{18}O$ variability: ENSO influence on the Southern Westerlies variability

Increased variability on centennial to millennial timescales in central and southern Chilean records after about 7 cal kyr BP is a result of more frequent and stronger ENSO activity (e.g., *McGlone et al*., 1992; *Stuut et al*., 2006). A further intensification of ENSO activity is recorded after about 5 to 4 cal kyr BP and modern ENSO activity is indicated since ~3 cal kyr BP (e.g., *Lamy*, 2007; *Lamy et al*., 2001; *McGlone et al*., 1992; *Stuut et al*., 2006).

The $\delta^{18}O$ records of planktic and benthic foraminifera are characterized by intensified centennial- to millennial-scale variability after certain points in time that can be attributed to increasing ENSO activity. Intensification is indicated after 5.93 cal kyr BP in the $\delta^{18}O_{benthic}$ record from the Aysén fjord, with a second intensification step after 4.1 cal kyr BP (Fig. 7A). The $\delta^{18}O_{opima}$ record from Canal Concepción shows attenuated centennial- to millennial-scale variability, except for the time period between 3.8 and 2.35 cal kyr BP (Fig. 7B). As opposed to this, the variability in the

$\delta^{18}O_{bulloides}$ record from MD07-3124 is intensified after 7.17 cal kyr BP, with additional intensification steps at 5.8 and 4 cal kyr BP (Fig. 7C).

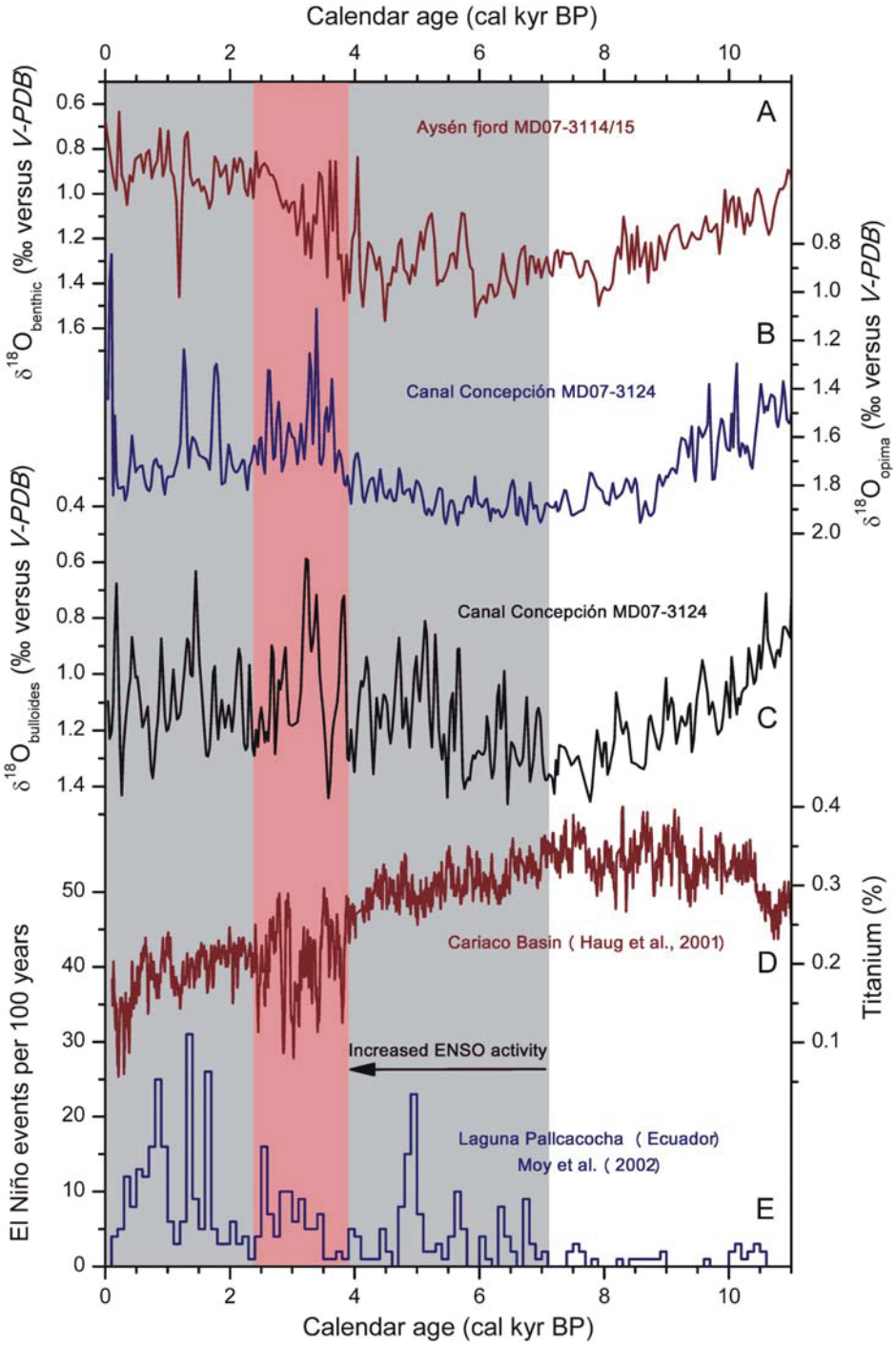

Fig. 7. Multi-proxy approach illustrating the ENSO effect on the centennial- to millennial-scale foraminiferal $\delta^{18}O$ variability. (A) $\delta^{18}O_{benthic}$ record from the Aysén fjord core MD07-3114/15. (B) $\delta^{18}O_{opima}$ record from the Canal Concepción core MD07-3124. (C) $\delta^{18}O_{bulloides}$ record from MD07-3124. (D) Titanium record from the Cariaco Basin (*Haug et al.*, 2001). (E) El Niño events per 100 years record from Laguna Pallcacocha in Ecuador (*Moy et al.*, 2002). The grey bar indicates the time of higher occurrence of ENSO events in the Laguna Pallcacocha record. The red bar signifies

a time period between 3.8 and 2.35 cal kyr BP with higher variability in the titanium record from the Cariaco Basin. This higher variability was interpreted to be due to a more frequent ENSO activity influencing rainfall-induced titanium input into the Cariaco Basin (*Haug et al*., 2001).

The titanium record from the Cariaco Basin in northern South America is interpreted as a proxy for rainfall-induced riverine input of titanium (*Haug et al*., 2001). The record indicates higher rainfall variability from 3.8 to 2.35 cal kyr BP as a result of increased ENSO activity (Fig. 7D). This perfectly correlates with the time period of increased variability in the $\delta^{18}O_{opima}$ record from Canal Concepción as well as intensification steps in the variability of the other two $\delta^{18}O$ records from the Aysén fjord and Canal Concepción (Fig. 7A-C).

The Laguna Pallcacocha record of El Niño events from Ecuador is based on sediment layers as a result of debris-flow activity. This debris-flow activity is initiated by high precipitation and high erosion during El Niño events (*Moy et al*., 2002). The record indicates a first establishment of ENSO variance at around 7.1 cal kyr BP and increasing activity afterwards (Fig. 7E). This correlates well with the first intensification in centennial- to millennial-scale $\delta^{18}O_{bulloides}$ variability at Canal Concepción after ~7.17 cal kyr BP. The $\delta^{18}O_{benthic}$ record from the Aysén fjord shows a later response to this intensified ENSO activity.

In summary, all three $\delta^{18}O$ records show a pronounced influence by ENSO activity on centennial to millennial timescales. Since this influence of ENSO changes can just be established through precipitation changes, because ENSO changes are known to strongly influence the strength and position of the southeast Pacific anticyclone which controls the strength and position of the Southern Westerlies (e.g., *Cerveny*, 1998; *Montecinos and Aceituno*, 2003; *Rutllant and Fuenzalida*, 1991) and because ENSO-induced SST changes just reach south up to 33-36°S (*Strub et al*., 1998), the centennial- to millennial-scale $\delta^{18}O_{bulloides}$ variability at Canal Concepción and $\delta^{18}O_{benthic}$ variability at the Aysén fjord are strongly influenced by precipitation changes on shorter timescales. The $\delta^{18}O_{opima}$ record from Canal Concepción just shows a strong precipitation signal between 3.8 and 2.35 cal kyr BP. The strong influence of ENSO changes is also a hint for a stronger control by low-latitude climatic changes on the middle and late Holocene variability in the $\delta^{18}O$ records compared to the early Holocene.

6. Conclusions

Since the Southern Westerlies play an important role in the global climate system by driving the ACC and consequently influencing the global thermohaline circulation, it is crucial to reconstruct changes in the Southern Westerlies dynamics in a reliable way. Because a multi-proxy study over a wide latitudinal range along the

Chilean coast is the most promising way to obtain reliable reconstructions to solve open questions about the dynamics of the Southern Westerlies during the Holocene on centennial- to multi-millennial timescales, we performed a study on high resolution marine sediment cores from the southern Chilean fjord system from the Aysén fjord (45°23'S) north of the northern margin of the Southern Westerlies core and Canal Concepción (50°31'S) at the northern margin of the core region and compared our results with reconstructions from within the core region of the Southern Westerlies (*Lamy et al*., 2010) and north of our study area (30-41°S; e.g., *Kaiser et al.,* 2008; *Lamy et al*., 1999, 2001, 2002).

Our results support the findings of *Lamy et al.* (2010) who reconstruct a latitudinal antiphasing of Southern Westerlies changes on multi-millennial timescales during the Holocene as a result of SST changes in the mid- and low-latitudes of the southern Pacific Ocean. A wet early Holocene reconstructed from fjord sediment cores from within the core region is also observed at the northern margin at Canal Concepción, but not north of the northern margin at the Aysén fjord. Consequently, the Southern Westerlies dynamics in the early Holocene resembles modern austral-summer conditions with the westerly winds confined and strengthened within the core region, but weakened north of the northern margin of the core region. Decreasing precipitation in the core region of the Southern Westerlies during the middle and late Holocene (*Lamy et al*., 2010), a small increase from 7 to 5.5 cal kyr BP and constant rainfall amounts at the northern margin of the region at the Canal Concepción site after 5.5 cal kyr BP and strongly increasing precipitation between 4.5 and 2.5 cal kyr BP and constantly high rainfall amounts after 2.5 cal kyr BP at the Aysén fjord site as well as increasing precipitation in the late Holocene north of the southern Chilean fjord system (*Kaiser et al*., 2008; *Lamy et al*., 1999, 2001, 2002) support the idea of a more austral-winter like pattern of the Southern Westerlies on multi-millennial timescale during the middle and late Holocene with less intense westerly winds in the core region but a more latitudinal extension of the same.

On centennial to millennial timescales, the planktic foraminiferal $\delta^{18}O$ record from Canal Concepción is characterized by increased variability after about 7.17 cal kyr BP. The benthic records show increased variability after 5.93 cal kyr BP (Aysén fjord record) and between 3.8 and 2.35 cal kyr BP (Canal Concepción record). A comparison with palaeoclimatic records from equatorial South America indicate that increasing ENSO activity during the middle and late Holocene is the trigger for this intensified variability in the $\delta^{18}O$ records. Since ENSO changes are known to strongly influence the southeast Pacific anticyclone and since ENSO-induced changes at these southern latitudes can just be induced by precipitation changes, the centennial- to millennial-scale $\delta^{18}O$ variability during the middle and late Holocene is strongly influenced by precipitation changes and thereby indicates a pronounced control by low-latitude climatic changes.

7. Acknowledgements

We would like to thank Dr. Birgit Plessen and Petra Meier for their help with the analytical work at the GFZ Potsdam. Further, we owe a debt of gratitude to all student assistants at the GFZ Potsdam and AWI Bremerhaven and to the scientific staff onboard the M/V Marion Dufresne for their help. Financial support was made available through the GFZ Potsdam, DFG (Deutsche Forschungsgemeinschaft, German Research Foundation), CSAG (Center for System Analysis of Geoprocesses) and CSEF (The Comer Science & Education Foundation).

8. References

Ashworth, A.C., Markgraf, V., Villagrán, C., 1991. Late Quaternary climatic history of the Chilean Channels based on fossil pollen and beetle analyses, with an analysis of the modern vegetation and pollen rain. Journal of Quaternary Science 6, 279-291.

Bianchi, C., Gersonde, R., 2004. Climate evolution at the last deglaciation: the role of the Southern Ocean. Earth and Planetary Science Letters 228, 407-424.

Cerveny, R., 1998. Present Climates of South America, in: Hobbs, J.E., Lindesay, J.A., Bridgman, H.A. (Eds.), Climates of the Southern Continents: Present, Past and Future. John Wiley and Sons, New York, pp. 107-135.

Coplen, T.B., 1996. Editorial: More uncertainty than necessary. Paleoceanography 11, 369-370.

Endlicher, W., 1991. Südpatagonien - klima- und agrarökologische Probleme an der Magellanstraße. Geographische Rundschau 43, 143-151.

Fleming, K., Johnston, P., Zwartz, D., Yokoyama, Y., Lambeck, K., Chappell, J., 1998. Refining the eustatic sea-level curve since the Last Glacial

Maximum using far- and intermediate-field sites. Earth and Planetary Science Letters 163, 327-342.

Gill, A.E., 1982. Atmosphere-Ocean Dynamics. Academic Press, San Diego.

Haberzettl, T., Corbella, H., Fey, M., Janssen, S., Lücke, A., Mayr, C., Ohlendorf, C., Schäbitz, F.,

Schleser, G.H., Wille, M., Wulf, S., Zolitschka, B., 2007. Lateglacial and Holocene wet-dry cycles in southern Patagonia: chronology, sedimentology and geochemistry of a lacustrine record from Laguna Potrok Aike, Argentina. The Holocene 17, 297-310.

Haug, G.H., Hughen, K.A., Sigman, D.M., Peterson, L.C., Röhl, U., 2001. Southward Migration of the Intertropical Convergence Zone Through the Holocene. Science 293, 1304-1308.

Heusser, C.J., 1989. Southern Westerlies during the Last Glacial Maximum. Quaternary Research 31, 423-425.

Holmes, M.E., Eichner, C., Struck, U., Wefer, G., 1999. Reconstruction of Surface Ocean Nitrate Utilization Using Stable Nitrogen Isotopes in Sinking Particles and Sediments, in: Fischer, G., Wefer, G. (Eds.), Use of Proxies in Paleoceanography: Examples from the South Atlantic. Springer-Verlag, Berlin, pp. 447-468.

Hromic, T., Ishman, S., Silva, N., 2006. Benthic foraminiferal distributions in Chilean fjords: 47°S to 54°S. Marine Micropaleontology 59, 115-134.

Hughen, K.A., Baillie, M.G.L., Bard, E., Beck, J.W., Bertrand, C.J.H., Blackwell, P.G., Buck, C.E., Burr, G.S., Cutler, K.B., Damon, P.E., Edwards, R.L., Fairbanks, R.G., Friedrich, M.,

Guilderson, T.P., Kromer, B., McCormac, G., Manning, S., Ramsey, C.B., Reimer, P.J., Reimer, R.W., Remmele, S., Southon, J.R., Stuiver, M., Talamo, S., Taylor, F.W., van der Plicht, J., Weyhenmeyer, C.E., 2004. Marine04 marine radiocarbon age calibration, 0-26 cal kyr BP. Radiocarbon 46, 1059-1086.

Hulton, N., Sugden, D., 1997. Dynamics of mountain ice caps during glacial cycles: the case of Patagonia. Annals of Glaciology 24, 81-89.

Hut, G., 1987. Report on the Consultants' Group Meeting on Stable Isotope Reference Samples for Geochemical and Hydrological Investigations. International Atomic Energy Agency (I.A.E.A.), Vienna, 16-18 September 1985.

Ingram, B.L., Southon, J.R., 1996. Reservoir Ages in Eastern Pacific Coastal and Estuarine Waters. Radiocarbon 38, 573-582.

Kaiser, J., Lamy, F., Hebbeln, D., 2005. A 70-kyr sea surface temperature record off southern Chile (Ocean Drilling Program Site 1233). Paleoceanography 20, PA4009, doi:10.1029/2005PA001146.

Kaiser, J., Schefuß,. E., Lamy, F., Mohtadi, M., Hebbeln, D., 2008. Glacial to Holocene changes in sea surface temperature and coastal vegetation in north central Chile: high versus low latitude forcing. Quaternary Science Reviews 27, 2064-2075.

Kilian, R., Baeza, O., Steinke, T., Arevalo, M., Rios, C., Schneider, C., 2007. Late Pleistocene to Holocene marine transgression and thermohaline control on sediment transport in the western Magellanes fjord system of Chile (53°S). Quaternary International 161, 90-107.

Kissel, C., shipboard scientists, 2007a. Cruise Report of MD159 - PACHIDERME IMAGES XV Cruise, Punta Arenas (Chile) - Punta Arenas (Chile), 6 - 28 February 2007.

Kissel, C., shipboard scientists, 2007b. Data Report of MD159 - PACHIDERME IMAGES XV Cruise, Punta Arenas (Chile) - Punta Arenas (Chile), 6 - 28 February 2007.

Koutavas, A., Sachs, J.P., 2008. Northern timing of deglaciation in the eastern equatorial Pacific from alkenone paleothermometry. Paleoceanography 23, PA4205, doi:10.1029/2008PA001593.

Kuhlbrodt, T., Griesel, A., Montoya, M., Levermann, A., Hofmann, M., Rahmstorf, S., 2007. On the driving processes of the Atlantic meridional overturning circulation. Reviews of Geophysics 45, RG2001, doi:10.1029/2004RG000166.

Lamy, F., 2007. Postglacial South Pacific, in: Elias, S.A. (Ed.), Encyclopedia of Quaternary Science, Volume 3. Elsevier B.V., Amsterdam, pp. 1855-1866.

Lamy, F., Hebbeln, D., Wefer, G., 1998. Late Quaternary precessional cycles of terrigenous sediment input off the Norte Chico, Chile (27.5°S) and palaeoclimatic implications. Palaeogeography, Palaeoclimatology, Palaeoecology 141, 233-251.

Lamy, F., Hebbeln, D., Wefer, G., 1999. High-Resolution Marine Record of Climatic Change in Mid-latitude Chile during the Last 28,000 Years Based on Terrigenous Sediment Parameters. Quaternary Research 51, 83-93.

Lamy, F., Hebbeln, D., Röhl, U., Wefer, G., 2001. Holocene rainfall variability in southern Chile: a marine record of latitudinal shifts of the Southern Westerlies. Earth and Planetary Science Letters 185, 369-382.

Lamy, F., Rühlemann, C., Hebbeln, D., Wefer, G., 2002. High- and low-latitude climate control on the position of the southern Peru-Chile Current during the Holocene. Paleoceanography 17, doi:10.1029/ 2001PA000727.

Lamy, F., Kaiser, J., Arz, H.W., Hebbeln, D., Ninnemann, U., Timm, O., Timmermann, A., Toggweiler, J.R., 2007. Modulation of the bipolar seesaw in the Southeast Pacific during Termination 1. Earth and Planetary Science Letters 259, 400-413.

Lamy, F., Kilian, R., Arz, H.W., Francois, J.-P., Kaiser, J., Prange, M., Steinke, T., 2010. Holocene changes of the southern westerly wind belt. Nature Geoscience (submitted for publication).

Lumley, S.H., Switsur, R., 1993. Late Quaternary chronology of the Taitao Peninsula, southern Chile. Journal of Quaternary Science 8, 161-165.

Mancini, M.V., 2009. Holocene vegetation and climate changes from a peat pollen record of the forest - steppe ecotone, Southwest of Patagonia (Argentina). Quaternary Science Reviews 28, 1490-1497.

Markgraf, V., 1989. Reply to C.J. Heusser's "Southern Westerlies during the Last Glacial Maximum". Quaternary Research 31, 426-432.

Markgraf, V., 1998. Past Climates of South America , in: Hobbs, J.E., Lindesay, J.A., Bridgman, H.A. (Eds.), Climates of the Southern Continents: Present, Past and Future. John Wiley and Sons, New York, pp. 249-264.

Markgraf, V., Dodson, J.R., Kershaw, A.P., McGlone, M.S., Nicholls, N., 1992. Evolution of late Pleistocene and Holocene climates in the circum-South Pacific land areas. Climate Dynamics 6, 193-211.

Massaferro, J., Brooks, S.J., Haberle, S.G., 2005. The dynamics of chironomid assemblages and vegetation during the Late Quaternary at Laguna Facil, Chonos Archipelago, southern Chile. Quaternary Science Reviews 24, 2510-2522.

Masson, V., Vimeux, F., Jouzel, J., Morgan, V., Delmotte, M., Ciais, P., Hammer, C., Johnsen, S., Lipenkov, V.Y., Mosley-Thompson, E., Petit, J.R., Steig, E.J., Stievenard, M., Vaikmae, R., 2000. Holocene Climate Variability in Antarctica Based on 11 Ice-Core Isotopic Records. Quaternary Research 54, 348-358.

Mayr, C., Wille, M., Haberzettl, T., Fey, M., Janssen, S., Lücke, A., Ohlendorf, C., Oliva, G., Schäbitz, F., Schleser, G.H., Zolitschka, B., 2007. Holocene variability of the Southern Hemisphere westerlies in Argentinean Patagonia (52°S). Quaternary Science Reviews 26, 579-584.

McCormac, F.G., Hogg, A.G., Blackwell, P.G., Buck, C.E., Higham, T.F.G., Reimer, P.J., 2004. SHCal04 Southern Hemisphere calibration, 0-11.0 cal kyr BP. Radiocarbon 46, 1087-1092.

McCulloch, R.D., Davies, S.J., 2001. Late-glacial and Holocene palaeoenvironmental change in the central Strait of Magellan, southern Patagonia. Palaeogeography, Palaeoclimatology, Palaeoecology 173, 143-173.

McGlone, M.S., Kershaw, A.P., Markgraf, V., 1992. El Niño/Southern Oscillation climatic variability in Australasian and South American paleoenvironmental records, in: Díaz, H.F., Markgraf, V. (Eds.), El Niño – Historical and Paleoclimatic Aspects of the Southern Oscillation. Cambridge University Press, Cambridge, pp. 435-462.

Mercer, J.H., 1982. Holocene glacier variations in southern South America. Striae 18, 35-40.

Meyers, P.A., 1994. Preservation of elemental and isotopic source identification of sedimentary organic matter. Chemical Geology 114, 289-302.

Meyers, P.A., 1997. Organic geochemical proxies of paleoceanographic, paleolimnologic, and paleoclimatic processes. Organic Geochemistry 27, 213-250.

Meyers, P.A., Teranes, J.L., 2001. Sediment Organic Matter, in: Last, W.M., Smol, J.P. (Eds.), Tracking Environmental Change Using Lake Sediments - Volume 2: Physical and Geochemical Methods. Kluwer, Dordrecht, pp. 239-269.

Miller, A., 1976. The Climate of Chile, in: Schwerdtfeger, W. (Ed.), World Survey of Climatology, Volume 12, Climates of central and South America. Elsevier Science, Amsterdam, pp. 113-145.

Montecinos, A., Aceituno, P., 2003. Seasonality of the ENSO-Related Rainfall Variability in Central Chile and Associated Circulation Anomalies. Journal of Climate 16, 281-296.

Moy, C.M., Seltzer, G.O., Rodbell, D.T., Anderson, D.M., 2002. Variability of El Niño/Southern Oscillation activity at millennial timescales during the Holocene epoch. Nature 420, 162-165.

Müller, P.J., Suess, E., 1979. Productivity, sedimentation rate, and sedimentary organic matter in the oceans – I. Organic carbon

preservation. Deep-Sea Research A26, 1347-1362.

Nadeau, M.-J., Schleicher, M., Grootes, P.M., Erlenkeuser, H., Gottdang, A., Mous, D.J.W., Sarnthein, J.M., Willkomm, H., 1997. The Leibniz-Labor AMS facility at the Christian-Albrechts University, Kiel, Germany. Nuclear Instruments and Methods in Physics Research B123, 22-30.

Pickard, G.L., 1971. Some Physical Oceanographic Features of Inlets of Chile. Journal of the Fisheries Research Board of Canada 28, 1077-1106.

Rabassa, J., Clapperton, C.M., 1990. Quaternary glaciations of the southern Andes. Quaternary Science Reviews 9, 153-174.

Reimer, P.J., Baillie, M.G.L., Bard, E., Bayliss, A., Beck, J.W., Bertrand, C.J.H., Blackwell, P.G., Buck, C.E., Burr, G.S., Cutler, K.B., Damon, P.E., Edwards, R.L., Fairbanks, R.G., Friedrich, M., Guilderson, T.P., Hogg, A.G., Hughen, K.A., Kromer, B., McCormac, G., Manning, S., Ramsey, C.B., Reimer, R.W., Remmele, S., Southon, J.R., Stuiver, M., Talamo, S., Taylor, F.W., van der Plicht, J., Weyhenmeyer, C.E., 2004. IntCal04 terrestrial radiocarbon age calibration, 0-26 cal kyr BP. Radiocarbon 46, 1029-1058.

Rutllant, J., Fuenzalida, H., 1991. Synoptic aspects of the central Chile rainfall variability associated with the Southern Oscillation. International Journal of Climatology 11, 63-76.

Schneider, C., Gies, D., 2004. Effects of El Niño-Southern Oscillation on southernmost South America precipitation at 53°S revealed from NCEP-NCAR reanalyses and weather station data. International Journal of Climatology 24, 1057-1076.

Schneider, C., Glaser, M., Kilian, R., Santana, A., Butorovic, N., Casassa, G., 2003. Weather Observations Across the Southern Andes at 53°S. Physical Geography 24, 97-119.

Sen Gupta, B.K., Machain-Castillo, M.L., 1993. Benthic foraminifera in oxygen-poor habitats. Marine Micropaleontology 20, 183-201.

Shackleton, N.J., Opdyke, N.D., 1973. Oxygen Isotope and Palaeomagnetic Stratigraphy of Equatorial Pacific Core V28-238: Oxygen Isotope Temperatures and Ice Volumes on a 10^5 Year and 10^6 Year Scale. Quaternary Research 3, 39-55.

Shulmeister, J., Lees, B.G., 1995. Pollen evidence from tropical Australia for the onset of an ENSO-dominated climate at c. 4000 BP. The Holocene 5, 10-18.

Silva, N., Calvete, C., Sievers, H.A., 1997. Características Oceanográficas Físicas y Químicas de Canales Australes Chilenos entre Puerto Montt y Laguna San Rafael (Crucero Cimar-Fiordo 1). Revista Ciencia y Tecnología del Mar 20, 23-106.

Steig, E.J., Hart, C.P., White, J.W.C., Cunningham, W.L., Davis, M.D., Saltzman, E.S., 1998. Changes in climate, ocean and ice-sheet conditions in the Ross embayment, Antarctica, at 6 ka. Annals of Glaciology 27, 305-310.

Stine, S., Stine, M., 1990. A record from Lake Cardiel of climate change in southern South America. Nature 345, 705-708.

Strub, P.T., Mesías, J.M., Montecino, V., Rutllant, J., Salinas, S., 1998. Coastal ocean circulation off western South America, in: Robinson, A.R., Brink, K. H. (Eds.), The Sea, Volume 11**,** The Global Coastal Ocean: Regional Studies and Syntheses. John Wiley and Sons, New York, pp. 273-313.

Stuiver, M., Reimer, P.J., Reimer, R.W., 2005. Calib 5.0 (WWW program and documentation).

Stuut, J.-B. W., Marchant, M., Kaiser, J., Lamy, F., Mohtadi, M., Romero, O., Hebbeln, D., 2006. The late Quaternary paleoenvironment of Chile as seen from marine archives. Geographica Helvetica 61, 135-151.

Syvitski, J.P.M., Burrell, D.C., Skei, J.M., 1987. Fjords: Processes and Products. Springer-Verlag, New York.

Tapia, R., Lange, C.B., Marchant, M., 2008. Living (stained) calcareous benthic foraminifera from recent sediments off Concepción, central-southern Chile (~36°S*).* Revista Chilena de Historia Natural 81, 403-416.

Tomczak, M., Godfrey, J.S., 2003. Regional Oceanography: An Introduction, second ed. Daya Publishing House, Delhi.

Villa-Martínez, R., Moreno, P.I., 2007. Pollen evidence for variations in the southern margin of the westerly winds in SW Patagonia over the last 12,600 years. Quaternary Research 68, 400-409.

von Reden, K.F., Jones, G.A., Schneider, R.J., McNichol, A.P., Cohen, G.J., Purser, K.H., 1992. The new National Ocean Sciences Accelerator Mass Spectrometer Facility at Woods Hole Oceanographic Institution: Progress and first results. Radiocarbon 34, 478-482.

von Reden, K.F., Schneider, R.J., Cohen, G.J., Jones, G.A., 1994. Performance characteristics of the 3 MV Tandetron AMS system at the National Ocean Sciences AMS facility. Nuclear Instruments and Methods in Physics Research B92, 7-11.

Wagner, S., Widmann, M., Jones, J., Haberzettl, T., Lücke, A., Mayr, C., Ohlendorf, C., Schäbitz, F., Zolitschka, B., 2007. Transient simulations, empirical reconstructions and forcing mechanisms for the Mid-holocene hydrological climate in southern Patagonia. Climate Dynamics 29, 333-355.

Wolff, T., Mulitza, S., Arz, H.W., Pätzold, J., Wefer, G., 1998. Oxygen isotopes versus CLIMAP (18 ka) temperatures: A comparison from the tropical Atlantic. Geology 26, 675-678.

5 SUMMARY AND CONCLUSIONS

The Chilean Fjord Region, located between ~42°S and ~55°S, is ideal for studying late Quaternary paleoenvironmental changes in the Southern Hemisphere as it is under the permanent influence of the Southern Westerly Winds (SWW) which play a fundamental role in the climate system at continental, hemispheric and global scales (e.g., *Moreno*, 1997). It is also under presently strong sea surface temperature (SST) and salinity gradients making this area very sensitive to track oceanographic changes over time.

This thesis focused in reconstructing the paleoenvironmental history of the Chilean Fjord Region and the adjacent Southeast Pacific over the last glacial period and the Holocene and its relationship to global and regional climate changes. This work was based on a multi-proxy approach performed on three sediment cores extracted between ~50°S and ~53°S. In order to describe regional patterns of paleoclimate changes and identify common forcing mechanisms, the Chilean fjord cores were compared with previous published records from the mid- and high-southern latitudes.

Core MD07-3128 recovered at ~53°S off the Pacific entrance of the Strait of Magellan, was the longest sediment core analyzed in this study, reaching back *ca*. 60 kyr BP. Its extraordinary high sedimentation rates over the last glacial (average of *ca*. 170 cm kyr^{-1}) allow for high-resolution reconstruction of the paleoceanographic changes off southernmost Chile during marine isotope stage (MIS) 3 (~60 to ~25 kyr BP) and MIS 2 (*ca*. 25 to ~11 kyr BP) and offer unique opportunities to improve our understanding regarding the pattern and timing of millennial-scale climate changes in the Southern Hemisphere that have been discussed controversially. This core, however, recorded unexpected low sedimentation rates during the Holocene and did not allow for a direct comparison with the SST records from within the fjords. Cores JPC-42 and MD07-3124, on the other hand, presented high sedimentation rates during the Holocene allowing for high resolution reconstruction of SST and main climate changes. Furthermore, these records together with surface sediment samples collected along the Chilean Fjord Region were used to evaluate the potential seasonality recorded in the alkenone-derived SST.

At ~53°S, the alkenone derived-SST record revealed that both, the millennial-scale SST variability recorded over the last glacial and the abrupt two-step warming occurring during the last deglacial (starting at ~18.7 kyr BP) follows the temperature changes recorded by Antarctic ice cores and ODP Site 1233 at 41°S (*Lamy et al.*, 2004; *Kaiser et al.*, 2005; *Lamy et al.*, 2007), thus confirming the existence of an “Antarctic”-type pattern of the SST variability off southern Chile (Manuscript 1). This new SST record narrows down the debate concerning the inter-hemispheric synchrony or asynchrony of the millennial-scale changes observed in southern Chile, since the

deglacial-SST variability at ~53°S evolved in synchrony with Antarctica, contrary to the asynchrony observed in some terrestrial records (e.g., cooling during the Younger Dryas cold phase; *Denton et al.*, 1999; *Moreno et al.*, 2001).

In Antarctica, millennial-scale temperature changes over the last glacial have been consistently explained by the bipolar seesaw concept that suggests anti-phase temperature changes between the Northern and Southern hemispheres (Antarctica warms while Greenland cools, and vice-versa) as a response to perturbations in the thermohaline circulation and heat transport (e.g., *EPICA Community Members*, 2004). The Antarctic-type pattern observed in the record at ~53°S corroborates that the seesaw mechanism was operating during the last glacial off southern Chile (*Kaiser et al*., 2005; *Lamy et al*., 2004) and extended into the last termination (e.g., *Lamy et al.*, 2007).

During the last glacial, sea surface temperatures off the Strait of Magellan cooled by about 7 °C compared with the early Holocene SST values, suggesting that the cold waters of the Subantarctic Front (SAF), at present located only ~5°S south of core MD07-3128 (where temperatures drops considerably by 6 °C; Fig.1, Manuscript 1) reached the core site as the result of its northward migration. These results are strongly consistent with the glacial pattern found at 41°S (ODP Site 1233; (*Kaiser et al.*, 2005) where a 6 °C glacial SST cooling has been explained by a 5–6° northward shift of the ACC and the SWW associated with an increase in the sea-ice extent around Antarctica during colder intervals (*Lamy et al.*, 2004; *Kaiser et al.*, 2005).

Additional support for the glacial northward migration of the Antarctic frontal system was provided by the paleoproductivity changes documented by core MD07-3128. This is the only record presently available off southern South America (south of 50°S) that examines the marine productivity changes over the last ~60 kyr BP, allowing illustrating a general picture of the primary productivity dynamics over time. Core MD07-3128 revealed an increase in the biogenic opal a proxy for siliceous community (primarily diatoms) during the last glacial and a decrease from the deglacial toward the Holocene. Superimposed on this general trend, large fluctuations on millennial-time scales were also observed. An increase of the siliceous plankton community over the calcareous characterized the colder intervals, while during the warmer ones this pattern was reversed. A northward shift of the Antarctic Ocean fronts and the opal-ooze belt (an area of massive opal export located currently just ~5°S south of core MD07-3128) can explain the increase of the siliceous community during millennial-scale colder intervals. The decreasing siliceous productivity from the deglaciation toward the Holocene, on the other hand, can be interpreted in terms of a poleward shift of the siliceous-ooze belt resulting in decreased diatom productivity in the study area.

Northward/southward shift of the Antarctic Ocean fronts related to an equatorward/poleward extension of the SWW is a simplest way to explain the paleoproductivity dynamics recorded during the last glacial/deglaciation off the Strait of Magellan. This agrees with previously published high-resolution multi-proxy data from mid-latitudes (*Lamy et al.*, 1999; *Mohtadi and Hebbeln*, 2004; *Kaiser et al.*, 2005), as well as with modelling studies (e.g., *Toggweiler et al.*, 2006). Moreover, glacial/interglacial paleoproductivity changes related to these migrations of the Antarctic Ocean fronts have also been suggested from biogenic opal accumulated in sediments of the Atlantic sector of the Southern Ocean (*Charles et al.*, 1991; *Kumar et al.*, 1995; *Anderson et al.*, 1998) in agreement with our paleoproductivity pattern found at ~53°S.

During the last glacial, the icefields in Patagonia expanded to form the larger Patagonian Ice Sheet (PIS) covering the southern Andes between ~40°S and ~55°S (e.g., *Hulton et al.*, 2002; *Glasser and Jansson*, 2008). For the Atlantic side of the Andes, an updated view of glacial and deglacial changes in the extension of the southern PIS has been recently presented by *Sugden et al.* (2009) based on extensive dating of terrestrial records. This reconstruction suggests five major advances of the southern PIS during the last glacial and/or stagnation phases of ice retreat during the last deglacial. In contrast to the eastern side of the Andes, little is known about the extent of the PIS on the Pacific continental margin or the effect of its advances and retreats on the coast of the Chilean margin. Core MD07-3128 was important in this context as it revealed several pulses in ice-rafted debris (or IRD) as well as surface ocean water changes most likely due to impact of the southern PIS, inferring a close to the core site during the last glacial.

During the coldest SST intervals of late MIS 3 and the Last Glacial Maximum (LGM), maxima in IRD corresponded, within age uncertainties, to the major terrestrial PIS advances recorded by *Sugden et al.* (2009) suggesting that both, the Atlantic and Pacific side of the southern PIS reacted in phase. Although this correspondence suggests that the IRD record off the Strait of Magellan primarily documents ice sheet advances, changes in the SWW were probably likewise important. Strong SWW would reduce the offshore movement of icebergs from southern PIS to the core site. However, it is likely that during glacier advances (primary cold phases during the glacial) the SWW intensities would have been slightly reduced off southernmost Chile as the core of the SWW moved northward. Thus, the offshore advection of icebergs would have been facilitated during intervals of southern PIS advances.

The southern PIS reached its maximum extension during the LGM, as suggested by the terrestrial record of *Sugden et al*. (2009) as well as the maxima pulses of IRD. During this time interval, the increase in the relative abundance of $C_{37:4}$ alkenones, as proxy for low salinity waters, suggests a reduction of surface waters

salinity probably induced by meltwater supply (Fig. 4; Manuscript 1). The input of fresh water induced a locally enhanced SST cooling (from~25 to 19 kyr BP) close to the southern Pacific PIS margin consistent with the fact that no similar long-term cooling was observed at ODP site 1233 or any other high resolution SST records from the Chilean margin. Interestingly, the $C_{37:4}$ alkenones relative abundance remains comparatively high during the deglaciation suggesting that relatively fresh surface water conditions persisted, perhaps due to a continuous supply of meltwater during ice sheet retreat (*Sugden et al.*, 2009).

After the lower temperatures recorded during the last glacial and the abrupt two-step warming occurring during the last deglaciation, the SST record at ~53°S shows maximum warm conditions in the early Holocene. Within the fjord, however, the Holocene SST evolution does not reveal an early Holocene Climate Optimum, as previously documented in the paleotemperature record from offshore records further north (e.g., *Kaiser et al.*, 2005) and Antarctica (e.g., *Masson et al.*, 2000). In contrast, core MD07-3124 at ~51°S showed that SSTs were warmer than present over most of the Holocene, except for the past ~0.6 kyr BP and for a centennial-scale cooling episode centered at *ca*. 5 kyr BP (Manuscript 2). The absence of an early Holocene Climate Optimum within the fjords has been related to a combination of factors including decreased inflow of the open marine waters due to lower sea-level stand, enhanced advection of colder and fresher inner fjord water and stronger SWW. The fact that alkenones in the inner fjord core JPC-42 (located near to the southern Patagonian icefield) were only present after ~8 kyr BP points to substantially reduced surface water salinities during the early Holocene, strongly consistent with increasing precipitation and runoff in the core of the SWW occurring at this time (*Lamy et al.*, 2010). A wetter climate was also observed in the inner Aysén fjord located at ~45°S (Manuscript 3) suggesting a more confined and strengthened SWW within the core (summer-like conditions) consistent with the finding of *Lamy et al*. (2010). During the late Holocene, however, the pattern was opposed; the precipitation decrease at ~45°S resembles austral-winter condition due to the northward expansion of the SWW, thus reducing the intensity of the SWW in the core area (Manuscript 3).

In the latest Holocene, on the other hand, the Chilean Fjord Region SST records show a pronounced cooling of >2 °C starting at around 1.1 kyr BP in core JPC-42 and ~0.9 kyr BP in core MD07-3124 and lasting until ~0.6 kyr BP in both cores (Manuscript 2). This cooling coincides with the transition from the globally known Medieval Warm Period (MWP) to the Little Ice Age (LIA). A similar 2 °C cooling has been observed in the late Holocene alkenone-based SST record from the Jacaf Fjord, located in northern Patagonia at ~44°S (*Sepúlveda et al.*, 2009) as well as at the Pacific coastal margin at 41°S and 44°S (GeoB 3313-1 and GeoB 7186; *Lamy et al.*, 2002; *Mohtadi et al.*, 2007) but with a smaller amplitude of only ~1–1.5 °C. This difference

suggests an amplification of the SST signal in the interior of the Chilean fjords. Furthermore, the available SST records from the Chilean fjords and the adjacent continental margin all show a pronounced late Holocene cooling suggesting that the cooling was not a local event but a regional feature affecting an area of *ca*. 10° latitude from ~41°S to ~51°S (Manuscript 2).

A comparison of SST results based on core MD07-3124 and terrestrial proxy for glacier clay input provide additional insight for glacier changes in southernmost Andes during the Holocene (Manuscript 4). These records show that glaciers from the southern Patagonian ice-field advanced even when the regional climate was relatively warmer. The main glacier advances labeled A6-A1 occurred only partly during regional cooling intervals (e.g., A2 and A6). Other glacier advances, (e.g., A5) occurred during warmer phases like the globally known Medieval Warm Period (MWP). Taken together, these results show that glacier advances, in very humid and westerly wind influenced mountain range areas, are driven by a strong increase in accumulation mass-balance and only minor by temperature changes.

Finally, surface sediment data from the complete latitudinal range of the Chilean fjords show that alkenone SSTs do not represent annual mean temperatures. Instead, they resemble austral spring temperatures in the northern fjords and austral summer temperatures further south, suggesting a delayed productivity season of alkenone-producing nanoplankton towards the south related to both light and temperature (Manuscript 2). These results are consistent with new SST data suggesting a strong offset of the alkenone-derived SST toward the summer season in the high northern latitudes (*Prahl et al.*, 2010).

In conclusion, the three sediment cores analyzed in this study corroborate the high sensitivity of the Chilean Fjord Region to track past regional and global climate changes.

References

Abarzúa, A. M., C. Villagrán, and P. I. Moreno (2004), Deglacial and postglacial climate history in east-central Isla Grande de Chiloe, southern Chile (43ºS), *Quaternary Research*, *62*(1), 49-59.

Aceituno, P. (1988), On the functioning of the Southern Oscillation in the South American sector. Part I: Surface climate, *Montly Weather Review*, *116*, 505-524.

Ackert, R. P., R. A. Becker, B. S. Singer, M. D. Kurz, M. W. Caffee, and D. M. Mickelson (2008), Patagonian glacier response during the late glacial-holocene transition, *Science*, *321*, 392-395.

Ahn, J., and E. J. Brook (2008), Atmospheric CO2 and climate on millennial time scales during the last glacial period, *Science*, *322*, 83-85.

Alley, R. B., P. A. Mayewski, T. Sowers, M. Stuiver, K. C. Taylor, and P. U. Clark (1997), Holocene climatic instability: A prominent, widespread event 8200 yr ago, *Geology*, *25*(6), 483-486.

Andersen, C., N. Koc, A. Jennings, and J. T. Andrews (2004a), Nonuniform response of the major surface currents in the Nordic Seas to insolation forcing: Implications for the Holocene climate variability, *Paleoceanography*, *19*(2), PA 2003, doi:10.1029/2002PA000873.

Andersen, C., N. Koc, and M. Moros (2004b), A highly unstable Holocene climate in the subpolar North Atlantic: evidence from diatoms, *Quaternary Science Reviews*, *23*(20-22), 2155-2166.

Anderson, R. F., N. Kumar, R. A. Mortlock, P. N. Froelich, P. Kubik, B. Dittrich-Hannen, and M. Suter (1998), Late-Quaternary changes in productivity of the Southern Ocean, *Journal of Marine Systems*, *17*(1-4), 497-514.

Andrews, J. T., L. M. Smith, R. Preston, T. Cooper, and A. E. Jennings (1997), Spatial and temporal patterns of iceberg rafting (IRD) along the East Greenland margin, ca 68 degrees N, over the last 14 cal ka, *Journal of Quaternary Science*, *12*, 1-13.

Aniya, M., and H. Enomoto (1986), Glacier variations and their causes in the Northern Patagonia Icefield, Chile, since 1944, *Arctic and Alpine Research*, *18*(3), 307-316.

Aniya, M. (1988), Glacier inventory of the Northern Patagonia Icefield, Chile, and variations 1994/1995 to 1985/86, *Arctic and Alpine Research*, *20*(2), 179-187.

Aniya, M., H. Sato, R. Naruse, P. Skvarca, and G. Casassa (1996), The use of satellite and airborne imagery to inventory outlet glaciers of the Southern Patagonia Icefield, South America, *Photogrammetric Engineering and Remote Sensing*, *62*(12), 1361-1369.

Aniya, M., H. Sato, R. Naruse, P. Skvarca, and G. Casassa (1997), Recent glacier variations in the Southern Patagonia Icefield, South America, *Arctic and Alpine Research*, *29*(1), 1-12.

Aniya, M. (1999), Recent glacier variations of the Hielos Patagonicos, South America, and their contribution to sea-level change, *Arctic Antarctic and Alpine Research*, *31*(2), 165-173.

Aravena, J., and B. Luckman (2008), spatio-temporal rainfall patterns in Southern South America, *International Journal of Climatology*, *2008*.

Arz, H. W., F. Lamy, A. Ganopolski, N. Nowaczyk, and J. Patzold (2007), Dominant Northern Hemisphere climate control over millennial-scale glacial sea-level variability, *Quaternary Science Reviews*, *26*(3-4), 312-321.

Bard, E., F. Rostek, J. L. Turon, and S. Gendreau (2000), Hydrological impact of Heinrich events in the subtropical northeast Atlantic, *Science*, *289*, 1321-1324.

Barker, S., P. Diz, M. J. Vautravers, J. Pike, G. Knorr, I. R. Hall, and W. S. Broecker (2009), Interhemispheric Atlantic seesaw response during the last deglaciation, *Nature*, *457*, 1097-1102.

Bartole, R., E. Colizza, S. DeMuro, and W. Colautti (2000), The Pacific entrance of the Magellan Strait: preliminary results of a seismic and sampling survey, *Terra Antarctica Reports*, *4*, 81-94.

Bendle, J., and A. Rosell-Mele (2004), Distrubution of UK37 and UK'37 in the surface waters and sediments of the Nordic Seas: Implications for paleoceanography, *Geochemistry Geophysics Geosystems*, *5*(11), doi: 10.1029/2004GC00741.

Benn, D. I., and C. M. Clapperton (2000), Pleistocene glacitectonic landforms and sediments around central Magellan Strait, southernmost Chile: evidence for fast outlet glaciers with cold-based margins, *Quaternary Science Reviews*, *19*(6), 591-612.

Bentley, M. J., D. A. Hodgson, J. A. Smith, C. Ó. Cofaigh, E. W. Domack, R. D. Larter, S. J. Roberts, S. Brachfeld, A. Leventer, C. Hjort, C.-D. Hillenbrand, and J. Evans (2009), Mechanisms of Holocene palaeoenvironmental change in the Antarctic Peninsula region, *The Holocene*, *19*(1), 51-69.

Bianchi, C., and R. Gersonde (2004), Climate evolution at the last deglaciation: The role of the Southern Ocean, *Earth and Planetary Science Letters*, *228*(3-4), 407-424.

Bianchi, G., and I. McCave (1999), Holocene periodicity in North Atlantic climate and deep-ocean flow south of Iceland, *Nature*, *397*, 515-517.

Birks, C. J. A., and N. Koc (2002), A high-resolution diatom record of late-Quaternary sea-surface temperatures and oceanographic conditions from the eastern Norwegian Sea, *Boreas*, *31*(4), 323-344.

Blisniuk, P. M., L. A. Stern, C. P. Chamberlain, B. Idleman, and P. K. Zeitler (2005), Climatic and ecologic changes during Miocene surface uplift in the Southern Patagonian Andes, *Earth And Planetary Science Letters*, *230*(1-2), 125-142.

Blunier, T., J. Chappellaz, J. Schwander, A. Dällenbach, B. Stauffer, T. F. Stocker, D. Raynaud, J. Jouzel, H. B. Clausens, C. U. Hammer, and S. J. Johnsen (1998), Asynchrony of Antarctic and Greenland climate change during the last glacial period, *Nature*, *394*, 739-743.

Blunier, T., and E. J. Brook (2001), Timing of millennial-scale climate change in Antarctica and Greenland during the last glacial period, *Science*, *291*(5501), 109-112.

Bond, G., W. Showers, M. Cheseby, R. Lotti, P. Almasi, P. DeMenocal, P. Priore, H. Cullen, I. Hadjas, and G. Bonani (1997), A pervasive millenial-scale cycle in North Atlantic Holocene and Glacial climates, *Science*, *278*, 1257-1266.

Bond, G., B. Kromer, J. Beer, R. Muscheler, M. N. Evans, W. Showers, S. Hoffmann, R. Lotti-Bond, I. Hajdas, and G. Bonani (2001), Persistent solar influence on north Atlantic climate during the Holocene, *Science*, *294*, 2130-2136.

Brambati, A. (2000), Palaeoclimatic and Palaeoenvironmental Records in Sediments from the Southern Ocean (Strait of Magellan and Ross Sea), *Terra Antarctica Reports*, *4*, 1-41.

Broecker, W., G. Bond, M. Klas, E. Clark, and J. McManus (1992), Origin of the northern Atlantic's Heinrich events, *Climate Dynamics*, *6*(3-4), 265-273.

Broecker, W. S., and G. H. Denton (1989), The role of ocean-atmosphere reorganizations in glacial cycles, *Geochimical et Cosmochimica Acta*, *53*, 2465-2501.

Broecker, W. S., and G. H. Denton (1990), What drives glacial cycles?, *Scientific American*, *262*, 49-56.

Broecker, W. S. (1997), Thermohaline circulation, the Achilles heel of our climate system: Will man-made CO2 upset the current balance?, *Science*, *278*, 1582-1588.

Calvo, E., J. O. Grimalt, and E. Jansen (2002), High resolution U-37(K) sea surface temperature reconstruction in the Norwegian Sea during the Holocene, *Quaternary Science Reviews*, *21*(12-13), 1385-1394.

Casassa, G., K. Smith, A. Rivera, J. Araos, M. Schnirch, and C. Schneider (2002), Inventory of glaciers in isla Riesco, Patagonia, Chile, based on aerial photography and satellite imagery, in

Annals of Glaciology, Vol 34, 2002, edited by J. G. S. R. Winther, pp. 373-378.

Casassa, G., A. Rivera, W. Haeberlib, G. Jones, G. Kaser, P. Ribstein, and C. Schneider (2007), Current status of Andean glaciers, *Global and Planetary Change*, *59*(1-4), 1-9.

Cavieres, L., A. Peñaloza, and M. Arroyo (2000), Altitudinal vegetation belts iin the high-Andes of central Chile (33°S), *Revista Chilena de Historia Natural*, *73*, 331-344.

Chaigneau, A., and O. Pizarro (2005), Surface circulation and fronts of the South Pacific Ocean, east of 120 degrees W, *Geophysical Research Letters*, *32*, L08605, doi:10.1029/2004GL022070.

Charles, C. D., P. N. Froelich, M. A. Zibello, R. A. Mortlock, and J. J. Morley (1991), Biogenic opal in southern ocean sediment over the last 450,000 years: Implicactions for surface water chemistry and circulation, *Paleoceanography*, *6*, 697-728.

Ciais, P., J.R. Petit, J. Jouzel, C. Lorius, N.I. Barkov, V. Lipenkov, and V. Nicolaïev (1992), Evidence for an early Holocene climatic optimum in the Antarctic deep ice-core record, *Climate Dynamics*, *6*, 169-177.

Coronato, A., F. Coronato, E. Mazzoni, and M. Vásquez (2008), The Physical Geography of Patagonia and Tierra del Fuego, in *The Late Cenozoic of Patagonia and Tierra del Fuego*, edited by J. Rabassa, p. 513, Elvesier, Amsterdam.

Coronato, A. M., A. Meglioli, and J. Rabassa (2004), Glaciations in the Magellan Straits and Tierra del Fuego, Southernmost South America, in *Quaternary Glaciations: Extent and chronology. Part III: South America, Asia, Africa, Australia and Antarctica* edited by J. Ehlers and P. Gibbard, pp. 45-48, Elsevier, Amsterdam, Developments in Quaternary Sciences 2, 45-48.

Crowley, T. J. (1992), North Atlantic Deep Water cools the Southern Hemisphere, *Paleoceanography*, *7*, 489-497.

Dansgaard, W., S. J. Johnsen, H. B. Clausen, D. Dahl-Jensen, N. S. Gundestrup, and C. U. Hammer (1984), North Atlantic climatic oscillations revealed by deep Greenland ice cores, in *Climate Processes and Climate Sensitivity*, edited by J. E. Hansen and T. Takahashi, pp. 288-298, American Geophysical Union, Washington, D.C.

DaSilva, J. L., J. B. Anderson, and J. Stravers (1997), Seismic facies changes along a nearly continuous 24 degrees latitudinal transect: the fjords of Chile and the northern Antarctic peninsula, *Marine Geology*, *143*(1-4), 103-123.

De Pol-Holz, R., O. Ulloa, L. Dezileau, J. Kaiser, F. Lamy, and D. Hebbeln (2006), Melting of the Patagonian Ice Sheet and deglacial perturbations of the nitrogen cycle in the eastern South Pacific, *Geophysical Research Letters*, *33, L04704, doi:10.1029/2005GL024477*.

deMenocal, P., J. Ortiz, T. Guilderson, and M. Sarnthein (2000), Coherent High- and Low-Latitude Climate Variability During the Holocene Warm Period, *Science*, *288*, 2198-2202.

Denton, G. H., C. J. Heusser, T. V. Lowell, P. I. Moreno, B. G. Andersen, L. E. Heusser, C. Schluchter, and D. R. Marchant (1999), Interhemispheric linkage of paleoclimate during the last glaciation, *Geografiska Annaler Series a-Physical Geography*, *81A*(2), 107-153.

Diraison, M., P. R. Cobbold, D. Gapais, E. A. Rossello, and C. Le Corre (2000), Cenozoic crustal thickening, wrenching and rifting in the foothills of the southernmost Andes, *Tectonophysics*, *316*(1-2), 91-119.

Divine, D. V., N. Koc, E. Isaksson, S. Nielsen, X. Crosta, and F. Godtliebsen (2010), Holocene Antarctic climate variability from ice and marine sediment cores: Insights on ocean-atmosphere interaction, *Quaternary Science Reviews*, *29*, 303-312.

EPICA Community Members (2004), Eight glacial cycles from an Antarctic ice core, *Nature*, *429*, 623-628.

EPICA Community Members (2006), One-to-one coupling of glacial climate variability in Greenland and Antarctica, *Nature*, *444*, 195-198.

Fairbanks, R. G. (1989), A 17,000 year glacio-eustatic sea-level record - Influence of glacial

melting rates on the Younger Dryas Event and deep-ocean Circulation, *Nature*, *342*, 637-642.

Fesq-Martin, M., A. Friedmann, M. Peters, J. Behrmann, and R. Kilian (2004), Late-glacial and Holocene vegetation history of the Magellanic rain forest in southwestern Patagonia, Chile, *Vegetation History and Archaeobotany*, *13*(4), 249-255.

Fischer, H., J. Schmitt, D. Luthi, T. F. Stocker, T. Tschumi, P. Parekh, F. Joos, P. Kohler, C. Volker, R. Gersonde, C. Barbante, M. Le Floch, D. Raynaud, and E. Wolff (2010), The role of Southern Ocean processes in orbital and millennial CO2 variations - A synthesis, *Quaternary Science Reviews*, *29*(1-2), 193-205.

Francois, R., M. A. Altabet, E. F. Yu, D. M. Sigman, M. P. Bacon, M. Frank, G. Bohrmann, G. Bareille, and L. D. Labeyrie (1997), Contribution of Southern Ocean surface-water stratification to low atmospheric CO2 concentrations during the last glacial period, *Nature*, *389*, 929-935.

Ganopolski, A., and S. Rahmstorf (2001), Rapid changes of glacial climate simulated in a coupled climate model, *Nature*, *409*, 153-158.

Garreaud, R. D. (2007), Precipitation and circulation covariability in the extratropics, *Journal of Climate*, *20*(18), 4789-4797.

Genty, D., D. Blamart, R. Ouahdi, M. Gilmour, A. Baker, J. Jouzel, and S. Van-Exter (2003), Precise dating of Dansgaard-Oeschger climate oscillations in western Europe from stalagmite data, *Nature*, *421*, 833-837.

Gersonde, R., X. Crosta, A. Abelmann, and L. Armand (2005), Sea-surface temperature and sea ice distribution of the Southern Ocean at the EPILOG Last Glacial Maximum - a circum-Antarctic view based on siliceous microfossil records, *Quaternary Science Reviews*, *24*(7-9), 869-896.

Gersonde, R., and Shipboard Scientists (2010), Report of FS Polarstern ANT-XXVI/2 cruise, Punta Arenas - Wellington, Alfred Wegener Institute for Polar and Marine Research, Bremerhaven.

Glasser, N., and K. Jansson (2008), The Glacial Map of southern South America, *Journal of Maps*, 175-196.

Glasser, N. F., S. Harrison, V. Winchester, and M. Aniya (2004), Late Pleistocene and Holocene palaeoclimate and glacier fluctuations in Patagonia, *Global and Planetary Change*, *43*(1-2), 79-101.

Glasser, N. F., K. N. Jansson, S. Harrison, and J. Kleman (2008), The glacial geomorphology and Pleistocene history of South America between 38 degrees S and 56 degrees S, *Quaternary Science Reviews*, *27*(3-4), 365-390.

Hajdas, I., G. Bonani, P. I. Moreno, and D. Ariztegui (2003), Precise radiocarbon dating of Late-Glacial cooling in mid-latitude South America, *Quaternary Research*, *59*(1), 70-78.

Hebbeln, D., and Shipboard Scientists (1995), *Cruise report of R/V Sonne Cruise SO-102, Valparaiso (Chile) - Valparaiso (Chile). May 09 - June 28, 1995*, 126 pp., Berichte, Fachbereich Geowissenschaften, Universität Bremen, Bremen.

Hebbeln, D., M. Marchant, T. Freudenthal, and G. Wefer (2000), Surface sediment distribution along the Chilean continental slope related to upwelling and productivity, *Marine Geology*, *164*(3-4), 119-137.

Hebbeln, D., and s. Scientists (2001), *PUCK: Report and preliminary results of R/V Sonne cruise SO156, Valparaiso (Chile)-Talcahuano (Chile), March 29 –May 14, 2001*, 195 pp., Berichte, Fachbereich Geowissenschaften, Universität Bremen, Bremen.

Hebbeln, D., M. Marchant, and G. Wefer (2002), Paleoproductivity in the southern Peru-Chile Current through the last 33,000 years, *Marine Geology*, *186*, 487-504.

Hebbeln, D., F. Lamy, M. Mohtadi, and H. Echtler (2007), Tracking the impact of glacial/interglacial climate variability on erosion of the Southern Andes, *Geology*, *35*, 131-134.

Heinrich, H. (1988), Origin and consequences of cyclic ice-rafting in the northeast Atlantic ocean, during the past 130,000 years, *Quaternary Research*, *29*, 143-152.

Heusser, L., and C. Heusser (2006), Submillennial palynology and palaeoecology of the last glaciation at Taiquemo (~50,000 cal yr, MIS 2-4) in southern Chile, *Quaternary Science Reviews, 25*(5-6), 446.

Heusser, L., C. Heusser, and N. Pisias (2006), Vegetation and climate dynamics of southern Chile during the past 50,000 years: results of ODP Site 1233 pollen analysis, *Quaternary Sciece Reviews, 25*(5-6), 474-485.

Hodell, D. A., S. L. Kanfoush, A. Shemesh, X. Crosta, C. D. Charles, and T. P. Guilderson (2001), Abrupt cooling of Antarctic surface waters and sea ice expansion in the South Atlantic sector of the Southern Ocean at 5000 cal yr B.P., *Quaternary Research*, *56*, 191-198.

Hulton, N., D. Sugden, A. Payne, and C. Clapperton (1994), Glacier modeling and the climate of Patagonia during the Last Glacial Maximum., *Quaternary Research*, *42*, 1-19.

Hulton, N. R. J., R. S. Purves, R. D. McCulloch, D. E. Sugden, and M. J. Bentley (2002), The Last Glacial Maximum and deglaciation in southern South America, *Quaternary Science Reviews*, *21*(1-3), 233-241.

Iizuka, y., T. Hondoh, and Y. Fujii (2008), Antarctic sea ice extent during the Holocene reconstructed from inland ince core evidence, *Journal of Geophysical Research*, *113, D15114, doi:10.1029/2007JD009326*.

Ingram, B. L., and J. R. Southon (1996), Reservoir ages in eastern Pacific coastal and estuarine waters, *Radiocarbon*, *38*(3), 573-582.

Jenny, B., B. L. Valero-Garces, R. Villa-Martinez, R. Urrutia, M. Geyh, and H. Veit (2002), Early to Mid-Holocene Aridity in Central Chile and the Southern Westerlies: The Laguna Aculeo Record (34(deg)S), *Quaternary Research*, *58*(2), 160-170.

Kaiser, J., F. Lamy, and D. Hebbeln (2005), A 70-kyr sea surface temperature record off southern Chile (ODP Site 1233). *Paleoceanography*, *20, PA4009*, doi:10.1029/2005PA001146.

Kaiser, J., E. Schefuss, F. Lamy, M. Mohtadi, and D. Hebbeln (2008), Glacial to Holocene changes in sea surface temperature and coastal vegetation in north central Chile: high versus low latitude forcing, *Quaternary Science Reviews*, *27*(21-22), 2064-2075.

Kaiser, J., and F. Lamy (2010), Links between Patagonian Ice Sheet fluctuations and Antarctic dust variability during the last glacial period (MIS 4-2), *Quaternary Science Reviews*, *29*, 1464-1471.

Kilian, R., O. Baeza, T. Steinke, M. Arevalo, C. Rios, and C. Schneider (2007a), Late Pleistocene to Holocene marine transgression and thermohaline control on sediment transport in the western Magellanes fjord system of Chile (53 degrees S), *Quaternary International*, *161*, 90-107.

Kilian, R., C. Schneider, J. Koch, M. Fesq-Martin, H. Biester, G. Casassa, M. Arevalo, G. Wendt, O. Baeza, and J. Behrmann (2007b), Palaeoecological constraints on late Glacial and Holocene ice retreat in the Southern Andes (53 degrees S), *Global and Planetary Change*, *59*(1-4), 49-66.

Kim, J. H., R. R. Schneider, D. Hebbeln, P. J. Muller, and G. Wefer (2002), Last deglacial sea-surface temperature evolution in the Southeast Pacific compared to climate changes on the South American continent, *Quaternary Science Reviews*, *21*(18-19), 2085-2097.

Klump, J., D. Hebbeln, and G. Wefer (2001), High concentrations of biogenic barium in Pacific sediments after Termination I -A signal of changes in productivity and deep water chemistry, *Marine Geology*, *177*(1-11).

Knorr, G., and G. Lohmann (2003), Southern Ocean origin for the resumption of Atlantic thermohaline circulation during deglaciation, *Nature*, *424*, 532-536.

Knutti, R., J. Flückiger, T. Stocker, and A. Timmermann (2004), Strong hemispheric coupling of glacial climate through freshwater discharge and ocean circulation, *Nature*, *430*, 851-856.

Kumar, N., R. F. Anderson, R. A. Mortlock, P. N. Froelich, P. Kubik, B. Dittrichhannen, and M. Suter (1995), Increased biological productivity and export productionn in the glacial Southern Ocean *Nature*, *378*(6558), 675-680.

Laj, C., C. Kissel, R. Leonhardt, M. Winklofer, A. Ferk, K. Fabian, and U. Ninemann (2009), Towards a global view of the laschamp excursion, *Geophysical Research Abstracts*, *11, EGU General Assembly, 2009*.

Lamy, F., D. Hebbeln, and G. Wefer (1998), Late quaternary precessional cycles of terrigenous sediment input off the Norte Chico, Chile (27.5 degrees S) and palaeoclimatic implications, *Palaeogeography Palaeoclimatology Palaeoecology*, *141*(3-4), 233-251.

Lamy, F., D. Hebbeln, and G. Wefer (1999), High-resolution marine record of climatic change in mid- latitude Chile during the last 28,000 years based on terrigenous sediment parameters, *Quaternary Research*, *51*(1), 83-93.

Lamy, F., J. Klump, D. Hebbeln, and G. Wefer (2000), Late Quaternary rapid climate change in northern Chile, *Terra Nova*, *12*(1), 8-13.

Lamy, F., D. Hebbeln, U. Rohl, and G. Wefer (2001), Holocene rainfall variability in southern Chile: a marine record of latitudinal shifts of the Southern Westerlies, *Earth and Planetary Science Letters*, *185*(3-4), 369-382.

Lamy, F., C. Ruhlemann, D. Hebbeln, and G. Wefer (2002), High- and low-latitude climate control on the position of the southern Peru-Chile Current during the Holocene, *Paleoceanography*, *17*(2), doi:10.1029/2001PA000727.

Lamy, F., J. Kaiser, U. Ninnemann, D. Hebbeln, H. Arz, and J. Stoner (2004), Antarctic Timing of Surface Water Changes off Chile and Patagonian Ice Sheet Response, *Science*, *304*, 1959-1962.

Lamy, F., J. Kaiser, H. W. Arz, D. Hebbeln, U. Ninnemann, O. Timm, A. Timmermann, and J. R. Toggweiler (2007), Modulation of the bipolar seesaw in the southeast pacific during Termination 1, *Earth and Planetary Science Letters*, *259*(3-4), 400-413.

Lamy, F., R. Kilian, H. W. Arz, J. P. Francois, J. Kaiser, M. Prange, and T. Steinke (2010), Holocene changes in the position and intensity of the southern westerly wind belt, *Nature Geoscience*, *3*, 695-699.

Latorre, C., P. Moreno, G. Vargas, A. Maldonado, R. Villa-Martínez, J. J. Armesto, C. Villagrán, M. Pino, L. Núñez, and M. Grosjean (2007), Late Quaternary environments and paleoclimate, in *The Geology of Chile*, edited by W. M. Gibbons, T., eds, pp. 390-328, The London Geological Society Press, London.

Lowell, T. V., C. J. Heusser, B. G. Andersen, P. I. Moreno, A. Hauser, L. E. Heusser, C. Schlüchter, D. R. Marchant, and G. H. Denton (1995), Interhemispheric correlation of Late Pleistocene glacial events, *Science*, *269*, 1541-1549.

MacAyeal, D. R. (1993), Binge/purge oscillations of the Laurentide ice sheet as a cause of the North Atlantic's Heinrich events, *Paleoceanography*, *8*(6), 775-784.

Maldonado, A., and C. Villagran (2002), Paleoenvironmental Changes in the Semiarid Coast of Chile (~32(deg)S) during the Last 6200 cal Years Inferred from a Swamp-Forest Pollen Record, *Quaternary Research*, *58*(2), 130-138.

Marchal, O., I. Cacho, T. F. Stocker, J. O. Grimalt, E. Calvo, B. Martrat, N. Shackleton, M. Vautravers, E. Cortijo, S. Van Kreveld, C. Anderson, N. Koc, M. Chapman, L. Sbaffi, J. C. Duplessy, M. Sarnthein, J. L. Turon, J. Duprat, and E. Jansen (2002), Apparent long-term cooling of the sea surface in the northeast Atlantic and Mediterranean during the Holocene, *Geochimica et Cosmochimica Acta*, *66*(15A), A482-A482.

Marchant, M., D. Hebbeln, and G. Wefer (1999), High resolution planktic foraminiferal record of the last 13,000 years from the upwelling area off Chile., *Marine Geology*, *161*, 115-128.

Marden, C. J., and C. M. Clapperton (1995), Fluctuations of the South Patagonian ice-field during the Last Glaciation and the Holocene, *Journal of Quaternary Science*, *10*(3), 197-209.

MARGO Project Members (2009), Constraints on the magnitude and patterns of ocean cooling at the Last Glacial Maximum, *Nature Geoscience*, *2*(411), 127-132.

Martin, J. H. (1990), Glacial-Interglacial CO2 change: The Iron Hypothesis, *Paleoceanography*, *5*(1), 1-13.

Mashiotta, T. A., D. W. Lea, and H. J. Spero (1999), Glacial-interglacial changes in Subantarctic sea surface temperature and delta O-18-water using foraminiferal Mg, *Earth and Planetary Science Letters*, *170*(4), 417-432.

Masson-Delmotte, V., B. Stenni, and J. Jouyel (2004), Common millennial-scale variability of Antarctic and Southern Ocean temperatures during the past 5000 years reconstructed from the EPICA Dome C ice core, *The Holocene*, *14*, 145-151.

Masson, V., F. Vimeux, J. Jouzel, V. Morgan, M. Delmotte, P. Ciais, C. Hammer, S. Johnsen, V. Y. Lipenkov, E. Mosley-Thompson, J. R. Petit, E. J. Steig, M. Stievenard, and R. Vaikmae (2000), Holocene climate variability in Antarctica based on 11 ice-core isotopic records, *Quaternary Research*, *54*(3), 348-358.

Mayewski, P. A., E. E. Rohling, J. C. Stager, W. Karlén, K. A. Maasch, L. D. Meeker, E. A. Meyerson, F. Gasse, S. van Kreveld, K. Holmgren, L. Lee-Thorp, G. Rosqvist, F. Rack, M. Staubwasser, R. Schneider, and
E. Steig (2004), Holocene climate variability, *Quaternary Research*, *62*, 243-255.

McCulloch, R. D., M. J. Bentley, R. S. Purves, N. R. J. Hulton, D. E. Sugden, and C. M. Clapperton (2000), Climatic inferences from glacial and palaeoecological evidence at the last glacial termination, southern South America, *Journal of Quaternary Sciences*, *15*(4), 409-417.

Melis, R., N. Pugliese, G. Salvi, S. Boschetti, and F. Pizzolato (2000), Micropalaeontological results of cores located in the Western Magellan Strait (MB91/47-MD91/40-MB/91/54R), *Terra Antarctica Reports*, *4*, 75-80.

Miller, A. (1976), The climate of Chile, in *World Survey of Climatology*, edited by W. Schwerdtfeger, pp. 113-145, Elsevier, Amsterdam.

Mix, A. C., R. Tiedemann, P. Blum, and S. Scientists (2003), *Southeast Pacific paleoceanographic transects*, 145 pp., Ocean Drilling Program, College Station, TX.

Mohtadi, M., and D. Hebbeln (2004), Mechanisms and variations of the paleoproductivity off northern Chile (24°S-33°S) during the last 40,000 years, *Paleoceanography*, *19*, PA2023.

Mohtadi, M., O. Romero, and D. Hebbeln (2004), Changing marine productivity off northern Chile during the past 19 000 years: a multivariable approach, *Journal of Quaternary Sciences*, *19*, 347–360.

Mohtadi, M., D. Hebbeln, and M. Marchant (2005), Upwelling and productivity along the Peru-Chile Current derived from faunal and isotopic compositions of planktic foraminifera in surface sediments, *Marine Geology*, *216*(3), 107-126.

Mohtadi, M., O. Romero, J. Kaiser, and D. Hebbeln (2007), Cooling of the southern high latitudes during the Medieval Period and its effect on ENSO, *Quaternary Science Reviews*, *26*, 1055-1066.

Moreno, P. I. (1997), Vegetation and climate near Lago Llanquihue in the Chilean Lake District between 20200 and 9500 14C yr BP, *Journal of Quaternary Science*, *12*, 485-500.

Moreno, P. I., T. V. Lowell, G. L. Jacobson, and G. H. Denton (1999), Abrupt vegetation and climate changes during the last glacial maximum and last termination in the Chilean Lake District: A case study from Canal de la Puntilla (41 degrees S), *Geografiska Annaler Series a-Physical Geography*, *81A*(2), 285-311.

Moreno, P. I., G. L. Jacobson, T. V. Lowell, and G. H. Denton (2001), Interhemispheric climate links revealed by a late-glacial cooling episode in southern Chile, *Nature*, *409*, 804-808.

Moreno, P. I., and A. L. León (2003), Abrupt vegetation changes during the last glacial to Holocene transition in mid-latitude South America, *Journal of Quaternary Science*, *18*(8), 787-800.

Moreno, P. I. (2004), The Last Transition from extreme glacial to extreme interglacial climate in NW Patagonia: regional and global implications, paper presented at Eos Trans. AGU, 85 (47), Fall Meet. Suppl.

Moreno, P. I., J. P. Francois, R. P. Villa-Martinez, and C. M. Moy (2009), Millennial-scale variability in Southern Hemisphere westerly wind activity over the last 5000 years in SW

Patagonia, *Quaternary Science Reviews*, *28*(1-2), 25-38.

Moros, M., P. De Deckker, E. Jansen, K. Perner, and R. Telford (2009), Holocene climate variability in the Southern Ocean recorded in a deep-sea sediment core off South Australia, *Quaternary Sciece Reviews*, *28*, 1932-1940.

Mortlock R., and P. N. Froelich (1989), A simple method for the rapid determination of biogenic opal in pelagic marine sediments, *Deep-Sea Research*, *36*(9), 1415-1426.

Moy, C. M., R. B. Dunbar, P. I. Moreno, J. P. Francois, R. Villa-Martinez, D. M. Mucciarone, T. P. Guilderson, and R. D. Garreaud (2008), Isotopic evidence for hydrologic change related to the westerlies in SW Patagonia, Chile, during the last millennium, *Quaternary Science Reviews*, *27*(13-14), 1335-1349.

Müller, P. J., and R. Schneider (1993), An automated leaching method for the determination of opal in sediments and particulate matter, *Deep-Sea Research*, *40*(3), 425-444.

Müller, P. J., G. Kirst, G. Ruhland, I. von Storch, and A. Rosell-Mele (1998), Calibration of the alkenone paleotemperature index UK'37 based on core-tops from the eastern South Atlantic and the global ocean (60°N-60°S). *Geochimica et Cosmochimica Acta*, *62*, 1757-1772.

Muñoz, R. C., and R. D. Garreaud (2005), Dynamics of the low-level jet off the west coast of subtropical South America, *Monthly Weather Review*, *133*(12), 3661-3677.

New, M., M. Todd, M. Hulme, and P. Jones (2001), Precipitation measurements and trends in the twentieth century, *International Journal of Climatology*, *21*(15), 1899-1922, doi:1810.1002/joc.1680.

Nielsen, S., N. Koc, and X. Crosta (2004), Holocene climate in the Atlantic sector of the Southern Ocean: Controlled by insolation or oceanic circulation?, *Geology*, *32*(4), 317-320.

Ninnemann, U. S., and C. D. Charles (2002), Changes in the mode of Southern Ocean circulation over the last glacial cycle revealed by foraminiferal stable isotopic variability, *Earth and Planetary Science Letters*, *201*(2), 383-396.

North Greenland Ice Core Project members (2004), High-resolution record of Northern Hemisphere climate extending into the last interglacial period, *Nature*, *431*, 147-151.

O'Brien, S. R., P. A. Mayewski, L. D. Meeker, D. A. Meese, M. S. Twickler, and S. I. Whitlow (1995), Complexity of Holocene Climate as Reconstructed from Greenland Ice Core, *Science*, *270*, 1962-1964.

Orsi, A. H., T. Whitworth, and W. D. Nowlin (1995), On the meridional extent and fronts of the Antarctic Circumpolar Current, *Deep-Sea Research Part I*, *42*(5), 641-673.

Peeters, F. J. C., R. Acheson, G. J. A. Brummer, W. P. M. de Ruijter, R. R. Schneider, G. M. Ganssen, E. Ufkes, and D. Kroon (2004), Vigorous exchange between the Indian and Atlantic oceans at the end of the past five glacial periods, *Nature*, *430*, 661-665.

Petit, J. R., J. Jouzel, D. Raynaud, N. I. Barkov, J. M. Barnola, I. Basile, M. Bender, J. Chappellaz, M. Davis, G. Delaygue, M. Delmotte, V. M. Kotlyakov, M. Legrand, V. Y. Lipenkov, C. Lorius, L. Pepin, C. Ritz, E. Saltzman, and M. Stievenard (1999), Climate and atmospheric history of the past 420,000 years from the Vostok ice core, Antarctica, *Nature*, *399*, 429-436.

Prahl, F. G., and S. G. Wakeham (1987), Calibration of unsaturation patterns in long-chain ketone compositions for paleotemperature assessment, *Nature*, *330*, 367-369.

Prahl, F. G., L. A. Muehhausen, and D. L. Zahnle (1988), Further evaluation of long-chain alkenones as indicators of paleoceanographic conditions, *Geochimica et Cosmochimica Acta*, *52*, 2303-2310.

Prahl, F. G., J. Dymond, and M. A. Sparrow (2000), Annual biomarker record for export production in the central Arabian Sea, *Deep-Sea Research Part Ii-Topical Studies in Oceanography*, *47*(7-8), 1581-1604.

Prahl, F. G., J.-F. Rontani, N. Zabeti, S. E. Walinsky, and M. A. Sparrow (2010), Systematic pattern in UK'37 - Temperature residuals for

surface sediments from high latitude and other oceanographic settings, *Geochimica et Cosmochimica Acta*, *74*, 131-143.

Rabassa, J., and C. Clapperton (1990), Quaternary Glaciations of the Southern Andes, *Quaternary Sciece Reviews*, *9*, 153-174.

Rabassa, J. (2008), Late Cenozoic Glaciations in Patagonia and Tierra del Fuego, in *The Late Cenozoic of Patagonia and Tierra del Fuego. Developments in Quaternary Science 11 series,*, edited by J. Rabassa, pp. 151-204, Elsevier, Amsterdam.

Reimer, P. J., M. G. L. Baillie, E. Bard, A. Bayliss, J. W. Beck, P. G. Blackwell, C. B. Ramsey, C. E. Buck, G. S. Burr, R. L. Edwards, M. Friedrich, P. M. Grootes, T. P. Guilderson, I. Hajdas, T. J. Heaton, A. G. Hogg, K. A. Hughen, K. F. Kaiser, B. Kromer, F. G. McCormac, S. W. Manning, R. W. Reimer, D. A. Richards, J. R. Southon, S. Talamo, C. S. M. Turney, J. van der Plicht, and C. E. Weyhenmeye (2009), INTCAL09 AND MARINE09 RADIOCARBON AGE CALIBRATION CURVES, 0-50,000 YEARS CAL BP, *Radiocarbon*, *51*(4), 1111-1150.

Rignot, E., A. Rivera, and G. Casassa (2003), Contribution of the Patagonia Icefields of South America to sea level rise, *Science*, *302*(5644), 434-437.

Rosell-Melé, A. (1998), Interhemispheric appraisal of the value of alkenone indices as temperature and salinity proxies in high-latitude locations, *Paleoceanography*, *13*(6), 694-703.

Rosell-Melé, A., E. Jansen, and M. Weinelt (2002), Appraisal of a molecular approach to infer variations in surface ocean freshwater inputs into the North Atlantic during the last glacial, *Global and Planetary Change*, *34*(3-4), 143-152.

Schilt, A., M. Baumgartner, T. Blunier, J. Schwander, R. Spahni, H. Fischer, and T. F. Stocker (2010), Glacial-interglacial and millennial-scale variations in the atmospheric nitrous oxide concentration during the last 800,000 years, *Quaternary Science Reviews*, *29*(1-2), 182-192.

Schneider, C., M. Glaser, R. Kilian, A. Santana, N. Butorovic, and G. Casassa (2003), Weather observations across the Southern Andes at 53(degrees)S, *Physical Geography*, *24*(2), 97-119.

Schulz, H. M., A. Schoner, and K. C. Emeis (2000), Long-chain alkenone patterns in the Baltic Sea - an ocean-freshwater transition, *Geochimica et Cosmochimica Acta*, *64*(3), 469-477.

Schulz, M., and A. Paul (2002), Holocene Climate Variability on Centennial-to-Millennial Time Scales: 1. Climate Records from the North-Atlantic Realm, in *Climate Development and History of the North Atlantic Realm*, edited by G. Wefer, Berger, W., Behre K-E. Jansen E., pp. 41-54, Springer -Verlag Berlin Heidelberg.

Sepúlveda, J., S. Pantoja, K. A. Hughen, S. Bertrand, D. Figueroa, T. León, J. Drenzek, and C. Lange (2009), Late Holocene sea-surface temperature and precipitation variability in northern Patagonia, Chile (Jacaf Fjord, 44ºS), *Quaternary Research*, *72*, 400-409.

Shaffer, G., S. Salinas, O. Pizarro, A. Vega, and S. Hormazabal (1995), Currents in the deep ocean off Chile (30°S). *Deep-Sea Research*, *42*, 425-436.

Sievers, H. A., and N. Silva (2008), Water masses and circulation in austral Chilean channels and fjords, in *Progress in the oceanographic knowledge of Chilean interior waters, from Puerto Montt to Cape Horn*, edited by N. Silva and S. Palma, pp. 53-, Comité Oceanográfico Nacional - Pontificia Universidad Católica de Valparaíso.

Silva, N., H. A. Sievers, and R. Prado (1995), Características oceanográficas y una proposición de circulación, para algunos canales australes de Chile entre 41°20´S, 46°40´S, *Revista Biología Marina de Valparaíso*, *30*, 207-254.

Silva, N., C. Calvete, and H. A. Sievers (1997), Características oceanográficas, físicas y químicas de canales australes chilenos entre Puerto Montt y laguna San Rafael (Cimar FIORDO 1), *Ciencia y Tecnologia del Mar*, *20*, 23-106.

Silva, N., C. Calvete, and H. A. Sievers (1998), Masas de agua y circulación general para algunos canales australes chilenos entre Puerto

Montt y laguna San Rafael (Crucero CIMAR-Fiordo 1), *Ciencia y Tecnologia del Mar*, *21*, 17-48.

Silva, N., and R. Prego (2002), Carbon and nitrogen spatial segregation and stoichiometry in the surface sediments of southern Chilean inlets (41º-56ºS), *Estuarine Coastal and Shelf Science*, *55*, 764-775.

Singer, B. S., R. P. Ackert, and H. Guillou (2004), Ar-40/Ar-19 and K-Ar chronology of Pleistocene glaciations in Patagonia, *Geological Society of America Bulletin*, *116*(3-4), 434-450.

Steig, E. J., and R. B. Alley (2002), Phase relationships between Antarctic and Greenland climate records, in *Annals of Glaciology, Vol 35*, edited by E. W. Wolff, pp. 451-456.

Stephens, B. B., and R. F. Keeling (2000), The influence of Antarctic sea ice on glacial-interglacial CO2 variations, *Nature*, *404*(6774), 171-174.

Strub, P. T., J. M. Mesias, V. Montecino, J. Ruttlant, and S. Salinas (1998), Coastal ocean circulation off Western South America., in *The global coastal ocean. Regional studies and syntheses*, edited by A. R. Robinson and K. H. Brink, pp. 273-315, Wiley, New York.

Sugden, D. E., N. R. J. Hulton, and R. S. Purves (2002), Modelling the inception of the Patagonian icesheet, *Quaternary International*, *95-6*, 55-64.

Sugden, D. E., R. D. McCulloch, A. J. M. Bory, and A. S. Hein (2009), Influence of Patagonian glaciers on Antarctic dust deposition during the last glacial period, *Nature Geoscience*, *2*(4), 281-285.

Toggweiler, J. R. (1999), Variation of atmospheric CO2 by ventilation of the ocean's deepest water, *Paleoceanography*, *14*(5), 571-588.

Toggweiler, J. R., J. L. Rusell, and S. R. Carson (2006), Midlatitude westerlies, atmospheric CO2, and climate change during ice ages, *Paleoceanography*, *21*, doi:10.1029/2005PA001154.

Toggweiler, J. R. (2009), Shifting Westerlies, *Science*, *323*(5920), 1434-1435.

Villa-Martinez, R., C. Villagran, and B. Jenny (2003), The last 7500 cal yr BP of westerly rainfall in Central Chile inferred from a high-resolution pollen record from Laguna Aculeo (34 degrees S), *Quaternary Research*, *60*(3), 284-293.

Villa-Martinez, R., and P. I. Moreno (2007), Pollen evidence for variations in the southern margin of the westerly winds in SW Patagonia over the last 12,600 years, *Quaternary Research*, *68*(3), 400-409.

Villagran, C. (2001), A model for the history of vegetation of the Coastal Range of central-southern Chile: Darwin`s glacial hypothesis, *Revista Chilena de Historia Natural,* 74, 793-803.

Villagrán, C. (1988), Expansion of Magellanic moorland during the late Pleistocene: palynological evidence from northern Isla de Chiloe, Chile, *Quaternary Research*, *30*, 304-314.

Villagrán, C. (1990), Glacial climates and their effects on the history of the vegetation of Chile: A synthesis based on palynological evidence from Isla de Chiloé, *Review of Palaeobotany and Palynology*, *65*, 17-24.

Villagrán, C., and J. Varela (1990), Palynological evidence for increased aridity on the Central Chilean coast during the Holocene, *Quaternary Research*, *34*, 198-207.

Weaver, A. J., O. A. Saenko, P. U. Clark, and J. X. Mitrovica (2003), Meltwater pulse 1A from Antarctica as a trigger of the bolling- allerod warm interval, *Science*, *299*(5613), 1709-1713.

Williams, G., and K. Bryan (2006), Ice Age Winds: An aquaplanet model, *Journal of Climate*, *19*, 1706-1715.